ABSTRACT

GRENKO, JUDITH ANN. Characterization of Homoepitaxially-Grown AlGaN/GaN Heterostructures. (Under the direction of Dr. Mark A. L. Johnson).

The work in this dissertation is aimed at determining whether homoepitaxial growth of AlGaN/GaN heterostructures will significantly improve the 2DEG transport properties. Van der Pauw Hall measurements at RT and 77K were used to evaluate the 2DEG transport properties of AlGaN/GaN heterostructures grown on on-axis and vicinal surfaces of (0001) semi-insulating bulk GaN and vicinal surfaces of (0001) and $(1\bar{1}00)$ n-type bulk GaN. Analytical techniques such as SEM, CV, AFM, HRXRD, PL, CL, Raman spectroscopy, and TEM were used to determine structural, optical, and electronic properties of these heterostructures and to explain the Hall mobility and sheet carrier density.

AlGaN/GaN heterostructures with RT 2DEG sheet densities and mobilities modulated by the presence of a large silicon areal density (1.6×10^{14} cm^{-2}) at the bulk GaN/epitaxial interface were grown. The transport properties of the 2DEG were improved by eliminating Si from the AlGaN barrier and an unintentional 1000 ppm of Al from the n.i.d. GaN buffer. Hall sheet densities of 10^{13} cm^{-2} and mobilities of 2065 $cm^2V^{-1}sec^{-1}$ were comparable to the best reported and were only 30% lower than the value predicted for AlGaN/GaN heterostructures grown with atomically smooth interfaces and dislocation densities $< 2 \times 10^7$ cm^{-2}.

Magnesium (Mg) doping was incorporated into the GaN layer near the bulk/epitaxial interface in an attempt to compensate free electrons from the interfacial charge layer After

the 800^{o} C ex-situ anneal, sheet carrier densities on the order of 10^{15} cm^{-2} and RT and 77K mobilities of 567 $cm^{2}V^{-1}sec^{-1}$ and 2540 $cm^{2}V^{-1}sec^{-1}$, respectively, were determined by Hall measurements. Raman spectroscopy provided evidence for increased Mg donors and nitrogen vacancy formation in these heterostructures and was consistent with expected lower formation energy in the presence of Mg.

Characterization of Homoepitaxially-Grown AlGaN/GaN Heterostructures

by
Judith A. Grenko

A dissertation submitted to the Graduate Faculty
of North Carolina State University
in partial fulfillment of the
requirements for the Degree of
Doctor of Philosophy

Materials Science and Engineering

Raleigh, North Carolina

2009

APPROVED BY:

_____	_____
Dr. Mark A. L. Johnson Committee Chair	Dr. Doug W. Barlage
_____	_____
Dr. Jay Narayan	Dr. John Hren

DEDICATION

To Claude, Anne, and Lew

BIOGRAPHY

Judith Ann Grenko was born and reared in Reading, Pennsylvania. She attended Governor Mifflin High School in Shillington, PA. After high school, she enrolled at the University of Pittsburgh in Pittsburgh, PA. She earned her Bachelor of Science in Chemical Engineering in 1982. She continued her academic studies at the University of Pittsburgh and earned dual Master of Science degrees in Chemical and Petroleum Engineering in 1984.

Upon completion of her Master degree work, Judith joined the Lightwave Components division of AT&T Microelectronics in Reading, PA. Her industrial experience comprised wafer fabrication of optoelectronic devices including positive-intrinsic-negative (PIN) diodes, light emitting diodes (LEDs) and light amplification by stimulated emission of radiation (LASER) devices for long wavelength applications as well as the epitaxial growth of 1.3 μm, 1.5 μm distributed-feedback (DFB) and electroabsorption-modulated (EML) lasers by organometallic vapor phase epitaxy. Judith received the Optical Society of America Award for Outstanding Excellence in 2000.

After eighteen years of industrial experience, Judith decided to pursue her Doctor of Philosophy degree at North Carolina State University. She joined the group of Dr. Zlatko Sitar and published her research on the selective-photoelectrochemical etching (PEC) of AlGaN/GaN and AlN/GaN structures. Judith was offered the opportunity to join the group of Dr. Mark A. L. Johnson to pursue her interest in the epitaxial growth of electronic devices of III-V wide bandgap materials. Her work focused on the homoepitaxial growth of AlGaN/GaN heterostructures on low dislocation density substrates with an interest in improving their two-dimensional electron gas transport properties.

ACKNOWLEDGEMENTS

I would thank Joe Matthews for his tireless effort in maintaining the laboratory equipment in the Montieth Research Center device fabrication clean room, MOCVD equipment room and device testing room. I am grateful to him for his processing of the ohmic contact metals on the AlGaN/GaN heterostructures grown on vicinal semi-insulating substrates as well as on the non-polar and polar n-type substrates. Little did I realize that his willing assistance in this contact metallization, opened a rich opportunity for me to understand the interplay of epitaxy and device fabrication issues in III-V wide bandgap materials. I would also like to thank Joe for the myriad discussions about life, politics and the economy that made the day to day wide bandgap research a thought-provoking experience in the larger spectrum of life in these last three years.

Special thanks to Dr. Tanya Paskova for her enlightening discussions with regard to III-Nitride substrates and high resolution X-ray diffraction (HRXRD). Her words encouraged me to pursue my HRXRD and Raman spectroscopy characterization at SMIF Labs this past year.

I would also like the thank Dr. Simon Lappi for sharing his time and his knowledge of Raman spectroscopy with me. Simon was truly one of those mentors that I wished I had met earlier in my graduate program. His innate curiosity about a wide variety of subjects increased my desire to delve deeper into my research. Simon's exceptional ability to challenge the student is a reflection of his selfless passion for teaching others.

Finally, I would like to thank my husband, Lew, for his patience during my graduate work, for his constant encouragement when I felt anything but hopeful, and for the hours of

technical discussions with him that began over eighteen years ago. I am blessed to have him as my life-long partner.

TABLE OF CONTENTS

LIST OF TABLES xii

LIST OF FIGURES xiv

1. INTRODUCTION 1

1.1 Brief History 2

1.2 Figures of Merit 3

1.3 Growth of bulk crystals of GaN 7

1.3.1 High Pressure Solution Growth 7

1.3.2 Sublimation Growth 9

1.3.3 HVPE Growth 10

1.4 Properties of Nitrides 13

1.4.1 Spontaneous polarization 13

1.4.2 Piezoelectric polarization 14

1.4.3 Polarization charge density 15

1.5 Heterostructures 16

1.5.1 Cubic materials system 16

1.5.2 Wurtzite materials system 17

1.6 Motivation for this dissertation 20

1.7 Experimental Strategy 26

1.8 References 28

1.9 Tables 33

1.10 Figures 37

2. EXPERIMENTAL PROCEDURES IN PRELIMINARY ANALYSIS 56

2.1 Heterostructure Growth 57

2.2 Analytical Instrumentation 57

2.2.1 SEM/Cathodoluminescence 57

2.2.2 Bandgap measurements 59

2.2.3 High Resolution X-ray Diffractometry (HRXRD) 60

2.2.4 Reflectance Spectroscopy 62

2.2.5 Secondary Ion Mass Spectroscopy (SIMS) 63

2.2.6 Atomic Force Microscopy (AFM) 64

2.2.7 Photoluminescence (PL) 64

2.2.8 Van der Pauw Hall Measurements (Hall) 65

2.2.9 Raman Spectroscopy 67

2.3 References 70

2.4 Tables 71

2.5 Figures 73

3. MODULATION OF MOBILITY IN HOMOEPITAXIALLY-GROWN AlGaN/GaN HETEROSTRUCTURES 90

3.1 Abstract 91

3.2 Introduction 91

3.3 Study of AlGaN/GaN Heterostructures 94

3.3.1 Experimental 94

3.3.2 Van der Pauw Hall Measurements 95

3.4 Discussion 95
3.5 Acknowledgements 98
3.6 References 99
3.7 Tables 100
3.8 Figures 101
4. OPTIMIZATION OF HOMOEXPITAXIALLY-GROWN AlGaN/GaN HETEROSTRUCTURES 105
4.1 Abstract 106
4.2 Introduction 106
4.3 Study of AlGaN/GaN Heterostructures 109
4.3.1 Experimental 109
4.3.2 Results and Discussion 111
4.3.3 Analysis of Polarization Charge 116
4.4 Conclusions 117
4.5 Acknowledgements 118
4.6 References 119
4.7 Tables 121
4.8 Figures 124
5. IMPACT OF INTERFACE IMPURITIES ON HETEROSTRUCTURES 130
5.1 Introduction 131
5.2 Experimental 133
5.3 Results and Discussion 134

5.4 References 137

5.4 Figures 139

6. POISSON SOLVER CALCULATIONS 142

6.1 Heterostructures with and without Si-doping 143

6.1.1 Poisson solutions for AlGaN/GaN heterostructures 143

6.2 Heterostructures with Mg-doping 145

6.2.1 Poisson solutions for Mg-doped heterostructures 149

6.3 References 152

6.4 Tables 153

6.5 Figures 155

7. PHYSICAL PROPERTIES OF AlGaN/GaN HETERO-STRUCTURES GROWN ON VICINAL SUBSTRATES 159

7.1 Abstract 160

7.2 Introduction 160

7.3 Experimental Procedure 163

7.4 Results and Discussion 166

7.4.1 AFM 166

7.4.2 HRXRD 167

7.4.3 PL 171

7.4.4 CL 173

7.4.5 Hall Measurements 175

7.4.6 Raman Spectroscopy 177

7.4.7 TEM 188

7.5 Analysis of Heterostructure Results....189
7.6 Conclusions....192
7.7 Acknowledgements....193
7.8 References....194
7.9 Tables....200
7.10 Figures....201
8. PHYSICAL PROPERTIES OF AlGaN/GaN HETERO-STRUCTURES GROWN ON NONPOLAR M-PLANE BULK GaN AND POLAR C-AXIS N-TYPE BULK GaN SUBSTRATES....229
8.1 Abstract....230
8.2 Introduction....231
8.3 Experimental Procedure....233
8.4 Results and Discussion....236
8.4.1 AFM....236
8.4.2 HRXRD....238
8.4.3 PL....240
8.4.4 CL....241
8.4.5 Raman Spectroscopy....241
8.4.6 Hall Measurements....243
8.4.7 TEM....248
8.5 Conclusions....249
8.6 Acknowledgements....251
8.7 References....252

8.8 Tables 255
8.9 Figures 256
9. SUMMARY AND CONCLUSIONS 269
9.1 Summary of Experimental Work 270
9.1.1 Heterostructures without Mg 270
9.1.2 Heterostructures with Mg pre-ex situ anneal 272
9.1.3 Heterostructures with Mg post-ex situ anneal 272
9.2 Conclusions 275
9.3 Future Directions 276
9.4 References 278
9.5 Figures 279

LIST OF TABLES

Table 1.1 Properties of some substrate materials for GaN growth [3]. 33

Table 1.2 Physical properties of important semiconductors for high-voltage power devices [7]. 33

Table 1.3 Normalized Figures of Merit for Various Semiconductors [15]. 34

Table 1.4 Lattice constants, bandgaps and binding energies of hexagonal InN, GaN, and AlN [54]. 34

Table 1.5 Spontaneous polarization, piezoelectric and dielectric constants of AlN, GaN and InN [54]. 35

Table 1.6 Predicted values of $2C_{13}/C_{33}$ from [56] and the references therin. 35

Table 1.7 World class results for AlGaN/GaN HFETS. 36

Table 2.1 XRD, PL, and AFM characterization results for $Al_xGa_{1-x}N$/GaN heterostructures. 71

Table 2.2 Van der Pauw Hall results for $Al_xGa_{1-x}N$/GaN heterostructures. 72

Table 3.1 Van der Pauw measurements for $Al_{0.25}Ga_{0.75}N$/GaN heterostructures. 100

Table 4.1 Van der Pauw measurements for $Al_{0.25}Ga_{0.75}N$/GaN heterostructures. 121

Table 4.2 XRD, PL and AFM characterization for all $Al_xGa_{1-x}N$/GaN hetero-structures. Last four entries are heterostructures grown with "Al-free TMG". Complete data set shown for comparison. 122

Table 4.3 Van der Pauw measurements for $Al_{0.25}Ga_{0.75}N$/GaN heterostructures grown with "Al-free TMG". 123

Table 6.1 Calculated sheet resistances, layer sheet densities and electron eigenvalues for $Al_{0.25}Ga_{0.75}N$/GaN heterostructures with n-$Al_{0.25}Ga_{0.75}N$ and with n.i.d. $Al_{0.25}Ga_{0.75}N$ barriers. 153

Table 6.2 Calculated sheet resistances, layer sheet densities and electron eigenvalues for $Al_{0.25}Ga_{0.75}N$/GaN/Mg-doped GaN compensation layer heterostructures with n.i.d. $Al_{0.25}Ga_{0.75}N$ and with n-$Al_{0.25}Ga_{0.75}N$ barriers. 154

Table 7.1 γ values for selected vicinal substrates. 200

Table 8.1 Comparison of sheet densities and Hall mobilities for heterostructure growth on different substrates. 255

LIST OF FIGURES

Figure 1.1 Bandgap Energy as a function of lattice constant for several direct and indirect bandgap semiconductors. 37

Figure 1.2 The Ideal Drift Region in a unipolar device and its Electric Field Distribution [9]. 38

Figure 1.3 Equilibrium N_2 pressure over III-Nitrides [17, 21-23]. 39

Figure 1.4 Different polarities (Ga- and N-faced) of wurtzite GaN [54]. 40

Figure 1.5 Spontaneous polarization is a property of point group crystals that lack a center of symmetry. The polarization vector leads to an accumulation of charges of opposite sign at each of the interfaces which sets up a sizeable electric field within the material. 41

Figure 1.6 The polarization charge for an AlGaN/GaN heterostructure grown on a bulk GaN substrate is described by the above equation [56]. 41

Figure 1.7 In Type I materials, formation of the two-dimensional electron gas is assisted by carrier diffusion resulting from the bandgap difference at the heterointerface. Depletion of the carriers from the larger to smaller bandgap material is necessary to satisfy a continuous Fermi level [60]. 42

Figure 1.8 In an AlGaAs/GaAs heterostructure, carriers confined to the GaAs layer form a 2DEG. Confinement of the ionized impurities to the AlGaAs layer has consequences for carrier mobility within the 2DEG [61]. 43

Figure 1.9 (a) Polarization dipole across the AlGaN layer (b) Band diagram for AlGaN/GaN and the parameters determining the sheet carrier density and critical thickness, d_{CR}, of the of the AlGaN layer [66]. 44

Figure 1.10 (a) Theoretically calculated sheet carrier density vs. AlGaN thickness (b) Theoretically calculated sheet carrier density vs. alloy composition and the least square fit [66]. 44

Figure 1.11 Thermal conductivity measurements of unintentionally-doped HVPE-grown bulk GaN substrates and Fe-doped HVPE-grown bulk GaN substrate [67]. 45

Figure 1.12 Thermal conductivity measurements for GaN thin films on different host substrates [67]. 46

Figure 1.13 Chemical and structural mismatch introduces a high density of defects at the SiC/GaN nucleation interface locally limiting thermal conductivity. 46

Figure 1.14 Low dislocation density bulk GaN substrates realize high thermal conductivity which is essential to optimize heat dissipation in high-power transistors [69]. 47

Figure 1.15 When $\psi^{*}\psi$ is high the wavefunction will be in the triangular quantum well [70]. 48

Figure 1.16 Electron mobility of AlGaAs heterostructures versus year (Courtesy AT&T Bell Laboratories Corporation, Murray Hill, NJ). 49

Figure 1.17 Electron mobility as a function of temperature for n-AlGaN/GaN heterostructures with fixed AlGaN spacer thickness. (b) 2DEG mobility as a function of not-intentionally-doped AlGaN thickness at RT and 77K [71]. 50

Figure 1.18 The slip system $\{11\bar{2}2\}<112\bar{3}>$ gives the highest net force for a dislocation [72]. 51

Figure 1.19 Critical thickness calculated as a function of Al content. The critical thickness for an $Al_{0.25}Ga_{0.78}N$ film is ~600 Å. 52

Figure 1.20 (a) Experimental $\mu(T)$ and $n_s(T)$ (b) Fit and contributions from different scattering centers [75]. 53

Figure 1.21 AlGaN/GaN heterostructures grown on (0001) S.I. GaN substrates with (a) undoped AlGaN barriers with 5 nm AlGaN spacers and (b) 20 nm undoped AlGaN barriers would be compared to assess the contributions from spontaneous polarization, piezoelectric polarization and ionized donors to the 2DEG carrier density. 54

Figure 1.22 AlGaN/GaN heterostructures with (a) 15 nm doped AlGaN barriers and 5 nm undoped AlGaN spacers grown on (0001) S.I. bulk GaN substrates would be compared to (b) heterostructures with 15 nm doped AlGaN barriers and 5 nm doped AlGaN spacers grown on $(1\bar{1}00)$ non-polar bulk GaN substrates to assess improvements in structural and electrical properties. 55

Figure 2.1 Schematic of the AlGaN/GaN heterostructure for the growths in this project. 73

Figure 2.2 Schematic diagram of the conventional self-biased thermionic tungten hairpin electron gun [1]. 74

Figure 2.3 Electron ray traces through a schematic SEM column with a condensor lens and a probe-forming or objective lens [2]. 75

Figure 2.4 Monochromator with entrance slits to limit intensity. Light is reflected by collimator, C, to a grating, D, and collected at mirror, E, and refocused to the exit slit. 76

Figure 2.5 Photomultiplier tube multiplies the signal produced by the incident light by 10^8 from which single photons can be resolved. 76

Figure 2.6 (a) $Al_xGa_{1-x}N$ materials exhibit a bowing parameter as a function of alloy composition [3]. (b) Thin films of $Al_xGa_{1-x}N$ were grown by MOCVD. (c) Cathodoluminescence was used to assign an Al mole fraction to an emission energy. A bowing parameter, b=1 eV, was used. 77

Figure 2.7 Conduction band offsets for $Al_xGa_{1-x}N$ calibration runs. 78

Figure 2.8 (a) Lattice planes in real space where the distance between planes is *d*. (b) Ewald sphere in reciprocal space where the distance between reciprocal lattice point is 1/*d*. 78

Figure 2.9 Typical DCXRD scan for $Al_xGa_{1-x}N$ calibration runs. The symmetric rocking curve FWHM gives us a measure of the tilt and twist of the film. 79

Figure 2.10 Trimethylgallium (TMG) flow was the control lever used to obtain the desired bandgap for the $Al_xGa_{1-x}N$ barrier layer. 80

Figure 2.11 HRXRD **(** $\omega-2\theta$ **)** scans of $Al_xGa_{1-x}N$/GaN heterostructures showed pendulosung fringes which were used to determine $Al_xGa_{1-x}N$ barrier thickness and out-of-plane strain. The Chi-Squared value reflects the actual placement of the $Al_xGa_{1-x}N$ peak and spacing of pendulosung fringes vs. theoretically expected. The R Factor measures disagreement between F_{obs} and calculated structure factors, F_{calc}. 81

Figure 2.12 Thickness measurements for the $Al_xGa_{1-x}N$ calibration runs were determined by reflectance. Growth rate data indicated that Al incorporation is achieved by reducing trimethylgallium (TMG) flow. 82

Figure 2.13 (a) Schematic of SIMS process. (b) Secondary ions leaving the surface. (c) A crater of controlled size and depth allows raster resolution. 83

Figure 2.14 SIMS analysis using Cs^+ primary ion to assess oxygen concentration in $Al_xGa_{1-x}N$ film. Unintentional doping in GaN materials may be due to high oxygen incorporation. 83

Figure 2.15 SIMS analysis using the O^{2+} primary ion to assess silicon contamination at the epitaxial/bulk GaN interface. 84

Figure 2.16 (a) AFM is based on Hooke's Law. (b) The tip is most commonly scanned across the surface in contact mode. 84

Figure 2.17 Steps and terrace are evidence of step flow mode growth. Terrace terminations are indications of dislocations. 85

Figure 2.18 Schematic of a photoluminescence set up. 86

Figure 2.19 Several luminescent transitions can be seen by photoluminescence analysis [7]. 86

Figure 2.20 PL mapping of $Al_xGa_{1-x}GaN$/GaN heterostructures grown on 18 x 18 mm^2 bulk GaN substrates. 87

Figure 2.21 Illustration of the Hall Effect. The z-direction is out of the plane of the paper. The externally applied magnetic field is along the z-direction [8]. 88

Figure 2.22 Regions of the electromagnetic spectrum and energy units [11]. 88

Figure 2.23 Schematic representation of the phonon dispersion. Phonon branches along the [111] in the zincblende structure (stacking order ABCABC…) are folded to approximate those of the wurzite structure (stacking order ABABAB…) along the [0001] [12]. 89

Figure 3.1 CV profile of free carrier concentration versus depth for semi-insulating substrates. 101

Figure 3.2 SIMS analysis confirming atomic silicon concentration at the epitaxy/bulk GaN interface. 102

Figure 3.3 AFM image of the surface roughness of an $Al_{0.25}Ga_{0.75}N$/GaN heterostructure grown on a low dislocation density (0001) bulk GaN substrate. 103

Figure 3.4 Buffer-modulated behavior of room temperature Hall mobility and carrier density. 104

Figure 4.1 (a) 1 μm thick n.i.d. GaN buffer followed by 5 nm undoped $Al_{0.25}Ga_{0.75}N$ spacer then 15 nm of n-$Al_{0.25}Ga_{0.75}N$. (b) 1, 2, and 2.5 μm thick n.i.d. GaN buffers followed by 20 nm of undoped $Al_{0.25}Ga_{0.75}N$. 124

Figure 4.2 SIMS analysis performed with O^{2+} primary ion shows ~1000 ppm unintentional Al in the GaN buffer (b) has been reduced by 3 orders of magnitude. 125

Figure 4.3 (a) RT mobility data suggest mobility modulation may occur at a greater GaN buffer thickness than 0.75 μm for heterostructures grown without ~1000 ppm unintentional Al in the GaN buffer. (b) 2DEG sheet density as a function of GaN buffer thickness for heterostructures grown with unintentional Al in the GaN buffer and without. 126

Figure 4.4 (a) Conductivity as a function of GaN buffer thickness for hetero-structures grown with ~1000 ppm unintentional Al in the GaN buffer and without. (b) Sheet resistance data showed comparable results for heterostructures grown with unintentional Al in the GaN buffer and without. 127

Figure 4.5 Elimination of ~1000 ppm unintentional Al from the GaN buffer resulted in shift toward higher RT sheet densities and mobilities. 128

Figure 4.6 TEM image of AlGaN (dark side)/ GaN (light side) interface is abrupt to within a monolayer. White arrow points to a screw component of a mixed dislocation with burgers vector $\frac{1}{3}\left[11\bar{2}3\right]$. 129

Figure 5.1 SIMS analysis of regrowth surface capped with Ni after CF_4/O_2 plasma treatment. Si interfacial layer removed by CF_4/O_2 plasma but reintroduced during Ni evaporation. 139

Figure 5.2 XPS analysis of regrowth surface after CF_4/O_2 plasma treatment. Relative ratio of the C 1s to the Ga 2p peaks for the CF_4/O_2 treated versus the control surface indicated increased carbon in addition to fluorine contamination. 140

Figure 5.3 SEM micrograph of semi-insulating bulk GaN substrate after photo-assisted etching. Localized etching may be the result of domains across the crystal surface. 141

Figure 6.1 Schematic of heterostructure with 15 nm Si-doped $Al_{0.25}Ga_{0.75}N$ barrier, 5 nm n.i.d. $Al_{0.25}Ga_{0.75}N$ spacer and 2μm n.i.d. GaN buffer. 155

Figure 6.2 Schematic of heterostructure with 20 nm n.i.d. $Al_{0.25}Ga_{0.75}N$ barrier and 2 μm n.i.d. GaN buffer. 155

Figure 6.3 Band diagram with eigenwavefunctions for heterostructure of Fig. 6.1. 156

Figure 6.4 Schematic of Mg-doped heterostructure growth (a) on S.I. c-axis bulk GaN (b) on n-type c-axis bulk GaN (c) on n-type m-plane bulk GaN substrate. 157

Figure 6.5 Energy band diagram for Mg-doped heterostructure of Fig. 6.4(a). Depletion widths are marked at the n^-/p^- interface between the 2000 Å n.i.d. GaN and the 3000 Å p-GaN layer and the p^-/n^+ interface created by the Mg-doped GaN layer and the Si spike at the bulk GaN interface. 157

Figure 6.6 2DEG sheet density behavior as a function of ionized acceptor concentration shows that Mg acceptor concentrations exceeding 1×10^{17} cm^{-3} result in a precipitous drop in sheet density. The upper limit of sheet density for Mg-doped structures is $\sim 7.7 \times 10^{12}$ cm^{-2}. 158

Figure 7.1 CV profile of free carrier concentration versus depth for the semi-insulating GaN substrate. 201

Figure 7.2 SIMS analysis confirming atomic silicon concentration at the epi-taxy/bulk GaN interface. 201

Figure 7.3 (a) Schematic of heterostructure grown on S.I. bulk GaN vicinal substrates. (b) The heterostructure growth on the 0.7^o offcut sub-strate was not interrupted after the p-GaN layer. 202

Figure 7.4 (a) AFM RMS roughness data for 10 x 10 μm scans of vicinal substrates as received and after p-GaN growth show increased roughness after p-GaN growth for offcuts of 0.3^o and 0.4^o (b) AFM RMS roughness data for 10 x 10 μm^2 scans of vicinal substrates after n.i.d. GaN and $Al_xGa_{1-x}N$ growth show roughnesses $\leq$ 1.2 nm for offcuts $\geq 0.5^o$. 203

Figure 7.5 (a), (b), (c) AFM scans of AlGaN/GaN heterostructures grown on vicinal substrates with offcut angle as indicated from <0001> toward $<10\bar{1}0>$ and (d) from <0001> toward $<11\bar{2}0>$. 204

Figure 7.6 AFM roughness analysis after complete heterostructure growth indicates that vicinal substrates with offcut angles between 0.5^o and 1.8^o had an RMS roughness $\leq$ 1.2 nm. 205

Figure 7.7 Simulated alloy composition and thickness for $Al_xGa_{1-x}N$ barrier. 206

Figure 7.8 (a) FWHM of the symmetric (002) scan is essentially constant for all vicinal substrates studied. The in-plane FWHM decreased for vicinal offcuts $\geq 0.5^o$ (b) Screw dislocation density is given directly by β_{002}. Edge dislocation density is a function of both β_{105} and β_{002}. 207

Figure 7.9 (a) Reciprocal space maps for heterostructures show less dispersion in the $Al_xGa_{1-x}N$ film for the higher vicinal offcut. 208

Figure 7.10 Photoluminescence transitions of GaN involve band-to-band, conduction band to acceptor, and deep donor 1 to valence band or deep donor 2 to valence band. 209

Figure 7.11 Pseudo-Voigt peak fitting analysis was used to locate PL transitions and peak fitting was used to determine the FWHM of each peak. 209

Figure 7.12 Increased magnesium incorporation at lower vicinal offcuts is suggested by increased AFM roughness and increased CB $\rightarrow$ ACC and DD $\rightarrow$ VB PL transitions normalized to the BE. 210

Figure 7.13 Cathodoluminescence transitions in GaN involve band-to-band, conduction band to acceptor and deep donor 1 to acceptor pair recombination. 211

Figure 7.14 Pseudo-Voigt fit of cathodoluminescence transitions in AlGaN/GaN heterostructure. 211

Figure 7.15 The DD $\rightarrow$ ACC to CB $\rightarrow$ ACC transition intensity ratio as measured by CL shows no trend with respect to offcut of the vicinal substrate. 212

Figure 7.16 Only the CB $\rightarrow$ Mg acceptor transition was visible for the p-GaN/ n.i.d. GaN/$Al_xGa_{1-x}N$ heterostructure growth on S.I. GaN template. 212

Figure 7.17 $V_N \rightarrow$ VB transition at 3.347 eV and the CB $\rightarrow$ Fe acceptor transition at 2.926 eV were observed for growth of a heterostructure with 1.5 μm of n.i.d. GaN followed by 20 nm $Al_xGa_{1-x}N$ barrier on a S.I. GaN template. 213

Figure 7.18 2DEG sheet density for heterostructure of Fig. 7.3(a), calculated by Poisson solver, is maximum for an ionized acceptor concentration of 1 x 10^{15} cm^{-3} and drops precipitously for ionized acceptor concentration exceeding 1 x10^{17} cm^{-3}. 214

Figure 7.19 (a) Hall sheet density correlated to SIMS integrated area for Mg in layers described in Fig.7.3 (a) and (b) as a function of vicinal offcut (b) Hall sheet density correlated to SIMS integrated area for Mg spike and Mg in n.i.d. GaN layers. 215

Figure 7.20 Raman selection rules allow three vibrations for the $Z(X,-)\bar{Z}$ configuration, two transverse optical modes: E_2(low) and E_2(high) with atomic displacements perpendicular to the c-axis, and a longitudinal optical A_1 mode with atomic displacement parallel to the c-axis [42]. 216

Figure 7.21 Compilation of biaxial stress based on internal stress rates for the E_2(low), E_2(high) and A_1(LO) modes for heterostructures grown on vicinal substrates. 217

Figure 7.22 (a) A_1(LO) Raman shift and analysis before and after ex situ anneal shows no discernable trend associated with vicinal offcut. (b) Intensity and FWHM of A_1(LO) mode. 218

Figure 7.23 The alloy composition predicted by the A_1(LO) Raman shift where b_{A1}(LO)= -75 cm^{-1} [53] was higher than that determined as a function of alloy composition by HRXRD, but the trend was consistent. 219

Figure 7.24 (a) Integrated area between 260 – 400 cm^{-1} represents hole density. (b) Raman intervalence band correlates with the DD1 $\rightarrow$ ACC transition measured by CL. 220

Figure 7.25 (a) Integrated area between 260 – 400 cm^{-1} representing hole density is less after the ex situ anneal. (b) Difference in integrated area relative to SIMS areal density for vicinal offcut substrate. (c) Acceptor compensation assessed by Raman compared to Hall sheet density. 221

Figure 7.26 Absorbance and energy of the intersubband transition peak. 222

Figure 7.27 (a) L^+ branch of LOPC at 419.4 cm^{-1} before and L^+ branch of LOPC at 484.8 cm^{-1} after ex situ anneal. (b) L^- branch pair of LOPC at 846.5 cm^{-1}, 905.6 cm^{-1} before ex situ anneal. (c) Isolated hydrogen before and after ex situ anneal. (d) L^- branch of LOPC after ex situ anneal. 223

Figure 7.27 (e) Defect LVM associated with nitrogen vacancies. (f) Ga-H and Mg-H complexes associated with the NH_3 bending stretch. (g) The carrier density dependence of the axial LOPC-mode frequency in n-type wurtzite GaN [42]. 224

Figure 7.28 High angle diffraction TEM image of GaN buffer for heterostructure grown on a 1.4^o offcut substrate. There is no evidence of dislocations or stacking faults. 225

Figure 7.29 High angle diffraction TEM image of GaN/AlGaN interface shows GaN/AlGaN interface roughness >10 Å. 226

Figure 7.30 (a) Heterostructure schematic, and (b) corresponding energy diagram showing 1500 Å undepleted region where V_N might form as supported by (c) the formation energy diagram [61]. 227

Figure 7.31 (a) Hall sheet density compared to integrated intensity of the intersubband transition plasmon peak. (b) Intensity of each plasmon peak as a function of Raman shift. 228

Figure 8.1 CV profile of free carrier concentration versus depth for the n-type GaN substrate. 256

Figure 8.2 Schematic of heterostructure grown on (a) semi-insulating c-axis vicinal substrates. (b) n-type c-axis substrates. (c) n-type m-plane nonpolar substrates. 256

Figure 8.3 AFM image of non-polar surface after full heterostructure growth. The RMS roughness for this 5 x 5 μm^2 area was 0.756 nm. Triangular-shaped defects are oriented in the $[000\bar{1}]$. 257

Figure 8.4 Reciprocal space map of the $1\bar{1}0$ symmetric reflection. The horizontal axis (in this orientation) defines the compositional fluctuation of the $Al_xGa_{1-x}N$ barrier. Lateral components of broadening do not apply to the symmetric reflection. 258

Figure 8.5 Reciprocal space map of the $20\bar{1}$ asymmetric reflection. The horizontal axis (in this orientation) defines compositional fluctuation. Lateral components of broadening expand along the Omega (horizontal) axis. 259

Figure 8.6 PL analysis reveals the CB $\rightarrow$ VB transition at 3.354 eV and the CB $\rightarrow$ ACC transition corresponding to an ionization energy of 0.16 eV and the CB $\rightarrow$ Ga_N corresponding to an ionization energy of 0.937 eV. 260

Figure 8.7 CL analysis revealed only the CB $\rightarrow$ VB transition at 3.423 eV and a weak CB $\rightarrow$ ACC transition corresponding to an ionization energy of 0.16 eV. 261

Figure 8.8 Porto notation for nonpolar m-plane GaN and the allowed modes by Raman selection rule [37]. 262

Figure 8.9 Raman shifts from HFET structure on m-plane bulk-GaN. 263

Figure 8.10 (a) Hall mobility vs. sheet density for all substrates studied reveal higher mobilities for bulk n-GaN (c-axis) as well as m-plane bulk GaN at RT and (b) at 77K. 264

Figure 8.11 (a) Hall mobility vs. temperature and (b) sheet density vs. temperature for c-axis bulk n-GaN and m-plane bulk GaN. 265

Figure 8.12 High angle dark field image of dislocation-free, stacking fault-free GaN buffer in heterostructure growth on m-plane non-polar bulk GaN substrate. 266

Figure 8.13 High angle dark field image showing GaN/interface with PdAu and Pt protective layers added during FIB processing. 267

Figure 8.14 High angle diffraction image of GaN/AlGaN interface revealing GaN/AlGaN interface roughness $\leq$ 2 Å. 268

Figure 9.1 $Al_{0.25}Ga_{0.75}N$/GaN heterostructures grown (a) with 15 nm n-AlGaN barriers and 5 nm n.i.d. AlGaN spacers (Type I) (b) with 20 nm n.i.d. AlGaN barriers (Type II) on n.i.d. GaN buffers on S.I. (0001) bulk GaN measured RT Hall sheet densities of 10^{13} cm^{-2} for the 2DEG. However, μ_{RT}^{2DEG} was modulated by charge at the epitaxy/bulk GaN interface. 279

Figure 9.2 $Al_{0.25}Ga_{0.75}N$/GaN heterostructures grown with 20 nm n.i.d. AlGaN barrier/ 200 nm n.i.d. GaN buffer/ 300 nm Mg-doped GaN layer on (a) S.I. and (b) n-type (0001) bulk GaN substrates. (c) 15 nm n-AlGaN barrier/5 nm n.i.d. AlGaN spacer/ 200 nm n.i.d. GaN buffer/ 300 nm Mg-doped GaN on n-type $(1\bar{1}00)$ bulk GaN substrate. The Mg-doped GaN layer was intended to compensate charge at the epitaxy/bulk GaN interface. 279

1. INTRODUCTION

1.1 Brief History

Gallium Nitride (GaN) is a direct, wide bandgap semiconductor that is important in the fabrication of high power, high frequency, and high temperature devices such as power amplifiers and field effect transistors (FET) [1, 2]. Until recently, GaN substrates with large enough area for growing GaN films have been scarce. Sapphire (Al_20_3) and silicon carbide (SiC) are the most popular substrates used currently. However, the low thermal conductivity of sapphire, found in Table 1.1 [3], presents a serious challenge for the packaging of high power devices. Long term reliability may be compromised due to the thermally-induced stress on the contacting pads which serve as a conducting path.

When non-native substrates are used, there is a large misfit of the GaN film to the substrate which is accommodated by matching integral multiples of lattice planes across the film-substrate interface. There is one extra half plane, or dislocation, corresponding to each domain [4, 5]. Since the initial misfit strain, ε, defined by the film and substrate lattice spacing, d_f and d_s respectively,

$$\varepsilon = d_f / d_s - 1 \tag{1.1}$$

can be large, this matching of integral multiples of lattice planes leaves a residual strain ε_r given by

$$\varepsilon_r = md_f / nd_s - 1 \tag{1.2}$$

where $m$and n are simple integers [6]. For perfect planar matching, $md_f = nd_s$, and the residual strain ε_r is zero. However, if ε_r is finite, then two domains may alternate with a

certain frequency to provide for a perfect matching according to

$$(m+\alpha)d_f = (n+\alpha)d_s \tag{1.3}$$

where α is the frequency factor [6]. Hence, GaN films having a large misfit relative to the Al_2O_3, SiC and Si substrates can grow epitaxially in the form of single crystals by domain matching epitaxy (DME).

The ten times higher thermal conductivity [3] of SiC relative to Al_20_3 does make it a more attractive substrate for high power applications where heat must be dissipated to achieve high breakdown voltages. Silicon substrates are least expensive and have three times higher thermal conductivity [3] than Al_20_3. Additionally, they have the potential of integrating GaN optoelectronics with silicon devices. But GaN substrates are desirable because of their large bandgap, high thermal conductivity, high breakdown voltage due to their critical electric field, and their large saturation drift velocity as shown in Table 1.2 [7].

1.2 Figures of Merit

Ren and Zolper formulated the combined figure of merit (CFOM) [3] for substrates based on their materials properties. The combined figure of merit,

$$CFOM = \frac{KE_c^2 \varepsilon \mu v_s *}{(KE_c^2 \varepsilon \mu v_s)_{Si}} \tag{1.4}$$

is a means of benchmarking the predicted FET temperature, power, and frequency performance. GaN is clearly favored compared to other substrates. GaN's large saturation drift velocity results in short transit times. And since breakdown field is proportional to bandgap energy, GaN devices are capable of operating at higher voltages which is evident by examination of this material's critical electric field. Only diamond and AlN have a higher

critical electric field, E_c [7]. Additionally, since GaN is a direct bandgap material, as illustrated in Fig. 1.1, it affords the opportunity for fabrication of photonic as well as electronic devices.

But, the power semiconductor device figure of merit for resistive loss is given by the Baliga Figure of Merit (BFOM) [8]. That FOM is based on the specific on-state resistance in the ideal drift region of a unipolar device as shown in Fig. 1.2 [9]. On-state resistance is high for materials with low intrinsic carrier concentration. And while most semiconductors are doped, either intentionally or by background impurities, the higher breakdown voltage performance of wide bandgap semiconductors is associated with the reduced impact ionization coefficient at any given electric field when compared to silicon. The advantage of materials with reduced impact ionization coefficients [10] is the higher maximum voltage they can support before the onset of significant current flow across the depletion regions of the device. This impact ionization process determines the current flowing through the depletion region as avalanche breakdown in the presence of a large electric field. Based on GaN's E_c, it requires an order of magnitude higher electric field in GaN than in silicon, to accelerate mobile carriers until they gain sufficient energy to create electron-hole pairs upon collision with the lattice. Simply stated, in pure GaN, ideally with no defects, higher electric fields can be tolerated before the device breaks down.

To derive the BFOM, we consider the specific on-state resistance, $R_{on,sp}$, in the ideal drift region of a unipolar device that is proportional to the depletion width, which is inversely related to the atomic concentration of dopant atoms in the drift layer,

$$R_{on,sp} = \left(\frac{W_D}{q \mu_n N_D} \right) \tag{1.5}$$

where W_D is the depletion width, q is electron charge, μ_n is the electron mobility and N_D is carrier concentration. Depletion width is inversely proportional to one of the semiconductor's fundamental material properties,

$$W_D = \frac{2V_{BD}}{E_c} \tag{1.6}$$

where V_{BD} is the breakdown voltage and E_c is the critical electric field. Since the carrier concentration can be expressed as,

$$N_D = \frac{\varepsilon_s E_c^2}{2 \cdot q \cdot V_{BD}} \tag{1.7}$$

where ε_s is the semiconductor dielectric constant, the above relationships can be combined to express the specific resistance in the ideal drift region as

$$R_{on-ideal} = \frac{4V_{BD}^2}{\varepsilon_s \mu_n E_c^3}. \tag{1.8}$$

The denominator of the above expression is the low frequency Baliga Figure of Merit,

$$BFOM = \varepsilon_s \mu_n E_c^3 \tag{1.9}$$

which relates material properties to low resistive loss in a device.

But for high frequency applications where fast switching is important, it is necessary to include switching losses that are due to the charging and discharging of the input capacitance of the FET. This input capacitance has been found to dominate the switching loss component in high frequency applications. Specific input capacitance, $C_{in,sp}$, is

inversely related to the depletion width as follows,

$$C_{in,sp} = \frac{\varepsilon_s}{W_D} = \frac{\varepsilon_s}{2 \cdot V_G^{1/2} \cdot V_{BD}^{1/2}} \tag{1.10}$$

where V_G is the gate drive voltage. By taking the inverse product of the specific on-state resistance and the specific input capacitance, an expectation of the performance of the device can be obtained by looking at the Baliga high frequency figure of merit [11],

$$BHFFOM = \frac{1}{R_{on,sp} \cdot C_{on,sp}} = \frac{\mu E_c^2 V_G^{1/2}}{2V_{BD}^{3/2}} \tag{1.11}$$

The above figure of merit can be distilled to one depending solely on materials properties as follows,

$$BFOM = \mu E_c^2 \tag{1.12}$$

These are the materials properties that relate device performance to low switching loss in devices.

But to be complete, others have devised figures of merits. In 1965, Johnson [12] devised the power frequency figure of merit for low voltage transistors. Keyes [13] incorporated the thermal limitation in switching behavior of transistors used in integrated circuits in 1972. Then, in 1982, Baliga formulated his figure of merit for low frequency devices where conduction losses dominate and in 1989, he formulated his high frequency figure of merit. Others [14] then incorporated the impact of the thermal conductivity of the material to Baliga's figure of merit and those values are reported in Table 1.3 [15]. GaN, with a thermal conductivity lower than that of diamond and AlN, boasts a respectable figure of merit for electronic devices making it a very desirable semiconductor material.

1.3 Growth of bulk crystals of GaN

Due to differences in the thermal expansion coefficients and the lattice mismatch between non-native substrates and nitride films, homoepitaxial growth of GaN layers on gallium nitride single crystalline substrates is a preferred approach to reduce the dislocation density of epitaxial GaN layers in devices. However, the fabrication of bulk crystals of gallium nitride requires extremely high temperatures, T^M~2800K [16] and very high decomposition pressures at melting, p_{N2}~45 kbar [17, 18]. Hence, established equilibrium growth techniques such as Czochralski or Bridgman growth from stoichiometric melts cannot be used under practical laboratory conditions. Instead, GaN single crystals have been grown by methods requiring lower temperatures.

1.3.1 High Pressure Solution Growth

One laboratory method to grow single crystals of GaN with low defect densities has been from solution in liquid gallium under a high pressure of N_2 gas [19]. For the crystallization of GaN, gas chambers with volumes up to 1500 cm^3 are used. The maximum pressure reaches 20 kbar and maximum temperature is 2000K. Crucibles made from either graphite or hexagonal BN can accommodate up to 100 cm^3 of liquid gallium. This type of high pressure reactor is equipped with in situ annealing under vacuum conditions and electronic control for cooling and programming of temperature and pressure. Pressure can be stabilized within 10 bar and temperature is measured by thermocouples arranged along the furnace [20].

Figure 1.3 shows the equilibrium p_{N2} – T curves for AlN, GaN and InN [17, 21-23]. The curves for GaN and InN deviate from linear dependence at higher pressures due to the non-ideal behavior of N_2 gas. The diagram indicates that at a pressure of 1 bar, GaN is stable up to ~1200 K in air or N_2. For GaN, the maximum equilibrium temperature determined by a nitrogen gas [N_2] pressure of 20 kbar is 1960 K. The discrepancy between the melting temperature for GaN and the maximum temperature available in the gas-containing pressure chamber causes a very low solubility of GaN in the liquid metal. The solubility of Nitrogen [N] in liquid Gallium [Ga] in a high temperature, high pressure system (2000 K, 20 kbar) is approximately one atomic percent [24]. This solubility is sufficient for effective crystallization from the solution. Dissolution of nitrogen in liquid gallium is kinetically limited by the 4.8 eV [24, 25] potential barrier at the gallium surface that a N_2 molecule must overcome to dissociate. Once this potential barrier is overcome, the heat of formation for the Ga to N bond is only 1.08 eV [26]. Since the N-N bonding energy is 2.34 eV [27], the formation of GaN is more energetically favorable. Gallium nitride crystals grown from solution form hexagonal platelets that grow at a rate of <1 mm/hr along $\{10\bar{1}0\}$ direction (perpendicular to the c-axis) and are single crystals of high structural morphology suggesting stable layer-by-layer growth. Their flat, mirror-like faces have been identified by X-ray photoelectron diffraction (XPD) measurements as $(000\bar{1})$ N-terminated [28]. GaN crystals grown from pure gallium solutions have high free electron concentrations of 3 - 6 x 10^{19} cm^{-3} with mobilities of 30 - 90 $cm^2V^{-1}s^{-1}$ [29]. The main residual impurity detected by SIMS is oxygen at a concentration of 10^{18} – 10^{19} cm^{-3}[30]. The N-vacancy is considered as an

additional source of free electrons [31, 32]. The most probable native defects in GaN crystals which are highly n-type are triple-valent Ga-vacancies (V_{Ga}^{3-}) [33]. This is due to their low formation energy even under strongly Ga-rich conditions of crystallization. The presence of negatively charged Ga vacancies at concentrations of 10^{18} cm^{-3} was detected by positron annihilation experiments [34]. Crystals grown from N solutions in pure Ga show strong yellow photoluminescence (PL) and a relatively weak PL signal close to the energy gap [20]. Xray diffraction analysis [35] reveals that the (0002) CuKα reflection depends on the size of the crystal.

Low angle grain boundaries are an additional defect revealed in these single crystal solution growth samples. The full widths at half maximum (FWHM) were 20 - 30 arcsec for 1 mm crystals and 30 - 40 arcsec for 1 – 3 mm ones. For larger platelets the rocking curves reveal multiple ~30 – 40 arcsec peaks showing a presence of low angle (1 – 3 arcmin) boundaries separating grains of 0.5 – 2 mm in size [35].

1.3.2 Sublimation Growth

A second method of growing bulk GaN is the sublimation method [36-38]. In this method, the source GaN powder and a seed crystal or a substrate facing the source are loaded into a crucible. Upon heating the crucible, the source powder sublimates and recrystallizes onto the seed crystal or on the substrate. When the system needs a reaction gas such as NH_3 for growth, the system is not sublimation, but may be considered a vapor phase epitaxy (VPE) process. The first GaN crystals grown by this method were grown by Ejder using metal Ga, N_2 and NH_3 [39]. The crystals obtained after 12 hrs of growth were whiskers a

few millimeters long and 1 – 5 μm in diameter, needles a few millimeters long and half a millimeter thick and platelets 0.1 – 20 μm thick and prisms. Zetterstorm reported colorless hexagonal crystals of GaN with the largest size of 5 mm long and 1 mm thick after 72 hr of growth [40]. These crystals were not large enough to be used as substrates and the shape of the crystals was not controlled. Typical growth temperatures were 1000 – 1100^{o}C and the growth pressure was atmospheric. Conditions producing a higher density of growing species on the substrate cause a high nucleation density and result in a uniformly thickened film as nuclei condense in a planar layer. The typical shape of bulk GaN was hexagonal habit form and it exhibited hexagonal crystal symmetry. It had uniform thickness ranging from 10 – 30 μm after growth for 1 hr. Selective sublimation [41] is also possible by depositing SiO_2 on a substrate and opening 60 μm x 60 μm windows. Using this technique, hexagonal GaN columns were selectively grown to a height of 200 μm and a diameter of 200 μm. Saturation of the crystal size with growth time is due to exhaustion of the source powder. Larger crystals require repeated growths with fresh source powder each time. This exhaustion of species is evidence that it is not a sublimation method but is instead more accurately VPE using a solid Ga source and NH_3.

1.3.3 HVPE Growth

Due to its relatively high growth rate (> 100 μm/hr), hydride vapor phase epitaxy (HVPE) has been used to grow large area GaN films and bulk GaN native substrates. In HVPE, HCl is reacted with liquid Ga to form GaCl gas and is transported to the growth zone kept at ~1030^{o}C where it is directly reacted with NH_3 resulting in growth of (0001) GaN on a

sapphire substrate. Freestanding (FS) HVPE GaN substrates are accomplished by separation of thick GaN films grown on sacrificial substrates such as sapphire and GaAs [42-46]. Dislocation densities less than 5 x 10^6 cm^{-2} and capacitance-voltage (CV) of the undoped GaN indicated a carrier concentration of 3 x 10^{15} cm^{-3} at the upper portion of the 200 – 300 μm thick films [42]. Since the GaN film thickness was comparable to the sapphire substrate, thermal expansion coefficient (TEC) differences resulted in substantial bowing across the 2 inch wafer. Laser–induced lift-off using a pulsed 355 nm Nd:YAG laser at an ambient temperature of 600^{o}C allowed the heat to diffuse to a depth that enabled extended areas of the film to release sequentially without catastrophic fracturing. Using this technique, crack-free, 10 cm^2 GaN substrates with little or no bowing and double crystal X-ray diffraction (DCXRD) full-width at half maximum (FWHM) measurements of ~150 arcsecs have been fabricated [42].

When GaAs is used as the starting substrate [44], aqua regia is used to dissolve it after GaN growth. Motoki et al used epitaxial lateral overgrowth and HVPE to fabricate 500 μm thick GaN films with DCXRD FWHM as low as 10^6 arcsecs and dislocation densities as low as 2 x 10^5 cm^{-2} in 20 x 30 mm^2 areas. These GaN substrates showed n-type conductivity with typical carrier concentrations of 5 x 10^{18} cm^{-3} and carrier mobilities of 170 $cm^2V^{-1}s^{-1}$.

In the void-assisted separation (VAS) method [47-49], a thick GaN layer grown by HVPE is separated as a result of thermal stress at a boundary consisting of numerous voids generated around a thin porous TiN layer inserted between the thick Ga layer and the base substrate during the cooling process after the growth. Freestanding GaN substrates with diameters of ~3.2 in. have been prepared by this method. Hall measurements revealed carrier

concentrations of 1 x 10^{18} cm^{-3} which is in agreement with SIMS measurements for silicon. Hall mobilities were in the range of 200-400 $cm^2V^{-1}s^{-1}$.

Since unintentionally-doped HVPE-grown GaN substrates have free carrier concentrations between low 10^{17} to high 10^{18} [46] rendering them inappropriate for electronic applications, Hanser et al have developed semi-insulating (S.I.) substrates by incorporating $Fe^{3+/2+}$ acceptors that lie 0.34 eV below the conduction band [50]. These iron-doped substrates reproducibly achieve resistivities of 3 x 10^5 Ω·cm at 250°C and should be able to block current leakage in high-power, high-frequency devices. The DCXRD FWHM of the (0002) peak is only 90 arcsec. Photoluminescence studies of these S.I. substrates are consistent with full compensation of Si and O shallow donors and low temperature near infrared (NIR) PL shows that the incorporation of Ga substitutional Fe^{3+} compensating centers is realized [46].

Nonpolar a-plane and m-plane substrates are of interest for applications such as high-efficiency optoelectronics, power switching and high-frequency electronics because the band-bending seen in GaN films grown on polar substrates should be mitigated using nonpolar substrates. Additionally, homoepitaxially-grown nonpolar GaN should have fewer extended defects and stacking faults than those grown heteroepitaxially on $(1\bar{1}02)$ r-plane sapphire [51] or $LiAlO_2$ substrates [52]. Hanser et al [53] have generated 10 x 5 – 20 x 5 mm^2 a-plane and m-plane bulk GaN substrates by using an XRD technique to orient GaN crystals grown in the [0001] direction and a multiwire saw to slice the substrates with the a-plane or m-plane surfaces to an accuracy of +/-0.1° in the nonpolar direction. Some nonpolar substrates are uniform and transparent but others have regions of discoloration at or near

surface hexagonal pitting defects introduced during the [0001] growth. In the thick GaN crystals, surface pits formed early in the growth can grow in size and leave an area within the crystal corresponding to a V-shape defect. The DCXRD FWHM values for these nonpolar surfaces are significantly lower by more than 5 times that of polar material sliced from boules indicating a much lower defect density and an absence of anisotropic defect distribution in the native nonpolar material.

1.4 Properties of Nitrides

The wurtzite group-III nitrides InN, GaN, and AlN are tetrahedrally coordinated semiconductors with a hexagonal Bravais lattice with four atoms per unit cell [54]. The hexagonal crystal structure of Group III-nitrides can be described by edge length, $\mathbf{a_0}$, of the basal hexagon, the height, $\mathbf{c_0}$, of the hexagonal prism and the microscopic dimensionless parameter, **u**, defined as the anion-cation bond length along the (0001) axis. Because of the different cations and ionic radii (Al^{3+}: 0.39 Å, Ga^{3+}: 0.47 Å, In^{3+}: 0.79 Å [55]), InN, GaN and AlN have different lattice constants, bandgaps and binding energies [56, 57] as shown in Table 1.4. The nearest neighbor anion-cation pairs in these wurtzite crystals form electric dipole moments in the direction $N \rightarrow (In, Ga, Al)$. In the absence of shear strains, the net polarization in the c-plane vanishes because of the sixfold rotational symmetry about the c-axis. Along the c-axis, however, there is a non-vanishing net polarization.

1.4.1 Spontaneous polarization

The unique feature of the nitride-based materials system is that they exhibit spontaneous polarization P_{SP}. Spontaneous polarization is a property of point group crystals

that lack a center of symmetry. Spontaneous polarization is independent of strain and is absent in zincblende material where every ion is at a point of full cubic symmetry. Due to the increasing non-ideality of the crystal structure, **u** increases, $\mathbf{c_0/a_0}$ decreases, and difference from the ideal ratio of the lattice constants of a close-packed hexagonal structure, $\mathbf{c_0/a_0}$=1.633, increases as well [56]. The most common growth direction of hexagonal GaN is normal to the {0001} basal plane, where the atoms are arranged in bilayers consisting of two closely spaced hexagonal layers, one with cations and the other with anions, so that the bilayers have polar faces, either Ga- or N-faced. By Ga-faced we mean Ga on the top position of the {0001} bilayer, corresponding to the [0001] polarity in Fig. 1.4 [54]. The orientation of the spontaneous polarization is defined assuming that the positive direction goes from the metal (cation) to the nearest neighbor nitrogen atom (anion) along the c-axis as shown in Fig. 1.5. This polarization vector leads to an accumulation of charges of opposite sign at each of the interfaces which sets up as sizeable electric field within the material. The sign of the spontaneous polarization of these Group-III nitrides is found to be negative as shown in Table 1.5.

1.4.2 Piezoelectric polarization

Strain at the heterointerfaces can also contribute a piezoelectric component. The piezoelectric tensor has three independent components for the (C_{6v}) point group. Two of these components measure the piezoelectric polarization P_{PE} induced along the c-axis or in the basal plane as defined by the relation:

$$P_{PE} = e_{33}\varepsilon_z + e_{31}(\varepsilon_x + \varepsilon_y) \tag{1.13}$$

where e_{31}, e_{33} ($C \cdot m^{-2}$) are the piezoelectric coefficients and $\varepsilon_z = (c - c_0 / c_0)$ is the strain along the c-axis, the in-plane strain $\varepsilon_x = \varepsilon_y = (a - a_0 / a_0)$ is assumed to be isotropic and a and c are the lattice constants of the strained layer. The relation between the lattice constants and the hexagonal AlGaN system is given by:

$$\frac{c - c_0}{c_0} = -2\frac{C_{13}}{C_{33}}\frac{a - a_0}{a_0} \tag{1.14}$$

where C_{11} and C_{33} are elastic constants [56] shown in Table 1.5. Using Eq. (1.13) and (1.14), the amount of piezoelectric polarization in the direction of the c-axis can be determined by:

$$P_{PE} = 2\frac{a - a_0}{a_0}\left(e_{31} - e_{33}\frac{C_{13}}{C_{33}}\right) \tag{1.15}$$

Eq. (1.15) is valid in the linear regime for small strain values [59]. From Eq. (1.15) it follows that the piezoelectric polarization is negative for tensile and positive for compressively-strained AlGaN barriers.

1.4.3 Polarization charge density

AlGaN barriers grown on GaN buffer layers are under tensile strain and in this case, the sum of the piezoelectric and spontaneous polarization is,

$$P = P_{PE} + P_{SP} \tag{1.16}$$

Hence the fixed polarization charge density for growth of AlGaN/GaN heterostructures grown on bulk GaN substrates as illustrated in Fig. 1.6 is defined by,

$$\sigma(P_{PE} + P_{SP}) = P_{bottom} - P_{top} = P_{SP(botttom)} - \{P_{SP(top)} + P_{PE(top)}\} \tag{1.17}$$

It is because of this polarization-induced charge that a two dimensional electron gas (2DEG) can be confined in the layer with the smaller bandgap close the interface.

1.5 Heterostructures

1.5.1 Cubic materials system

In a Type I heterostructure interface the energy gap of the smaller bandgap material is aligned within the larger bandgap material. Consequently, there is a barrier to the flow of both electrons and holes from the smaller to the larger bandgap material. In cubic material systems such as GaAs and InP, the channel formation from carriers accumulated along the junction between a heavily doped, high bandgap region and a lightly doped low bandgap region is the result of carrier diffusion from the heavily doped to the lightly doped region. This diffusion is enhanced significantly by the bandgap difference between the two regions. This is the principle behind a heterojunction field effect transistor (HFET) in cubic materials systems as illustrated in Fig. 1.7 [60]. Since the GaAs conduction band edge lies lower in energy than the $Al_xGa_{1-x}As$ donor states, electrons from the donors will move into the GaAs region. The carriers from $Al_xGa_{1-x}As$ region deplete in order to satisfy the requirement of a continuous Fermi level throughout the heterostructure or superlattice. This carrier depletion in turn leads to appreciable band bending which is impurity-concentration and layer-thickness dependent. As illustrated in Fig. 1.8 [61], the dopants in the AlGaAs barrier raise the Fermi level, E_F, within the potential energy well. In both the doped and the modulation-doped superlattice structures, the carriers confined to the GaAs layer will form a two-dimensional electron gas (2DEG). The most important feature of the modulation-doped

superlattice structure is that essentially all the mobile carriers, in this case, electrons, are confined to the GaAs layer and the ionized impurities are confined in the in the AlGaAs layer. Since ionized impurities are known to act as scattering centers, their confinement to the larger bandgap material enables high carrier mobility in the 2DEG channel located in smaller bandgap material. The spatial separation of the ionized impurities from the carriers in an irreversible manner allows the electron density in the GaAs channel to greatly exceed the density of the unintentionally present neutral or ionized impurity scattering centers in the channel. This leads to a considerable change in mobility behavior in the temperature and carrier density regimes where impurity scattering mechanisms are important. Mobility enhancement can also occur in undoped structures. Dingle and Stormer [61] showed that the room temperature mobility enhancement in their first observation of a 2DEG channel was a factor of 2 greater in modulation doped than in undoped superlattices or in GaAs heterostructures of equivalent electron concentration. This observation caused them to report that the most dramatic influence of modulation doping would be in the temperature dependence of mobility and to predict values of 10^4 $cm^2V^{-1}s^{-1}$ in heterostructures with carrier densities on the order of 10^{12} cm^{-2}.

1.5.2 Wurtzite materials system

In wurtzite heterostructures, specifically AlGaN/GaN heterostructures, the carrier accumulation is mainly due to polarization charges developed along the heterojunction in the high bandgap AlGaN side. The polarization discontinuity across the material interface results in a strong electric field that induces the free electrons to congregate preferentially to form a 2DEG in the GaN layer at the AlGaN/GaN interface. The large conduction band

discontinuity (ΔE_c) leads to a high 2DEG sheet charge density. This carrier accumulation can occur without the contribution of carrier diffusion from a heavily doped barrier. Wurtzite HFETs use the piezoelectric strain primarily, rather than dopants to raise the E_F within the potential well and to populate it with electrons.

If the $Al_xGa_{1-x}N$ barrier is coherently strained as the Aluminum [Al] concentration and /or the barrier layer thickness increases, an electron sheet concentration as high as 10^{13} cm^{-2} or more can be generated by the piezoelectric effect [62, 63]. On the premise that strain in a heterostructure decreases once the layer thickness exceeds the critical thickness, Bykhovski, Gaska and Shur [64] used elastic isotropy approximation to calculate the strain as a function of $Al_xGa_{1-x}N$ thickness to find critical thickness as a function of aluminum content, *x*. Then they used capacitance-voltage measurements on thin fully strained $Al_xGa_{1-x}N$ films of different thicknesses to extract the experimental strain and to determine the microscopic dimensionless parameter **u**. They concluded that an increase in aluminum content in the AlGaN barrier leads to a higher built-in strain as a result of piezoelectric doping of strained AlGaN/GaN heterostructures and that piezoelectric doping is a possible substitute for conventional impurity doping.

Others [65] argued that the sum of the various space charges is zero since the heterostructure itself must be charge neutral in the absence of an externally applied field and that polarization-induced charges constitute a dipole whose net contribution to the total space charge must also be zero. Hence they discounted piezoelectric doping. However, if the $Al_xGa_{1-x}N$ barrier in an $Al_xGa_{1-x}N$/GaN heterostructure is intentionally doped, the charge density in the 2DEG is not proportional to the amount of dopant (Si, a shallow donor in GaN)

introduced into the $Al_xGa_{1-x}N$ layer [66]. This experimental observation suggested that dopants play only a secondary role in determining the sheet charge density while the primary driver determining sheet carrier concentration is the strain-induced polarization at the bottom and top surfaces of the AlGaN layer. Fig. 1.9(a) illustrates the polarization dipole set up across the $Al_xGa_{1-x}N$ layer. The magnitude of the electric field inside the $Al_xGa_{1-x}N$ is dependent only on the magnitude of the sheet charge density, $\sigma_{(P_{SP}+P_{PE})}$, at the top and bottom faces as given in Eq. (1.17). Since the electric field is constant, the energy of the $Al_xGa_{1-x}N$ layer is reflected in the potential drop across the two faces of the crystal and is continuously increasing with thickness, d, of $Al_xGa_{1-x}N$ crystal. Beyond a critical thickness, d_{CR}, (Fig. 1.9(b)) in this case the minimum $Al_xGa_{1-x}N$ layer thickness required to form a 2DEG, it is energetically more favorable to the crystal to create a compensating charge of opposite polarity to the polarization charge which would lower the electric field inside the $Al_xGa_{1-x}N$ [66]. The configuration with the lowest energy would require the compensating charges i.e. a negative charge sheet 2DEG close to the positive polarization charge sheet at the lower $Al_xGa_{1-x}N$/GaN interface and a positive charge sheet at the top surface of the $Al_xGa_{1-x}N$ layer. Such a positive sheet charge can arise from ionized donor states at the surface. Since the Fermi level at the surface is pinned at a level φ_S below the conduction band of the $Al_xGa_{1-x}N$ due to the presence of these donor-like states, the negative sheet charge will occupy the energy levels between the Fermi level and $(\varphi_{S\partial} - \Delta E_C)$ below the Fermi level, denoted as E_{fo}. An electrostatic analysis given by Vetury et al gives:

$$q \cdot n_s = \sigma_{(P_{SP}+P_{PE})} \cdot (1 - d / d_{CR}) - \varepsilon \cdot E_{fo} / d \qquad (1.18)$$

and

$$d_{CR} = \varepsilon \cdot (q \cdot \varphi_S - \Delta E_C) / \sigma_{(P_{SP}+P_{PE})} \tag{1.19}$$

where q is electronic charge, n_s is sheet density, ε is the dielectric constant.

From Eq. (1.18), Vetury used a surface pinning level φ_S of 1.42 eV, for an Al mole fraction, x of 0.27, and experimentally varied the $Al_xGa_{1-x}N$ thickness to generate Fig. 1.10(a). The critical thickness below which no 2DEG is formed is 3.5 nm. Beyond an $Al_xGa_{1-x}N$ thickness 25 nm, the sheet carrier density saturates at the maximum $\sigma_{(P_{SP}+P_{PE})}$ suggested by Eq. (1.18). Additionally, Vetry showed the actual versus predicted sheet carrier density for a fixed 31 nm $Al_xGa_{1-x}N$ film by experimentally varying the Al mole fraction as is shown in Fig. 1.10(b). Vetry concluded that the close agreement between the theoretically calculated sheet charge and the experimentally determined one indicated that the formation of surface states at a particular energy level after a certain critical thickness of $Al_xGa_{1-x}N$ is a correct hypothesis. By a similar electrostatic argument, Ibbetson et al [65] identified fixed surface states at the top of the $Al_xGa_{1-x}N$ layer as the important source of electrons in the 2DEG.

1.6 Motivation for this dissertation

The performance of high power transistor devices is intimately connected to the substrate thermal conductivity. Mion and Muth measured thermal conductivity, K, on different thicknesses of not intentionally doped bulk GaN substrates and showed that the thermal conductivity increased with substrate thickness as shown in Fig. 1.11 [67]. The highest thermal conductivity they measured was on Fe-doped bulk GaN substrates at 230

$W \cdot m^{-1}K^{-1}$. It would seem logical that since SiC has a thermal conductivity that is that is 1.5 times higher than that of the highest thermal conductivity measured for GaN, SiC would be natural choice as a substrate for high power devices. However, when Mion and Muth calculated the average channel temperature over the gate length for the temperature field solution of the time-independent heat equation for a GaN film on an Fe-doped GaN substrate, they found temperature to be 108.3°C compared to 113.9°C for a GaN film on a SiC substrate. Their result defied the expectation for a 1.5 times improvement in K for SiC over GaN.

The reason that measured thermal conductivities of GaN thin films (see Fig. 1.12) are lower when grown heteroepitaxially on sapphire, silicon, and silicon carbide substrates is that the substantial in-plane lattice mismatch between the GaN thin film and the host substrate generates a thermally resistive and defective nucleation layer that contributes to lower than expected K and high dislocation density, ρ_D. The electrical analog of this series resistance behavior can be found in electrical resistors as shown in Fig. 1.13. This high ρ_D consequently inhibits the sheet charge and carrier mobility of AlGaN/GaN devices grown on non-native substrates. Since homoepitaxial growth requires no nucleation layer prior to growth of the GaN buffer, growth on bulk GaN substrates with dislocation densities of 10^6 cm^{-2} or less should lead to significantly improved thermal and electrical characteristics for HFETs. Furthermore, the substrate/epitaxy interface for homoepitaxial GaN structures are nearly strain-free, thereby eliminating a source of reliability loss and backgating in HFET structures [68]. Meon and Muth plotted thermal conductivity as a function of dislocation

density for several GaN films cited in the literature [69]. As shown in Fig. 1.15, for ρ_D of 10^{10} cm^{-2} at the nucleation interface, thermal conductivity of GaN drops to ~100 W·m^{-1}K^{-1}, effectively forming a thermal insulating barrier at the nucleation interface between two high thermal conductivity layers. They concluded that K can be fit with an empirical function of the type:

$$K = 230 \tanh^{0.12}(5x10^6 / \rho_D) \tag{1.20}$$

A homoepitaxial approach using bulk GaN substrates requires no nucleation interface layer and can result in a dislocation density below 10^6 cm^{-2}, reflecting the defect density of the underlying substrate.

In order to understand the charge density in a 2DEG layer, we self-consistently solve the one-dimensional Schrodinger and Poisson equations,

$$\frac{-h^2}{2}\frac{d}{dz}\left(\frac{1}{m_c}\frac{d\Psi(z)}{dz}\right) + (V(z) + \Delta E(z))\Psi(z) = E\Psi(z) \tag{1.21}$$

The sheet charge density at the AlGaN/GaN interface can be determined as,

$$\frac{dD(z)}{dz} = \frac{d}{dz}\left(-\varepsilon(z)\frac{dV(z)}{dz} + P(z)\right) = \rho(z) \tag{1.22}$$

where $\Psi(z)$ is the electron wave function, $\Delta E(z)$ is the conduction band offset, $V(z)$ is the electrostatic potential, $D(z)$ is the electric displacement, $P(z)$ is the total polarization, $\varepsilon(z)$ is the dielectric constant, and $\rho(z)$ is charge density. As previously mentioned, the carrier confinement at the interface is explained by the concerted effects of conduction band offset and piezoelectric and pyroelectric polarization. But Al content and barrier thickness also

play a role in increasing the probability, $\Psi^*\Psi$ for the electron wavefunction to be in the triangular well as shown in Fig. 1.15. Davidsson et al [70] performed simulations which took into account the Al content, x, the thickness of the AlGaN layer, and the free electron concentration as input parameters. By adding up the electrons localized in the electronic states, Ψ_i, the 2DEG concentration of 2.5 x 10^{13} cm^{-2} was determined for their heterostructure. Their simulations predicted the expected increase in 2DEG concentration as Al concentration increased and as the AlGaN layer thickness increased for both $x = 0.20$ and $x = 0.40$ in the AlGaN layers. But Davidsson et al did not include the parameters which reflect physical deviation from an ideal structure like interface roughness and alloy mixing.

Another parameter that is equally as important as 2DEG carrier density in the HFET is mobility, μ. The approximation of the mobility function can be written as a combination of the influences from lattice vibrations (phonons) and from impurities by Matthiessen's Rule,

$$\mu = \frac{1}{\frac{1}{\mu_{lattice}} + \frac{1}{\mu_{impurities}}} \tag{1.23}$$

Figure 1.15 shows the bulk GaAs mobility has a $T^{3/2}$ dependence at high temperatures due to lattice scattering and a $T^{-3/2}$ dependence at low temperatures as limited by impurity scattering. Minimizing ionized impurity scattering and interface scattering increases μ_{2DEG}. The advantage of a traditional HFET is that the electrons have a high mobility because the impurity scattering has been strongly reduced by the spatial separation of the electrons and

the ionized donors. Figure 1.16 illustrates that in 1978, the 77K mobility in AlGaAs/GaAs heterostructures was only 20,000 $cm^2V^{-1}s^{-1}$ but in a little over ten years, mobilities 3 orders of magnitude higher were being realized due to improvements in epitaxial growth techniques.

Mobilities for AlGaN/GaN heterostructures grown on sapphire substrates are much lower than those measured for AlGaAs/GaAs heterostructures however. Shen et al [71] showed the temperature dependence of mobility for unintentionally-doped and modulation-doped $Al_{0.22}Ga_{0.78}N$/GaN heterostructures with Si-doped $Al_{0.22}Ga_{0.78}N$/GaN barriers of thicknesses 25, 50 and 100 nm, each with 3 nm $Al_{0.22}Ga_{0.78}N$ spacers (Fig. 1.17). Their modulation-doped work clearly showed the decrease in 2DEG mobility and sheet concentration as a function of thickness of the Si-doped $Al_{0.22}Ga_{0.78}N$ layer at 300K and 77K. Unintentionally-doped AlGaN spacer thickness was varied to determine elastic strain relaxation as a function of barrier thickness. They used X-ray reciprocal space maps of the $(11\bar{2}4)$ reflections to determine if the growth was pseudomorphic or the degree to which the film was relaxed. The thickness at which partial relaxation of the $Al_{0.22}Ga_{0.78}N$ layer occurs corresponds to the thickness at which a dramatic decrease in 2DEG mobility and sheet concentration is observed in $Al_{0.22}Ga_{0.78}N$/GaN heterostructures, presumably due to elastic strain relaxation. One reason for this degradation is that the polar optical scattering and the optical impurity scattering are weakened due to the increase of the 2DEG at the heterointerface. Defects such as misfit dislocations, induced by the relaxation in the $Al_{0.22}Ga_{0.78}N$ layer also give strong scattering because these defects are charged. Srinivasan

et al [72] showed that the slip system with the largest net force, F_{net} can be summarized as follows,

$$F_{net} = F_{due_to_lattice_mismatch} - F_{due_to_line_tension} - F_{on_the_dislocation} \qquad (1.24)$$

is the $\{11\bar{2}2\}<11\bar{2}3>$(Fig. 1.18). This leads to a burgers vector, $b=\frac{1}{3}\left[11\bar{2}3\right]$ for the dislocation. Therefore, by performing calculations for varying aluminum content in the AlGaN layer using the Matthews and Blakeslee isotropic approximation [73], one can see that for an $Al_{0.25}Ga_{0.75}N$ film, the critical thickness is about 600 Å (Fig. 1.19).

One goal of this project was to achieve world record mobility by growing AlGaN/GaN HFETs on low defect density bulk GaN substrates. Table 1.7 is a compilation of success others have had in growing AlGaN/GaN HFETs on several different substrates. The Al content in the $Al_xGa_{1-x}N$ film was varied between $x=0.15$ to $x=0.30$. The reported sheet densities, n_s, range from 0.45 x 10^{13} cm^{-2} at room temperature (RT) with μ_{2DEG} of ~1200 $cm^2V^{-1}s^{-1}$ to 1.6 x 10^{13} cm^{-2} with μ_{2DEG} of ~1740 $cm^2V^{-1}s^{-1}$. The highest RT μ_{2DEG} reported was 2050 $cm^2V^{-1}s^{-1}$ grown on an Al_2O_3 substrate and had an n_s of 0.45 x 10^{13} cm^{-2}. Ando [74] showed that when the Fermi level lies in excited subbands, intersubband scatterings can become important. He showed that electrons in excited subbands have mobilities much higher than that in the lowest subband. However, strong intersubband scatterings reduce the mobility of the lowest subband from that in the single subband case. Since this latter effect dominates the former, the net average mobility becomes smaller when excited subbands become populated by electrons. In order to predict the highest mobility

that can be expected for $Al_xGa_{1-x}N$/GaN heterostructures, Bougrioua et al developed a model that took into account scattering mechanisms that limit low-field mobility such as acoustic and optical phonons, background and remote impurities, alloy disorder, interface roughness and Coulomb effect due to dislocations. By using measured parameters (dislocation density, Al content, barrier thickness), and reasonable values for roughness (0.1 to 0.2 nm) and a background concentration of ~2 x 10^{17} cm^{-3}, they fit mobility versus temperature behavior (see Fig. 1.20). This model enabled them to explain low RT μ_{2DEG} (1000 $cm^2V^{-1}sec^{-1}$ @ 300K) as the consequence of high surface roughness associated with high Al content. For moderate Al content, yielding a perfectly smooth interface and $Al_xGa_{1-x}N$ surface, they calculated RT μ_{2DEG} values exceeding 2000 $cm^2V^{-1}sec^{-1}$ [75]. Finally, by reducing dislocation density $\leq$ 7 x 10^7 cm^{-2}, they predicted RT μ_{2DEG} would reach 3000 $cm^2V^{-1}sec^{-1}$ [75].

1.7 Experimental Strategy

Our strategy, as schematically illustrated in Fig. 1.21, was to grow $Al_{0.25}Ga_{0.75}N$/GaN heterostructures on semi-insulating (0001) bulk GaN substrates to remove the thermally resistive nucleation layer and to improve the AlGaN/GaN interface roughness. These homoepitaxially-grown $Al_{0.25}Ga_{0.75}N$/GaN heterostructures would have 15 nm doped AlGaN barriers with 5 nm undoped AlGaN spacers and 20 nm undoped AlGaN barriers in order to separate the contributions from spontaneous polarization, piezoelectric polarization, and ionized donors to the sheet carrier density.

Additionally, in order to obtain high-power performance in enhancement-mode AlGaN/GaN HFET devices, it is necessary to shift $V_{threshold}$ to ensure a zero drain current at

zero bias. This threshold shift can be accomplished by eliminating the spontaneous polarization present in wurtzite GaN and instead doping the AlGaN barriers of AlGaN/GaN heterostructures grown on nonpolar bulk GaN substrates. In order to assess whether there are improved structural and electrical properties for modulation-doped AlGaN/GaN nonpolar heterostructures relative to piezoelectrically-strained AlGaN/GaN polar heterostructures, $Al_{0.25}Ga_{0.75}N$/GaN heterostructures with doped AlGaN barriers would be compared to $Al_{0.25}Ga_{0.75}N$/GaN heterostructures grown on $(1\bar{1}00)$ bulk GaN substrates as shown in Fig. 1.22.

1.8 References

[1] L.F. Eastman and U.K. Mishra, *IEEE Spectrum*, May Issue (2002) 28.

[2] S. Pearton, F. Ren, A. Zhang, and K.P. Lee, *Mat. Sci. & Eng.,* **R30** (2000) 55.

[3] F. Ren and J.C. Zolper, *Wide Energy Bandgap Electronic Devices*, World Scientific (2003) 179.

[4] J. Narayan, P. Tiwari, X. Chen, R. Chowdhury, and T. Zheleva, *Appl. Phys. Lett*., **61** (1992) 1290.

[5] J. Narayan, U.S. Patent No. 5,406,123 (April 11, 1995).

[6] J. Narayan and B.C. Larson, *J. Appl. Phys*., **93** (2003) 278.

[7] F. Ren and J.C. Zolper, *Wide Energy Bandgap Electronic Devices*, World Scientific (2003) 302.

[8] B.J. Baliga, *J. App. Phys.,* **53** (1982) 1759.

[9] B.J. Baliga, *Silicon Carbide Power Devices*, World Scientific (2005) 11.

[10] A.G. Chynoweth, *Phys. Rev.,* **31** (1960) 1161.

[11] B.J. Baliga, *IEEE Elec. Dev. Lett.,* **10** (1989) 455.

[12] E. Johnson, *RCA Rev,* (1965) 163.

[13] R.W. Keyes, *RCA Rev*., (1972) 225.

[14] K. Shenai, R.S. Scott, and B.J. Baliga, *IEEE Trans. Elect. Dev.,* **36** (1989) 1811.

[15] T.P. Chow and R. Tyagi, *IEEE Trans. Elect. Dev.,* **41** (1994) 1481.

[16] V. Vechten, *Phys. Rev., B* **7** (1973) 1479.

[17] J. Karpinski and S. Porowski, *J. Cryst. Growth*, **66** (1984) 1.

[18] J. Karpinski and Porowski, S., *J. Cryst. Growth,* **66** (1984) 11.

[19] I. Grzegory, S. Krukowski, J. Jun, M. Boaekowski, M. Wroblewski, and S. Porowski, *AIP Conf. Proc.,* **309** (1994) 565.

[20] I. Grzegory, M. Bockowski, B. Lucznik, S. Krukowski, M. Wroblewski, and S. Porowski, *MRS Internet J. of Nit. Sem. Res.,* **1** (1996) 20.

[21] G.A. Slack and T.F. McNelly, *J. Cryst. Growth,* **34** (1976) 276.

[22] I. Grzegory, *Proc. of Joint XV AIRAPT and XXXV EHPRG Conf.*, World Scientific (1996) 14.

[23] Grzegory et al, *J. Phys. Chem. Solids,* **56** (1995) 639.

[24] S. Porowski, I. Grzegory, and S. Krukowski, *High Pressure Mat. Res. Symp*. (1998) 349.

[25] S. Krukowski, Z Romanowski, I. Grzegory, and S. Porowski, *J.Cryst. Growth,* **189-190** (1998) 159.

[26] O. Kubaschewski and E. LL. Evans, *Metallurgical Thermochemistry*, Pergamon Press (1958) 246.

[27] R.C. Weast, M.J. Astle, and W.H. Beyer, *CRC Handbook of Chemistry and Physics*, CRC Press (1987) F-170.

[28] M. Steelmann-Eggebert, J.L. Weyher, H. Obloh, H. Zimmerman, A. Rar and S. Porowski, *Appl. Phys. Lett.,* **71** (1997) 2635.

[29] P. Perlin, J. Camassel, W. Knap, T. Taliercio, and J.C. Chervin, *Appl. Phys. Lett*., **67** (1995) 2524.

[30] I. Gzegory and S. Porowski, *Gallium Nitride and Related Semiconductors*, Inspec (1999) 359.

[31] P. Boguslawski, E. Briggs, and J. Bernholz, *Phys. Rev. B,* **51** (1995) 17255.

[32] W. Kim, A.E. Botchkarev, A. Salvador, G. Popovici, H. Tang, and H. Morkoc, *J. Appl. Phys*., **82** (1997) 1.

[33] J. Neugebauer and C.G. Van de Walle, *Phys. Rev. B,* **50** (1994) 8067.

[34] K. Saarinen et al, *Phys. Rev. Lett*., **79** (1997) 3030.

[35] M. Leszczynski et al, *J. Cryst. Growth,* **169** (1996) 235.

[36] S. Kurai, T. Abe, Y. Naoi, and S. Sakai, *Jpn. J. Appl. Phys.,* **35** (1996) L77.

[37] S. Kurai, Y. Naoi, S. Abe, S. Ohmi, and S. Sakai, *Jpn. J. Appl. Phys.,* **35** (1996) 1637.

[38] C.M. Balkas et al, *Mater. Res. Soc., Symp. Proc.,* **449** (1997) 41.

[39] E. Ejder, *J. Cryst. Growth,* **22** (1974) 44.

[40] R.B. Zetterstorm, *J. Mat. Sci*., **5** (1970) 1102.

[41] Y. Naoi et al, *Proc. 2nd Int. Conf. on Nitride Semiconductors,* (1997) L184.

[42] M.K. Kelly, R.P. Vaudo, V.M. Phanse, O. Ambacher, M. Stutzmann, *Jpn. J. Appl. Phys*., **38** (1999) L217.

[43] S.S. Park, I.-W. Park, and S.H. Choh, *Jpn. J.Appl. Phys.,* **39** (2000) L1141.

[44] K. Motoki, T. Okahisa, N. Matsumoto, M. Matsushima, H. Kimura, H. Kasai, K. Takemoto, K. Uematsu, Y. Masahiro, M. Nakayama, S. Nakahata, M. Ueno, D. Hara, Y. Kumagai, A. Koukitu, and H. Seki, *Jpn. J. Appl. Phys.,* **40** (2001) L140.

[45] T. Yoshida, Y. Oshima, T. Eri, K. Ikeda, S. Yamamoto, K. Watanabe, M. Shibata, and T.J. Mishim, *J. Cryst. Growth,* **310** (2008) 5.

[46] J.A. Frietas, Jr., M. Gowda, J.G. Tischler, J.-H. Kim, L. Liu, and D. Hanser, *J. Cryst. Growth*, **310** (2008) 3968.

[47] Y. Oshima, T. Eri, M Shibata, H. Sunakawa, K Obayashi, T. Ichihashi, and A. Usui, *Jpn. J. Appl. Phys.,* **42** (2003) L1.

[48] Y. Oshima, T. Eri, M Shibata, H. Sunakawa, and A. Usui, *Phys. Stat. Sol. (a),* **194** (2002) 554.

[49] A. Usui, T. Ichihashi, K. Kobayashi, H. Sunakawa, Y. Oshima, T. Eri, and M. Shibata, *Phys. Stat. Sol. (a),* **194** (2002) 572.

[50] R. Heitz, P. Maxim, L. Eckey, P. Thurian, A. Hoffman, I. Broser, K. Pressai, and B.K., Meyer, *Phys. Rev. B,* **55** (1997) 4382.

[51] B.A. Haskell, F. Wu, S. Matsuda, M.D. Craven, P.T. Fini, S.P. DenBaars, J.S. Speck, and S. Nakamura, *Appl. Phys. Lett.* **83** (2003) 1554.

[52] B.A. Haskell, T.J. Baker, M.B. McClaurin, F. Wu, P.T. Fini, S.P. DenBaars, J.S. Speck, and S. Nakamura, *J. Electron. Mater.,* **34** (2005) 357.

[53] D. Hanser, L. Liu, E.A. Preble, K. Udwary, T. Paskova, and K.R. Evans, *J. Cryst. Growth,* **310** (2008) 3953.

[54] O. Ambacher, *J. Phys. D,* **31** (1998) 2653.

[55] R.D. Shannon and C.T. Prewitt, *Acta Cryst., B* **25** (1997) 925.

[56] F. Bernardini, V. Fioretini, and D. Vanderbilt, *Phys. Rev. B,* **56** (1997) R10024.

[57] J.H. Edgar (ed), *Group III Nitrides,* London: INSPEC (1994).

[58] A.F. Wright, *J. Appl. Phys.,* **82** (1997) 2833.

[59] O. Ambacher, B. Foutz, J. Smart, J.R. Shealy, N.G. Weimann, K. Chu, M. Murphy, A.J. Sierakowski, W.J. Schaff, and L.F. Eastman, *J. Appl. Phys.,.* **87** (2000) 334.

[60] R.A. Kiehl, P.M. Solomon, and D.J. Frank, *IBM J. Res. Develop.,* **34** (1990) 506.

[61] R. Dingle, H.L. Stormer, A.C. Gossard, and W. Wiegmann, *Appl. Phys. Lett*., **33** (1978) 665.

[62] P.M. Asbeck, E.T. Yu, S.S. Lau, G.J. Sullivan, J. Van Hove, and J.M. Redwing, *Electron. Lett.,* **33** (1997)1230.

[63] E.T. Yu, G.J. Sullivan, P.M. Abeck, C.D. Wang, D. Qiao, and S.S. Lau, *Appl. Phys. Lett*., **71** (1997) 2794.

[64] A.D. Bykhovski, R. Gaska, M.S. Shur, *Appl. Phys. Lett.,* **73** (1998), 3577.

[65] J.P. Ibbetson, P.T. Fini, K.D. Ness, S.P. DenBaars, J.S. Speck, and U.K. Mishra, *Appl. Phys. Lett.,* **77** (2000), 250.

[66] R. Vetury, I.P. Smorchkova, C.R. Elsass, B. Heying, S. Keller, and U.K. Mishra, *Mat. Res. Soc. Symp.,* **622** (2000) T2.5.1.

[67] C. Mion et al, *Superlattices and Microstructures,* **40** (2006) 338.

[68] J. Wurfl, *Microelectron. Reliab*., **39** (1999) 1737.

[69] C. Mion et al, *Appl. Phys. Lett*., **89** (2006) 092123.

[70] S.K. Davidsson, M. Gurusinghe, T.G. Andersson, and H. Zirath, *J. Electron. Mater.*, **33** (2004) 440.

[71] B. Shen, T. Someya, and Y. Arakawa, *Appl. Phys. Lett.*, **76** (2000) 2746.

[72] S. Srinivasan, L. Geng, R. Lui, and F.A. Ponce, *Appl. Phys. Lett*., **83** (2003) 5187.

[73] J.W. Matthews and A.E. Blakeslee, *J. Cryst. Growth,* **27** (1974) 118.

[74] T. Ando, *J. Phys. Soc. Jpn*., **51** (1982) 3900.

[75] Z. Bougrioua, M. Azize, P. Lorenzini, M. Laugt, and H. Haas, *Phys. Stat. Sol. (a),* **202** (2005) 536.

1.9 Tables

Table 1.1 Properties of some substrate materials for GaN growth [3].

Table 1: Properties of some substrate materials for GaN growth

Substrate	E_g (eV)	K (W/cm°C)	E_c (MV/cm)	ε	μ (cm^2/Vs)	v_s (cm/s)	$\frac{KE_c^2\varepsilon\mu v_s}{(KE_c^2\varepsilon\mu v_s)_{Si}}$ *
Si	1.1	1.31	0.3	11.8	1350	$1x10^7$	1
GaN	3.39	1.3	3.3	9	1200	$2.5x10^7$	153
SiC	2.86	4.9	2	10	650	$2x10^7$	136
Sapphire	—	0.25	—	—	—	—	—
AlN	6.2	3.4	—	300	300	$1.5x10^7$	—
GaAs	1.43	0.53	0.4	8500	8500	$2x10^7$	10

*Combined figure of merit for high temperature / high power / high frequency applications from Fan Ren & John C. Zolper, *Wide Energy Bandgap Electronic Devices*, World Scientific Publishing (2003) 179.

Table 1.2 Physical properties of important semiconductors for high-voltage power devices [7].

Table 2: Physical properties of important semiconductors for high-voltage power devices.

Material	E_g (eV)	n_i (cm^{-3})	ε_r	μ_n (cm/Vs)	E_c (MV/cm)	v_{sat} (10^7 cm/s)	K (W/cm K)	Direct / Indirect
Si	1.1	1.5×10^{10}	11.8	1350	0.3	1.0	1.5	I
Ge	0.66	2.4×10^{13}	16.0	3900	0.1	0.5	0.6	I
GaAs	1.4	1.8×10^{6}	12.8	8500	0.4	2.0	0.5	D
GaP	2.3	7.7×10^{-1}	11.1	350	1.3	1.4	0.8	I
InN	1.86	$\sim 10^3$	9.6	3000	1.0	2.5	—	D
GaN	3.39	1.9×10^{-10}	9.0	900	3.3	2.5	1.3	D
3C-SiC	2.2	6.9	9.6	900	1.2	2.0	4.5	I
4H-SiC	3.26	8.2×10^{-9}	10.0	720[a], 650[c]	2.0	2.0	4.5	I
6H-SiC	3.0	2.3×10^{-6}	9.7	370[a], 50[c]	2.4	2.0	4.5	I
Diamond	5.45	1.6×10^{-27}	5.5	1900	5.6	2.7	20	I
BN	6.0	1.5×10^{-31}	7.1	5	10	1.0*	13	I
AlN	6.1	$\sim 10^{-31}$	8.7	1100	11.7	1.8	2.5	D

Note: a-mobility along a-axis, c-mobility along c-axis, *-estimate
Fan Ren & John C. Zolper, *Wide Energy Bandgap Electronic Devices*, World Scientific Publishing (2003) 302.

Table 1.3 Normalized Figures of Merit for Various Semiconductors [15].

Table 3: Normalized Figures of Merit for Various Semiconductors

Material	$JM = \left(\frac{E_c \cdot v_{sat}}{\pi}\right)^2$	$KM = K\left(\frac{v_{sat}}{\varepsilon}\right)^2$	$BM = \left(\varepsilon\mu E_c^3\right)$	$BHFM = \left(\mu E_c^2\right)$	$QF1 = K \cdot BM$	$QF2 = K \cdot BM \cdot E_c$
Si	1.00	1.00	1.00	1.00	1.00	1.00
Ge	----	----	0.13	0.28	0.05	0.02
Diam. (s)	5330	31	14860	1080	198100	5784410
Diam. (p)	6220	32	11700	850	155990	4554840
InP	13	0.72	10	6.6	26	38
InN (m=3000)	58	6	46	19	150	460
InN (m=30000)	58	6	450	155	1500	4570
AlN(m=14)	5120	2.6	390	14	660	25520
AlN(m=1090)	5120	2.6	31670	1100	52890	2058620
GaAs	11	0.45	25	16	9.4	16
GaN	**790**	**1.8**	**910**	**100**	**910**	**10300**
GaP	37	0.73	16	3.8	9.4	41
6H-SiC	260	5.1	90	13	300	2440
3C-SiC	110	5.8	40	12	130	550
4H-SiC	410	5.1	290	34	950	9630

T. Paul Chow and Ritu Tyagi, *Wide Bandgap Compound Semiconductors for Superior High-Voltage Unipolar Power Devices*, IEEE Trans. Elect. Dev. 41 (1994) 1481-1483.

JM - Johnson Figure of Merit - basic limit on device performance of a typical transistor.

KM - Keyes Figure of Merit - switching speed of transistors for computer logic applications

BM - Baliga Figure of Merit - defined material parameters for minimizing conduction losses in power FETs, assuming only ON-resistance, valid only for low frequency applications, uses no assumption about the heat sink material or geometry of the device.

BHFM - Baliga High Frequency Figure of Merit - considered the effects of switching losses due to the charging and discharging of the input capacitance of the FET.

QF1 - Shenai et al Figure of Merit 1 - proposed to incorporate all possible device and heat sink designs used in power devices.

QF2 - Shenai et al Figure of Merit 2 - based on the assumption of a perfect heat sink with the active area assumed to be at ambient temperature.

Table 1.4 Lattice constants, bandgaps and binding energies of hexagonal InN, GaN and AlN [54].

Wurtzite, 300 K	AlN	GaN	InN
a_0 (Å)[b]	3.112	3.189	3.54
c_0 (Å)[b]	4.982	5.185	5.705
c_0/a_0 (exp.)[b]	1.6010	1.6259	1.6116
c_0/a_0 (calc.)[a]	1.6190	1.6336	1.6270
u_0[a]	0.380	0.376	0.377
a_{Bohr} (Å)[a]	5.814	6.04	6.66
E_B(M–N)[c] (eV)[b]	2.88	2.20	1.98

[a] From [16].

[b] From [17].

[c] M = In, Ga or Al, N = nitride.

Table 1.5 Spontaneous polarization, piezoelectric and dielectric constants of AlN, GaN and InN [54].

Wurtzite	AlN	GaN	InN
P_{SP} (C m^{-2})	−0.081	−0.029	−0.032
e_{33} (C m^{-2})	1.46[a] 1.55[b]	0.73[a] 1[c] 0.65[d] 0.44[e]	0.97[a]
e_{31} (C m^{-2})	−0.60[a] −0.58[b]	−0.49[a] −0.36[c] −0.33[d] −0.22[e]	−0.57[a]
e_{15} (C m^{-2})	−0.48[b]	−0.3[c] −0.33[d] −0.22[e]	
ε_{11}	9.0[b]	9.5[f]	
ε_{33}	10.7[b]	10.4[f]	

[a] From [16].
[b] From [26].
[c] From [27].
[d] From [28].
[e] From [29].
[f] From [30].

Table 1.6 Predicted values of $2C_{13}/C_{33}$ from [56] and the references therein.

AlN	GaN	InN
0.607,[a] 0.509[b]	1.184,[c] 0.533,[d] 0.369[e]	0.665[c]
0.665,[f] 0.567,[g] 0.579[h]	0.510,[g] 0.509[h]	0.940,[g] 0.821[h]

[a]Measurements by Tsubouchi *et al.* (Ref. 16).
[b]Measurements by McNeil *et al.* (Ref. 17).
[c]Measurements by Sheleg and Savastenko (Ref. 18).
[d]Measurements by Polian *et al.* (Ref. 19).
[e]Measurements by Takagi *et al.* (Ref. 20).
[f]Calculations by Ruiz *et al.* (Ref. 10).
[g]Calculations by Kim *et al.* (Refs. 11 and 12).
[h]Present calculations.

Table 1.7 World class results for AlGaN/GaN HFETS.

x	$n_s(10^{13}/cm^2)$	$\mu(cm^2/V\text{-}s)$	Substrate	Reference
0.25	0.57-1.1	1213-1740	SI-GaN/Al_2O_3	E. Iliopoulos et al, *Superlatt. Microstruct.*, **40** (2006) 313.
0.33	0.96-1.6	1096-1864	SI-GaN/Al_2O_3	" " " "
0.3	1.1	1590	SI-SiC	P. Kordos, J. Bernat, M. Marso, *Microelectron. J.*, **36** (2005) 438.
0.27	1.05	950	Al_2O_3	M. Germain et al, *Mat. Res. Symp. Proc.*, **798** (2004) Y10.22.1.
0.27	0.98	1550	Al_2O_3	" " " " (this heterostructure has an AlN barrier)
0.3	1.01	2050	Al_2O_3	" " " " (this heterostructure has an AlN barrier)
0.25	0.45	1200	Si(111)	S.Iwakami et al, *Jpn. J. Appl. Phys.*, **43** (2004) L831.
0.15-0.35	0.5-1.3	1100-1500	Al_2O_3	Z.Bougrioua et al, *Phys. Stat. Sol.(b)*, **228** (2001) 625.
0.15-0.35	>1.4	<900	Al_2O_3	" " " "
0.26	?	1172	Al_2O_3	G. Y. Zhao et al, *Physica E*, **7** (2000) 963.

1.10 Figures

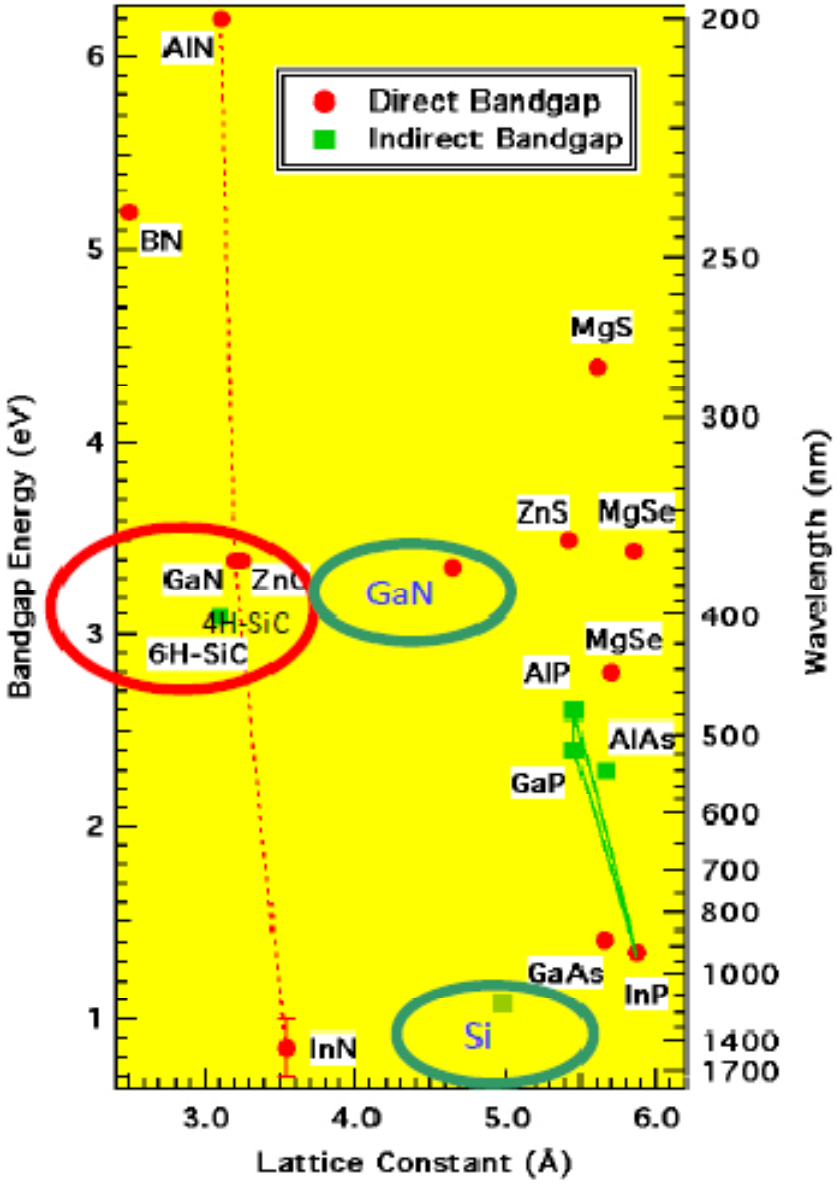


Figure 1.1 Bandgap Energy as a function of lattice constant for several direct and indirect bandgap semiconductors.

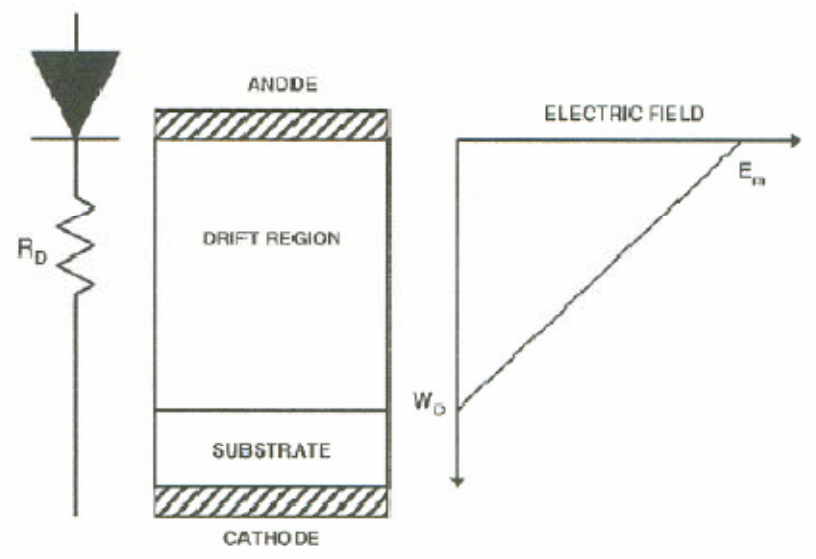


Figure 1.2 The Ideal Drift Region in a unipolar device and its Electric Field Distribution [9].

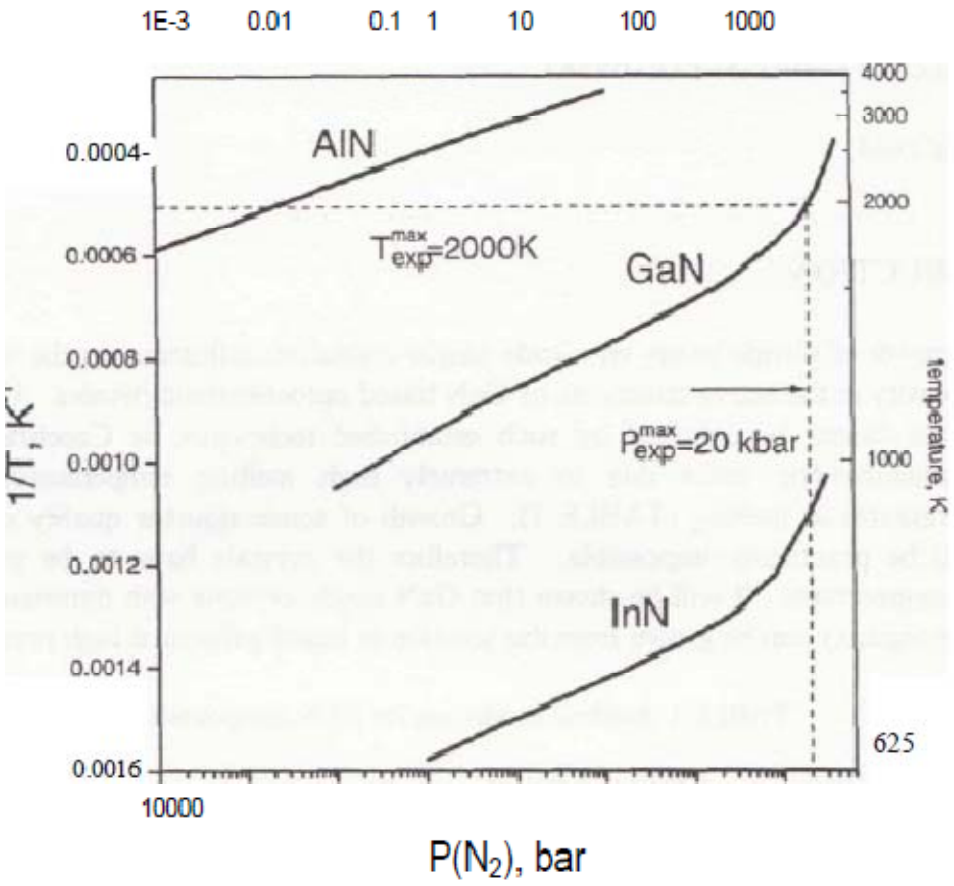


Figure 1.3 Equilibrium N_2 pressure over III-Nitrides [17, 21-23].

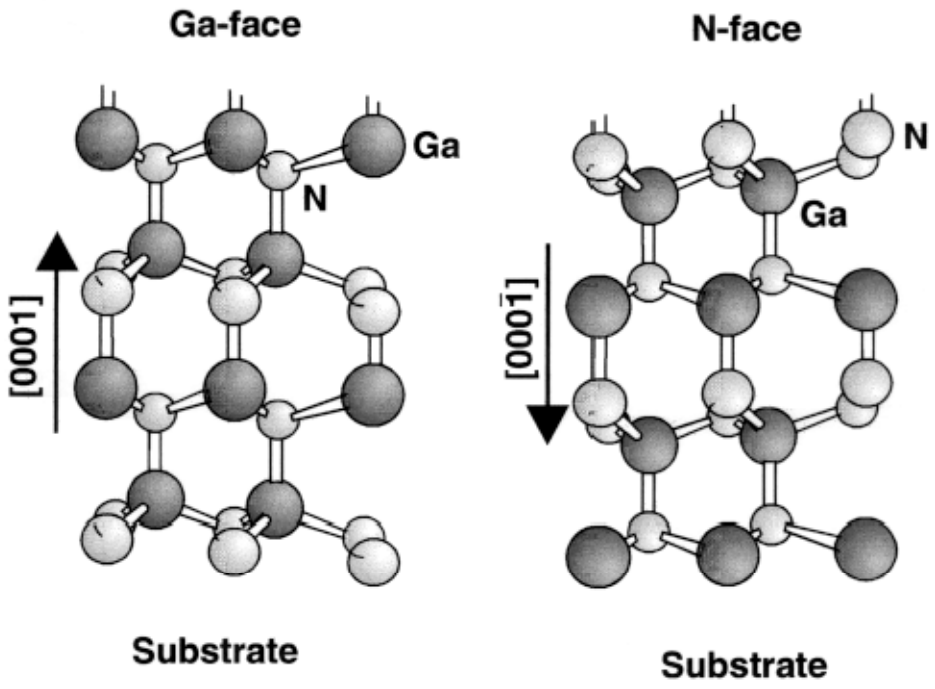


Figure 1.4 Different polarities (Ga- and N-faced) of wurtzite GaN [54].

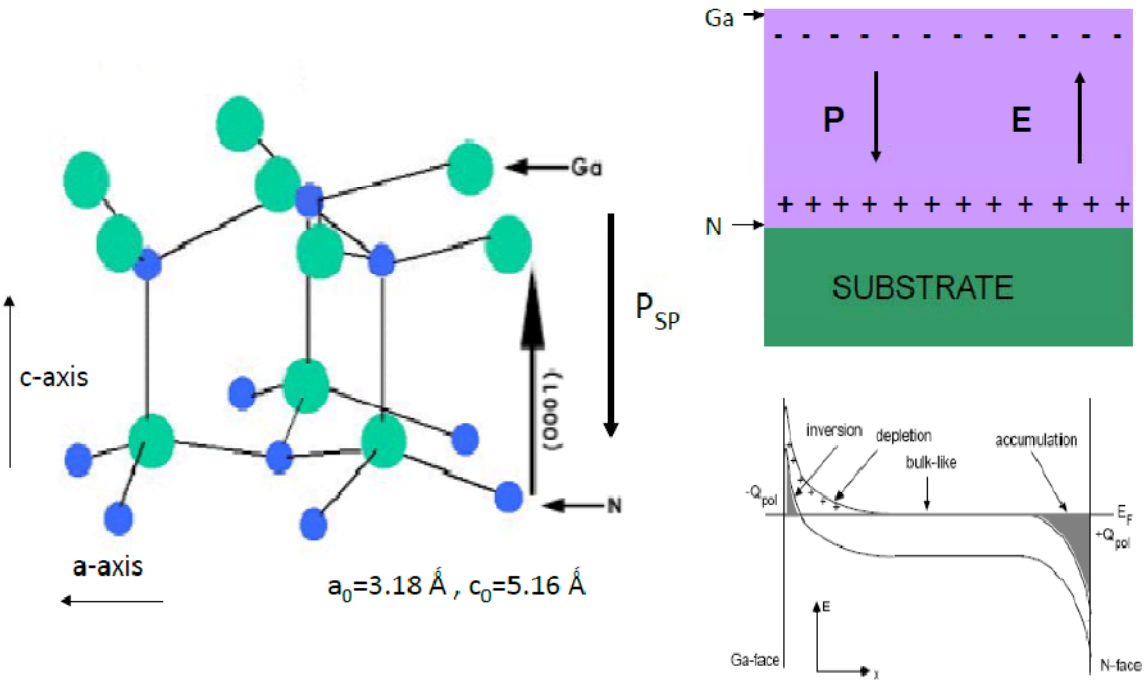


Figure 1.5 Spontaneous polarization is a property of point group crystals that lack a center of symmetry. The polarization vector leads to an accumulation of charges of opposite sign at each of the interfaces which sets up a sizeable electric field within the material.

$$\sigma(P_{SP}+P_{PE}) = P_{bottom} - P_{top} = P_{SP(bottom)} - \{P_{SP(top)} + P_{PE(top)}\}$$

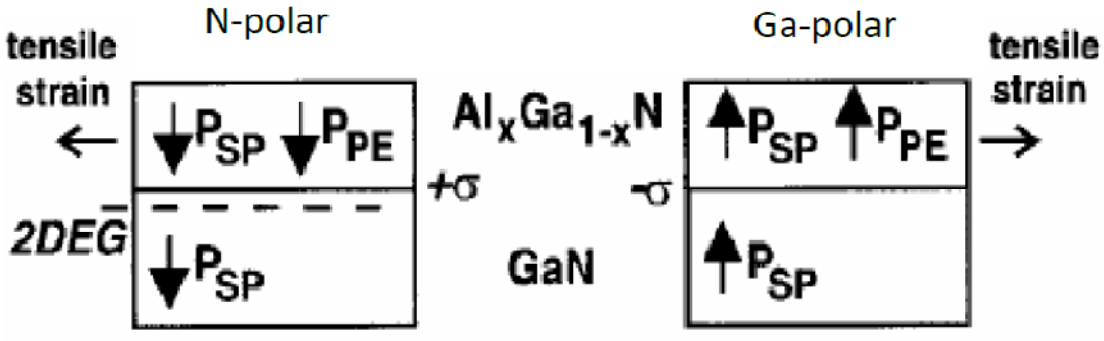


Figure 1.6 The polarization charge for an AlGaN/GaN heterostructure grown on a bulk GaN substrate is described by the above equation [56].

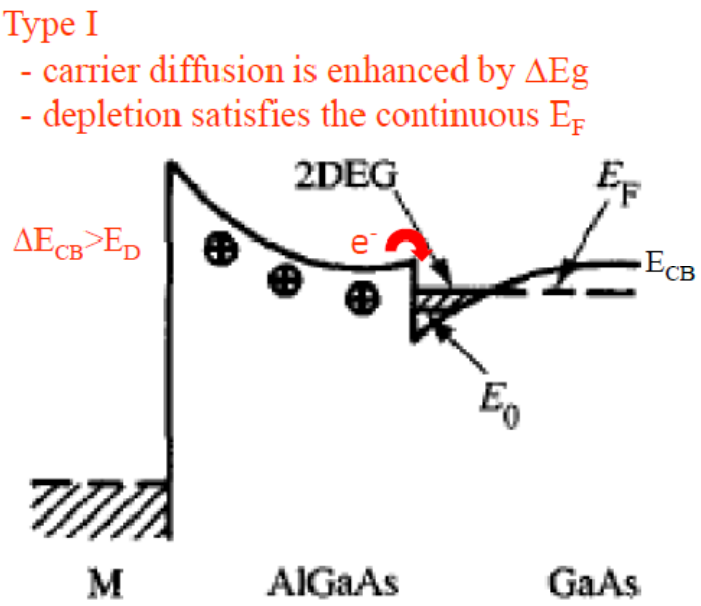


Figure 1.7 In Type I materials, formation of the two-dimensional electron gas is assisted by carrier diffusion resulting from the bandgap difference at the heterointerface. Depletion of the carriers from the larger to smaller bandgap material is necessary to satisfy a continuous Fermi level [60].

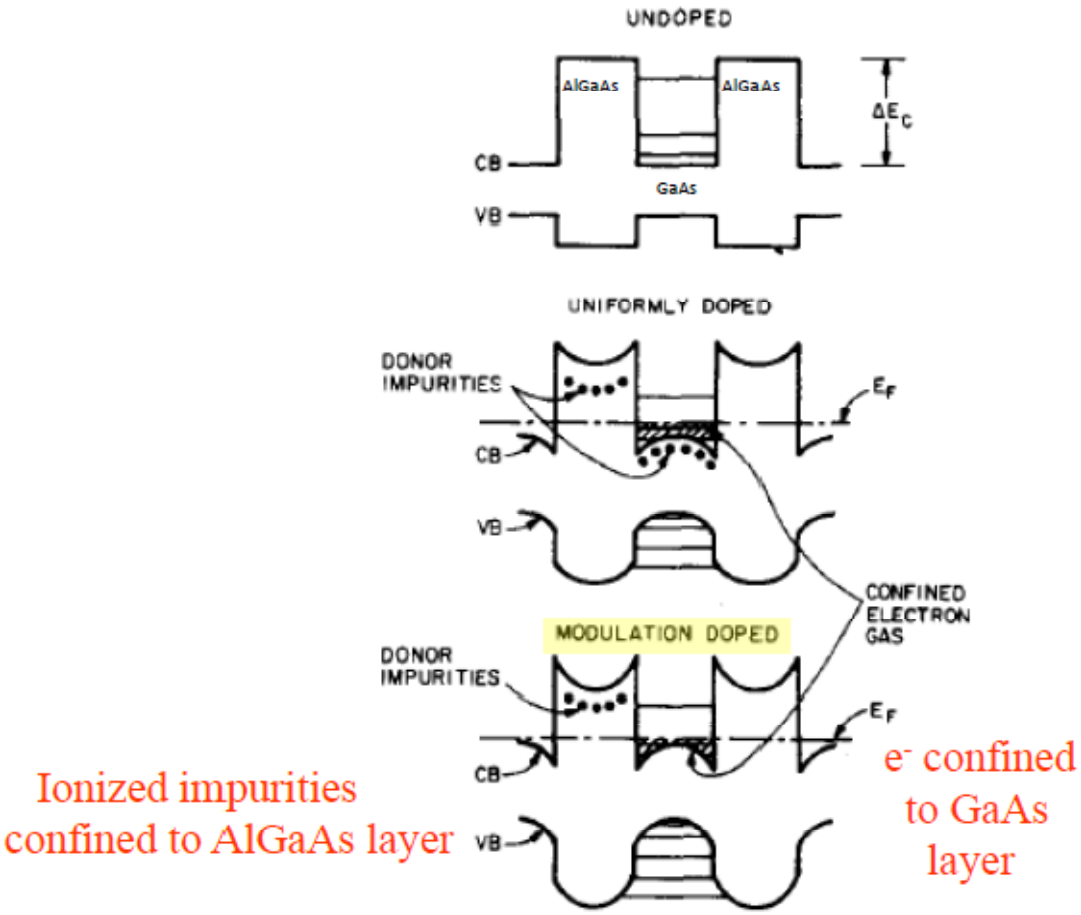


Figure 1.8 In an AlGaAs/GaAs heterostructure, carriers confined to the GaAs layer form a 2DEG. The confinement of the ionized impurities to the AlGaAs layer has consequences for carrier mobility within the 2DEG [61].

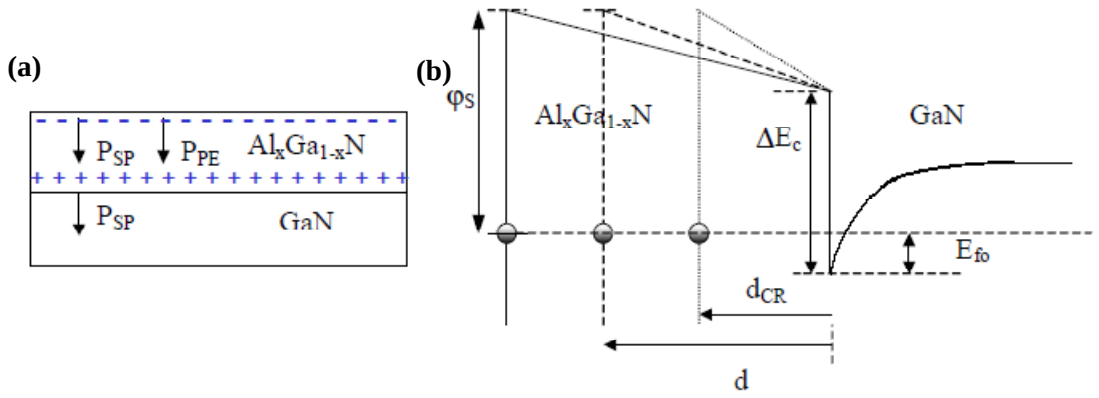


Figure 1.9 (a) Polarization dipole across the AlGaN layer. (b) Band diagram for AlGaN/GaN and the parameters determining the sheet carrier density and critical thickness, d_{CR}, of the AlGaN layer [66].

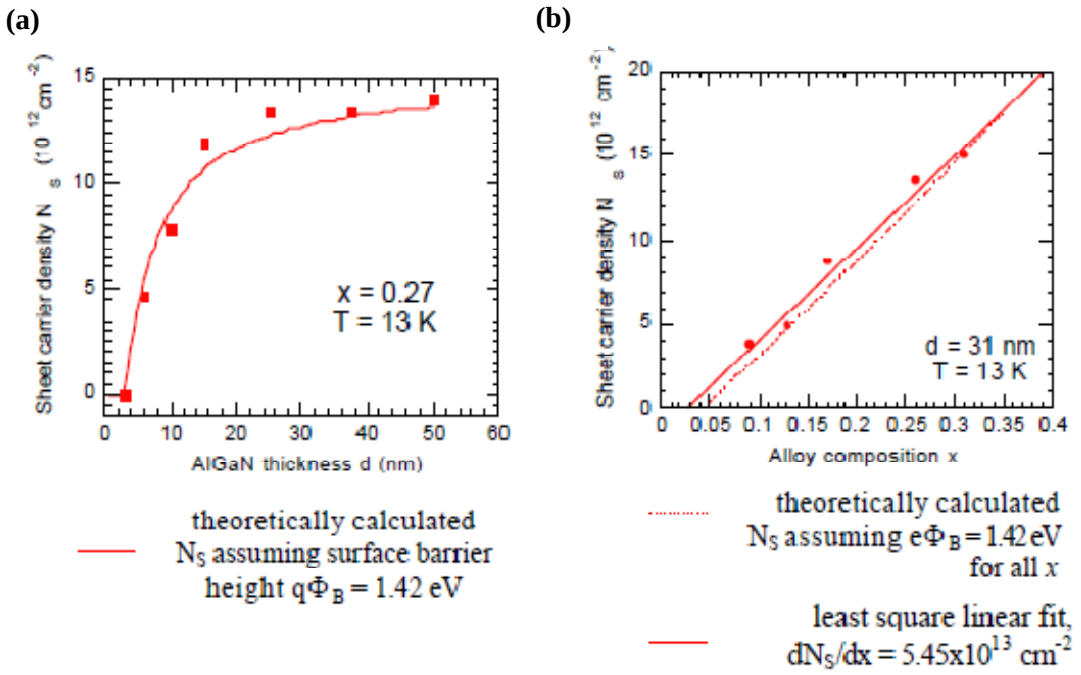


Figure 1.10 (a) Theoretically calculated sheet carrier density vs. AlGaN thickness (b) Theoretically calculated sheet carrier density vs. alloy composition and the least square fit [66].

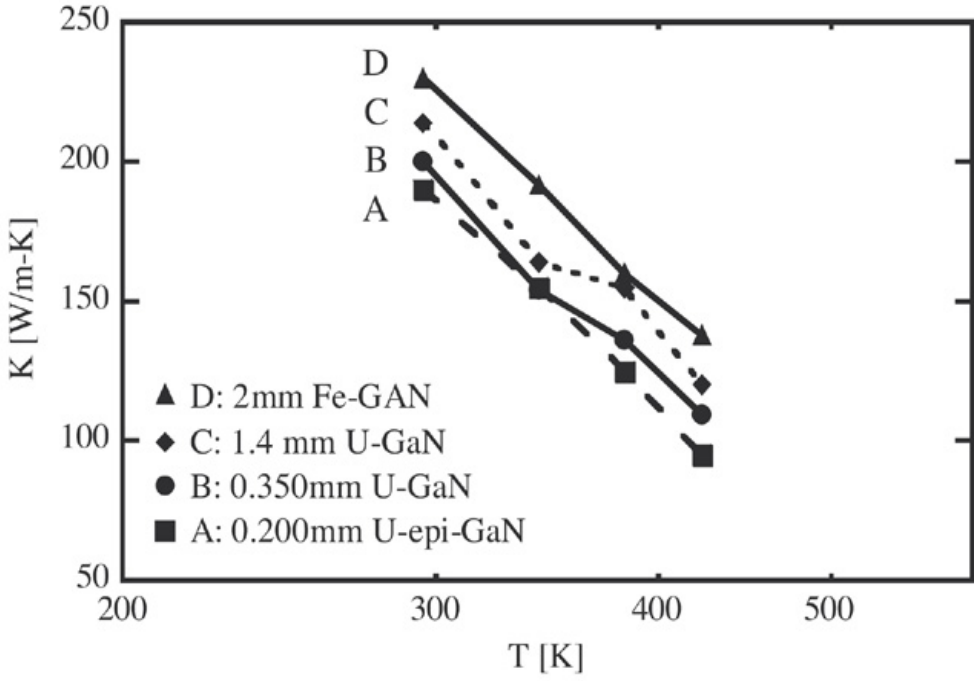


Figure 1.11 Thermal conductivity measurements of unintentionally-doped HVPE-grown bulk GaN substrates and Fe-doped HVPE-grown bulk GaN substrate [67].

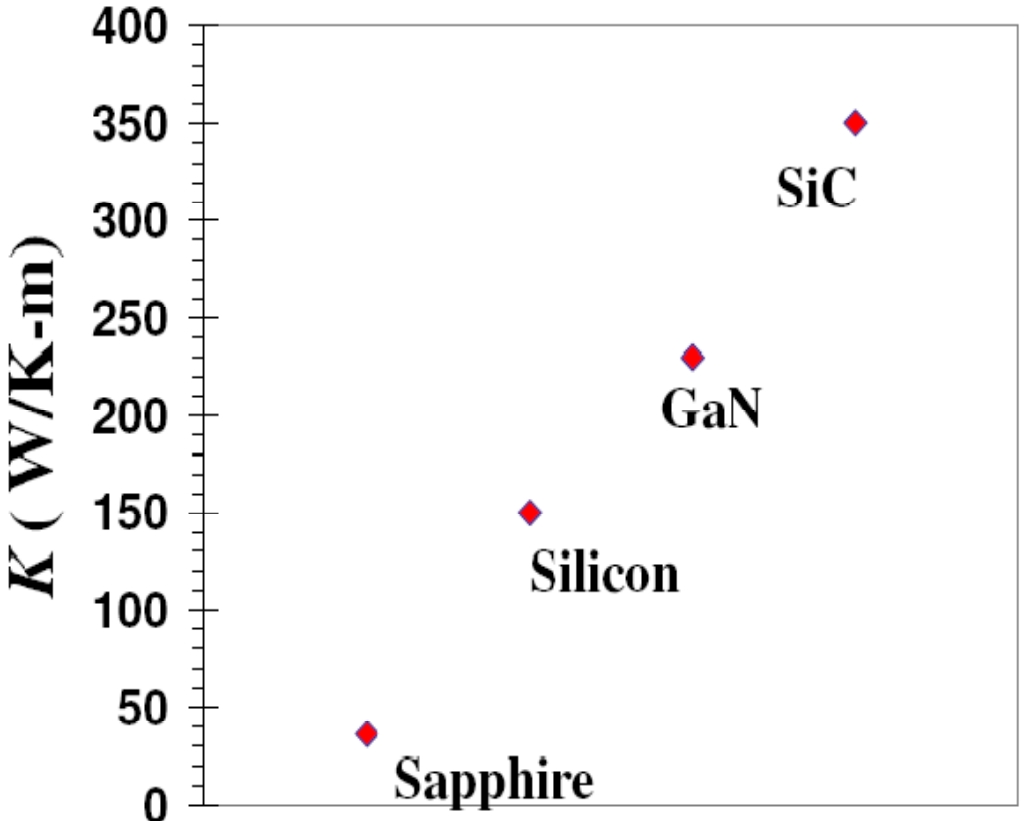


Figure 1.12 Thermal conductivity measurements for GaN thin films on different host substrates [67].

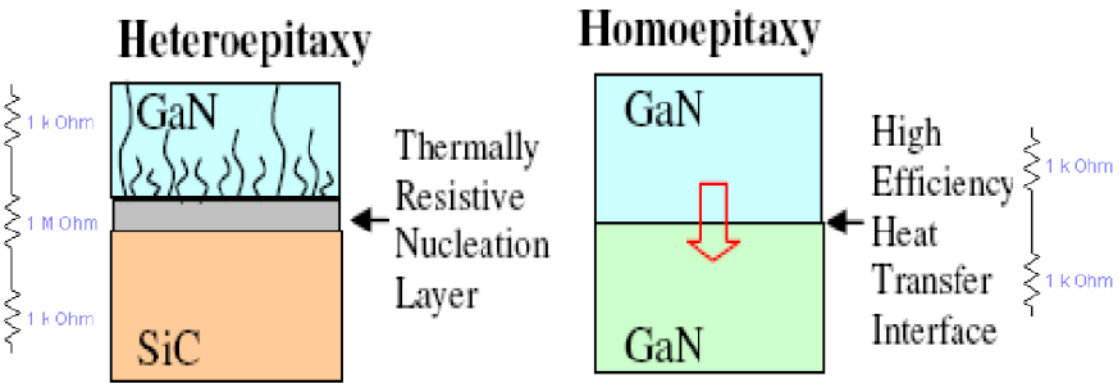


Figure 1.13 Chemical and structural mismatch introduces a high density of defects at the SiC/GaN nucleation interface locally limiting thermal conductivity.

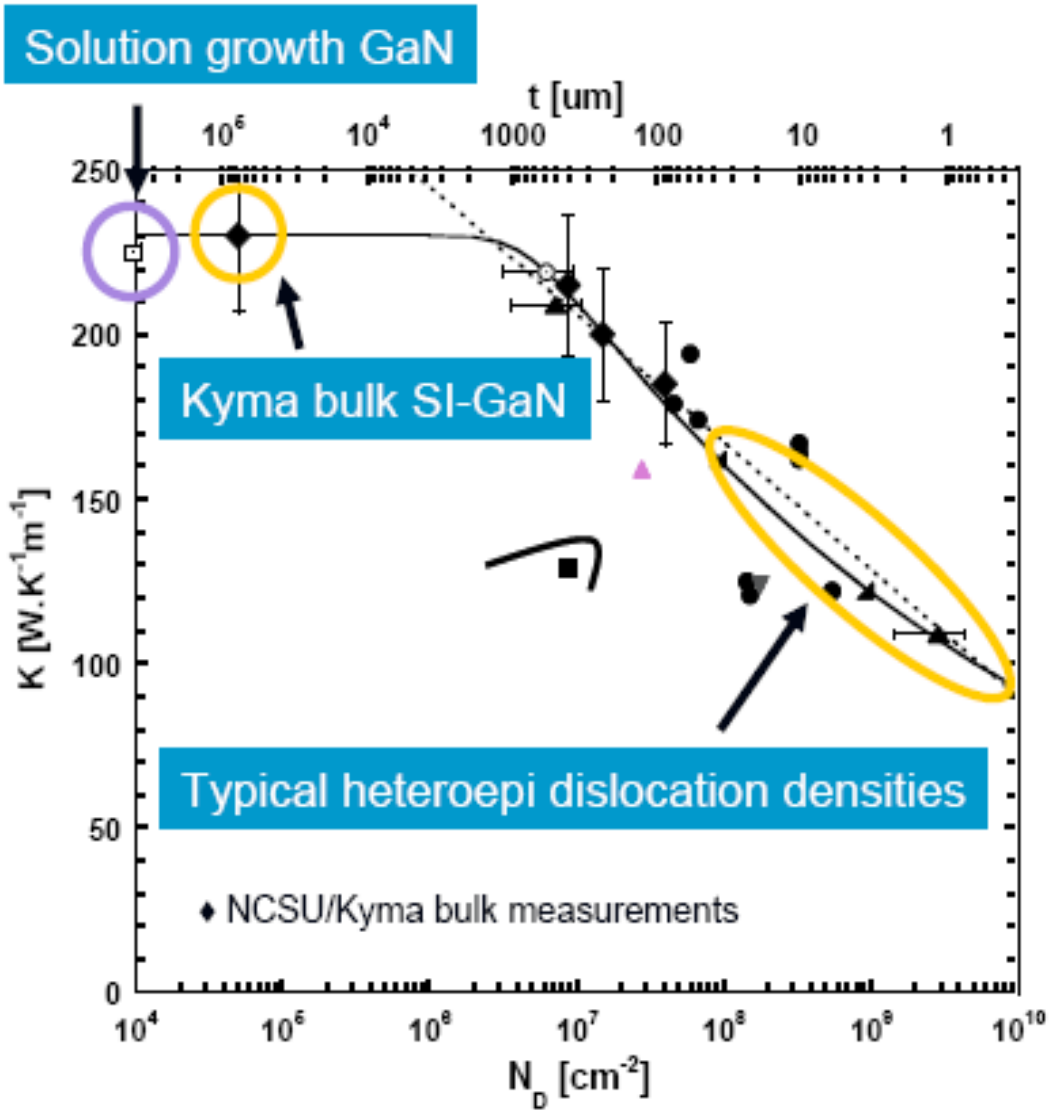


Figure 1.14 Low dislocation density bulk GaN substrates realize high thermal conductivity which is essential to optimize heat dissipation in high-power transistors [69].

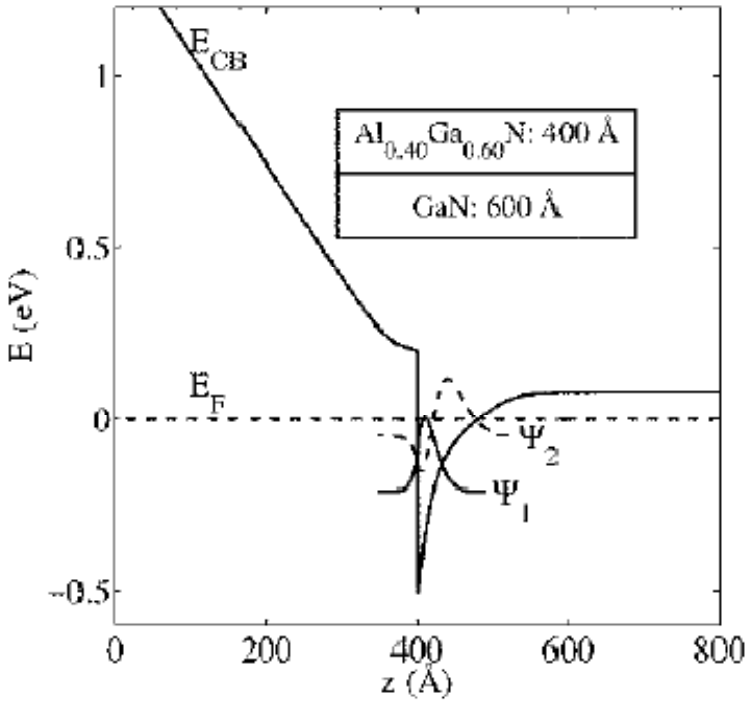


Figure 1.15 When $\psi^{*}\psi$ is high the wavefuntion will be in the triangular quantum well [70].

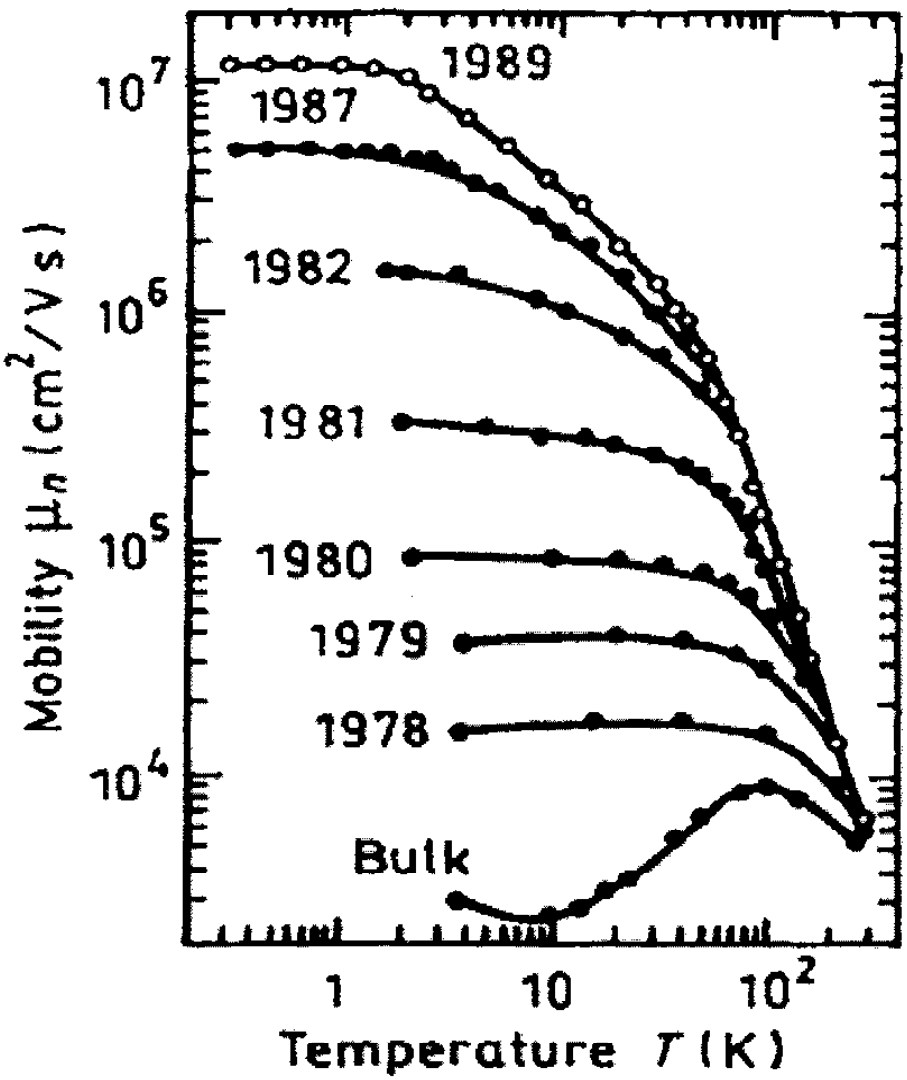


Figure 1.16 Electron mobility of AlGaAs heterostructures versus year. (Courtesy AT&T Bell Laboratories Corporation, Murray Hill, NJ)

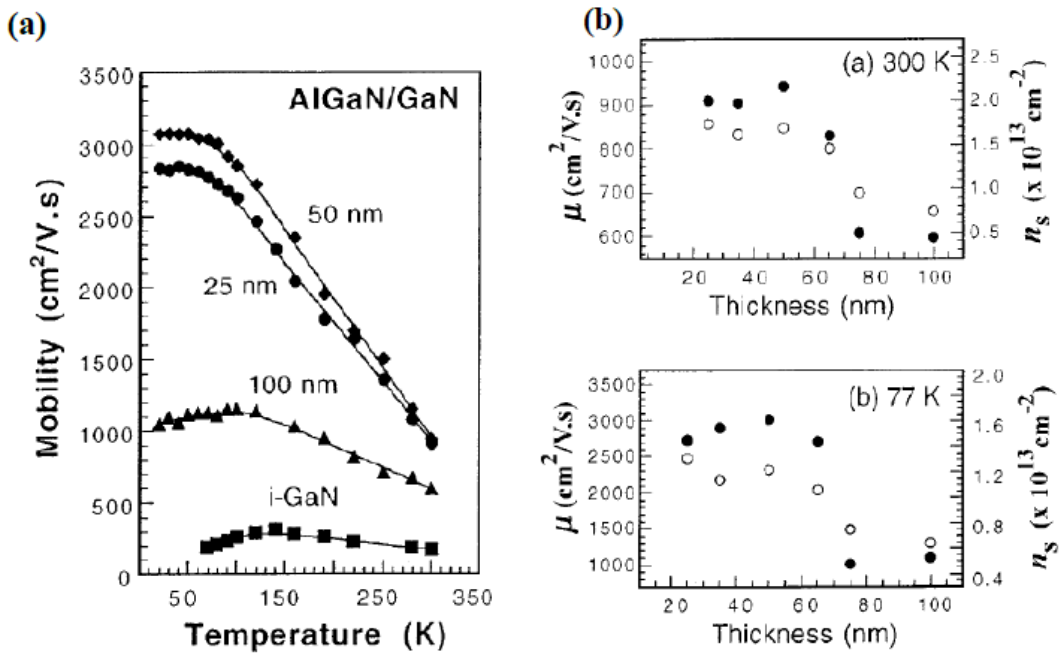


Figure 1.17 (a) Electron mobility as a function of temperature for n-AlGaN/GaN heterostructures with fixed AlGaN spacer thickness. (b) 2DEG mobility as a function of not-intentionally-doped AlGaN thickness at RT and 77K [71].

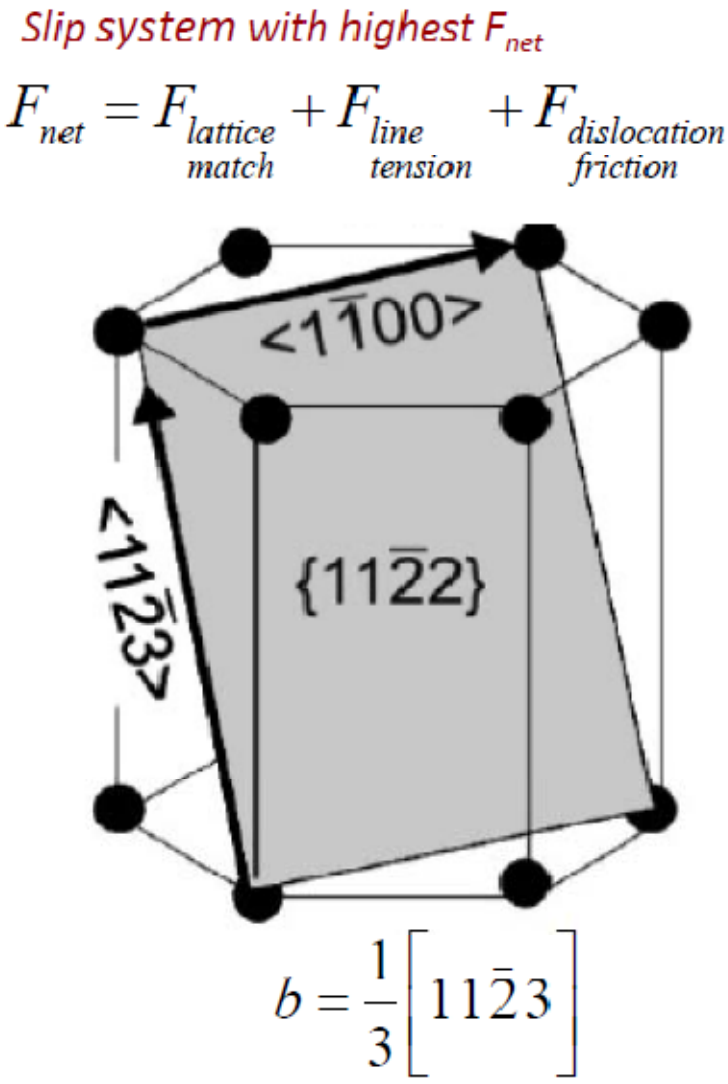


Figure 1.18 The slip system $\{11\bar{2}2\}<112\bar{3}>$ gives the highest net force for a dislocation [72].

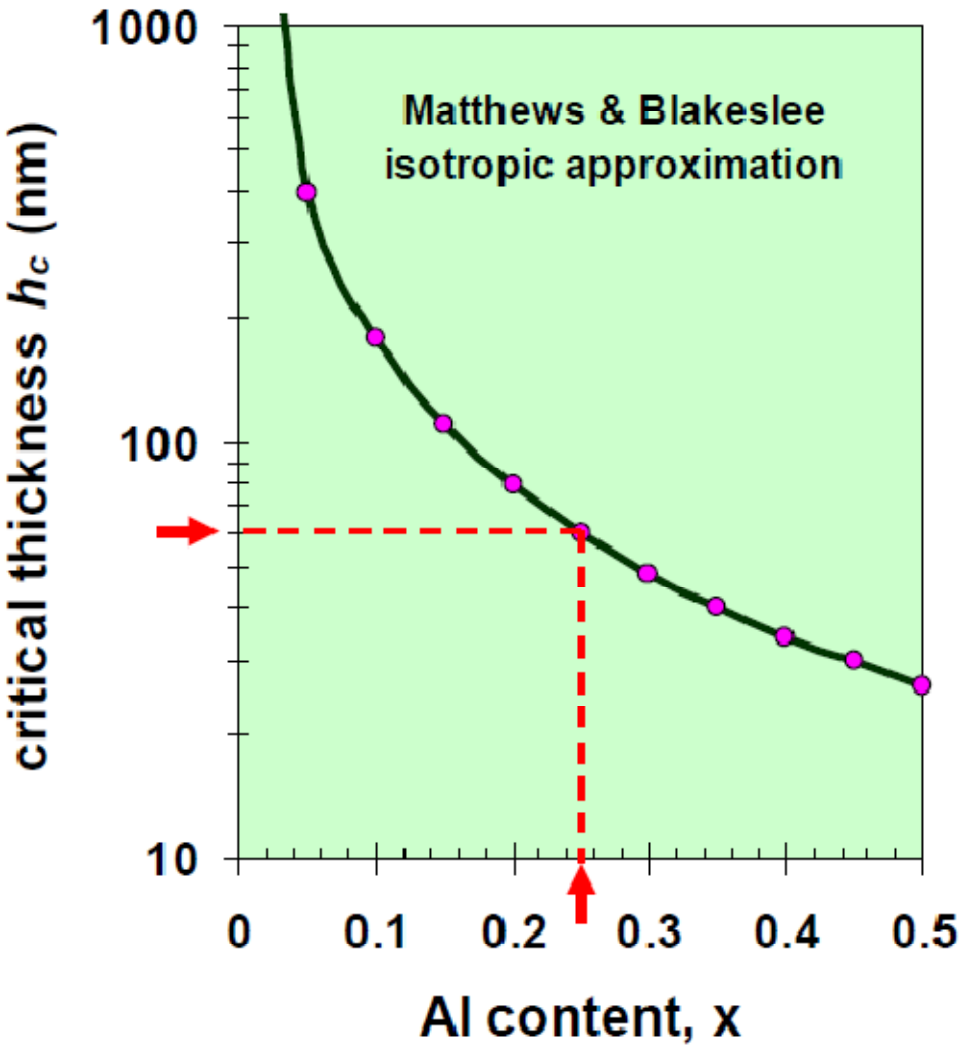


Figure 1.19 Critical thickness calculated as a function of Al content. The critical thickness for an $Al_{0.25}Ga_{0.78}N$ film is ~600 Å.

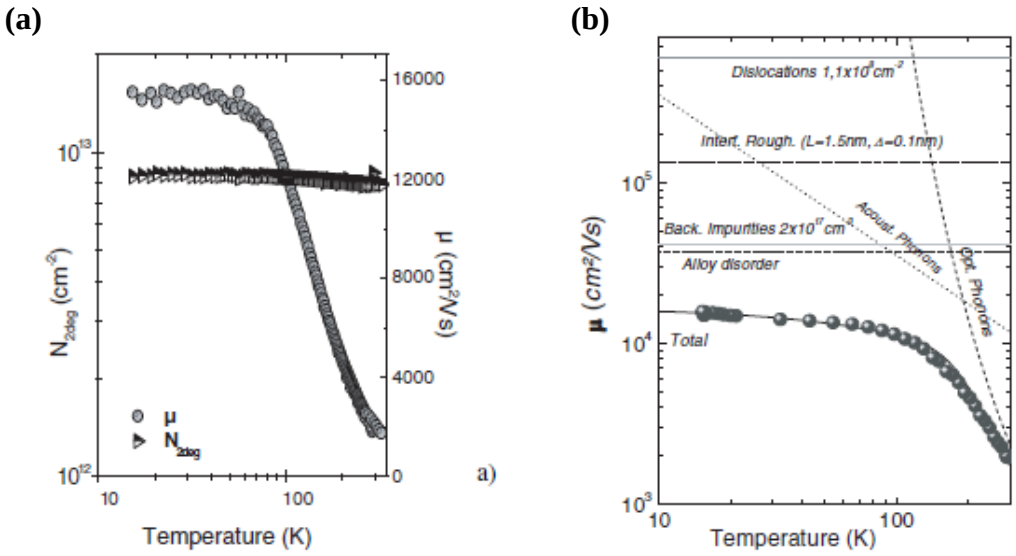


Figure 1.20 (a) Experimental μ(T) and n_s(T) (b) Fit and contributions from different scattering centers [75].

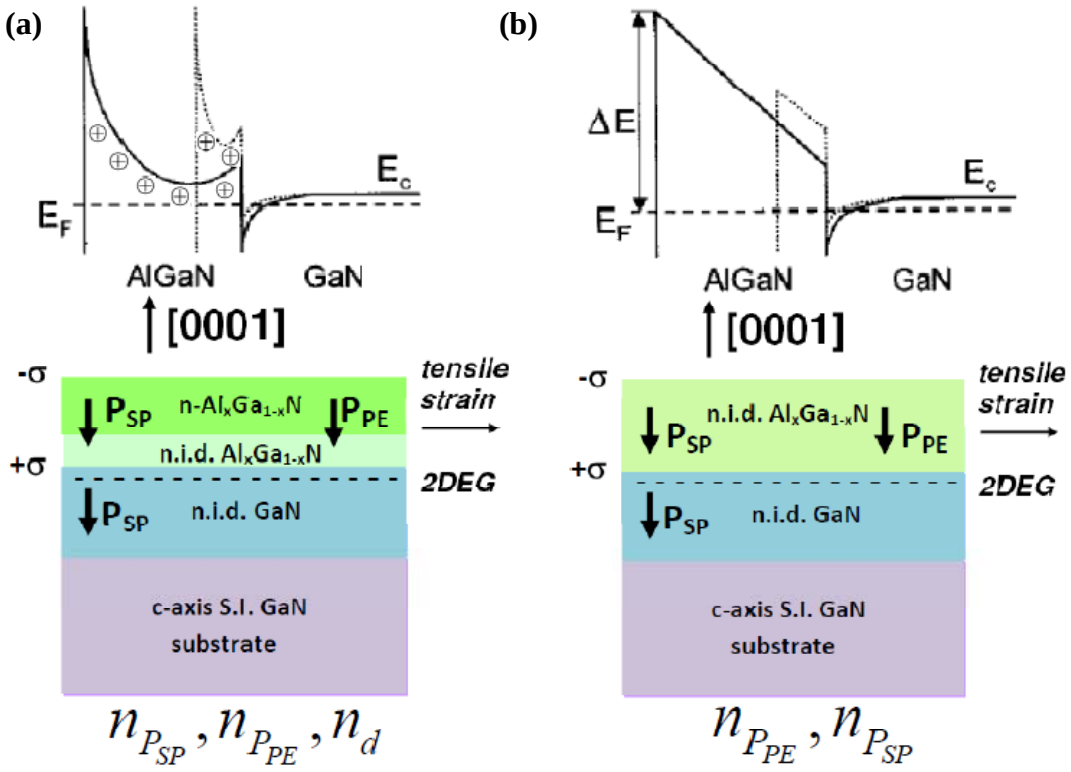


Figure 1.21 AlGaN/GaN heterostructures grown on (0001) S.I. GaN substrates with (a) undoped AlGaN barriers with 5 nm AlGaN spacers and (b) 20 nm undoped AlGaN barriers would be compared to assess the contributions from spontaneous polarization, piezoelectric polarization and ionized donors to the 2DEG carrier density.

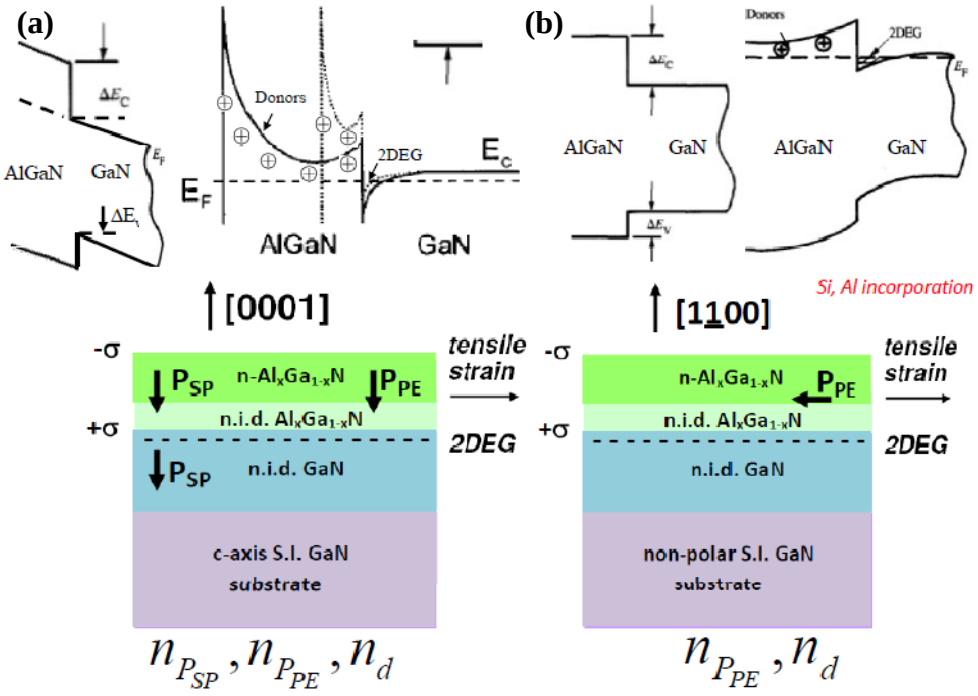


Figure 1.22 AlGaN/GaN heterostructures with (a) 15 nm doped AlGaN barriers and 5 nm undoped AlGaN spacers grown on (0001) S.I. bulk GaN substrates would be compared to (b) heterostructures with 15 nm doped AlGaN barriers and 5 nm doped AlGaN spacers grown on $(1\bar{1}00)$ nonpolar bulk GaN substrates to assess improvements in structural and electrical properties.

2. EXPERIMENTAL PROCEDURES IN PRELIMINARY ANALYSIS

2.1 Heterostructure Growth

The AlGaN/GaN heterostructures in this study were grown by organometallic vapor phase epitaxy (OMVPE) in a vertical reactor at 1040^{o}C and 60 torr on 450 μm thick, semi-insulating bulk GaN substrates. Trimethygallium (TMG), Trimethylaluminum (TMAl), ammonia (NH_3) and silane were used as precursors. The Fe-doped, c-axis GaN substrates were grown in a conventional vertical hydride vapor phase epitaxy (HVPE) reactor at a growth rate of approximately 100 mm/ hr. Cathodoluminescence (CL), double crystal X-ray diffraction (DCXRD), photoreflectance and photoluminescence were used to verify bandgap and layer thicknesses of the heterostructure illustrated in Fig. 2.1. Capacitance-voltage (CV) measurements were used to ascertain free carrier concentrations of the substrate as well as the film. Secondary ion mass spectroscopy (SIMS) confirmed atomic impurity concentrations. Atomic force microscopy was employed to assess film surface roughness. Photoluminescence and Raman spectroscopy were employed to understand the carrier transitions occurring within the heterostructure. Van der Pauw Hall measurements were carried out at room temperature and 77K to determine sheet resistance, sheet density and carrier mobility.

2.2 Analytical Instrumentation

2.2.1 SEM/Cathodoluminescence

Cathodoluminescence relies on the thermionic emission of electrons from a tungsten filament to impinge onto a semiconductor material resulting in the promotion of electrons from the valence band (VB) to the conduction band (CB), leaving behind a hole. When an

electron and hole recombine, it is possible for a photon to be emitted. In addition to band to band edge recombination, excitonic, donor to VB, CB to acceptor, donor-acceptor pair and excited state transitions generate photons of different energies. The photon energy will be determined by the initial and final states. Non-recombination processes, such as thermalization, or hot carrier events, where an electron is brought to the edge of the CB or VB, can also occur.

Cathodoluminescence is performed in a scanning electron microscope. This environment enables the required electron emission as well and the focus of those electrons. The operator chooses a gun voltage between 1 and 30 kV. The gun voltage is the difference between that at the tungsten filament, the cathode, and the anode. The anode is at ground. A bias resistor (see Fig. 2.2) is set between the Wehnelt grid cap and the filament. This allows the filament to be heated by passing a current through it, otherwise known as Joule heating. The filament is heated to a temperature such that thermal energy, kT, can overcome the cathode's work function (E_w) to release electrons. The biased Wehnelt cap restricts electron emission to the filament tip because the electrons are attracted to the positive field at the tip and repelled by the negative field at the edges of the grid cap. The Wehnelt cap provides the focusing action to form an initial crossover, d_0, or focused spot. A series of magnets, referred to as lenses, collimate the electrons into a tightly focused beam (see Fig. 2.3). The condenser lens determines the beam current and possible spot size, d_1. The objective lens determines the final spot size, d_2.

When this highly focused beam of electrons impinges on the sample, it induces it to emit light from a localized area. This light is collected by an elliptical mirror. Then a fiber

optic will transfer the light out of the microscope where it will be separated by a monochromator (Fig. 2.4) and then detected with a photomultiplier tube (PMT) illustrated in Fig. 2.5. A charge couple device, CCD array, can be used to measure the entire energy spectrum by removing the monochromator output slit so that the whole dispersion plane falls onto the CCD array. By keeping the monochromator slit in place, the less expensive, but highly robust, PMT can detect a signal to be used for imaging, referred to as panchromatic imaging, and by scanning the grating, a highly-sensitive energy spectrum can be obtained.

2.2.2 Bandgap measurements

As the Al mole fraction, x, in an $Al_xGa_{1-x}N$ film is increased, the bandgap begins to deviate from that predicted by Vegard's Law [3, 4] as shown in Fig. 2.6(a). Cathodoluminescence was used to collect the energy spectrums of varying aluminum compositions of 800 nm thick $Al_xGa_{1-x}N$ films grown on 50 mm round Al_2O_3 substrates as per the schematic in Fig. 2.6(b). We used experimental data [4] to find the energy gap of $Al_xGa_{1-x}N$ $(0 \le x \le 1)$ plotted as a function of Al composition with a bowing parameter, b=1.0 eV, in order to determine the Al compositions of our films. The difference in the $Al_xGa_{1-x}N$ bandgap measured by CL from the bandgap of GaN film measured by CL,

$$\Delta E_g = E_{g(Al_xGa_{1-x}N)} - E_{g(GaN)} \tag{2.1}$$

was used to determine the conduction band discontinuity to valence band discontinuity of ~75:25 [5] for the AlGaN/GaN system as given by,

$$\Delta E_{CB} = 0.75 \cdot \Delta E_g \tag{2.2}$$

Figure 2.7 shows the conduction band offset, ΔE_{CB} as a function of Al content for the

calibration runs performed.

2.2.3 High Resolution X-Ray Diffractometry (HRXRD)

X-ray wavelengths compare with the energy transitions of the inner orbitals in atoms. It is the property of the monochromatic X-ray that enables a range of structural parameters to be studied. The AlGaN films grown on sapphire substrates were measured using a Philips X'pert MRD triple axis diffracted beam system. Bragg's Law,

$$\lambda = 2d\sin\theta \tag{2.3}$$

where λ is wavelength, d is interplanar spacing and θ is the Bragg angle is the basis of X-ray diffraction: The Bragg angle is the angle between the incident beam and reflecting plane (Fig 2.8(a)). When an Ewald sphere is drawn with its center on the incident beam and its circumference passing through the origin, the radius of the that sphere is,

$$r = \frac{1}{\lambda} \tag{2.4}$$

and the angle between the beams in the Ewald sphere is 2θ (Fig. 2.8(b)). The distance between the ends of the incident and diffracted ray is,

$$\frac{2\sin\theta}{\lambda} = \frac{1}{d} \tag{2.5}$$

The triangle within the Ewald sphere is a geometrical representation of Bragg's Law. For the general case with the factor n in the Bragg equation, the length of this line is $\frac{n}{d}$. This represents the n th order reflection from the lattice. The reciprocal space interference points have the Miller indices hkl, $2h2k2l$ and $3h3k3l$ for the series of reflections from the set of

(hkl) planes. In reciprocal space, a series of equally spaced planes is represented by a series of points $\frac{1}{d}$ apart. Each point in reciprocal space represents a Bragg reflection. If we assume the radius of the Ewald sphere is $\frac{1}{\lambda}$ then the distance between the reciprocal lattice point and the origin is $\frac{1}{d}$. The following equations give the relationship between the X and the Y values in reciprocal space and the diffractometer angles, Omega (ω) and 2Theta (2θ),

$$X = R(\cos\omega - \cos(2\theta - \omega) \tag{2.6}$$

$$Y = R(\sin\omega - \sin(2\theta - \omega) \tag{2.7}$$

where R is the radius of the Ewald sphere. The 2θ scan appears as an arc along the Ewald sphere circumference. The scan subtends an angle equal to the scan range at the center of the Ewald sphere. Thus, 2θ scan appears as an arc of the same length for any reflection but the orientation of the arc depends on the reflection chosen. The ($\omega - 2\theta$) or ($2\theta - \omega$) scan is always a straight line pointing away from the origin of the reciprocal space. In reciprocal space, the length of the line decreases as the $\frac{1}{d}$ value for the reflection increases.

An example of single scan for the calibration runs is shown in Fig. 2.9. From the $\omega - 2\theta$ rocking curve we can find the $Al_xGa_{1-x}N$ composition. We know theoretically, GaN 2θ= 34.7709° and AlN 2θ= 36.1753°, therefore, $\Delta(2\theta_{AlN} - 2\theta_{GaN})$= 1.4044°. For the GaN 2θpeak on the X-ray data, we can calculate the expected AlN 2θ peak. Apply $d = \frac{n\lambda}{2\sin\theta}$ to find the d-spacing for GaN, $Al_xGa_{1-x}N$ and AlN. By applying Vegard's Law,

$$x_{AlN} \cdot d_{AlN} + (1 - x_{AlN}) \cdot d_{GaN} = d_{Al_xGa_{1-x}N} \tag{2.8}$$

and by iteratively solving, x_{AlN} was found for the 12% film to be $Al_{0.10}Ga_{0.90}N$, for the 19% film to be $Al_{0.16}Ga_{0.84}N$ and for the 25% film to be $Al_{0.27}Ga_{0.73}N$. From this data, we were able to ascertain that trimethylgallium flow was the process control lever to obtain the desired bandgap for our $Al_xGa_{1-x}N$ barrier layer (see Fig. 2.10).

2.2.4 Reflectance Spectroscopy

Thicknesses of our calibration runs were determined by reflectance interference measurements obtained using a Perkin Elmer Lambda 9 spectrophotometer. It is equipped with two sources, a white light and deuterium lamp. A monochromator, slewed from the near infrared through the visible and into the ultraviolet spectrum, detects the reflectance, t, or the fraction of incident electromagnetic power reflected as

$$t = \frac{\lambda_1 \lambda_2}{(\lambda_1 - \lambda_2) 2 n_{eff}} \tag{2.9}$$

where λ is wavelength and n_{eff} is the refractive index of the film. Figure 2.12(a) is a compilation of reflectance spectrums for the calibration runs. Film growth rates calculated from reflectance thickness measurements were used for both not-intentionally-doped GaN and $Al_xGa_{1-x}N$ layers and correlated with Al composition as shown in Fig. 2.12(b).

2.2.5 Secondary Ion Mass Spectroscopy (SIMS)

In SIMS, when a primary ion, O^{2+}or Cs^{-} penetrates the semiconductor surface, energy is lost through collision cascade and the primary ion becomes implanted into the semiconductor. In the process, secondary particles, including ions, leave the surface at low energy. The escape depth of the sputtered species is only a few angstroms. Since some species have approximately the same mass as others, the correct mass resolution must be chosen in order to separate similar peaks. For instance, ^{24}Mg=23.985 amu, has an interference with double-carbon, $^{12}C - {}^{12}C$ = 24.000 amu. Since the difference between those two species, ΔM is 0.015 amu, a mass resolution, $\frac{M}{\Delta M}$ of 1600 is required to separate ^{24}Mg and $^{12}C - {}^{12}C$. An implant standard is measured prior to the semiconductor sample to verify the known profile for the species of interest. Raster resolution techniques are used, i.e., the crater diameter is kept at the same diameter but the sputtered area is reduced by one-half thereby increasing the sputtering rate by four times, to enable concentration and depth profiles to be accurate within 10 – 15% of the implant standard.

Figure 2.14 shows SIMS analysis using primary ion, Cs- shows ^{16}O concentration on the order of 2x10^{17} cm-3. Unintentional doping in GaN materials may be high because of oxygen doping. Carriers behave according to the exponential function,

$$n = N_D \cdot \exp(-E_D / kT) \tag{2.10}$$

where $E_{D_{Si}}$ = 30 meV and the donor ionization energy of oxygen in GaN is $E_{D_{O^{2-}}}$ = 29 meV. SIMS analysis, shown in Fig. 2.15, was instrumental in revealing a Si spike at the

substrate/epitaxial interface possibly due to colloidal silica contributed during substrate polishing or thermal etching and recapture [6] and/or diffusion post-HVPE.

2.2.6 Atomic Force Microscopy (AFM)

In the most common mode of AFM, contact mode, the tip is scanned across the surface at a constant repulsive force, typically 100 nN – 1000 nN. The force F is given by Hooke's Law,

$$F = -k\Delta z \tag{2.11}$$

where k is the spring constant, typically 1 N/m, and Δz is the displacement, typically 100 nm as illustrated in Fig. 2.16(a) and (b). The surface roughness is a measure of the localized height as given by the deflection. Typical surface roughness for as-received bulk GaN substrates was ~2.5 nm for this set of substrates. In addition to surface roughness measurements, the AFM can give insight as to the growth mechanism. The 5 □m x 5 □m^2 scan in Fig. 2.17 illustrates the step flow growth mode that resulted in a root mean square (RMS) surface roughness of 0.994 nm.

2.2.7 Photoluminescence (PL)

Room temperature (RT) photoluminescence was performed using a HeCd or an excimer (XeCl) laser. The 325 nm HeCd laser had an excitation intensity of 2.5 $W \cdot cm^{-2}$ at the sample surface. Photons were analyzed with a double monochromator with a spatial resolution of 1-2 meV and detected by a lock-in-amplifier. A simple schematic of the photoluminescence apparatus is given in Fig. 2.18. In photoluminescence measurements, energy of the excitation source, which has a bandgap in excess of that of semiconductor, is

absorbed in a process called photo-excitation illustrated in Fig. 2.19 [7]. Photo-excitation causes electrons within the semiconductor to move in excited state. When these electrons return to their ground state, the release of excess energy may be a radiative (photons) or non-radiative process. Thermalization of the carrier is non-radiative event. The most common radiative transition is between states in the conduction band and valence band and is a means of determining the bandgap of the material. Transition energies from ionized donor impurity states to the acceptor states, and the amount of photoluminescence measured in those transitions, can give insight as to impurity concentrations. Localized defect levels serve as traps or non-radiative recombination centers. Since localized defects are detrimental to the semiconductor, quantification of the amount of radiative recombination can be used to evaluate the properties of the semiconductor. Photoluminescence mapping using a 308 nm excimer laser enabled the wavelength uniformity of the $Al_xGa_{1-x}N$ to be measured across the 18 x 18 mm^2 substrates. An example of PL mapping of AlGaN/GaN heterostructures grown on 18 x 18 mm^2 bulk GaN substrates is given in Fig. 2.20. Table 2.1 is a summary of the XRD, PL, and AFM characterization results for the AlGaN/GaN heterostructures grown during the preliminary analysis.

2.2.8 Van der Pauw Hall Measurements (Hall)

We performed Hall-effect measurements to determine sheet densities and Hall mobility for our AlGaN/GaN heterostructures. When a magnet field is applied perpendicular to the applied current direction in the semiconductor, a transverse field is perpendicular to both the direction of the applied field, E_x and the magnetic field, B_z, or the y-direction as shown in Fig. 2.21 [8]. By putting a voltmeter across the sample the Hall voltage, V_H can be

measured. The applied field E_x drives a current J_x in the sample. The electrons move in the –x direction, with drift velocity v_{dx} [9]

$$-I = qAev_x \tag{2.12}$$

Because of the magnetic field, there is a Lorentz force acting on each electron and given by $F_y = -ev_{dx}B_z$. The force on an electron is in the –y-direction as given by the right-hand rule for the vector notation,

$$F = q\,\mathbf{v} \times \mathbf{B} \tag{2.13}$$

All moving charges experience this Lorentz force. Electrons as well as holes are deflected to the bottom of the sample because electrons flow in the opposite direction to holes and have opposite charge. Sheet resistance is defined by

$$R_{12,34} = \frac{V_{34}}{I_{12}} \tag{2.14}$$

where the current I_{12} enters the sample through contact 1 and leaves through contact 2 and $V_{34} = V_3 - V_4$ Eight measurements $R_{21,34}, R_{32,41}, R_{43,12}, R_{14,23}$ yield eight values for sheet resistance. Sheet resistance, R_s, is determined from the characteristic resistances,

$$\begin{aligned} R_A &= (R_{21,34} + R_{12,43} + R_{43,12} + R_{34,21})/4 \\ R_B &= (R_{32,41} + R_{23,34} + R_{14,23} + R_{41,32})/4 \end{aligned} \tag{2.15}$$

and by fitting the following algorithm,

$$\exp(-\pi R_A / R_s) + \exp(-\pi R_B / R_s) = 1 \tag{2.16}$$

The Hall measurement is carried out in the presence of a magnetic field. Hall voltage is

determined by forcing direct current into lead 1 and removing it from lead 2, I_{13}. Hall voltage, V_{24P}, is measured between leads 2 and 4 with a positive magnetic field (+z-direction) for I_{13}. Four measurements are taken in the positive magnetic field direction, $V_{24N}, V_{42N}, V_{13N}, V_{31N}$ and four are taken when the magnetic field is reversed. Sheet carrier density is given by

$$n_s = \frac{8x10^{-8} \cdot IB}{qV \cdot \{(V_{24P} - V_{24N}) + (V_{42N} - V_{42P}) + (V_{13P} - V_{13N}) + (V_{31P} - V_{13N})\}} \quad (2.17)$$

and Hall mobility is given by

$$\mu = \frac{1}{qn_s R_s} \quad (2.18)$$

A permanent magnet or an electromagnet in the range of 500 to 5000 gauss is required. Direct currents usually range from 10 μA to 100 mA but for semi-insulating material a current as low as 1 nA is required. The voltmeter must have high input impedence and cover a range from 1 μV to 1V [10]. Table 2.2 is a summary of the van der Pauw results for AlGaN/GaN heterostructures grown during the preliminary analysis.

2.2.9 Raman Spectroscopy

Vibrational transitions which are observed in the infrared (IR) or Raman (R) spectra (10^2–10^4 cm^{-1}) region (Fig. 2.22) originate from vibrations of nuclei constituting the molecule. Infrared absorption spectra originate in photons in the infrared region that are absorbed by transitions between two vibrational levels of the molecule in the electronic

ground state [11]. Infrared absorption involves a dipole moment because there must be a net difference in dipoles in order to see a signal. Raman spectra have their origin in the electronic polarization caused by ultraviolet, visible, and near-IR light [11]. If a molecule is irradiated by monochromatic light of frequency ν , then, because of the electronic polarization induced in the molecule by this incident beam, the light of frequency ν ("Raleigh scattering") as well as that of frequency $\nu \pm \nu_i$ ("Raman scattering") is scattered where ν_i represents a vibrational frequency of the molecule [11]. Therefore, the Raman spectra are presented as shifts from the incident frequency in the ultraviolet, visible and near IR region. Vibrational scattering efficiency is higher in covalent crystals than in ionic crystals because the valence electrons are less localized. Therefore, a larger fluctuation of the polarizability can be induced by lattice vibration. The mix of covalent and ionic bonding in nitride semiconductors lends itself ideally to study by Raman spectroscopy.

The phonon dispersion curve of the hexagonal structure along the [0001] ($\Gamma \rightarrow A$ in the Brillouin zone) is approximated by folding the phonon dispersion of the cubic structure along [111].. By this folding, the TO phonon mode at the L point of the Brillouin zone in the cubic structure reduces to the E_2 mode at the Γ point of the Brillouin zone in the hexagonal structure as denoted by E_2^H , H for high frequency (see Fig. 2.23) . The E_2^L results from the zone folding of the transverse acoustic (TA) mode in the cubic structure. In the hexagonal structure, there is anisotropy in the macroscopic electric field induced by polar phonons. Thus, both the TO and LO modes split in the axial (or A_1) and the planar (or E_1)-type

modes where atomic displacement occurs along the c-axis or perpendicular to the c-axis, respectively [12].

First order Raman scattering is caused by phonons with wavevector $k \sim 0$ (Γ point) because of a momentum conservation rule in the light scattering process. In the wurtzite structure, group theory predicts eight sets of phonon normal modes at the Γ point, $2A_1 + 2E_1 + 2B_1 + 2E_2$. Two modes, A_1 and E_1 are acoustic, and the remaining six modes, $A_1 + E_1 + 2B_1 + 2E_2$, are optical. The A_1 and E_1 modes are both Raman and IR active, while the two E_2 modes are only Raman active, and the two B_1 modes are neither Raman nor IR active (silent modes). The acoustic mode, sometimes referred to as the transverse mode because it is perpendicular to the substrate's crystalline lattice (i.e. perpendicular to the c-axis) and therefore it cannot be seen in backscattering mode. The importance of the acoustic mode is that the electron-phonon interaction may affect the longitudinal optical (LO) mode.

2.3 References

[1] J. Goldstein, D. Newbury, D. Joy, C. Lyman, P. Echlin, E. Lifshin, L. Sawyer and J. Michael, *Scanning Electron Microscopy and X-Ray Microanalysis* (Springer Science, New York, NY, 2003), 30.

[2] J. Goldstein, D. Newbury, D. Joy, C. Lyman, P. Echlin, E. Lifshin, L. Sawyer and J. Michael, *Scanning Electron Microscopy and X-Ray Microanalysis* (Springer Science, New York, NY, 2003), 45.

[3] O. Ambacher, R. Dimitrov, D. Lentz, T. Metzger, W. Rieger, and M. Stutzmann, *J. Cryst. Growth*, **170** (1997) 335.

[4] F. Yun, M.A. Reshchikov, L. He, T. King, and H. Morkoc, *J. Appl. Phys.,* **92** (2002) 4837.

[5] G. Martin, A. Botchkarev, A. Rockett, and H. Morkoc, *Appl. Phys. Lett.,* **68** (1996) 2541.

[6] W. Lee, J.-H. Ryou, D. Yoo, J. Limb, and R.D. Dupuis, *Appl. Phys. Lett.,* **90** (2007) 093509-1.

[7] S.O. Kasap, *Principles of Electronic Materials and Devices* (McGraw Hill, New York, NY, 2006), 823.

[8] S.O. Kasap, *Principles of Electronic Materials and Devices* (McGraw Hill, New York, NY, 2006), 145.

[9] D.K. Schroder, *Semiconductor Material and Device Characterization* (J. Wiley, New York, NY 1998), 511.

[10] http://www.eeel.nist.gov/812/meas.htm

[11] K. Nakamoto, *Infrared and Raman Spectra of Inorganic and Coordination Compounds, Part A: Theory and Applications in Inorganic Chemistry* (J. Wiley, New York, NY. 1997), p. 10.

[12] H. Harima, *J. Appl. Phys.: Condens. Matter.,* **14** (2002) R967.

2.4 Tables

Table 2.1 XRD, PL, and AFM characterization results for $Al_xGa_{1-x}N$/GaN heterostructures.

WAFER I.D.	Targeted $Al_xGa_{1-x}N$ Layer Thickness (Å)	Simu-lated Layer Thick-ness (Å)	Target Al content	Simu-lated Comp. Match	PL spectral map median wavelength (nm)	RPM2000 median alloy concen. (%Al)	Peak Intensity (volt)	FWHM (nm)	AFM RMS Rough. (nm) (5x5μm²)	AFM Max Rough. (nm) (5x5μm²)
AE754.1	200	177.59	0.25	0.1739	326.1+/-3.157	22.7+/-1.842	0.014+/-0.005	11.8+/-3.460	2.652	83.974
AE774.2	200	172.96	0.22	0.1436	332.5+/-7.029	19.4+/-4.355	0.014+/-0.013	10.2+/-3.773	1.617	17.735
AE475.5	200	too broad	0.25	NA	322.3+/-6.476	24.9+/-3.767	0.094+/-0.061	24.3+/-4.653	1.971	62.577
AE811.2	200	too broad	0.25	NA	323.1+/-2.331	24.5+/-1.369	0.031+/-0.039	14.2+/-6.920	0.994	9.158
AE832.1	200	187.81	0.25	0.2014	321.4+/-4.990	25.4+/-2.904	0.017+/-0.009	17.5+/-7.582	3.269	54.497
AE853.1	200	153.69	0.25	0.2454	322.6+/-4.368	24.7+/-4.542	0.025+/-0.015	14.8+/-3.002	1.383	16.519
AE840.2	200	176.49	0.25	0.2211	322.2+/-3.049	25.0+/-1.767	0.002+/-0.001	1.20+/-1.079	3.581	27.571
AE816.4	200	214.55	0.25	0.2152	321.2+/-3.267	25.6+/-1.90	0.005+/-0.003	5.50+/-2.762	2.835	23.146

Table 2.2 Van der Pauw Hall results for $Al_xGa_{1-x}N/GaN$ heterostructures.

MOCVD RUN #	SUB-STRATE I.D.	Buffer Layer Thickness (microns)	Van der Pauw R_s (Ω/sq.)	2DEG Carrier Density, Ns (cm^{-2})	Hall Voltage Meas. μ ($cm^2V^{-1}s^{-1}$)	σ Conduct-ivity of 2DEG (Ω^{-1})	Remarks
M1610	AE754.1	0.5	400	2.13E+13	734	2.50E-03	
M1611	AE774.2	0.5	437	1.76E+13	810	2.28E-03	
M1647	AE816.4	0.75	431	9.75E+12	1487	2.32E-03	
M1627	AE811.2	1	425	9.26E+12	1588	2.35E-03	$\sigma = qn_s\mu$
M1640	AE840.2	1.5	450	7.70E+12	1805	2.22E-03	
M1630	AE832.1	2	437	1.06E+13	1345	2.29E-03	
M1618	AE475.5	1.25	615	8.00E+12	1270	1.63E-03	$10x10mm^2$ subst.
M1632	AE853.1	0.5	NA	NA	NA	NA	poor contacts

2.5 Figures

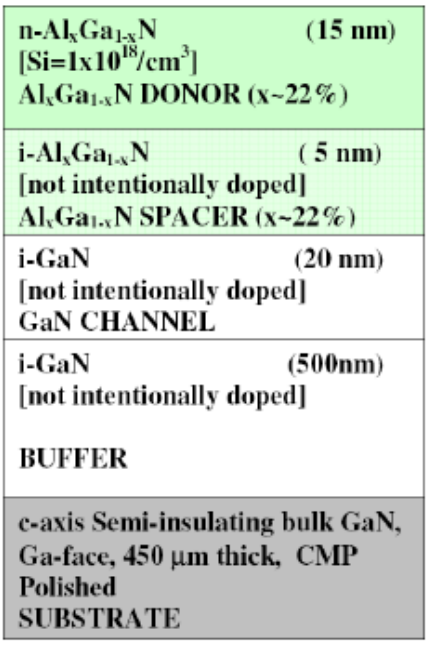


Figure 2.1 Schematic of the AlGaN/GaN heterostructure for the growths in this project.

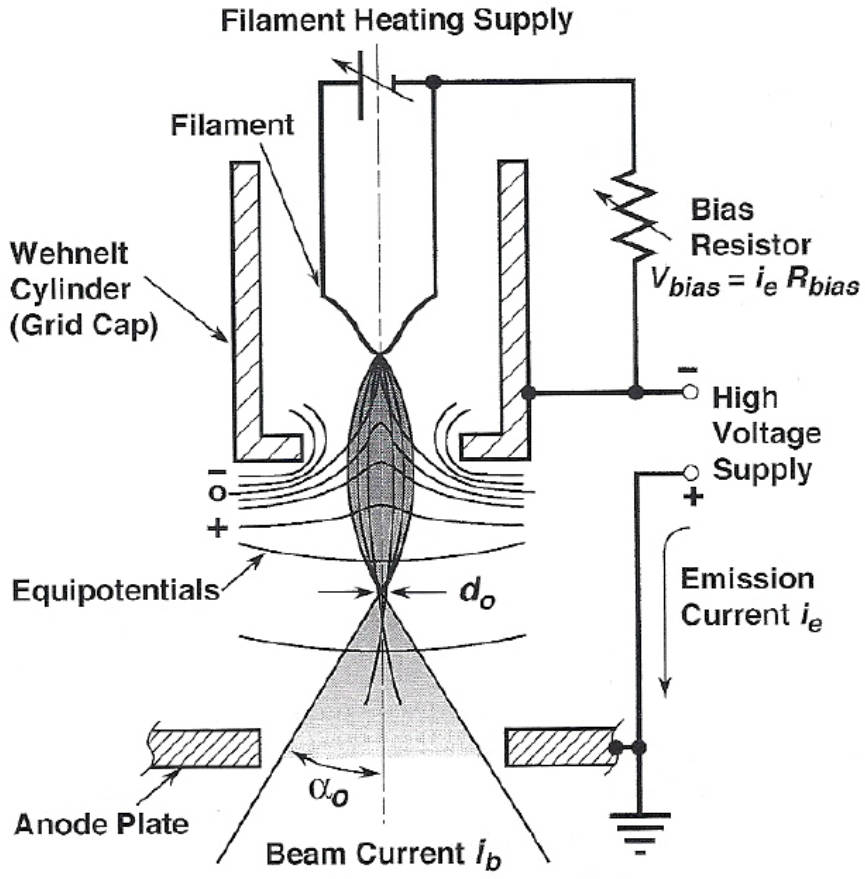


Figure 2.2 Schematic diagram of the conventional self-biased thermionic tungsten hairpin electron gun [1].

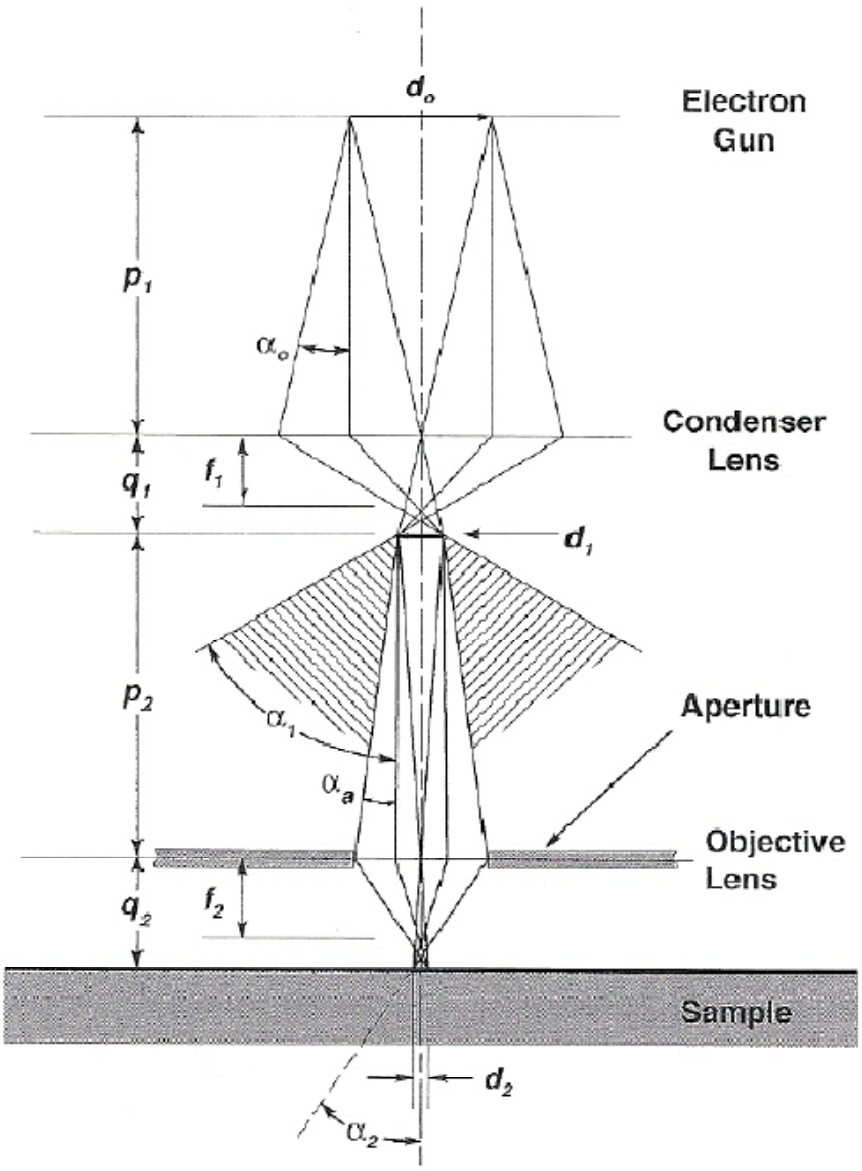


Figure 2.3 Electron ray traces through a schematic SEM column with a condensor lens and a probe-forming or objective lens [2].

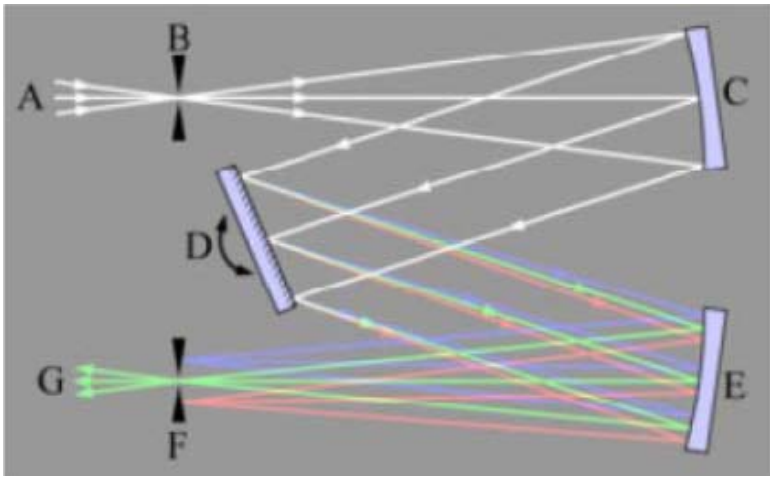


Figure 2.4 Monochromator with entrance slits to limit intensity. Light is reflected by collimator, C, to a grating, D, and collected at mirror, E, and refocused to the exit slit.

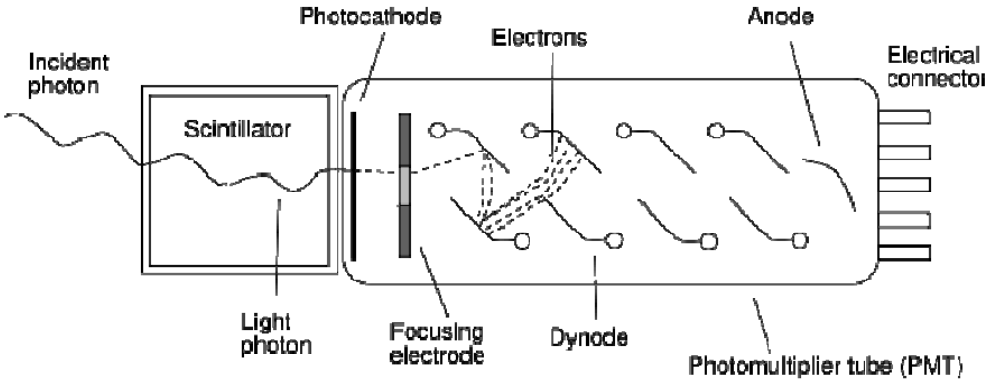


Figure 2.5 Photomultiplier tube multiplies the signal produced by the incident light by 10^8 from which single photons can be resolved.

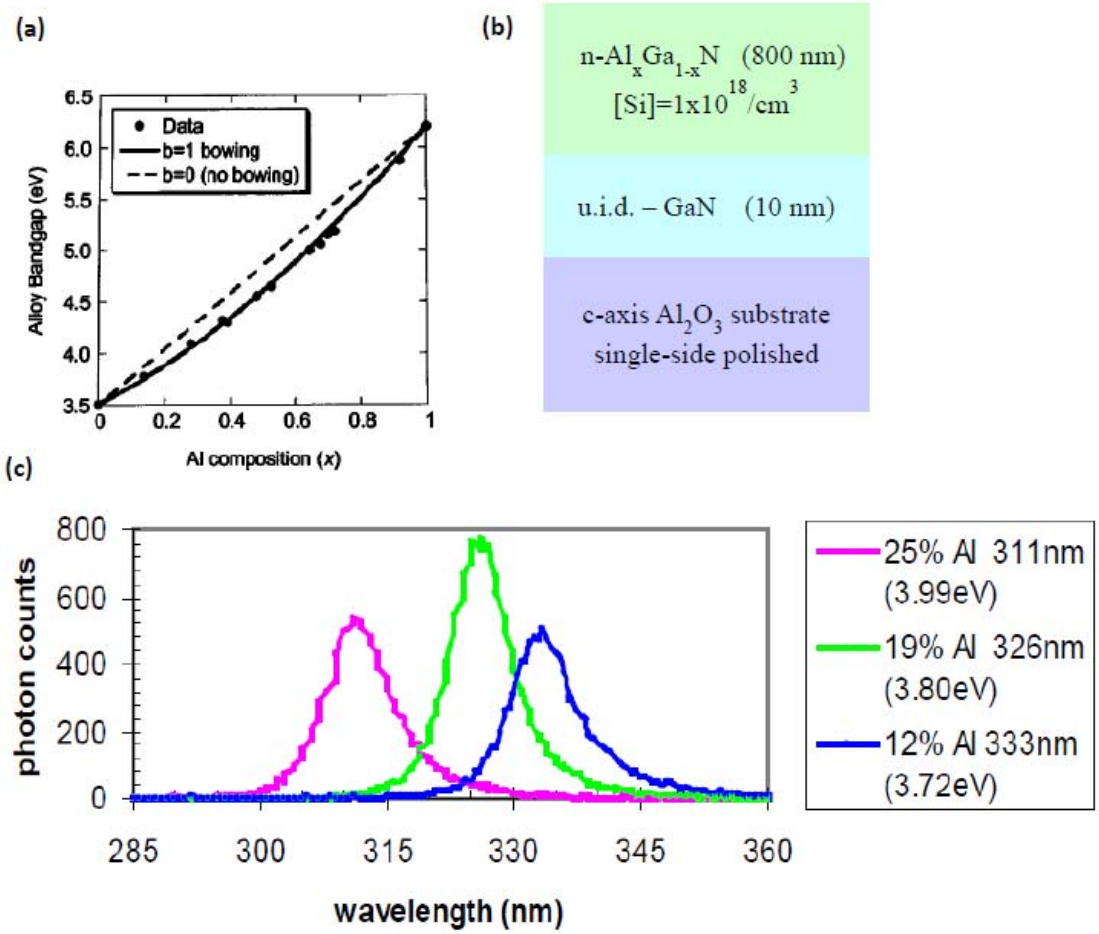


Figure 2.6 (a) $Al_xGa_{1-x}N$ materials exhibit a bowing parameter as a function of alloy composition [3]. (b) Thin films of $Al_xGa_{1-x}N$ were grown by MOCVD. (c) Cathodoluminescence was used to assign an Al mole fraction to an emission energy. A bowing parameter, b=1 eV, was used.

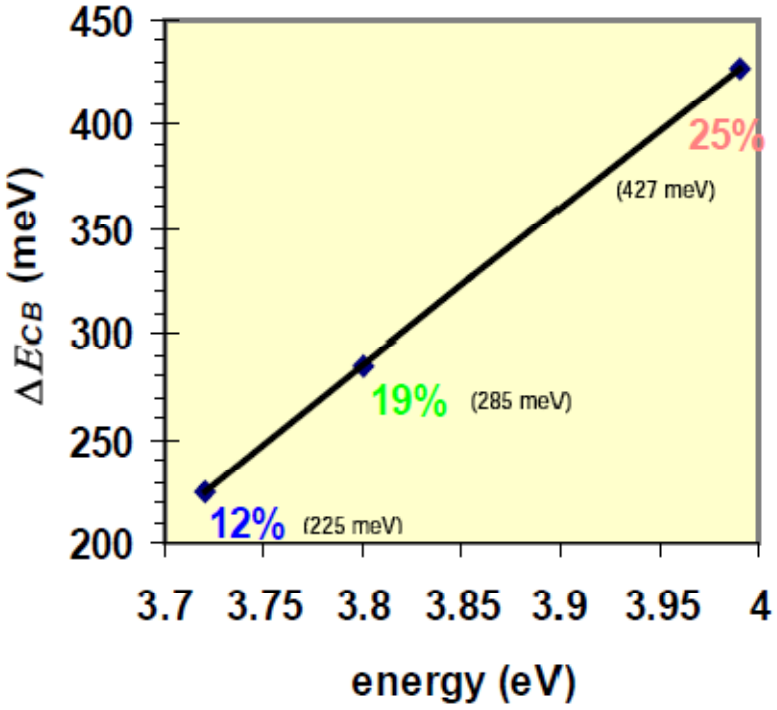


Figure 2.7 Conduction band offsets for $Al_xGa_{1-x}N$ calibration runs.

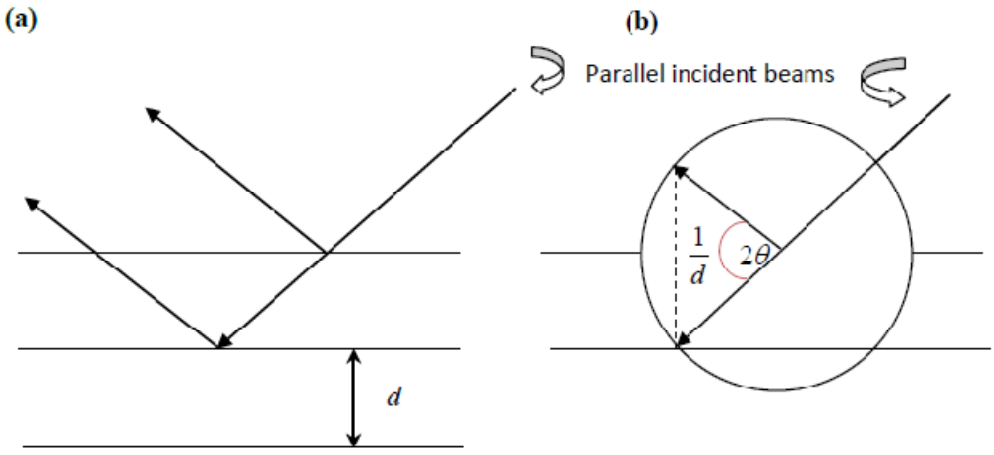


Figure 2.8 (a) Lattice planes in real space where the distance between planes is d. (b) Ewald sphere in reciprocal space where the distance between reciprocal lattice point is $\frac{1}{d}$.

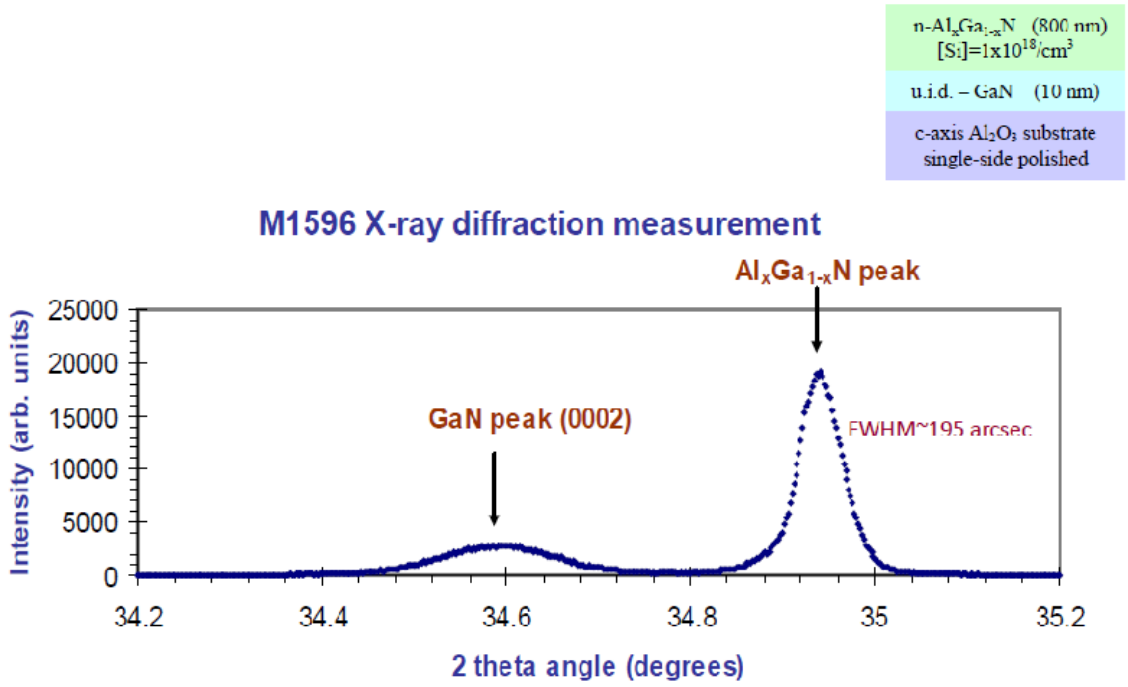


Figure 2.9 Typical HRXRD scan for $Al_xGa_{1-x}N$ calibration runs. The symmetric rocking curve FWHM gives us a measure of the tilt and twist of the film.

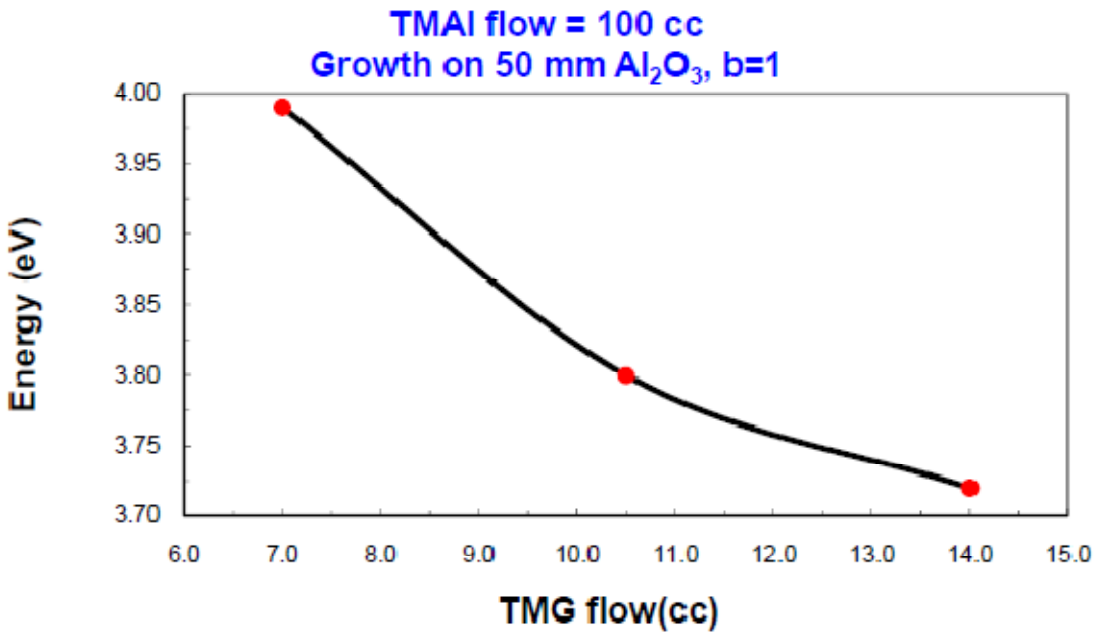


Figure 2.10 Trimethylgallium (TMG) flow was the control lever used to obtain the desired bandgap for the $Al_xGa_{1-x}N$ barrier layer.

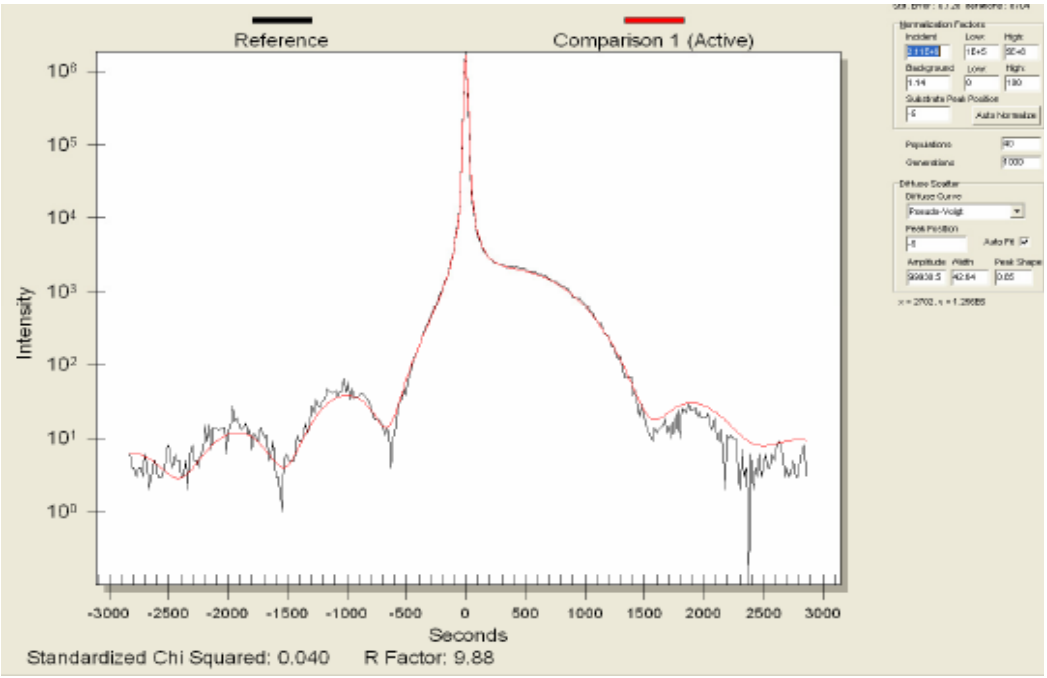


Figure 2.11 HRXRD $(\omega - 2\theta)$ scans of $Al_xGa_{1-x}N/GaN$ heterostructures showed pendulosung fringes which were used to determine $Al_xGa_{1-x}N$ barrier thickness and out-of plane strain. The Chi Squared value reflects the actual placement of the $Al_xGa_{1-x}N$ peak and spacing of pendulosung fringes vs.theoretically expected. The R Factor measures disagreement between F_{obs} and calculated structure factors, F_{calc}.

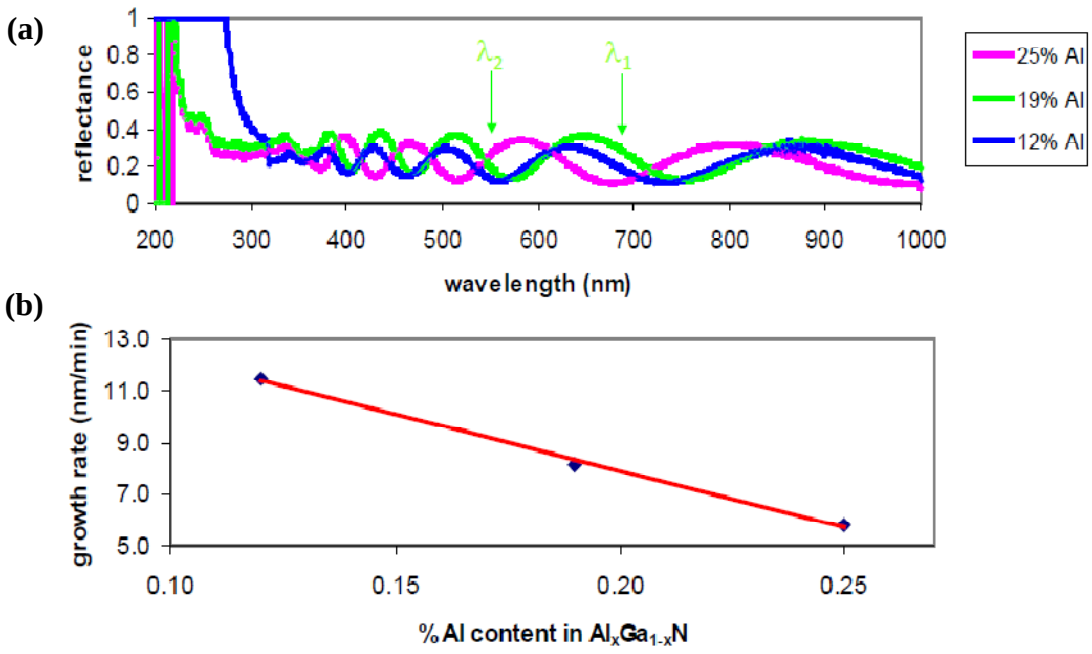


Figure 2.12 Thickness measurements for the $Al_xGa_{1-x}N$ calibration runs were determined by reflectance. Growth rate data indicated that Al incorporation is increased by reducing trimethylgallium (TMG) flow.

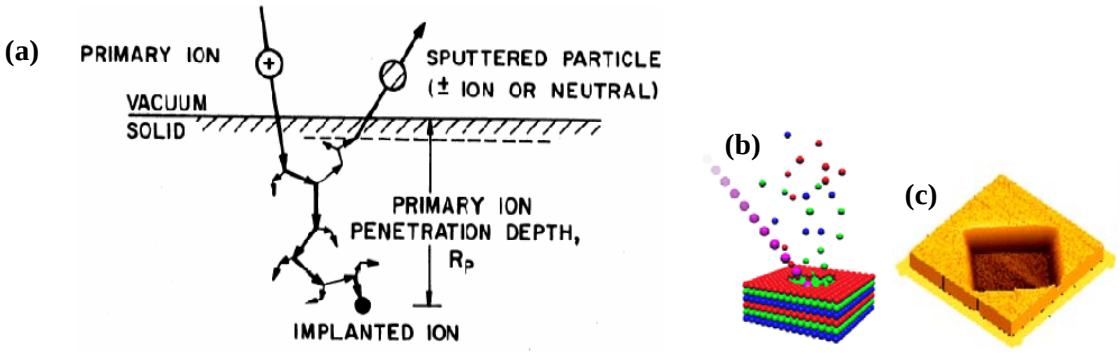


Figure 2.13 (a) Schematic of SIMS process. (b) Secondary ions leaving the surface. (c) A crater of controlled size and depth allows raster resolution.

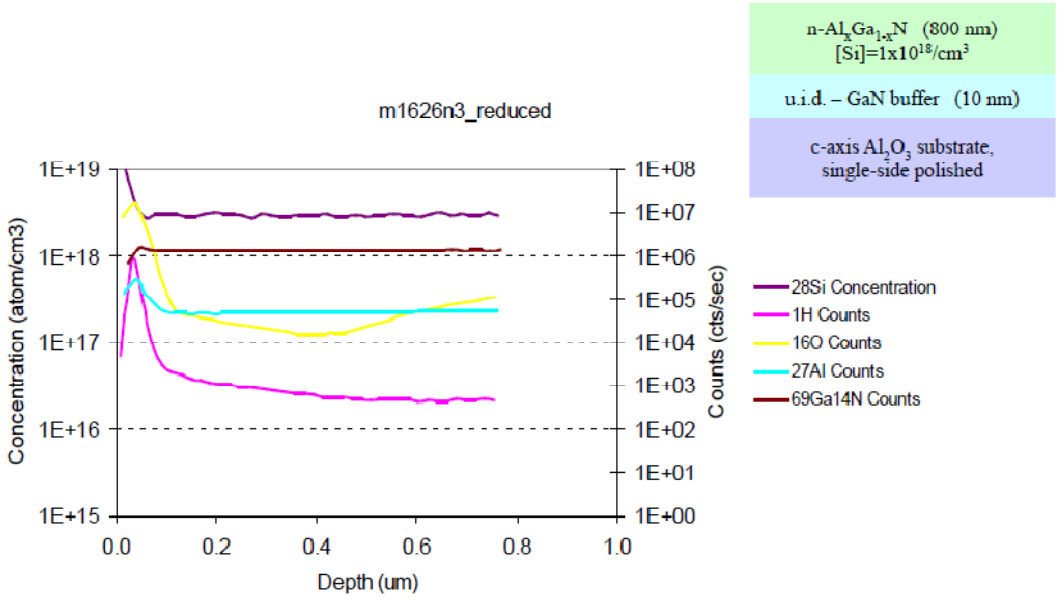


Figure 2.14 SIMS analysis using Cs^+ primary ion to assess oxygen concentration in $Al_xGa_{1-x}N$ film. Unintentional doping in GaN materials may be due to high oxygen incorporation.

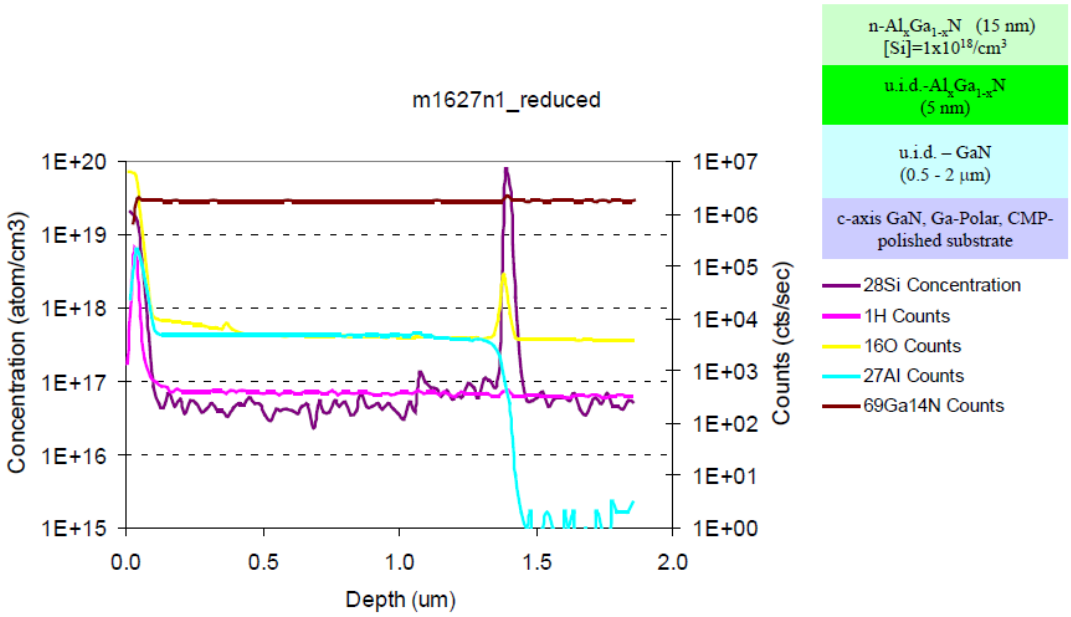


Figure 2.15 SIMS analysis using the O^{2+} primary ion to assess silicon contamination at the epitaxy/bulk GaN interface.

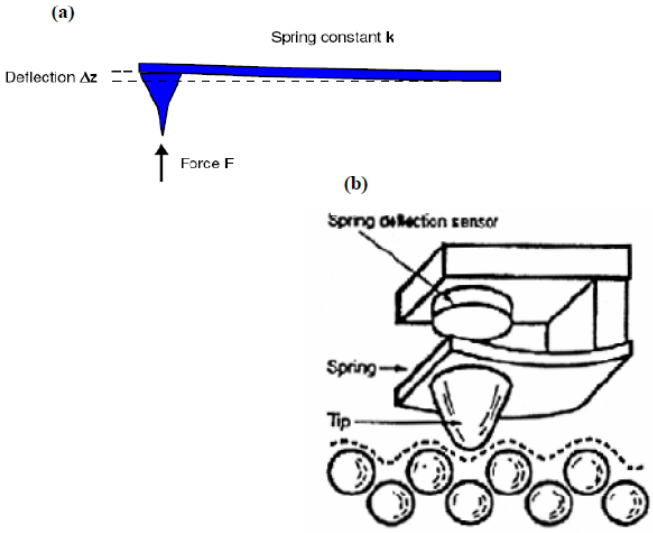


Figure 2.16 (a) AFM is based on Hooke's Law. (b) The tip is most commonly scanned across the surface in contact mode.

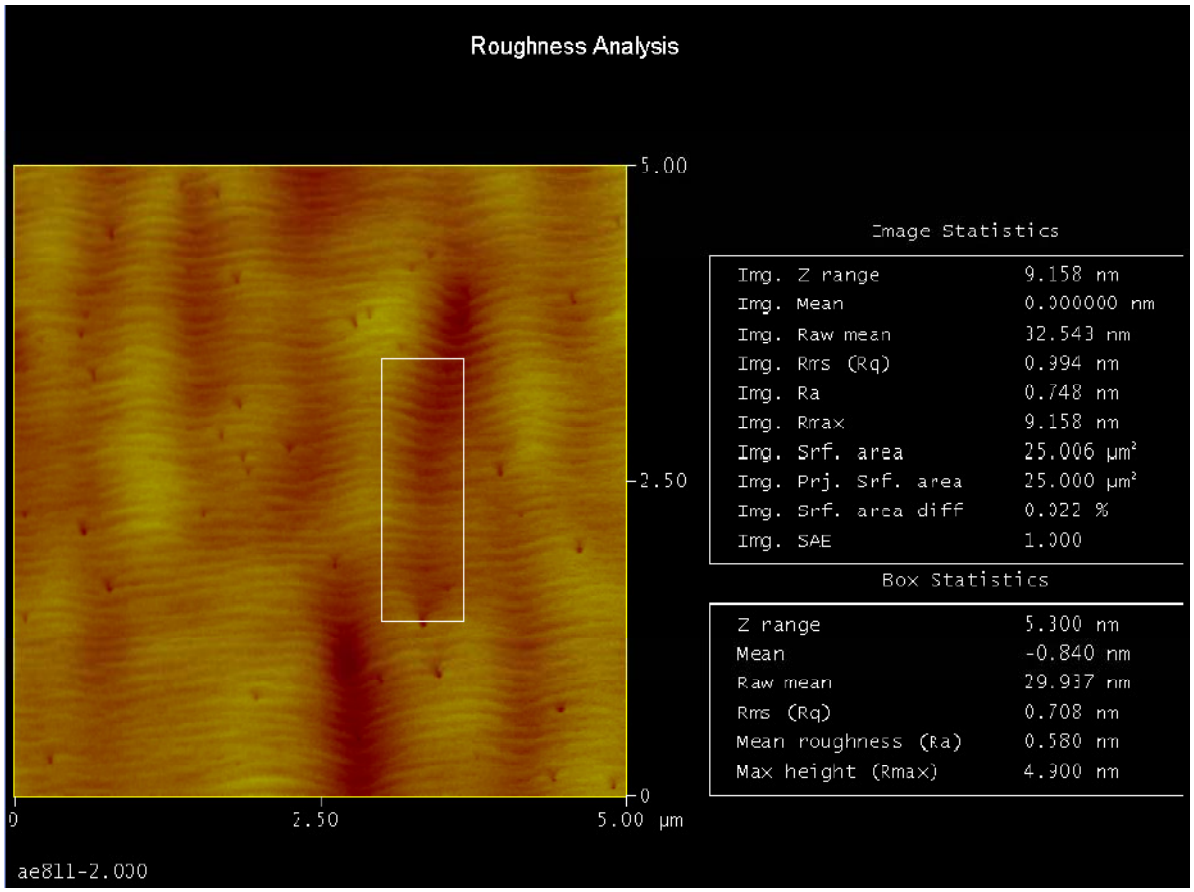


Figure 2.17 Steps and terrace are evidence of step flow mode growth. Terrace terminations are indications of dislocations.

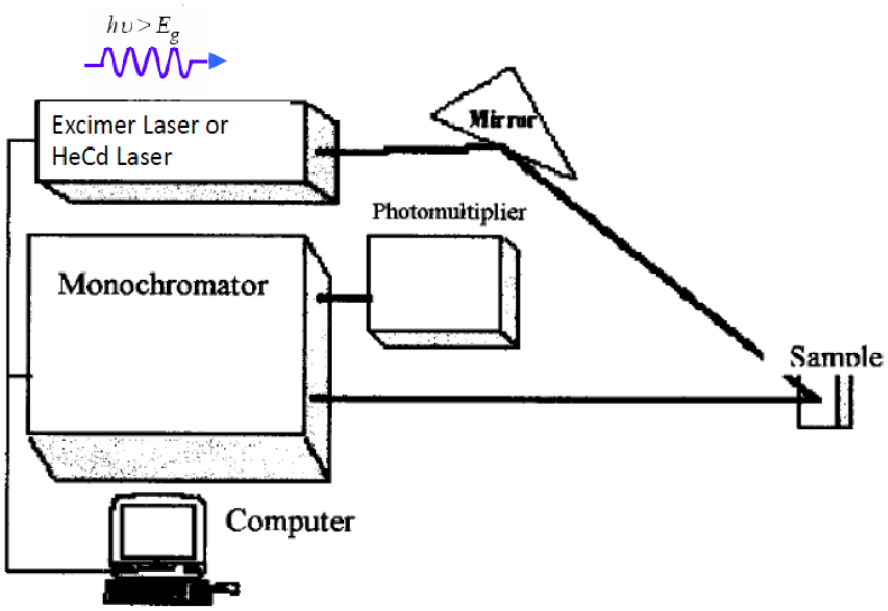


Figure 2.18 Schematic of a photoluminescence set up.

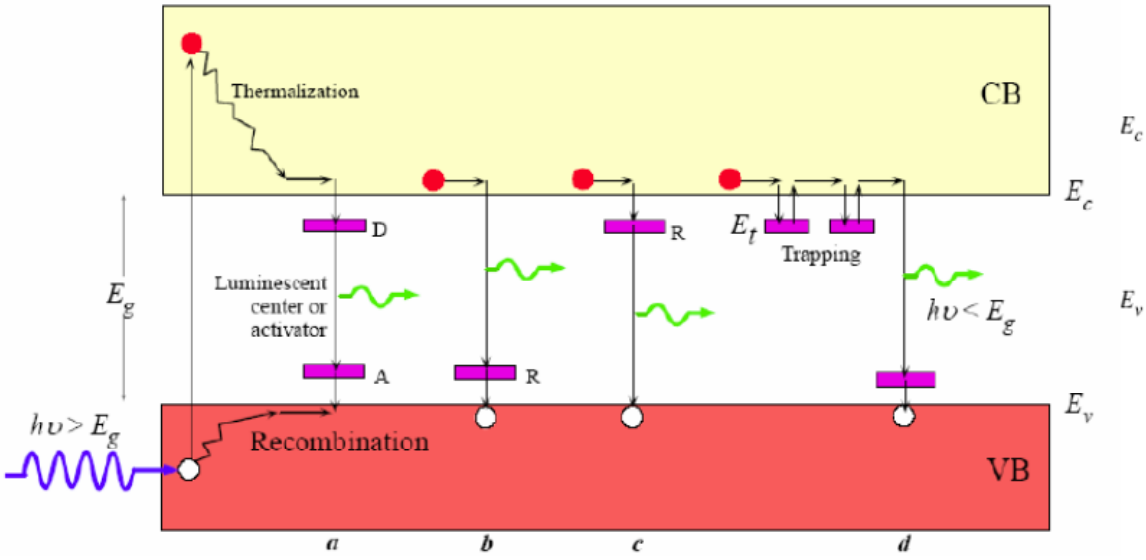


Figure 2.19 Several luminescent transitions can be seen by photoluminescence analysis [7].

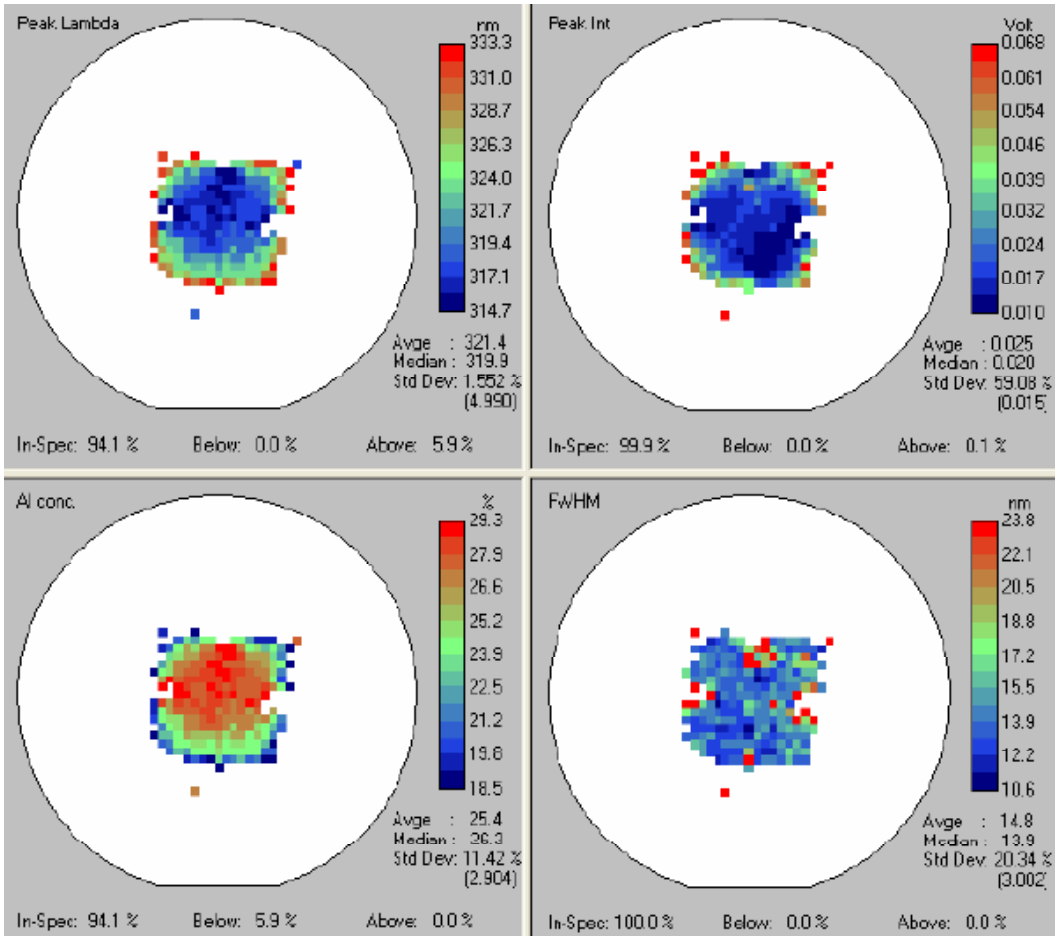


Figure 2.20 PL mapping of $Al_xGa_{1-x}GaN/GaN$ heterostructures grown on 18 x 18 mm^2 semi-insulating bulk GaN substrates.

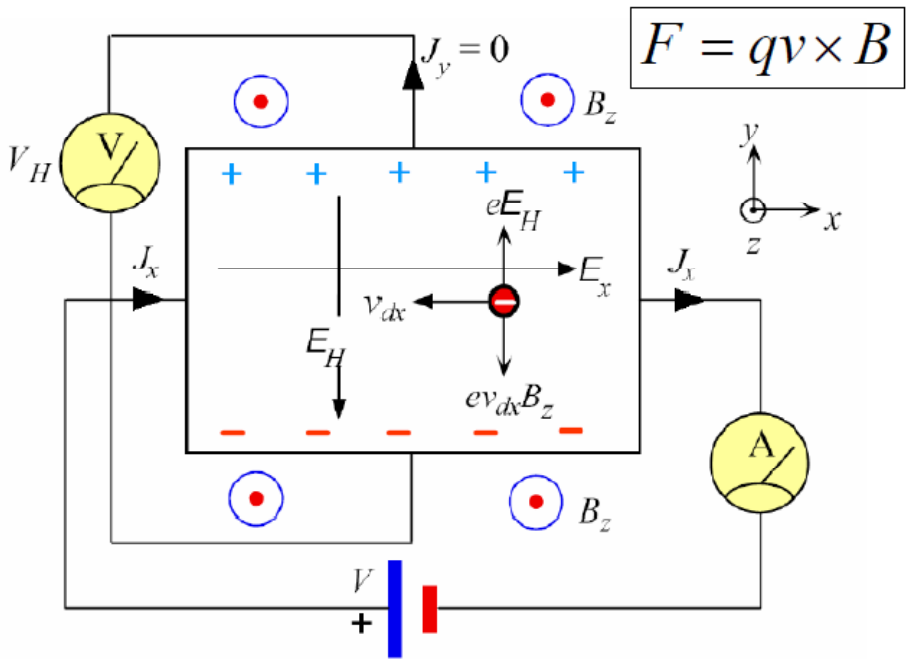


Figure 2.21 Illustration of the Hall Effect. The z-direction is out of the plane of the paper. The externally applied magnetic field is along the z-direction [8].

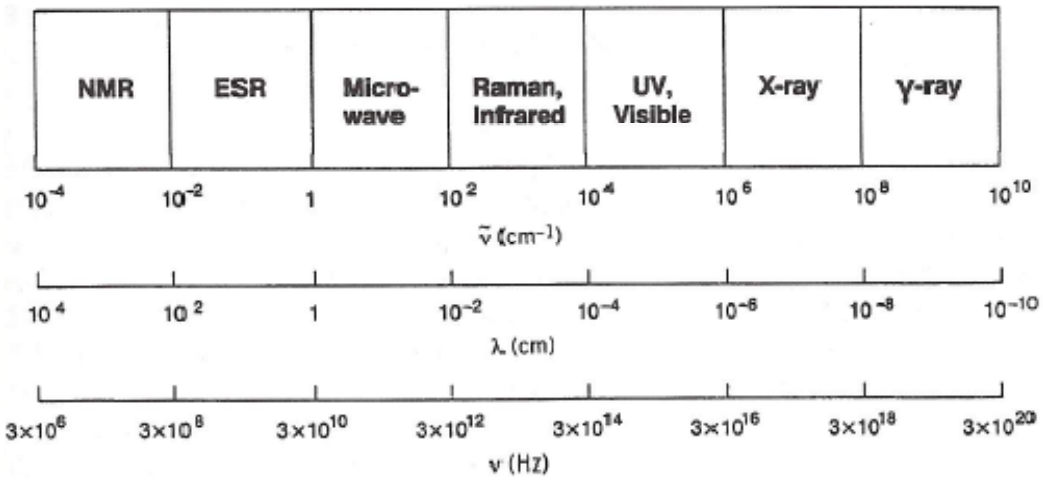


Figure 2.22 Regions of the electromagnetic spectrum and energy units [11].

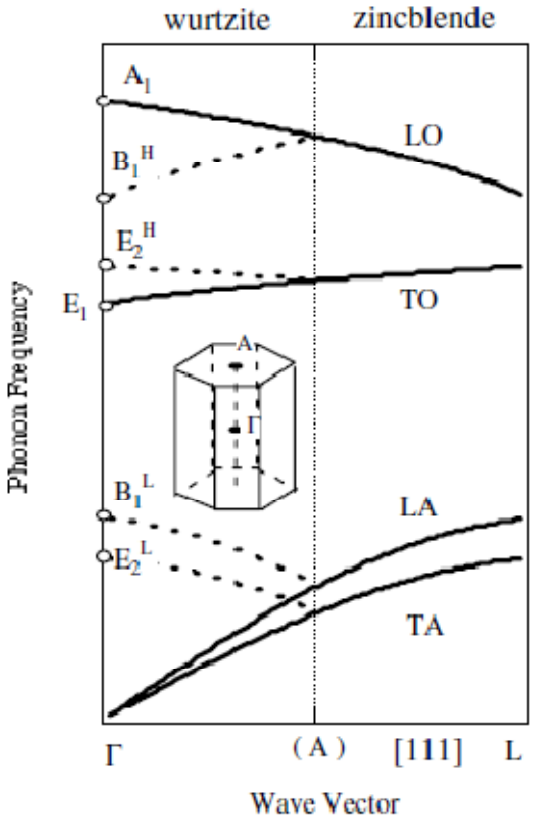


Figure 2.23 Schematic representation of the phonon dispersion. Phonon branches along the [111] in the zincblende structure (stacking order ABCABC…) are folded to approximate those of the wurtzite structure (stacking order ABABAB...) along the [0001] [12].

3. MODULATION OF MOBILITY IN HOMOEPITAXIALLY-GROWN AlGaN/GaN HETEROSTRUCTURES

J.A. Grenko, C.L. Reynolds, Jr., and M.A.L. Johnson
Department of Materials Science and Engineering
North Carolina State University, Box 7919, Raleigh, NC 27695

C.W. Ebert
Veeco Turbodisc, 392 Elizabeth Avenue, Sommerset NJ 08873

A.D. Hanser, E.A. Preble, T. Paskova, and K.R. Evans
Kyma Technologies, 8829 Midway West Road, Raleigh, NC 27617

3.1 Abstract

We report on the growth of $Al_{0.25}Ga_{0.75}N$/GaN heterostructures on low dislocation density semi-insulating c-axis GaN substrates. Room temperature Hall mobilities up to 1805 $cm^2V^{-1}s^{-1}$ at sheet carrier densities of $0.77x10^{13}$ cm^{-2} have been measured. By varying the GaN buffer layer thickness in these homoepitaxially-grown $Al_{0.25}Ga_{0.75}N$/GaN heterostructures, we observed a buffer-induced modulation of the room temperature 2DEG sheet carrier densities and Hall mobilities. The increase in sheet carrier density and corresponding decrease in mobility as the GaN buffer layer thickness is reduced below 0.75 μm is related to the presence of Si impurities at the bulk GaN substrate/epitaxial interface. Capacitance-voltage measurements and SIMS analysis confirm the presence of Si impurities at the surface prior to and after epitaxial growth. The factor of 2 reduction in the room temperature mobility is consistent with a predicted theoretical mobility reduction based on intersubband scattering. We have also been able to separate the contributions to the 2DEG carrier density from the ionized donors and the polarization field; the magnitude of each is ~$5x10^{12}$ cm^{-2}.

3.2 Introduction

AlGaN/GaN heterostructures are attractive for use in RF and high-power applications due to their high critical electric field [1] and high thermal conductivity which should enable them to exhibit high breakdown voltage (V_{BD}) performance and high unity current gain frequency (f_T). Another unique feature of these nitride-based materials is that they are comprised of point group crystals that lack a center of symmetry which enables them to

exhibit spontaneous polarization. It is this polarization vector that leads to an accumulation of charges of opposite sign at each of the interfaces and sets up a sizeable electric field within the material. Consequently, a two-dimensional electron gas (2DEG) can be easily formed at the AlGaN/GaN interface without intentional doping of the AlGaN. In addition, when doped with donors, electrons in the vicinity of the heterojunction transfer across the interface to the lowest conduction band states of the narrower-gap material (GaN). The 2DEG is further bound to the interface via the coulombic attraction to the ionized donors. It is expected that this polarization-assisted, coulombic attraction of electrons to the ionized donors across the junction should give rise to high sheet carrier densities. And, since the mobile donor electrons are spatially separated from the ionized impurities, the scattering rate in the 2DEG should be significantly reduced and improved low temperature mobilities should be realized as long as surface roughness scattering is minimized [2].

AlGaN/GaN heterostructures are typically grown on non-native substrates with 2DEG carrier mobilities reported in the range of 1200 to 2050 $cm^2V^{-1}s^{-1}$ and sheet carrier densities from 0.5 to $1x10^{13}$ cm^{-2} [3-8]. A requirement for growth of GaN-based device structures on non-native substrates, such as sapphire, SiC and Si(111), is the formation of a low temperature nucleation layer prior to the high temperature GaN buffer growth. This nucleation layer compensates for the lattice mismatch and thermal expansion coefficient difference between the GaN buffer and the substrate. However, the chemical and structural mismatch that the nucleation layer causes at the interface introduces a high density of defects, e.g. threading dislocations and stacking faults. Direct evidence for the deleterious impact of the nucleation layer is that measured thermal conductivities are significantly less

than theoretical estimates, 230 $W \cdot m^{-1}K^{-1}$ for GaN films with dislocation densities greater than $5x10^6$ cm^{-2} [9]. AlGaN/GaN HFET structures grown on low defect density ($<10^6$ cm^{-2}) native bulk GaN substrates should offer better thermal management. This in turn should enhance RF performance by increasing f_T since f_T decreases significantly with temperature because of the decrease in saturation velocity [10].

Electron transport properties in the 2DEG have been studied extensively in the Si [11] and AlGaAs/GaAs systems [12]. In addition to the electron scattering at low temperatures attributed to ionized impurity scattering and surface roughness scattering, it has been predicted that scattering of electrons between subbands should occur when more than one electron subband is occupied [11]. It has also been shown that electrons in excited subbands have a mobility that is much higher than that in the lowest subband [13]. However, strong intersubband scattering reduces the mobility of the lowest subband from that of the single-subband case [13]. In this study, we show that by varying the thickness of the not-intentionally doped (n.i.d.) GaN buffer, we observe a buffer-induced modulation of room temperature mobility and sheet carrier density that is consistent with intersubband scattering.

3.3 Study of AlGaN/GaN heterostructures

3.3.1 Experimental

The AlGaN/GaN heterostructures in this study were grown by organometallic vapor phase epitaxy (OMVPE) in a vertical reactor at 1040^{o}C and 60 torr on 450 μm thick, semi-insulating bulk GaN substrates. These Fe-doped, c-axis GaN substrates were grown in a conventional vertical hydride vapor phase epitaxy (HVPE) reactor at a growth rate of approximately 100 μm/hr. Capacitance-voltage (CV) measurements (Fig. 3.1) indicated that the free carrier concentration in the semi-insulating GaN substrate was $5x10^{13}$ cm^{-3}. The same CV measurements showed a free carrier concentration $>10^{18}$ cm^{-3} in the first 20 nm of the substrate. Secondary ion mass spectroscopy (SIMS) measurements of AlGaN/GaN heterostructures on these semi-insulating bulk GaN substrates (Fig. 3.2) confirmed the atomic silicon concentration ([Si]) to be $>10^{19}$ cm^{-3} at the bulk GaN/epitaxial interface. Areal silicon concentration ($[Si]_{areal}$) at the bulk GaN/epitaxial interface was determined to be $1.6x10^{14}$ cm^{-2}.

From the substrate, the heterostructures consisted of a not-intentionally doped (n.i.d.) GaN buffer layer, a 5 nm n.i.d. $Al_{0.25}Ga_{0.75}N$ spacer and 15 nm of n-$Al_{0.25}Ga_{0.75}N$ ([Si]:$3x10^{18}$ cm^{-3}). The GaN buffer thickness was varied from 0.5 to 2 μm. Representative atomic force microscopy (AFM) measurements (Fig. 3.3) reveal a surface roughness of 1 nm for a 5 x 5 μm^2 area of the $Al_{0.25}Ga_{0.75}N$/GaN heterostructure grown on a substrate that is typically characterized to have $< 5 \times 10^6$ cm^{-2} dislocations by scanning electron microscopy (SEM)/cathodoluminescence (CL) measurement. The $Al_{0.25}Ga_{0.75}N$/GaN heterojunction for

this AFM image was 1 μm from the bulk GaN/epitaxial interface. Step flow mode of growth is clearly evident in the inspection of the highlighted area.

3.3.2 Van der Pauw Hall measurements

Indium contacts were annealed to the heterostructure surface by placing the substrates in a nitrogen environment at 400°C for 120 seconds. Sheet resistance (R_s) of the 2DEG channel routinely measured 400- 450 Ω/sq. Standard Hall effect measurements were performed at room temperature in a 3000 Gauss magnetic field. Room temperature Hall mobilities (μ) for our $Al_{0.25}Ga_{0.75}N$/GaN heterostructures ranged from 734 to 1805 $cm^2V^{-1}s^{-1}$ while 2DEG carrier densities (n_s) varied from 0.8 to $2x10^{13}$ cm^{-3} as shown in Table 3.1 and Fig. 3.4 for varying buffer layer thicknesses. The conductivity, σ, of the 2DEG ($\sigma = n_s \cdot \mu \cdot q$), where q is the electronic charge, also remained relatively constant, ranging from 2.2 to $2.5x10^{-3}$ Ω^{-1}.

3.4 Discussion

The $Al_{0.25}Ga_{0.75}N$/GaN heterostructures grown in our study exhibit very interesting behavior in their electrical transport. Specifically, room temperature (RT) van der Pauw Hall measurements of $Al_{0.25}Ga_{0.75}N$/GaN films grown on various n.i.d.-GaN buffer layer thicknesses show a characteristic decline in mobility as the n.i.d.-GaN buffer thickness is decreased below 0.75 microns. A corresponding increase in the 2DEG carrier density is observed. We propose that modulation of the RT Hall mobility and sheet carrier density as the n.i.d. GaN buffer thickness is varied in our heterostructures may be attributed to the large $[Si]_{areal}$ concentration ($1.6x10^{14}$ cm^{-2}) measured at the epitaxy/bulk GaN interface.

For buffer thicknesses ≥ 0.75 μm, the mobility and 2DEG carrier density are nearly constant (within ~12%; see Fig. 3.4). Thus, comparing the sheet carrier concentration for heterostructures with thick buffers, ≥ 0.75 μm, to that for those with thin buffers, < 0.75 μm, enables us to estimate the excess sheet carrier density, Δn_s, associated with the interfacial Si,

$$\Delta n_s = n_s^{thin_buffer} - n_s^{thick_buffer} \tag{3.1}$$

for buffer thickness < 0.75 μm,

$$n_s^{thin_buffer} = \sum (n_s)_i / i \tag{3.2}$$

for buffer thickness ≥ 0.75 μm,

$$n_s^{thick_buffer} = \sum (n_s)_i / i \tag{3.3}$$

where i represents number of datum. The excess carrier density, Δn_s, is found to be 1.0×10^{13} cm^{-2} based on the Van der Pauw measurements in Table 3.1. This implies that ~6% of the interfacial Si (1.6×10^{14} cm^{-2}) contributes to the measured 2DEG carrier density for thin buffers, $n_s^{thin\ buffer}$. This suggests that Δn_s contributed from the interfacial Si increases the 2DEG sheet concentration to the level where higher subbands may be populated. And then, as predicted by the intersubband scattering model [11, 13], the RT Hall mobility rapidly declines. This behaviour, which is correlated to the proximity of the 2DEG channel to the epitaxy/bulk GaN interface is in agreement with Mori's prediction [11] of the scattering of electrons between subbands that should occur when more than one electron subband is occupied. This prediction was subsequently confirmed by Stormer [12] in AlGaAs/GaAs heterostructures by separately determining the mobilities in each subband by magneto-resistance measurements (Shubnikov-de-Haas effect). The observed RT Hall mobility

reduction by a factor of 2 at sheet carrier densities of $2x10^{13}$ cm^{-2} is consistent with the theoretically predicted mobility reduction by a factor of 3 based on intersubband scattering [12]. An alternative explanation for the significant decrease in μ and increase in n_s with decreasing buffer thickness observed in Table 3.1 and Fig. 3.4 is simply parallel conduction at the bulk GaN/epitaxial interface. Only Shubnikov-de-Haas measurements can distinguish between the two mechanisms.

A similar buffer-induced modulation of the carrier density in AlGaAs/GaAs heterostructures [14] was shown to be attributed to the silicon impurities at the substrate/epitaxial interface. The influence of this silicon was to shift the threshold voltage V_{th} negatively and to cause poor pinch-off characteristics in depletion mode field effect (DFET) devices. Their observed V_{th} dependence was modeled by SIGMA, a one-dimensional device simulator which solved for the charge distribution under the gate as a function of gate bias. SIGMA predicted that under conditions of high silicon and low carbon concentrations, a secondary 2DEG was formed at the substrate interface which led to significantly lower V_{th} and softening of the pinch off [15]. This extra 2DEG was also observed by Kusters et al using Shunikov-de-Haas (SDH) effect measurements in order to study parallel conduction mechanisms in AlGaAs/GaAs heterostructures [16]. Their confirmation strengthened the argument that interfacial impurities modulate the 2DEG and exert considerable influence on FET devices fabricated from such heterostructures. Indeed their work suggests the importance of performing SDH measurements to quantify the effect of buffer-induced modulation in the AlGaN/GaN materials system.

Furthermore, the total measured carrier density for AlGaN/GaN HFETs grown on buffers ≥ 0.75 μm can be expressed as two contributions,

$$n_s^{thick_buffer} = n_s^{id} + n_s^{polar} \tag{3.4}$$

where n_s^{id} represents electrons that have transferred from the ionized donors in the $Al_{0.25}Ga_{0.75}N$ to the triangular quantum well at the $Al_{0.25}Ga_{0.75}N$/GaN interface and n_s^{polar} is associated with charge due to the polarization field. We have further assumed that there is little, if any, contribution from the interfacial Si with the thicker buffers. Hence, analysis of the data in Table 3.1 and Fig. 3.4 enables us to estimate the ionized donor and polarization contributions to the measured 2DEG carrier density. For buffer thicknesses ≥ 0.75 μm, the average measured $n_s^{thick\ buffer}$ is 9.4 x10^{12} cm^{-2}. We can estimate n_s^{id} based on the Si-doping level (3x10^{18} cm^{-3}) and thickness (15 nm) of the doped AlGaN layer to be 4.5x10^{12} cm^{-2}. Thus, substitution of these values values into Eq. (3.4) yields 4.9x10^{12} cm^{-2} for the carrier density associated with the polarization field, n_s^{polar}. A subsequent experiment has confirmed this polarization charge density.

3.5 Acknowledgements

The authors acknowledge Kyma Technologies for the bulk GaN substrates used in this study. Special thanks to Fred Stevie, NCSU Analytical Instrumentation Facility, for the SIMS analysis.

3.6 References

[1] F. Ren and J. Zolper, *Wide Energy Bandgap Electronic Devices* (World Scientific Publishing, Singapore, 2003) 179.

[2] A. Hartstein, T. H. Ning and A. B. Fowler, *Surf. Sci.,* **58** (1976) 178.

[3] E. Iiopoulos et al, *Superlatt. Microstruct.,* **40** (2006) 313.

[4] P. Kordos, J. Bernat, and M. Marso, *Microelectron. J.,* **36** (2005) 438.

[5] M. Germain et al, *Mat. Res. Symp. Proc.,* **798** (2004) Y10.22.1.

[6] S. Iwakami et al, *Jpn. J. App. Phys.,* **43** (2004) L831.

[7] Z. Bougrioua et al, *Phys. Stat. Sol. (b),* **228** (2001) 625.

[8] G. Y. Zhao et al, *Physica E,* **7** (2000) 963.

[9] C. Mion and J. F. Muth, *Appl. Phys. Lett.,* **89** (2006) 092123.

[10] F. Ren and J. Zolper, *Wide Energy Bandgap Electronic Devices* (World Scientific Publishing, Singapore, 2003), 193.

[11] S. Mori and T. Ando, *Phys. Rev. B,* **19** (1979) 6433.

[12] H. L. Stormer, A. C. Gossard, and W. Weigmann, *Solid State Commun.,* **41** (1982) 707.

[13] T. Ando, J. Phys. *Soc. Jpn.,* **51** (1982) 3900.

[14] C. L. Reynolds, Jr. and T. H. H. Voung, *Appl. Phys. Lett.,* **61** (1992) 2308.

[15] T. H. H. Vuong, C. L. Reynolds, Jr., and J. Singleton, *Appl. Phys. Lett.,* **64** (1994) 667.

[16] R. M. Kusters, T. J. B. Janssen, C. J. G. M. Langerskt, J. Singleton, A. J. Perenboom, G. A. C. Jones, D. A. Ritchie, and J. E. F. Frost, *Semicond. Sci. Technol.,* **7** (1992) 961.

3.7 Tables

Table 3.1 Van der Pauw measurements for $Al_{0.25}Ga_{0.75}N/GaN$ heterostructures.

Buffer Layer Thick. (microns)	Van der Pauw R_s (Ω/sq.)	2DEG Carrier Density n_s ($x10^{13}cm^{-2}$)	Hall Voltage Meas. μ ($cm^2V^{-1}s^{-1}$)	Conductivity of 2DEG σ ($x\ 10^{-3}\ \Omega^{-1}$)
0.5	400	2.13	734	2.50
0.5	437	1.76	810	2.28
0.75	431	0.98	1487	2.32
1	425	0.93	1588	2.35
1.5	450	0.77	1805	2.22
2	437	1.06	1345	2.29

3.8 Figures

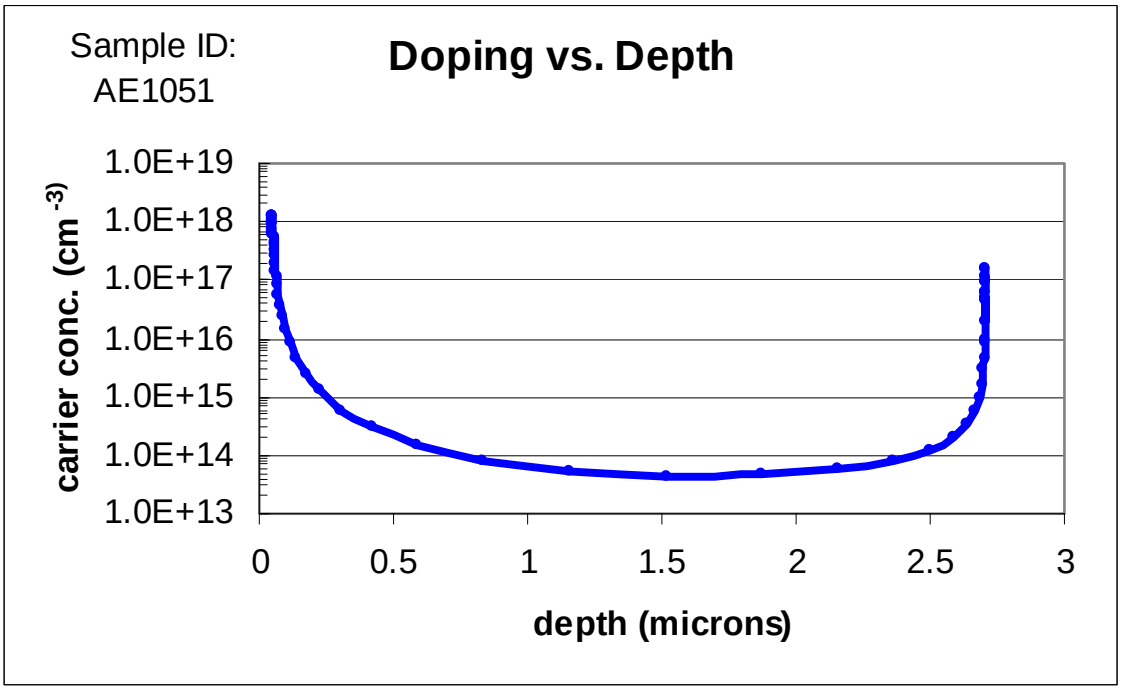


Figure 3.1 CV profile of free carrier concentration versus depth for semi-insulating substrates.

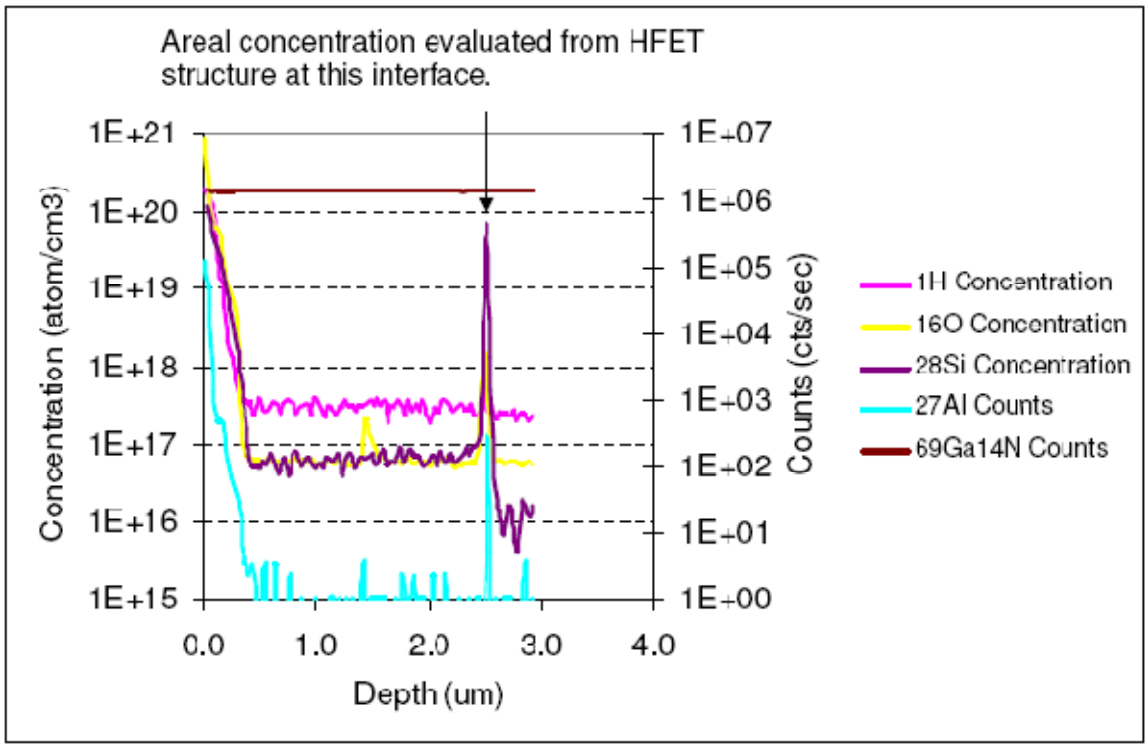


Figure 3.2 SIMS analysis confirming atomic silicon concentration at the epitaxy/bulk GaN interface.

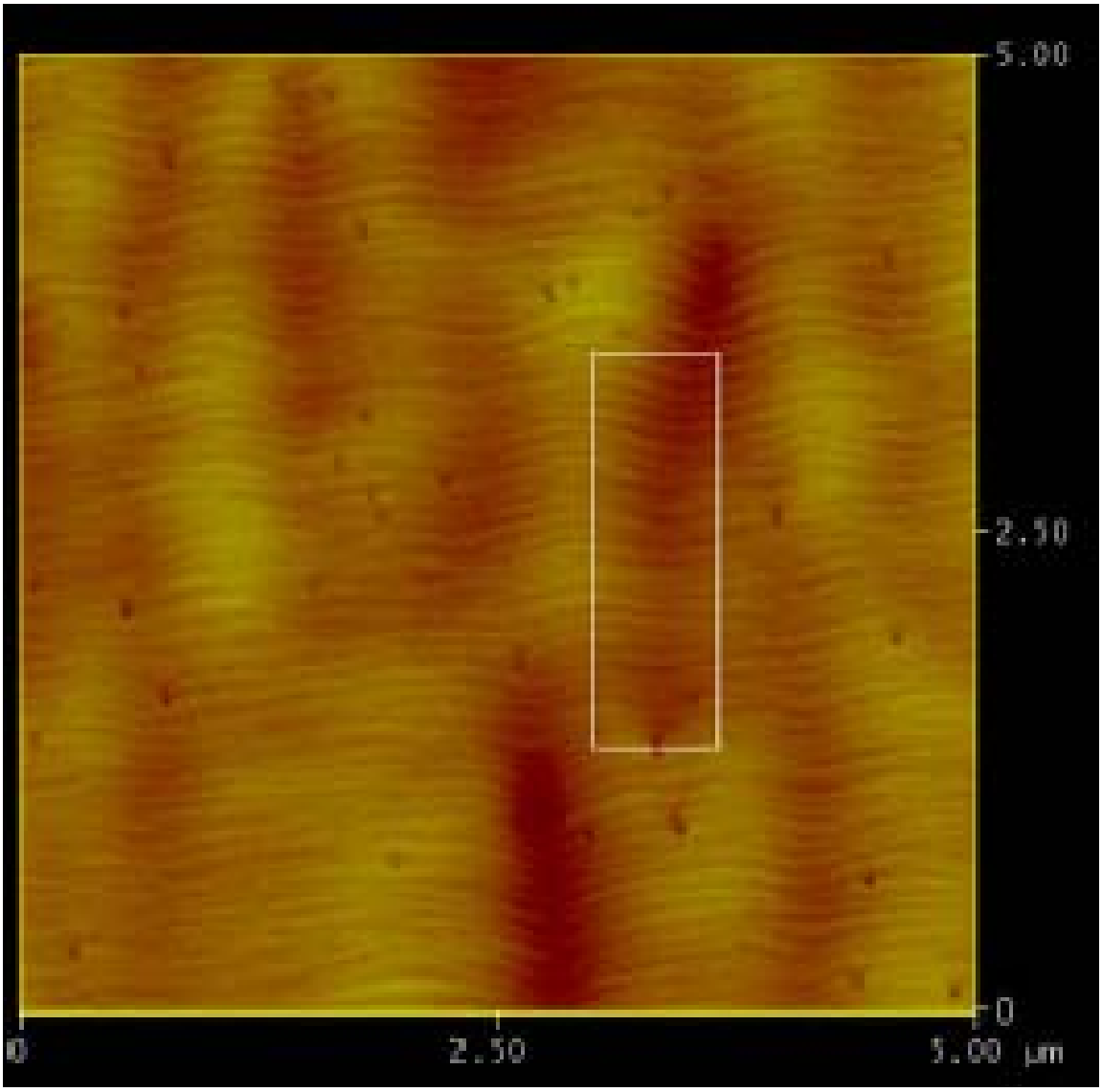


Figure 3.3 AFM image of the surface roughness of an $Al_{0.25}Ga_{0.75}N$/GaN heterostructure grown on a low dislocation density (0001) bulk GaN substrate.

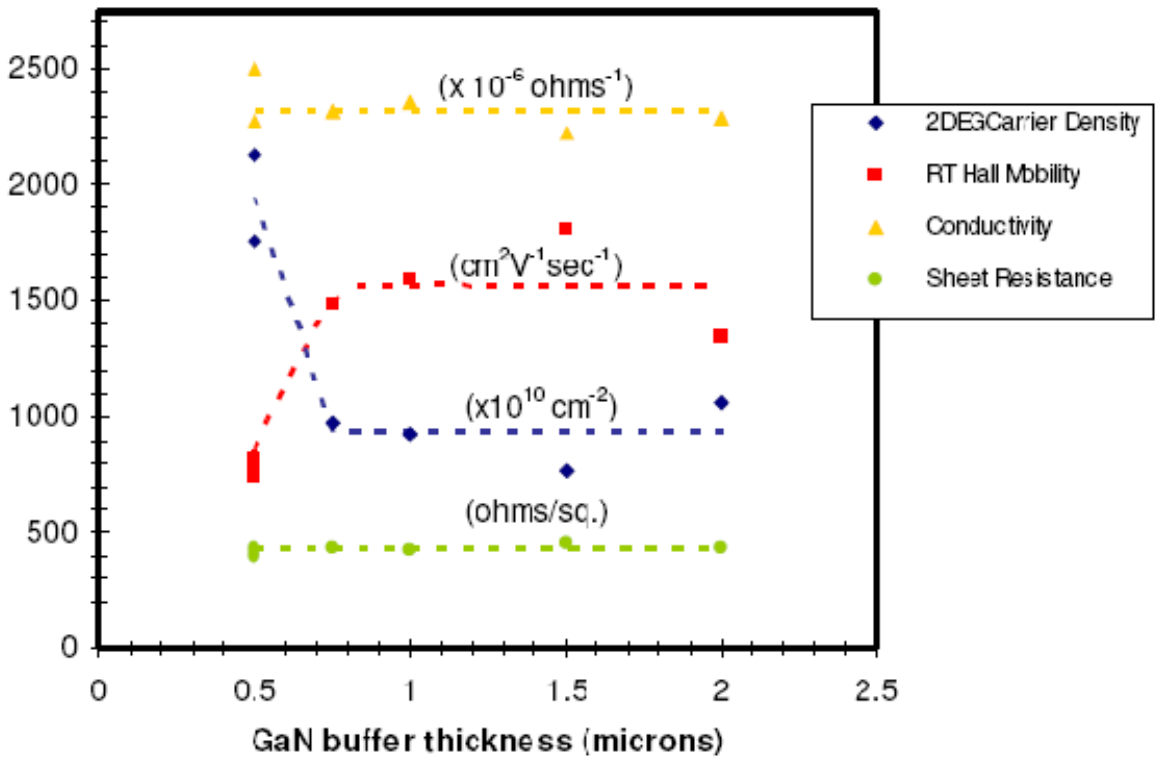


Figure 3.4 Buffer-modulated behavior of room temperature Hall mobility and carrier density.

4. OPTIMIZATION OF HOMOEPITAXIALLY-GROWN AlGaN/GaN HETEROSTRUCTURES

J.A. Grenko, C.L. Reynolds, Jr., D.W. Barlage, and M.A.L. Johnson
Department of Materials Science and Engineering
North Carolina State University, Raleigh, NC 27695

G. J. Duscher
Department of Materials Science and Engineering
University of Tennessee, Knoxville, TN

C.W. Ebert
Veeco Turbodisc, 392 Elizabeth Avenue, Sommerset NJ 08873

E.A. Preble, T. Paskova, and K.R. Evans
Kyma Technologies, 8829 Midway West Road, Raleigh, NC 27617

4.1 Abstract

We report on the growth of $Al_{0.25}Ga_{0.75}N$/GaN heterostructures on low dislocation density semi-insulating c-axis GaN substrates. Room temperature Hall mobilities up to 2065 $cm^2V^{-1}s^{-1}$ at sheet carrier densities of 8.25 x 10^{13} cm^{-2} have been measured. This work compliments prior studies in which we observed a buffer-induced modulation of the room temperature 2DEG sheet carrier densities and Hall mobilities by varying the GaN buffer layer thickness. Here, we focus on the optimization of the AlGaN/GaN 2DEG properties by elimination of silicon doping and unintentional Al in the n.i.d. GaN buffer layer. The 15% improvement in room temperature mobility and sheet density relative to previous results is consistent with those predicted by Poisson solver calculations. Use of thick GaN buffers has minimized the theoretical mobility reduction based on intersubband scattering and has enabled us to determine the 2DEG carrier density associated with the polarization field to be ~5x10^{12} cm^{-2}.

4.2 Introduction

AlGaN/GaN heterostructures are attractive for use in RF and high-power applications due to GaN's high critical electric field [1] and high thermal conductivity which should enable them to exhibit high breakdown voltage (V_{BD}) performance and high unity current gain frequency (f_T). The electric field that is induced by the polarization vector leads to an accumulation of charges of opposite sign at each of the interfaces and the formation of a two-dimensional electron gas (2DEG) at the AlGaN/GaN interface without intentional doping of the AlGaN [2]. In modulation doping, the conduction band of the $Al_{0.25}Ga_{0.75}N$ barrier bends

to spatially separate the ionized donors in the intentionally doped part of the barrier from the electrons in the potential well. The presence of the sheet charge from the polarization field enables one to eliminate intentional silicon doping in the $Al_{0.25}Ga_{0.75}N$ barrier to eliminate any possible contribution of scattering centers that may result from the introduction of dopants during growth. Thus, the 2DEG sheet density due soley to the polarization charges can be assessed. In doing so, the scattering rate in the 2DEG should be significantly reduced and improved low temperature mobilities should be realized as long as surface roughness scattering is minimized [3].

AlGaN/GaN heterostructures are typically grown on non-native substrates, and 2DEG mobilities and sheet carrier densities have been reported in the range of 1200 - 2050 $cm^2V^{-1}s^{-1}$ and sheet carrier densities from 0.5 - $1x10^{13}$ cm^{-2}, respectively [4-9]. A requirement for heteroepitaxial growth of GaN-based device structures on non-native substrates, such as sapphire, SiC and Si(111), is the formation of a low temperature nucleation layer prior to the high temperature GaN buffer growth. This nucleation layer compensates for the lattice mismatch and thermal expansion coefficient differences between GaN and the substrate. However, the presence of this nucleation layer at the interface introduces a high density of defects, e.g., threading dislocations and stacking faults due to the chemical and structural mismatch. Direct evidence for the deleterious impact of the nucleation layer is that measured thermal conductivities are significantly less than theoretical estimates, 230 $W{\cdot}m^{-1}K^{-1}$, for GaN films with dislocation densities greater than $5x10^6$ cm^{-2} [10]. AlGaN/GaN HFET structures grown on low defect density ($<10^6$ cm^{-2}) native bulk GaN substrates should offer better thermal management. This in turn should enhance RF

performance by increasing the high unit current gain frequency since f_T decreases significantly with temperature because of the decrease in saturation velocity [11].

Electron transport properties in the 2DEG have been studied extensively in the Si [12] and AlGaAs/GaAs systems [13]. In addition to the electron scattering at low temperatures attributed to ionized impurity scattering and surface roughness scattering, it has been predicted that scattering of electrons between subbands should occur when more than one electron subband is occupied [12]. It has also been shown that electrons in excited subbands have a mobility that is much higher than that in the lowest subband [14]. However, strong intersubband scattering reduces the mobility of the lowest subband from that of the single-subband case [14]. In this study, we build upon previous work [15] that demonstrated buffer-induced modulation of room temperature mobility and sheet carrier density consistent with intersubband scattering by varying the thickness of the nominally undoped (n.i.d.) GaN buffer. Only a thick (> 0.75 μm) GaN buffer design ensures minimal impact of interfacial impurity-induced intersubband scattering to the 2DEG associated solely with the polarization field to be investigated.

An additional observation made during the initial study of $Al_{0.25}Ga_{0.75}N$ /GaN heterostructures was the presence of an unintentional background level of aluminum on the order of 0.1% (~10^{20} atoms·cm^{-3}) in the n.i.d. GaN layer as shown by secondary ion mass spectroscopy (SIMS) concentration depth profiles. The source of the aluminum contamination was determined to be the trimethylgallium (TMG) bubbler, therefore an alternate TMG bubbler was used in the present investigation. Since aluminum acts as a scattering center for carriers and thus degrades mobility; this study was designed to separate

the impact of the ~1000 ppm unintentional Al in the GaN buffer from the elimination of ionized Si impurities.

4.3 Study of AlGaN/GaN heterostructures

4.3.1 Experimental

The AlGaN/GaN heterostructures in this study were grown by organometallic vapor phase epitaxy (OMVPE) in a vertical reactor at 1040^{o}C and 60 torr on 450 μm thick, 18 x 18 mm^2 semi-insulating bulk GaN substrates. These Fe-doped, c-axis GaN substrates were grown in a conventional vertical hydride vapor phase epitaxy (HVPE) reactor at a growth rate of approximately 100 μm/hr. Capacitance-voltage (CV) measurements indicated that the free carrier concentration in the semi-insulating GaN substrate was $5x10^{13}$ cm^{-3} [15]. The same CV measurements showed a free carrier concentration $>10^{18}$ cm^{-3} in the first 20 nm of the substrate. Secondary ion mass spectroscopy (SIMS) measurements of AlGaN/GaN heterostructures on these semi-insulating bulk GaN substrates [15] confirmed peak atomic silicon concentrations [Si] to be $>10^{19}$ cm^{-3} at the bulk GaN/epitaxial interface [15], which corresponds to an areal concentration ($[Si]_{areal}$) of $1.6x10^{14}$ cm^{-2} [15].

Since the source of the unintentional aluminum in the GaN buffer of the previous study was determined to be the trimethylgallium (TMG) bubbler, an alternate TMG bubbler was used in this investigation. It was important to understand sources of carrier scattering and to separate the effect of removing unintentional aluminum in the GaN buffer from that of removing silicon dopant from the $Al_{0.25}Ga_{0.75}N$ barrier. One $Al_{0.25}Ga_{0.75}N$ /GaN experiment was performed using the new "aluminum-free TMG" bubbler but intentionally-doping the

$Al_{0.25}Ga_{0.75}N$ barrier as illustrated in Fig. 4.1(a). The remaining runs were performed without intentional Si doping in the $Al_{0.25}Ga_{0.75}N$ barrier (see the schematic in Fig. 4.1(b)). The GaN buffer thickness was varied from 1.0 μm to 2.5 μm to eliminate the mobility modulation effect associated with interfacial charge as described in Table 4.1. Every effort was made to match the execution of the heterogrowth structures with those previously reported [15]. SIMS analysis using an O^{2+} primary ion beam used to assess the Al concentration in the GaN buffer showed the ~1000 ppm unintentional Al in GaN buffer (Fig. 4.2(a)) was reduced by 3 orders of magnitude (Fig. 4.2(b)). Atomic force microscopy (AFM) surface roughness was assessed by 5 x 5 μm^2 scans of each heterostructure grown on a substrate that is typically characterized to have 5 x 10^6 cm^{-2} dislocations by panchromatic cathodoluminescence (CL) measurements in a scanning electron microscope (SEM). High resolution X-ray diffraction (HRXRD) scans were performed with a Bede diffractometer using CuKα X-rays. High resolution rocking curves of the (002) reflection were used to generate alloy and thickness data. Room temperature photoluminescence (PL) was performed using an excimer (308 nm) laser with an excitation intensity of 2.5 $W \cdot cm^{-2}$ at the sample surface. Room temperature Hall measurements were used to determine the mobility and sheet carrier concentration. Protective layers of PdAu and Pt were deposited on the AlGaN surface prior to thinning for transmission electron microscopy (TEM) by focused-ion beam (FIB) technique. TEM images were acquired with a VG603 microscope equipped with a Nion aberration correcting lens at an accelerating voltage of 300 kV.

4.3.2 Results and Discussion

XRD, PL and AFM data for all heterostructures grown in the previous buffer modulation study [15] as well as in this study are presented in Table 4.2. The last four entries are heterostructures grown with the new "Al-free TMG" bubbler. The complete set of data is shown for comparison. PL and AFM analyses were similar for both groups while the XRD simulation for the $Al_{0.25}Ga_{0.75}N$ barrier showed slightly higher Al composition and correspondingly lower layer thickness. In addition to the spacing between the pendulosung fringes being greater, they were less distinct than in the first group of heterostructures. This qualitative observation is confirmed by the low Chi-Squared value which reflects the actual placement of the $Al_xGa_{1-x}N$ peak and spacing of the pendulosung fringes relative to the theoretically expected ones. The R Factor, which indicates agreement between the observed structure factor, F_{obs}, and calculated, F_{calc}, is ~10% for these four heterostructures. It is worthwhile noting that the distribution of Chi-Squared and R-factor values within this latter group has less deviation than the previous population.

The tabular results for the van der Pauw Hall sheet density and mobility measurements can be found in Table 4.3. Room temperature (RT) measurements were made at two different currents for each heterostructure. The reproducibility of the Hall measurements at both currents is indicative that measurements were taken in the linear I-V regime. Again, the data suggest that there is modulation of the mobility and sheet density for heterostructures grown with thinner n.i.d GaN buffers due to proximity of the 2DEG channel to the mobile charge at the epitaxial/substrate interface. Also, the mobility for the heterostructure with the n-$Al_{0.25}Ga_{0.75}N$ barrier, M1702, is suppressed relative to that of the

heterostructure with the undoped $Al_{0.25}Ga_{0.75}N$ barrier, M1703. This suggests that mobility degradation due to increased sheet densities in the 2DEG associated with the ionized donors may be limited by electron-electron or optical phonon scattering. The difference in sheet concentration between doped and undoped AlGaN barriers is 5.5 x 10^{12} cm^{-2}. This result is consistent with earlier conclusions [15] that the carrier density associated with ionized donors is $n_s^{id} = 4.5 \times 10^{12}$ cm^{-2} and with the intended doping level and thickness.

The significantly higher average RT mobility ($\mu_{RT}^{avg} = 1993$ $cm^2V^{-1}sec^{-1}$) for heterostructures grown with 2 and 2.5 μm GaN buffers reaffirms that mobile carriers at the epitaxy/bulk GaN substrate interface can reduce the expected RT mobility by 65%. Secondly, we suggest that the presence of ~1000 ppm [Al] in the n.i.d. GaN layer may have provided partial screening of the 2DEG carriers from these mobile carriers at the interface. We substantiate this suggestion in three ways. Firstly, Fig. 4.3(a) shows that the transition to the unmodulated mobility in our previous study occurred for GaN buffer thickness $\geq 0.75\mu m$. It is clear that for heterostructures grown without Al scattering centers in Fig. 4.3(a), this transition does not occur until GaN buffer thickness $\geq 1.75\mu m$. Further investigations should be performed to delineate the modulation boundary.

Secondly, since the supposition is that the ~1000 ppm Al in the GaN buffer is a random solid solution, one would expect that the sheet resistance, R_s, of the 2DEG would be higher than undoped GaN. Inspection of Fig. 4.4(b) reveals that R_s for heterostructures grown with unintentional Al in the GaN buffer have a 10% higher sheet resistance than heterostructures in our current study.

Thirdly, considering the atomic volume of GaN, N_{GaN} = 8.9 x 10^{22} atoms·cm^{-3}, then there are 8.9 x 10^{19} Al atoms·cm^{-3} for 1000 ppm Al in the GaN. This enables one to estimate the distance between Al scattering centers as

$$l_{Al} = \sqrt[3]{\frac{1}{N_{Al}}} = 2.2x10^{-7}\,cm. \tag{4.1}$$

On the basis of the experimentally measured average RT mobility, μ_{RT} of 1556 $cm^2V^{-1}sec^{-1}$ for heterostructures with GaN buffers >0.75 μm, the mean scattering time, τ, is

$$\tau = \frac{m_e^* \mu_{RT}}{e} = 2x10^{-13}\ \text{sec} \tag{4.2}$$

for a reduced mass for GaN, $m_e^* = 0.23m_e$ where m_e is the rest mass of an electron and e is electron charge. Assuming a low field velocity, v, of 2 x 10^6 cm·s^{-1}, the mean free path, l_{MFP}, determined from the mobility measurements is

$$l_{MFP} = v\tau = 4x10^{-7}\,cm \tag{4.3}$$

which is on the order of the separation between Al scattering centers, Eq. (4.1). Furthermore, we might expect that if Al scattering centers can reduce the mean free path this significantly, then we should see an improvement in μ_{RT} for heterostructures grown with Al-free TMG. This behavior may not be evident by inspection of Fig. 4.3(b) but is confirmed by Fig. 4.4(a) which shows that conductivity σ(ohms^{-1}), which is the product of $en_s\mu_{RT}$, is 15% higher for heterostructures grown in this study. Simply looking at average μ_{RT} and average n_s values for GaN buffer thickness >0.75 μm and >1.75 μm for heterostructure from [15] and from this

study, respectively, one would conclude that the 12% improvement in μ_{RT} and 12% decrease in n_s would result in an essentially constant σ which is clearly not the case. These data reinforce that elimination of the 1000 ppm [Al] may also have reduced optical phonon scattering which is known to be relevant at room temperature. There is also considerably less scatter in the σ data , suggesting that if Al is screening the mobile carriers, that screening may be a function of the electric field induced during van der Pauw measurements.

The RT mobility versus sheet carrier density in Fig. 4.5 reinforces the discussion above. The lower μ_{RT} at correspondingly higher n_s for both populations is the result of electron-electron scattering for higher densities of state in the $Al_xGa_{1-x}N$ barrier. The higher μ_{RT} at fixed n_s for the heterostructures grown in this study relative to [15] demonstrates that unintended Al in the GaN buffer layer partially screened the 2DEG from mobile carriers at the epitaxy/bulk interface but also acted as scattering centers. The improvement in σ is responsible for the upward shift in the trend line for heterostructures grown without the 1000 ppm unintentional Al. The full impact of removing the silicon from the $Al_xGa_{1-x}N$ barrier, can only be realized by performing low temperature (LT) Hall measurements to assess ionized impurity scattering as it affects μ_{LT} of heterostructures with and without Si in the $Al_xGa_{1-x}N$ barrier. The maximum mobility, 2065 $cm^2V^{-1}s^{-1}$, observed in this study is comparable to the best that have been reported and only 30% below that predicted for AlGaN/GaN HFETS with similar threading dislocation densities [16].

A TEM image of the AlGaN/GaN interface in the $10\bar{1}0$ zone axis is shown in Fig.

4.6. The high angle dark field image (HADF) reveals perfect atomic order in the GaN buffer layer (light, left side). No dislocations were observed in the limited GaN buffer area of view near the interface. However, the arrow in the AlGaN layer (darker, right) points to a screw component of a mixed dislocation with burgers vector $\frac{1}{3}\left[11\bar{2}3\right]$. The straight rows of Ga atoms (light atoms) above the arrow begin to bend as expected by the classic spiral behavior of a screw dislocation. The presence of a screw dislocation creates the dark area associated with the strain field of the dislocation. Phonons impinging on these dislocations are scattered and transfer momentum to the dislocations in a process known as dislocation damping. The evidence of the mixed dislocation near the interface supports the suggestion that optical phonon scattering is one of the mechanisms limiting the 2DEG mobility. The interface between the GaN and the AlGaN layers is reasonably abrupt. However, closer inspection of the interface reveals a surface roughness of ~1.2 Å, or on the order of the radius of a Ga atom. We believe this low roughness value is a direct reflection of the low dislocation density in the GaN buffer layer where the 2DEG resides. It has been shown that for AlGaN barriers with moderate Al composition, it is because of the perfectly smooth interface and AlGaN surface, that the calculated room temperature mobility is expected to reach values higher than 2000 $cm^2V^{-1}s^{-1}$ [16]. Lastly, lower magnification TEM images revealed the AlGaN layer thickness to be ~141 Å. The error in this measurement is estimated to be as high as 15% because of the difficulty in delineating the interface between the AlGaN surface and the PdAu protective layer applied during focused-ion beam (FIB) preparation.

4.3.3 Analysis of Polarization Charge

In order to understand the sheet carrier density results of our heterostructures, we used a Poisson solver [17, 18] to simulate the expected conduction band energy, $E_{CB}^{\min}$, at the bottom of the potential well and sheet density n_s based on the heterostructure design given in Fig. 4.1(b). The expected polarization charge density, $\sigma_{(P_{SP}+P_{PE})}$, can be determined by applying an electrostatic analysis [19]:

$$q \cdot n_s = \sigma_{(P_{SP}+P_{PE})} \cdot (1 - d / d_{CR}) - \varepsilon \cdot E_{fo} / d \tag{4.4}$$

where ε is the dielectric constant, d is the $Al_xGa_{1-x}N$ layer thickness, d_{CR} is the critical $Al_xGa_{1-x}N$ layer thickness to sustain a polarization dipole and $E_{fo} = E_f - E_{CB}^{\min}$. The sheet density predicted by the Poisson solver is 9.544 x 10^{12} cm^{-2} and $E_{CB}^{\min}$ is -0.229 eV. Using d_{CR} = 35 Å and ε = 8.9, the $\sigma_{(P_{SP}+P_{PE})}$ is determined to be 3.05 x 10^{-7} coul·cm^{-2}. If we consider that sheet density contributed by the polarization, n_s^{polar}, was determined to be 5.0 x $10^{12}cm^{-2}$ [15], then for these heterostructures grown without 1000 ppm [Al] in the GaN buffer, the sheet charge contributed by the charge at the epitaxy/bulk interface can be determined by

$$n_{id}^{charge} = n_s^{1\mu m(n.i.d.-AlGaN)} - n_s^{polar} \tag{4.5}$$

for $n_s^{1\mu m(n.i.d.-AlGaN)} = 1.2x10^{13} cm^{-2}$, then $n_s^{charge} = 7.0x10^{12} cm^{-2}$. This reinforces the suggestion that the Al in GaN buffer screened the mobile charge from the epitaxy/bulk GaN interface. And if we use the n_s determined from the heterostructure shown in Fig. 4.1(a), then the

sheet charge, $n_s^{1\mu m(n-AlGaN)} = 1.75x10^{13} cm^{-2}$. Since

$$n_s^{1\mu m(n-AlGaN)} - n_s^{polar} - n_s^{charge} = n_s^{id} \tag{4.6}$$

we arrive at our earlier conclusion that $n_s^{id} = 5.5x10^{12} cm^{-2}$. Therefore, from both studies we show that the carrier density associated with the polarization field is $n_s^{polar} = 5x10^{12} cm^{-2}$. Hence, using $d = 12$ nm based on our HRXRD data and a corresponding $E_{CB}^{\min}$ of -0.178 eV, we find $\sigma_{(P_{SP}+P_{PE})} = 2.82x10^{-7}$ coul·cm^{-2} which is in excellent agreement with that calculated from the Poisson solver.

4.4 Conclusions

The RT mobility versus sheet carrier density in Fig. 4.5 reinforces all points that have been made. The lower μ_{RT} at correspondingly higher n_s for both populations is the result of electron-electron scattering for higher carrier densities in the 2DEG. The higher μ_{RT} at fixed n_s for the heterostructures grown in this study relative to [15] demonstrates that unintended Al in the GaN buffer layer acted as scattering centers. However, data also suggest that these Al scattering centers may have served to screen carriers in the 2DEG from those at the epitaxy/bulk interface. The improvement in σ is responsible for the upward shift in the trend line for heterostructures grown without the 1000 ppm Al contamintation. The full impact of removing the silicon from the $Al_xGa_{1-x}N$ barrier can only be realized by performing low temperature (LT) Hall measurements to assess the various scattering mechanisms that limit mobility. μ_{LT}. Additionally low temperature studies may assist in the determination of

the optimal undoped AlGaN barrier thickness next to the 2DEG for heterostructures grown with Si in the $Al_xGa_{1-x}N$ barrier.

4.5 Acknowledgements

The authors acknowledge Kyma Technologies for the bulk GaN substrates used in this study. Special thanks to Fred Stevie, NCSU Analytical Instrumentation Facility, for the SIMS analysis.

4.6 References

[1] F. Ren and J. Zolper, Wide *Energy Bandgap Electronic Devices* (World Scientific Publishing, Singapore, 2003) 179.

[2] O. Ambacher, *J. Phys. D: App. Phys.,* **31** (1998) 2653.

[3] A. Hartstein, T. H. Ning and A. B. Fowler, *Surf. Sci.,* **58** (1976) 178.

[4] E. Iiopoulos et al, *Superlatt. Microstruct.,* **40** (2006) 313.

[5] P. Kordos, J. Bernat, and M. Marso, *Microelectron. J.,* **36** (2005) 438.

[6] M. Germain et al, *Mat. Res. Symp. Proc.,* **798** (2004) Y10.22.1.

[7] S. Iwakami et al, *Jpn. J. App. Phys.,* **43** (2004) L831.

[8] Z. Bougrioua et al, *Phys. Stat. Sol. (b),* **228** (2001) 625.

[9] G. Y. Zhao et al, *Physica E,* **7** (2000) 963.

[10] C. Mion and J. F. Muth, *Appl. Phys. Lett.,* **89** (2006) 092123.

[11] F. Ren and J. Zolper, *Wide Energy Bandgap Electronic Devices* (World Scientific Publishing, Singapore, 2003) 193.

[12] S. Mori and T. Ando, *Phys. Rev. B,* **19** (1979) 6433.

[13] H. L. Stormer, A. C. Gossard, and W. Weigmann, *Solid State Commun.,* **41** (1982) 707.

[14] T. Ando, *J. Phys. Soc. Jpn.,* **51** (1982) 3900.

[15] J.A. Grenko, C.W. Ebert, C.L. Reynolds, Jr., M.A.L. Johnson, A.D. Hanser, E.A. Preble, T. Paskova, and K.R. Evans, *Phys. Stat. Solidi (c),* **6** (2009) S1037.

[16] Z. Bougrioua, M. Azize, P. Lorenzini, M. Laugt, and H. Haas, *Phys. Stat. Sol. (a),* **202** (2005) 536.

[17] G. L. Snider, I.-H. Tan, and E.L. Hu, *J. App. Phys.,* **68** (1990) 2849.

[18] I.-H. Tan, G.L. Snider, and E.L. Hu, *J. App. Phys.,* **68** (1990) 4071.

[19] R. Vetury, I.P. Smorchkova, C.R. Elsass, B. Heying, S. Keller, and U.K. Mishra, U.K., *Mat. Res. Soc. Symp.*, **622** (2000) T2.5.1.

4.7 Tables

Table 4.1 Van der Pauw measurements for $Al_{0.25}Ga_{0.75}N$/GaN heterostructures.

Substrate I.D.	*Growth Run*	*Description starting from the top of heterostructure*
AE888.4	M1702	15 nm n-$Al_{0.25}Ga_{0.75}N$/5 nm i-$Al_{0.25}Ga_{0.75}N$/ 1 μm i-GaN/Kyma SI substrate
AE914.2	M1703	20 nm i-$Al_{0.25}Ga_{0.75}N$/1 μm i-GaN/Kyma SI substrate
AE922.3	M1720	20 nm i-$Al_{0.25}Ga_{0.75}N$/2.5 μm i-GaN/Kyma SI subsrate
AE922.4	M1721	20 nm i $Al_{0.25}Ga_{0.75}N$/2 μm i GaN/Kyma SI substrate

Table 4.2 XRD, PL and AFM characterization for all $Al_xGa_{1-x}N$/GaN hetero-structures. Last four entries are heterostructures grown with "Al-free TMG". Complete data set shown for comparison.

SUBST. I.D.	Targeted $Al_xGa_{1-x}N$ Layer Thickness (Å)	Simu-lated Layer Thick-ness (Å)	Target Al content	Simu-lated Comp. Match	Chi-squared	R-factor (%)	PL spectral map median wavelength (nm)	RPM2000 median alloy concen. (%Al)	Peak Intensity (volt)	FWHM (nm)	AFM RMS Rough. (nm) ($5x5\mu m^2$)	AFM Max Rough. (nm) ($5x5\mu m^2$)
AE754.1	200	177.59	0.25	0.1739	0.033	9.60	326.1+/-3.157	22.7+/-1.842	0.014+/-0.005	11.8+/-3.460	2.652	83.974
AE774.2	200	172.96	0.22	0.1436	0.036	9.37	332.5+/-7.029	19.4+/-4.355	0.014+/-0.013	10.2+/-3.773	1.617	17.735
AE475.5	200	too broad	0.25	NA	0.168	12.99	322.3+/-6.476	24.9+/-3.767	0.094+/-0.061	24.3+/-4.653	1.971	62.577
AE811.2	200	too broad	0.25	NA	too broad	too broad	323.1+/-2.331	24.5+/-1.369	0.031+/-0.039	14.2+/-6.920	0.994	9.158
AE832.1	200	187.81	0.25	0.2014	0.062	9.88	321.4+/-4.990	25.4+/-2.904	0.017+/-0.009	17.5+/-7.582	3.269	54.497
AE853.1	200	153.69	0.25	0.2454	0.141	23.74	322.6+/-4.368	24.7+/-4.542	0.025+/-0.015	14.8+/-3.002	1.383	16.519
AE840.2	200	176.49	0.25	0.2211	0.062	15.38	322.2+/-3.049	25.0+/-1.767	0.002+/-0.001	1.20+/-1.079	3.581	27.571
AE816.4	200	214.55	0.25	0.2152	-	-	321.2+/-3.267	25.6+/-1.90	0.005+/-0.003	5.50+/-2.762	2.835	23.146
AE888.4	200	118.75	0.25	0.2343	0.027	10.98	332.9+/-13.79	18.6+/-13.7	0.003+/-0.002	2.30+/-1.000	3.237	33.401
AE914.2	200	115.97	0.25	0.2979	0.028	11.69	307.0+/-11.45	26.5+/-13.9	0.005+/-0.002	1.70+/-1.000	3.654	91.489
AE922.3	200	109.6	0.25	0.2774	0.024	9.62	318.3+/-6.273	26.2+/-13.7	0.005+/-0.002	1.70+/-1.000	0.787	29.036
AE922.4	200	107.59	0.25	0.3049	0.027	10.22	319.6+/-6.353	26.5+/-13.9	0.005+/-0.002	1.70+/-1.000	0.958	25.648

Table 4.3 Van der Pauw measurements for $Al_{0.25}Ga_{0.75}N/GaN$ heterostructures grown with "Al-free TMG".

SUBST. I.D.	GROWTH #	GaN buffer thickness (μm)	Hall Current (amps)	Hall Voltage (volts)	R_{sheet} ($\Omega_{/sq.}$)	n_s at 3kG (cm^{-2})	μ ($cm^2V^{-1}s^{-1}$)	$qn_s\mu$ (x 10^{-3} Ω^{-1})
AE888.4	M1702	1.00	$100x10^{-6}$	8.56E-03	397	1.75E+13	898	2.52
AE888.4	M1702	1.00	$200x10^{-6}$	1.72E-02	399	1.75E+13	897	2.51
AE914.2	M1703	1.00	$100x10^{-6}$	1.25E-02	404	1.20E+13	1286	2.48
AE914.2	M1703	1.00	$200x10^{-6}$	2.52E-02	400	1.19E+13	1311	2.50
AE922.3	M1720	2.50	$100x10^{-6}$	1.84E-02	383	8.16E+12	1999	2.61
AE922.3	M1720	2.50	$200x10^{-6}$	3.63E-02	380	8.26E+12	1991	2.63
AE922.4	M1721	2.00	$100x10^{-6}$	1.73E-02	375	8.69E+12	1918	2.67
AE922.4	M1721	2.00	$200x10^{-6}$	3.64E-02	367	8.25E+12	2065	2.72

4.8 Figures

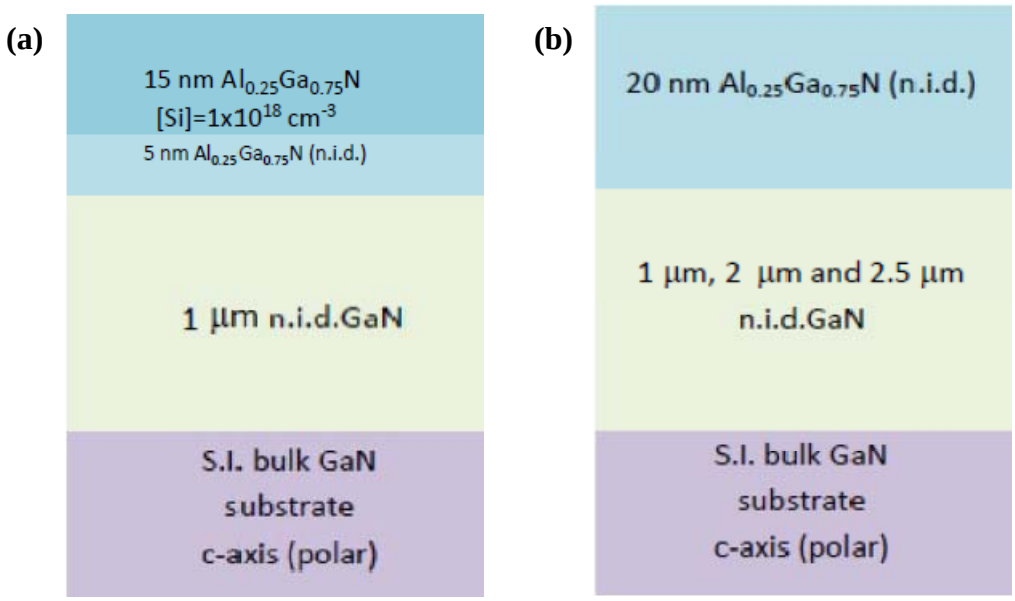
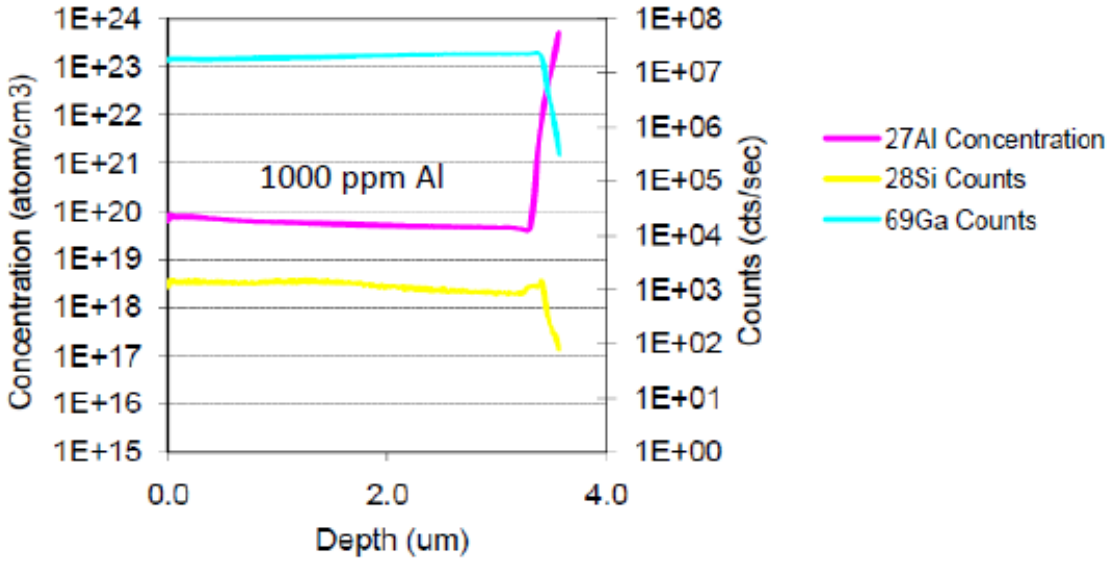


Figure 4.1 (a) 1 µm thick n.i.d. GaN buffer followed by 5 nm undoped $Al_{0.25}Ga_{0.75}N$ spacer then 15 nm of n-$Al_{0.25}Ga_{0.75}N$. (b) 1, 2, and 2.5 µm thick n.i.d. GaN buffers followed by 20 nm of undoped $Al_{0.25}Ga_{0.75}N$.

(a)



(b)

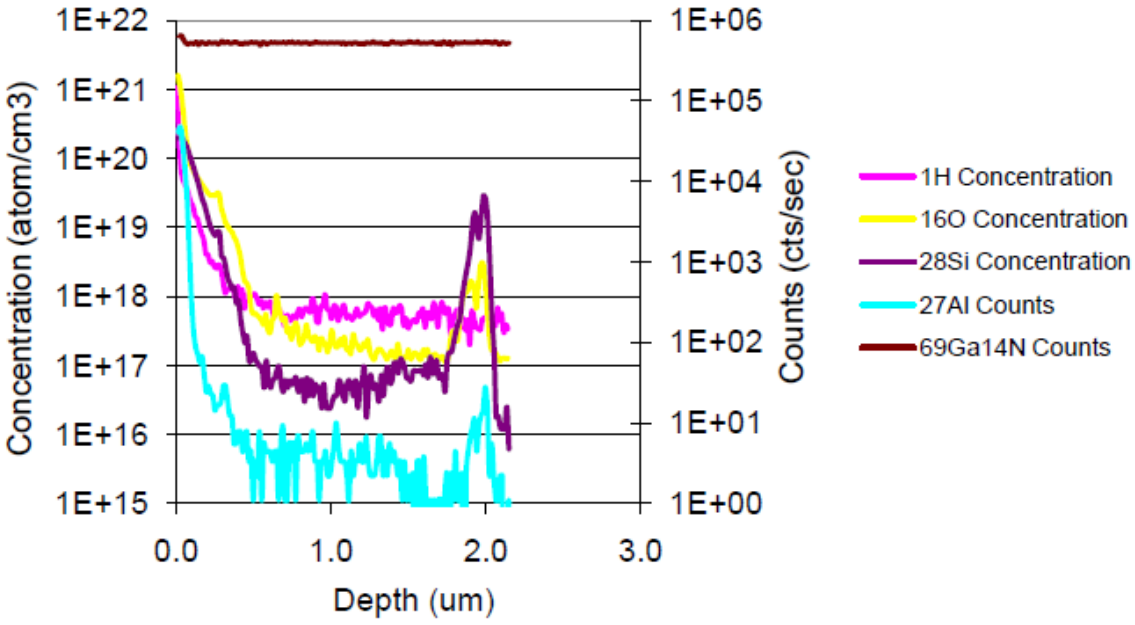


Figure 4.2 (a) SIMS analysis performed with O^{2+} primary ion shows ~1000 ppm unintentional Al in the GaN buffer (b) has been reduced by 3 orders of magnitude.

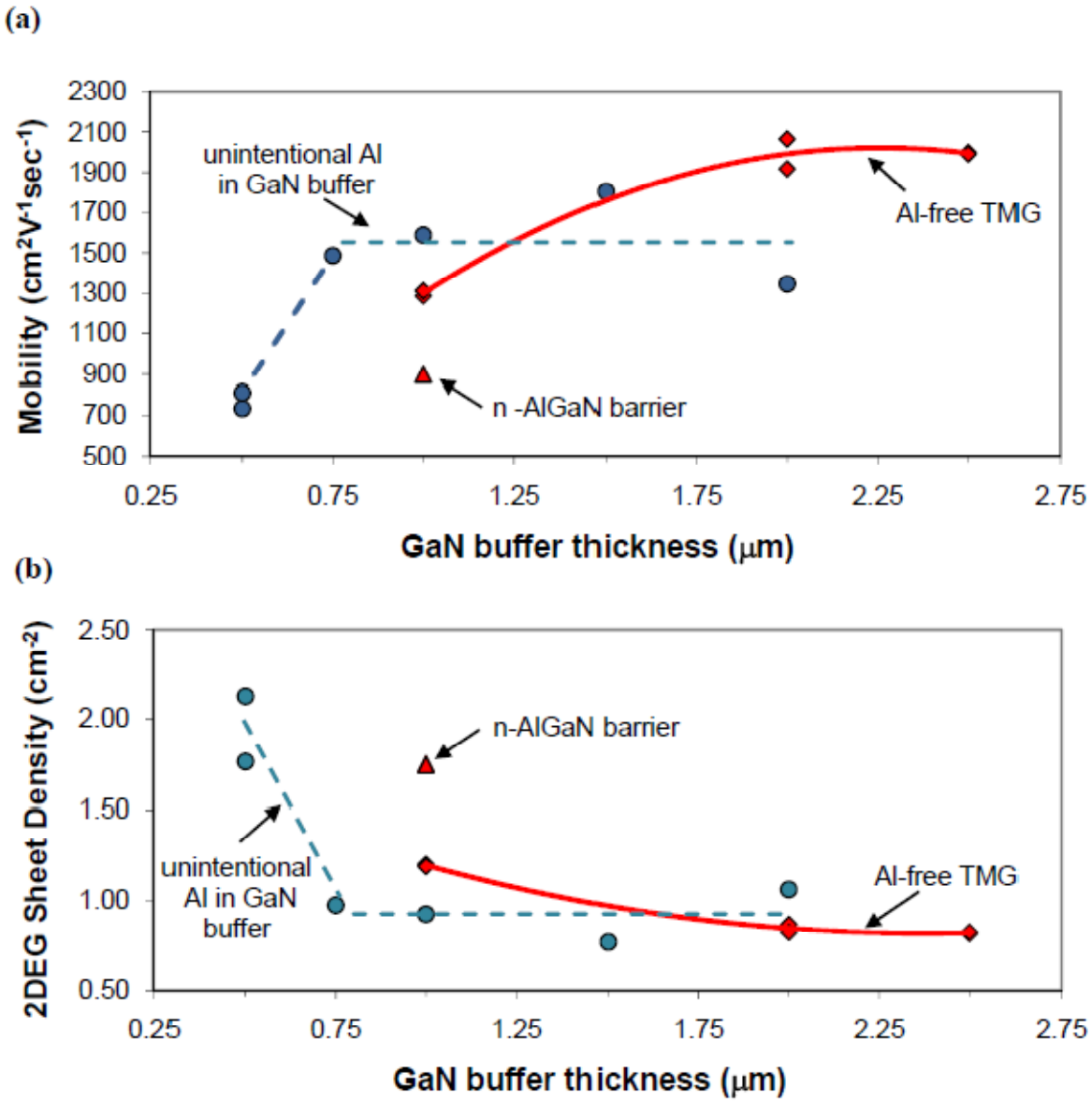


Figure 4.3 (a) RT mobility data suggest mobility modulation may occur at a greater GaN buffer thickness than 0.75 μm for heterostructures grown without ~1000 ppm unintentional Al in the GaN buffer. (b) 2DEG sheet density as a function of GaN buffer thickness for heterostructures grown with unintentional Al in the GaN buffer and without.

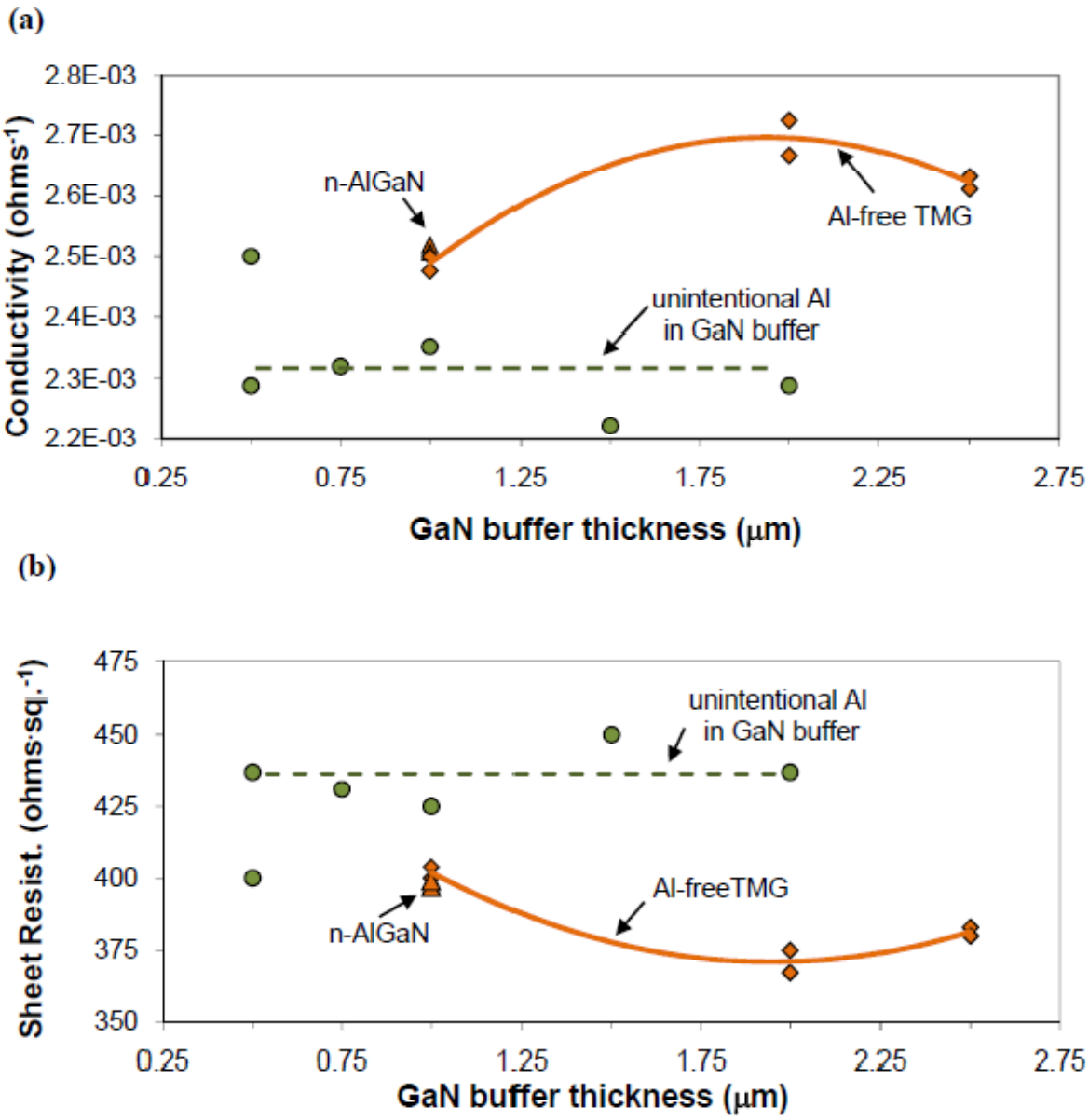


Figure 4.4 (a) Conductivity as a function of GaN buffer thickness for hetero-structures grown with ~1000 ppm unintentional Al in the GaN buffer and without. (b) Sheet resistance data showed comparable results for heterostructures grown with unintentional Al in the GaN buffer and without.

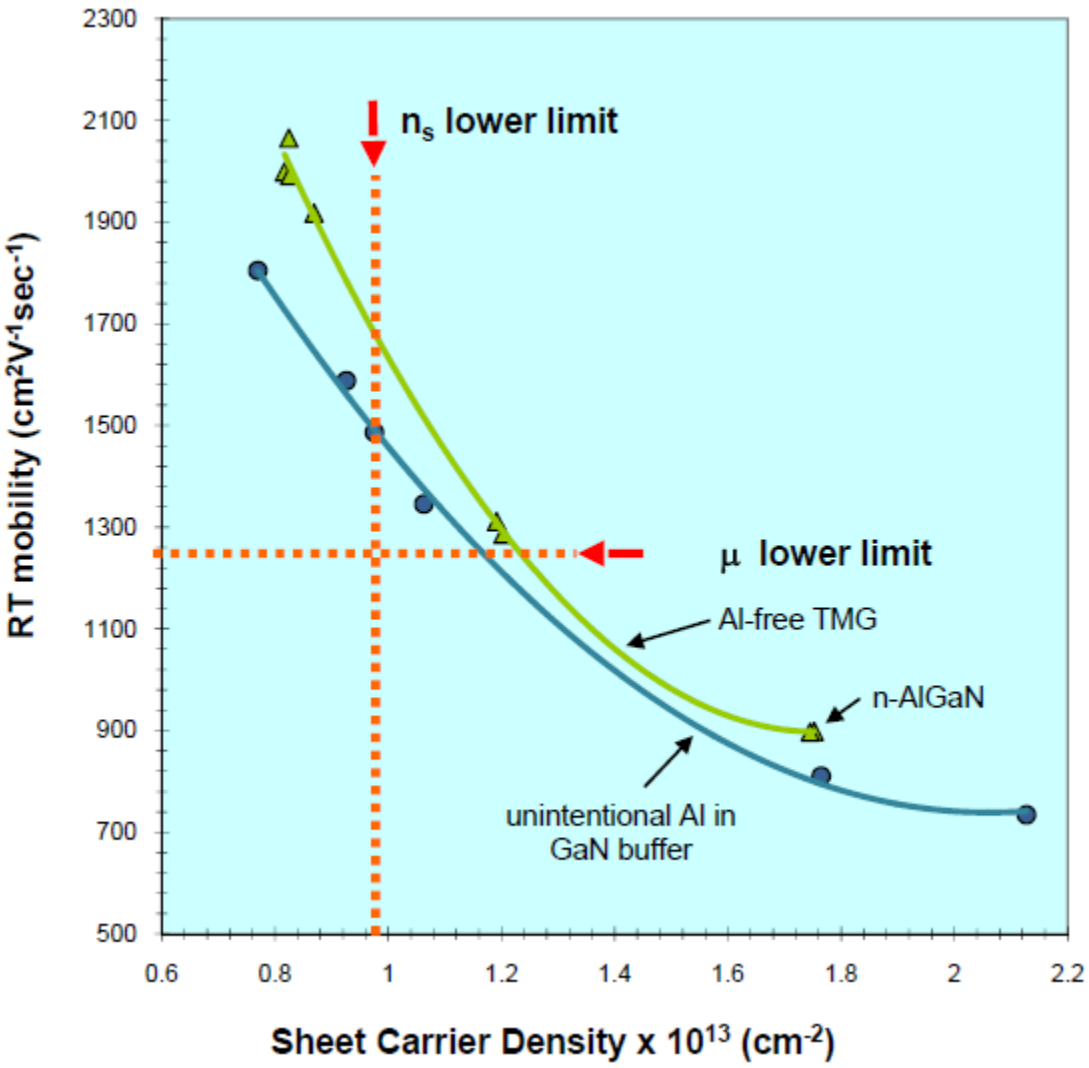


Figure 4.5 Elimination of ~1000 ppm unintentional Al from the GaN buffer resulted in shift toward higher RT sheet densities and mobilities.

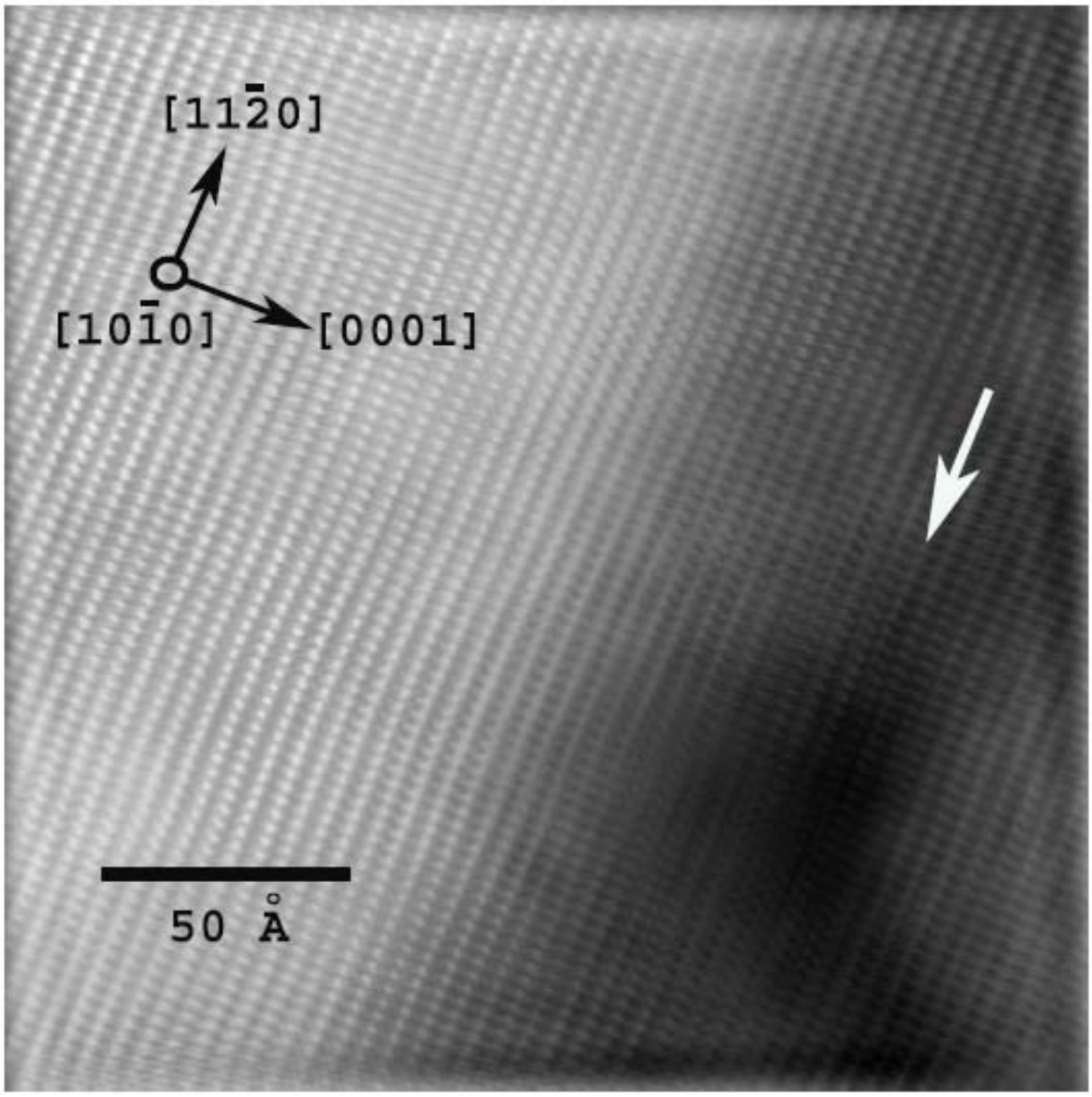


Figure 4.6 TEM image of AlGaN (dark side)/ GaN (light side) interface is abrupt to within a monolayer. White arrow points to a screw component of a mixed dislocation in the AlGaN layer with burgers vector $\frac{1}{3}\left[11\bar{2}3\right]$.

5. IMPACT OF INTERFACE IMPURITIES ON HETEROSTRUCTURES

5.1 Introduction

For growth of III-nitride-based HFET structures on freestanding semi-insulating GaN substrates, the GaN regrowth interface between the epitaxial layer and the substrate is a critical region of the device. Unfortunately, this interface contains impurities such as Si, O, and C [1] which may induce additional charge layers near the interface. Other groups [2] have studied the impact of interface impurities on HFET structures and found that the presence of C on semi-insulating GaAs substrates introduced side-gating, the electrical crosstalk between neighboring FETs. Subjecting the GaAs substrate to an ultraviolet ozone clean prior to growth reduced the concentration of C at the interface. [3-6]. Properties of the GaAs 2DEG channel improved with increasing distance from the substrate [2] by reducing the charge contributed by electrically-active Si at the substrate interface. Our investigations [7] have shown that as long as the $Al_{0.25}Ga_{0.75}N$ barrier is adequately distanced from the bulk GaN substrate, the sheet density reduces to contributions from ionized donors, n_s^{id} and polarization, n_s^{polar}.

Others [8] have concluded that because of current growth and substrate preparation technologies, the introduction of a thin layer of Si impurities seems inevitable near the regrowth interface. As such, they have studied the role of Fe doping at the regrowth interface on the confinement and localization of the 2DEG. They proposed that compensation of silicon impurities by Fe doping was effective as long as the charge layer is removed prior to the epitaxial growth. In order to remove the interface charge layer, they employed surface layer chemical etching, dry etching by inductively-coupled plasma (ICP), in situ thermal

etching, and photo-enhanced chemical (PEC) etching [9]. PEC etching has been used to selectively etch GaN from AlGaN/GaN structures using dilute solutions of KOH and H_3PO_4 [10, 11]. In PEC etching, electron-hole pairs are photogenerated in a semiconductor placed in an electrolytic solution and illuminated with photons of energy greater than its bandgap. The holes are transported to the semiconductor-electrolyte interface for bond-breaking reactions with the semiconductor. Meanwhile, the electrons are swept to the cathode to reduce the probability of unwanted electron-hole recombination. Youtsey [12] proposed that the following oxidation reaction is responsible for the decomposition of GaN,

$$2GaN + 6h^+ \rightarrow 2Ga^{3+} + N_2 \tag{5.1}$$

The formation of bubbles on the sample surface during etching was evidence for the release of N_2 [11]. Bardwell [12] suggested a photoenhanced wet etching that does not require an electrical contact to be made to the sample and is able to etch nitrides deposited on insulating substrates, unlike PEC wet etching. The mechanism suggested involves the photolysis of peroxydisulfate,

$$S_2O_8^{2-} + photons \rightarrow 2SO_4^{-\bullet} \tag{5.2}$$

that results in the production of a sulfate ion radical. Subsequently, the sulfate ion radical is consumed,

$$SO_4^{-\bullet} + OH^- \rightarrow SO_4^{2-} + OH^{\bullet} \tag{5.3}$$

resulting in the production of hydroxide radicals. The method employed by Dupuis [9] is also an electrodeless photoassisted etching using a UV lamp as a light source and KOH and $K_2S_2O_8$ diluted in deionized water as etchants. Under optimized etching conditions, a

smooth surface with an RMS roughness of 0.1~0.2 nm for a 1 x 1 μm^2 scan area was reported. Capacitance-voltage measurements indicated no charge near the epitaxial growth interface.

5.2 Experimental

The semi-insulating (S.I.) (0001) bulk GaN substrates used in this experiment had areal Si concentrations of 1.6 x 10^{14} cm^{-2} [7] at the regrowth interface. Two different approaches were employed to remove this interfacial layer: photo-assisted chemical etching and CF_4 plasma etching. Substrates were etched for 60 min. in a parallel plate RF induction plasma system using a gas mixture of CF_4/O_2 as a source at a power of 100 W. Atomic force microscopy (AFM) was used to assess surface roughness. The chemical properties of the GaN regrowth surface were characterized using X-ray photoelectron spectroscopy (XPS). Nickel was evaporated onto the CF_4-etched substrate to protect the surface prior to SIMS analysis. SIMS analysis was performed using a Cs^+ primary ion and an implant standard of Si in GaN to determine the ^{28}Si concentration at the regrowth surface of $Al_{0.25}Ga_{0.75}N$/GaN heterostructures grown on substrates prepared by CF_4/O_2 plasma etching and grown by organometallic vapor phase epitaxy (OMVPE) in a vertical reactor at 1040^oC and 60 torr. Photo-assisted wet etching was performed on a substrate using full flood exposure with a mercury (Hg) arc lamp at 700 W. The substrate was placed in a solution of 0.04 M KOH and 0.1 M $K_2S_2O_8$ diluted for 15 min. The etched wafer was imaged using a JEOL JSM 6400 SEM.

5.3 Results and Discussion

The CF_4/O_2 plasma etching has been shown to be effective in removing SiO_2 from the surface of GaN semiconductors [14]. However, the silicon on the surface of the bulk GaN substrates was attributed to colloidal silica contamination during polishing [14]. AFM measurements in a 5 x 5 μm^2 area of those surfaces after CF_4/O_2 plasma etch treatment varied between 0.1 to 0.4 nm. A S.I. bulk GaN substrate with no processing from the same group of substrates studied, had an RMS roughness of 2.6 nm. Figure 5.1 shows the ^{28}Si counts track with the ^{58}Ni counts suggesting that silicon contamination was removed from the regrowth surface by the CF_4/O_2 plasma etch treatment but may have been reintroduced during the nickel evaporation.

Heterostructures grown on CF_4/O_2 plasma etch treated surfaces had a root mean square (RMS) roughness measured by AFM was 4 – 6 nm on a 5 x 5 μm area of those surfaces. Typical RMS surface roughnesses for heterostructures grown on substrates with no processing was 1 – 2 nm The increased surface roughness may be explained by XPS analysis shown in Fig. 5.2. The relative ratios of the C 1s to the Ga 2p peak for the CF_4/O_2 plasma-etched versus the control surface indicated increased carbon counts in addition to the flourine F 1s at a binding energy of 689 eV and a F Auger series between 643 and 599 eV. To eliminate differences in charging and distance from the analyzer, the relative intensity calculations were based on the most intense, highest resolved Ga 2p peak at a binding energy of 1119 eV as follows,

$$\frac{\left(\frac{I_{C1s}}{I_{Ga2p}}\right)^{CH_4/O_2}}{\left(\frac{I_{C1s}}{I_{Ga2p}}\right)^{CONTROL}} = \frac{1.5}{0.7} \tag{5.4}$$

The carbon contamination on the CF_4/O_2 plasma etched surface is double that of the control surface. Others have reported that CF_4/O_2 produces a fluorinated amorphous carbon residue on SiO_2 sidewalls and on the etched surface and in fact this deposited residue has been adapted as an overcoat for photoresist hardening [16]. The deleterious effect of using substrates with carbon contamination for heterostructure growth at 1040^{o}C is that during heat-up of the substrate, prior to growth, the GaN surface begins to decompose. Ga vacancies are known to have relatively low formation energies [17, 18] in n-type GaN making it likely that substitutional carbon at the Ga site behaves as a shallow donor with a binding energy of 30 meV in GaN [19, 20]. A high density of substitutional C_{Ga} at the surface would provide a parallel conduction path for electron transport.

Figure 5.3 is an SEM image of the surface of the bulk GaN substrate after KOH / $K_2S_2O_8$ photoenhanced etching. Large areas across the region appear to be unetched, smooth Ga-face crystal. However, there are large (10 - 20 μm) irregularly-shaped depressions formed at a density of 5 x 10^6 cm^{-2} across the entire surface. The morphology exhibited neither hexagonal features nor distinct pyramids as has been observed in Ga-face or N-face [21] surfaces respectively [22]. It was clear from the first results of the photoassisted wet etch that several substrates would be required to optimization conditions to create a smooth regrowth surface. Bardwell has reasoned that electrodeless wet etch is made possible by

photochemically generating $OH^{\bullet}$ free radicals. Furthermore, the use of 254 nm mirrors with the UV source yielded ~90% photons with $\lambda \leq$ 310 nm, i.e. 90% of photons capable of producing either electron-hole pairs and of photolyzing $S_2O_8^{2-}$ versus an efficiency of only 15% with 365 nm mirrors [13]. Since photons at 365 nm can only generate electron-hole pairs in GaN, the presence of a cathode is imperative to prevent unwanted electron-hole recombination.

5.4 References

[1] W. Lee, J.-H. Ryou, D. Yoo, J. Limb, and R.D. Dupuis, *Appl. Phys. Lett.,* **90** (2007) 093509.

[2] C.L. Reynolds, Jr., H.H. Vuong, and L.J. Peticolas, *IEEE Trans. Electron Dev.,* **39** (1992) 2459.

[3] M.L. Gray, C.L. Reynolds, Jr., and J.M. Parsey, Jr., *J. Appl. Phys.,* **68** (1990) 169.

[4] J.A. McClintock, R.A. Wilson, and N.E. Byer, *J. Vac. Sci. Technol.,* **20** (1982) 241.

[5] A.J. Springthorpe, S.J. Ingrey, B. Emmerstorfer, P. Mandville, and W.T. Moore, *Appl. Phys. Lett.,* **50** (1987) 77.

[6] W.M. Lau, N.S.McIntyre, and S. Ingrey, *Semiconductor-Based Heterostructures: Interfacial Structure and Stability,* M.L. Green, J.E.E. Baglin, G.Y. Chin, H.W. Deckman, W. Mayo, and D. Narasinham, Eds. Warrendale, PA: The Metallurgical Soc. (1986) 95.

[7] J.A. Grenko, C.W. Ebert, C.L. Reynolds, Jr., M.A.L. Johnson, A.D. Hanser, E.A. Preble, T. Paskova, and K.R. Evans, *Phys. Stat. Solidi (c),* **6** (2009) S1037.

[8] W. Lee, J.-H. Ryou, and R.D. Dupuis (unpublished).

[9] J.–H. Ryou, J.P. Liu, Y. Zhang, C.A. Horne, W. Lee, S.-C. Shen, and R.D. Dupuis, *Phys. Stat. Solidi (c),* **5** (2008) 1849.

[10] J.A. Grenko, C.L. Reynolds, Jr., R. Schlesser, K. Bachmann, Z. Rietmeier, R.F. Davis and Z. Sitar, *MRS Internet J. Nit. Sem. Res.,* **9** (2004) 1.

[11] J.A. Grenko, C.L. Reynolds, P. G. Kotula, Jr., R. Schlesser, J.J. Hren, K. Bachmann, and Z. Sitar, *J. Appl. Phys.,* **96** (2004) 5185.

[12] C. Youtsey, L.T. Romano, I. Adesida, *Appl. Phys. Lett.,* **73** (1998) 797.

[13] J.A. Bardwell, J.B. Webb, H. Tang, J. Fraser, and S. Moisa, *J. Appl. Phys.,* **89** (2001) 4142.

[14] F. Ren, S.J. Pearton, R.J. Shul, and J. Han, *J. Electron. Mat.,* **27** (1998) 175.

[15] D. Hanser, E. Preble, and K. Evans (private communication).

[16] A.J. van Roosmalen, A.D.M. van Arendosk, H.T. Arends and J. Schmidt, *Proc. 5th Symp. Plasma Processing* (Pennington, NJ; Electrochemical Soc., 1985), **85** 527.

[17] S. Limpijumnong and C.G. Van de Walle, *Phys. Rev. B*, **69** (2004) 2179.

[18] M.A. Reshchikov and H. Morkoc, *J. Appl. Phys.,* **97** (2005) 061301.

[19] R. Hirota, K. Kushida, J. Takahashi, and K. Kuriyama, *Nucl. Instrum. Methods Phys. Res. B*, **219** (2004) 792.

[20] H. Wang and A.-B. Chen, *J. Appl. Phys.,* **87** (2000) 7859.

[21] E. S. Hellman, *MRS Inter. J. Sem. Res.,* **3** (1998) 11.

[22] M. Sumiya, K. Yoshimura, T. Ito, K. Ohtsuka, and S. Fuke, *J. Appl. Phys.,* **88** (2000) 1158.

5.5 Figures

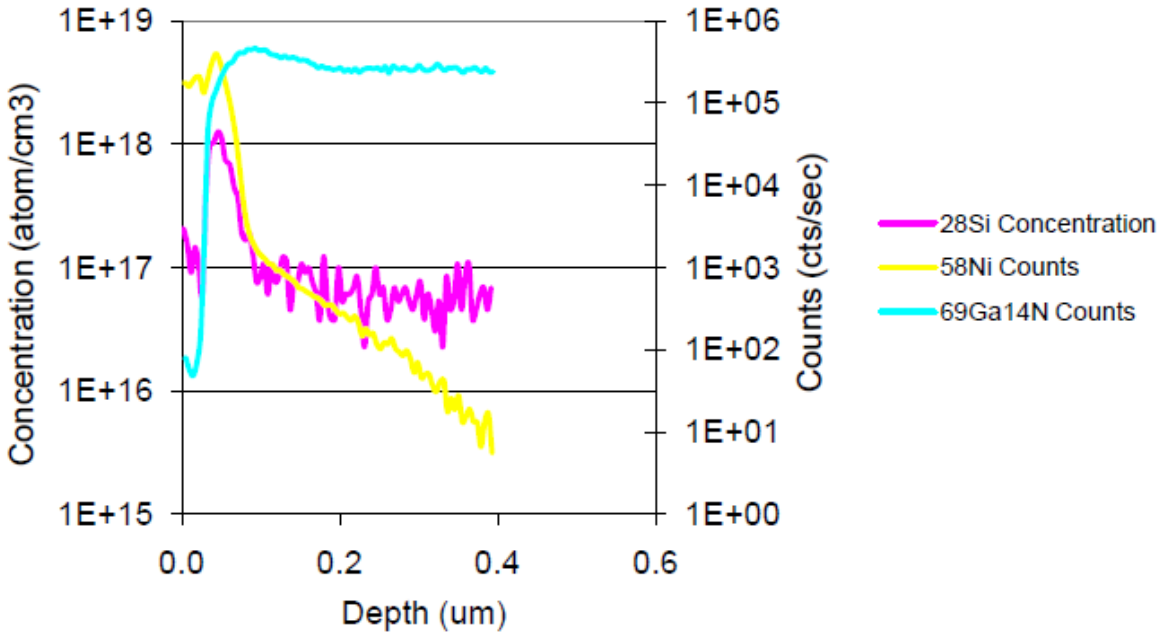


Figure 5.1 SIMS analysis of regrowth surface capped with Ni after CF_4/O_2 plasma treatment. Si interfacial layer removed by CF_4/O_2 plasma but reintroduced during Ni evaporation.

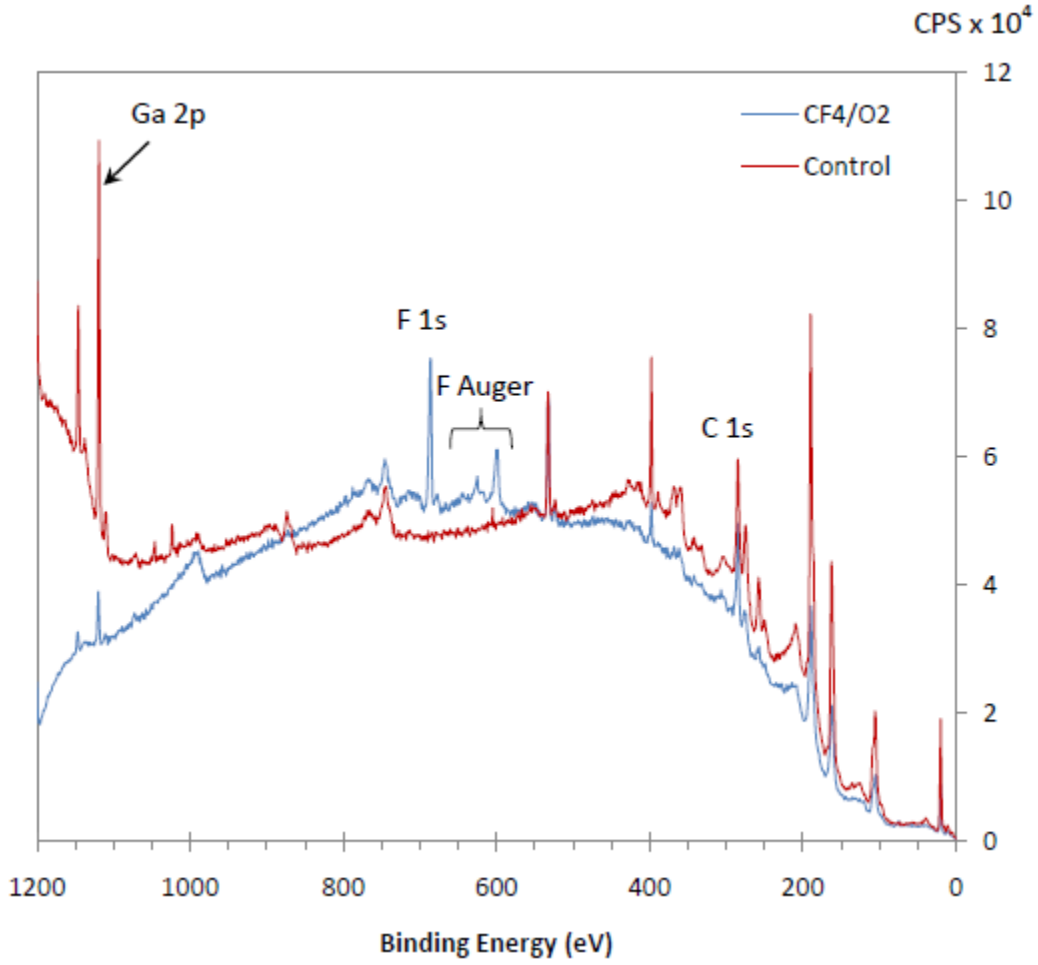


Figure 5.2 XPS analysis of regrowth surface after CF_4/O_2 plasma treatment. Relative ratios of the C 1s to the Ga 2p peaks for the CF_4/O_2 treated versus control surfaces indicated increased carbon in addition to fluorine contamination.

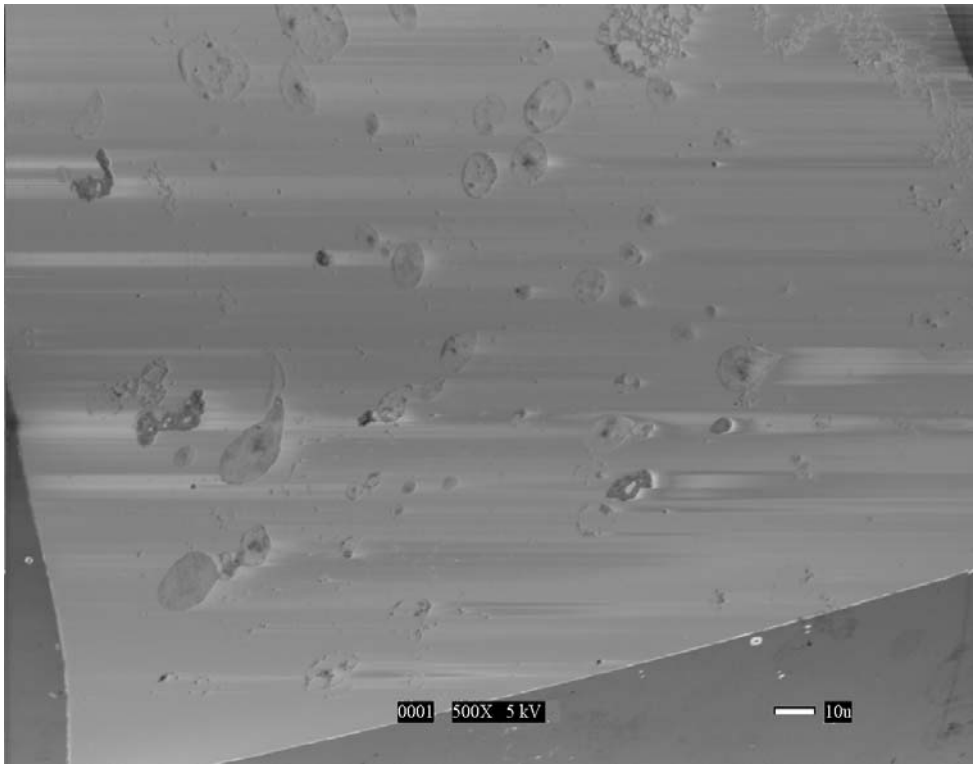


Figure 5.3 SEM micrograph of semi-insulating bulk GaN substrate after photo-assisted etching. Localized etching may be the result of domains across the crystal surface.

6. POISSON SOLVER CALCULATIONS

6.1 Heterostructures with and without Si-doping

A heterostructure design consisting of a 15 nm n-$Al_{0.25}Ga_{0.75}N$ barrier ([Si]: 1 x 10^{18} cm^{-3}) separated from the not-intentionally doped (n.i.d.) 2 μm thick GaN buffer by a 5 nm n.i.d. $Al_{0.25}Ga_{0.75}N$ spacer was compared to one with a 20 nm n.i.d. $Al_{0.25}Ga_{0.75}N$ barrier (see Fig. 6.1 and Fig.6.2). The thick n.i.d. GaN buffer is intended to delocalize the $Al_{0.25}Ga_{0.75}N$ barrier from the bulk GaN substrate. Theoretically, all of the 2DEG charge should be the result of polarization charges due to $P_{SP} + P_{PE}$. The difference in the 2DEG sheet charge between these two heterostructures is indicative of the contribution of electrons from the ionized Si donors.

6.1.1 Poisson solutions for AlGaN/GaN heterostructures

A freeware Poisson solver [1,2] was used to determine the subband energies, or electron eigenvalues, by solving the one-dimensional Schrodinger equation

$$\frac{-h^2}{2}\frac{d}{dz}\left(\frac{1}{m_c}\frac{d\Psi(z)}{dz}\right)+(V(z)+\Delta E(z))\Psi(z)=E\Psi(z) \tag{6.1}$$

and the Poisson equation

$$\frac{dD(z)}{dz}=\frac{d}{dz}(-\varepsilon(z)\frac{dV(z)}{dz}+P(z))=\rho(z) \tag{6.2}$$

where Ψ is the electron wave function, $\Delta E(z)$ is the conduction band offset, $V(z)$ is the electrostatic potential, $D(z)$ is the electric displacement, $P(z)$ is the total polarization, $\varepsilon(z)$ is the dielectric constant, $m_e(z)$ is the effective electron mass and $\rho(z)$ is the charge density.

This program uses the method of finite differences to find the one-dimensional band diagram of the semiconductor. It uses a Schottky barrier, in this case, 1.4 eV, as a boundary condition for the surface. All silicon donors are considered to be fully ionized. The calculations were performed under a no applied bias condition. It is important to note that all simulations contained a 45 Å silicon spike at the n.i.d. GaN epitaxy/bulk GaN interface. A 50 Å GaN layer is added to the heterostructure surface to ensure sufficient confinement at the edge of the Schrodinger mesh and is necessary for solution convergence.

The energy band diagram for the heterostructure of Fig. 6.1 is shown in Fig. 6.3 along with the eigenwavefunctions in the first 1000 Å in where the Schrodinger solution is performed. The confinement of electrons in the triangular well that falls below the Fermi level is confirmed by the presence of the subbands 1 and 2. The simulated energy band diagram is very similar for the heterostructure of Fig. 6.2. The structure sheet resistances and subband energies generated for each of these heterostructures are summarized in Table 6.1. Interestingly, the structure sheet resistances calculated for both the doped and undoped $Al_{0.25}Ga_{0.75}N$ barrier were twice that of our experimental results. This finding suggests an increased carrier contribution from a source other than the 2DEG channel.

The calculated sheet charge density for the Si-doped $Al_{0.25}Ga_{0.75}N$ barrier is 1.02×10^{13} cm^{-2} while that for the undoped $Al_{0.25}Ga_{0.75}N$ barrier heterostructure is 9.54×10^{12} cm^{-2} . The sheet charge density attributable to the electron contribution from ionized silicon donors is only 6.76×10^{11} cm^{-2}. These simulations are entirely consistent with our experimental data for heterostructures grown on n.i.d. GaN buffers $\geq$ 0.75 μm. In our experiments, the excess carrier concentration was twice the simulated contribution from

ionized silicon donors. The simulation showed an electron sheet density at the epitaxy/bulk interface of 2.41 x 10^{12} cm^{-2} for both heterostructures. We surmised a contribution four times that from our experimental data for doped $Al_{0.25}Ga_{0.75}N$ barriers grown on n.i.d. GaN buffers < 0.75 μm. The carriers were completely depleted at the surface, consistent with the mechanism of 2DEG channel population. Sheet density of the undoped $Al_{0.25}Ga_{0.75}N$ barrier portion of each heterostructure was slightly higher in the doped barrier due the band bending necessary to maintain a constant Fermi level.

6.2 Heterostructures with Mg-doping

A heterostructure containing a Mg-doped GaN layer intended to compensate the silicon spike ([Si] = 7x10^{18} cm^{-3}) at the bulk GaN/epitaxy interface was designed. Starting at the semi-insulating bulk GaN surface, 300 nm of p-GaN ([Mg]=3x10^{19} cm^{-3}), followed by 200 nm of n.i.d. GaN followed by 20 nm of undoped $Al_{0.25}Ga_{0.75}N$. The heterostructure is depicted in Fig. 6.4(a). Since p-n junctions were formed at the n.i.d.-GaN/p-GaN interface as well as the p-GaN/Si-spike at the bulk GaN surface, the depletion widths at the n^-/p^- and the p^-/n^+ junctions respectively were calculated as follows [3]. For a p-n junction where the n-type carriers, n^-, $N_d = 5x10^{16} cm^{-3}$ donor atoms and p-GaN ([Mg]=3x10^{19}) cm^{-3} p-type carriers, p^-, $N_a = 3x10^{17} cm^{-3}$ acceptor sites based on 1% ionization, and a depletion width, W_0, the built-in potential, V_0 is given by the following equation,

$$V_0 = \left(\frac{kT}{e}\right)\ln\left(\frac{N_d N_a}{n_i^2}\right) \tag{6.3}$$

where $\frac{kT}{e} = 0.0259$ volts and the intrinsic carrier concentration, n_i is given by,

$$n_i = \sqrt{N_c N_v} e^{E_g/kT} \tag{6.4}$$

where effective density of states in the conduction band, N_c for wurtzite GaN [4] is

$$N_c = 2.3x10^{14} T^{3/2} \tag{6.5}$$

and the effective density of states in the valence band, N_v for wurzite GaN [4] is

$$N_v = 8.9x10^{15} T^{3/2} \tag{6.6}$$

which yields $N_c = 1.2x10^{18} cm^{-3}$, $N_v = 4.62x10^{19} cm^{-3}$ and $n_i = 2.32x10^{-10} cm^{-3}$ resulting in $V_0 = 3.187$ volts. Consequently, $W_0 = W_n = 0.25\mu m$, meaning that the depletion region extends 2500 Å into the n^- region. Hence, the 200 nm n.i.d. GaN is fully depleted of carriers. Since the amount of charge, Q, on both sides of the metallurgical junction must be the same so that overall junction charge is neutral as given by,

$$Q = eN_a W_p = eN_d W_n \tag{6.7}$$

then the depletion width on the p-side, W_p , is given as,

$$W_p = \frac{N_d W_n}{N_a} \tag{6.8}$$

leading to a depletion region extending 417 Å into the p^- side of the n^-/p^- junction. Similarly, for the p^-/n^+ junction, where $N_d = 7x10^{18} cm^{-3}$ and $N_a = 3x10^{17} cm^{-3}$ ionized acceptors, then $W_p = 104.3$ nm. Hence, the depletion region extends 1043 Å into the p^- side of the junction. And consistent with previous calculations, the depletion width on the n^+ side is,

$$W_n = \frac{N_a W_p}{N_d} \tag{6.9}$$

resulting in a 45 Å depletion width on the n^+ side meaning the entire Si spike region is fully depleted.

Because semi-insulating nonpolar bulk GaN substrates are currently unavailable, n-type nonpolar substrates were used to compare 2 DEG sheet density and mobility of heterostructures grown on polar substrates as illustrated in Fig. 6.2(b). When an n-type substrate ([Si]=2.5x10^{18} cm^{-3}) was used, $V_0 = 3.289$ volts, $W_p = 103.9$ nm and $W_n = 125$ Å.

In order to determine the energy levels of the conduction band, E_C, and the valence band, E_V, the following methodology [5] was employed. For the n.i.d. GaN layer, silicon gives n-type doping with $N_d = 5x10^{16} cm^{-3}$ and since $N_d \gg n_i$, $n = N_d = 5x10^{16} cm^{-3}$. For intrinsic GaN,

$$n_i = N_c \exp\left[-\frac{\left(E_c - E_{F_i}\right)}{kT}\right] \tag{6.10}$$

whereas for unintentionally-doped GaN,

$$n = N_c \exp\left[-\frac{(E_c - E_{F_n})}{kT}\right] = N_d \tag{6.11}$$

where E_{F_i} and E_{F_n} are the Fermi energies for the intrinsic and n-type GaN. By dividing Eq. (6.11) by Eq. (6.10),

$$\frac{N_d}{n_i} = \exp\left[\frac{\left(E_c - E_{F_n}\right)}{kT}\right] \tag{6.12}$$

and

$$E_{F_n} - E_{F_i} = kT \cdot \ln\left(\frac{N_d}{n_i}\right) \tag{6.13}$$

and $E_{F_n} - E_{F_i} = 1.57\,\text{eV}$.

When the semiconductor is further doped with Mg, the acceptor concentration, assuming 1% ionization, is $N_a = 3x10^{17} cm^{-3}$ and $N_d = 5x10^{16} cm^{-3}$. The semiconductor is compensation-doped resulting in p-type GaN. Thus

$$p = N_a - N_d = (3x10^{17} - 5x10^{16}) = 2.5x10^{17} cm^{-3} \tag{6.14}$$

For intrinsic GaN,

$$n_i = N_v \exp\left[-\frac{(E_{Fi} - E_v)}{kT}\right] \tag{6.15}$$

whereas for doped GaN,

$$p = N_v \exp\left[-\frac{\left(E_{F_p} - E_v\right)}{kT}\right] = N_a - N_d \tag{6.16}$$

where E_{F_i} and E_{F_p} are the Fermi energies in the intrinsic and p-type GaN respectively. Dividing Eq. (6.16) by Eq. (6.15),

$$\frac{p}{n_i} = \exp\left[-\frac{(E_{F_p} - E_{F_i})}{kT}\right] \tag{6.17}$$

and from,

$$E_{F_p} - E_{F_i} = -kT \cdot \ln\left(\frac{p}{n_i}\right) \tag{6.18}$$

and $E_{F_p} - E_{F_i} = -1.62\,\text{eV}$. For $E_g = 3.4\,\text{eV}$, E_{F_i} =1.7 eV and $E_{F_n} = (E_{F_n} - E_{F_i}) + E_{F_i} = 3.27$ eV and $E_c - E_{F_n} = 0.13\,\text{eV}$ and for $E_{F_p} = E_{F_i} - (E_{F_p} - E_{F_i}) = 0.08$.

For the bulk GaN/epitaxial interface, $N_d = 7x10^{18} cm^{-3}$ and if the n-GaN is compensated by the atomic Mg species where $N_a = 3x10^{19} cm^{-3}$, then

$$p = N_a - N_d = 2.3x10^{19} \tag{6.19}$$

and from Eq.(6.18), $E_{F_p} - E_{F_i} = -1.7\,\text{eV}$. And for $n = N_d - n_i = 7x10^{18} cm^{-3}$, then by Eq. (6.13), $E_{F_n} - E_{F_i} = 1.7\,\text{eV}$. The calculated bandgap energies and depletion widths for the Mg-doped heterostructure depicted in Fig. 6.4 are shown in Fig. 6.5.

6.2.1 Poisson solutions for Mg-doped heterostructures

The Poisson solver was used to calculate subband energies for the heterostructure of Fig. 6.4. Again, a Schottky barrier of 1.4 eV, was used as a boundary condition for the surface. All silicon donors are considered to be fully ionized. However, the ionization of Mg acceptors was 1%. Again, calculations were performed under a no applied bias condition. The simulations contained a 45 Å silicon spike at the n.i.d. GaN epitaxy/bulk GaN interface. A 50 Å GaN layer is added to the heterostructure surface to ensure sufficient confinement at the edge of the Schrodinger mesh and is necessary for solution convergence. When the Mg acceptor concentration of 3 x 10^{17} cm^{-3} was used for the layer thicknesses given in Fig. 6.4, a triangular potential lying below the Fermi level was not formed. The reason is believed to be that the high acceptor concentration in the 3000 Å p-GaN layer

caused carrier depletion within the entire 2000 Å n.i.d.-GaN layer. That carrier depletion necessitated a considerable band bending in the n.i.d. GaN layer to maintain a constant Fermi level across the n^-/p-junction. When the Mg acceptor concentration was reduced to 1 x 10^{17} cm^{-3} the triangular potential well returned as a solution in the energy band diagram. Figure 6.6 is a graphic representation of the behavior seen in the Mg-doped heterostructures. Ionized acceptor concentrations exceeding 1 x 10^{17} cm^{-3}, result in a precipitous drop in 2DEG sheet density. Additionally, the upper limit of 2DEG sheet density for these Mg-doped heterostructures was ~ 7.7 x 10^{12} cm^{-2}.

When we view the simulation data for the Mg-doped heterostructure for different ionized acceptor concentrations, it is clear that an ionized acceptor concentration of 2 x 10^{17} cm^{-3} is sufficient to compensate the donors at the Si spike interface. But in doing so, the n-type carriers in the 2000 Å n.i.d. GaN layer are depleted; thus there can be no electron confinement in the potential well. However electron confinement in the potential well can be achieved with an ionized acceptor concentration of 1 x 10^{17} cm^{-3}, but that ionized acceptor concentration is insufficient for compensation of donors at the bulk/epitaxy interface. As shown in Table 6.2, the 3000 Å p-GaN layer has n-type carriers (7.8 x 10^{11} cm^{-2}) on the order of that seen for surface states. At 3 x 10^{15} cm^{-3} the n-type sheet density in the 3000 Å p-GaN is only an order of magnitude less than that at the $Al_{0.25}Ga_{0.75}N$ barrier/ n.i.d.GaN 2DEG interface. In other words, in addition to the sheet density confined within 50 - 100 Å of the interface, there is a large contribution of electrons from the 3000 Å p-GaN layer. One would expect erroneously high sheet charge densities and coincidently low mobilities because unlike the spatial separation of carriers expected at the $Al_{0.25}Ga_{0.75}N$/ GaN interface for the

design of Figs. 6.1 and 6.2, the mobile carriers from the 3000 Å p-GaN layer of the design of Fig. 6.4(a) can act as scattering centers.

We also calculated the sheet resistance, sheet density and electron eigenvalues expected for the heterostructure design of Fig. 6.4(c) as shown in Table 6.2. There is one caveat though; there is no spontaneous polarization term for the nonpolar heterostructure. However, the values listed in the tabular data are based on the same materials parameters used for the polar heterostructures. Growth of these nonpolar structures and van der Pauw Hall measurement of their 2DEG transport properties will enable us to separate ionized donor contributions from spontaneous polarization contributions.

6.3 References

[1] G. L. Snider, I.-H. Tan, and E.L. Hu, *J. App. Phys.*, **68** (1990) 2849.

[2] I.-H. Tan, G.L. Snider, and E.L. Hu, *J. App. Phys.*, **68** (1990) 4071.

[3] S.O. Kasap, *Principles of Electronic Materials and Devices* (McGraw Hill, New York, NY, 2006), 480.

[4] http://www.ioffe.run/SVA/NSM/Semicond/GaN/bandstr.html

[5] S.O. Kasap, *Principles of Electronic Materials and Devices* (McGraw Hill, New York, NY, 2006), 394.

6.4 Tables

Table 6.1 Calculated sheet resistances, layer sheet densities and electron eigenvalues for $Al_{0.25}Ga_{0.75}N$/GaN heterostructures with n- $Al_{0.25}Ga_{0.75}N$ and with n.i.d. $Al_{0.25}Ga_{0.75}N$ barriers.

Solutions for Heterostructure of:	***Fig. 6.1***	***Fig.6.2***
Sheet Resistance (Ω/square)	1228	1299
50 Å GaN sheet density, $n_{s,\ cm^{-2}}$	3.436E-13	3.419E-13
150 Å n-AlGaN sheet density, $n_{s,\ cm^{-2}}$	1.020E+03	NA
50 Å u.i.d. AlGaN sheet density, $n_{s,\ cm^{-2}}$	7.556E+10	NA
200 Å u.i.d. AlGaN sheet density, $n_{s,\ cm^{-2}}$	NA	6.276E+10
2000 Å u.i.d. GaN sheet density, $n_{s,\ cm^{-2}}$	1.022E+13	9.544E+12
45 Å n-GaN sheet density, $n_{s,\ cm^{-2}}$	2.407E+12	2.407E+12
Electron eigenvalue 1 (eV)	-8.524E-02	-7.772E-02
Electron eigenvalue 2 (eV)	1.747E-02	2.011E-02
Electron eigenvalue 3 (eV)	5.492E-02	5.621E-02
Electron eigenvalue 4 (eV)	7.424E-02	7.501E-02
Electron eigenvalue 5 (eV)	8.557E-02	8.604E-02
Electron eigenvalue 6 (eV)	9.237E-02	9.265E-02
Electron eigenvalue 7 (eV)	9.614E-02	9.627E-02

Table 6.2 Calculated sheet resistances, layer sheet densities and electron eigenvalues for $Al_{0.25}Ga_{0.75}N$/GaN/Mg-doped GaN compensation layer heterostructures with n.i.d. $Al_{0.25}Ga_{0.75}N$ and with n-$Al_{0.25}Ga_{0.75}N$ barriers.

Solutions for Heterostructure of:	***Fig. 6.4(a)***	***Fig.6.4(c)***
Sheet Resistance (Ω/square)	1428	1374
50 Å GaN sheet density, $n_{s,cm^{-2}}$	3.419E-13	3.419E-13
150 Å n-AlGaN sheet density, $n_{s,cm^{-2}}$	NA	7.172E+02
50 Å n.i.d. AlGaN sheet density, $n_{s,cm^{-2}}$	NA	7.087E+10
200 Å n.i.d. AlGaN sheet density, $n_{s,cm^{-2}}$	6.319E+10	NA
2000 Å n.i.d. GaN sheet density, $n_{s,cm^{-2}}$	7.705E+12	8.123E+12
3000 Å n.i.d. GaN sheet density, $n_{s,cm^{-2}}$	7.794E+11	7.794E+11
45 Å n-GaN sheet density, $n_{s,cm^{-2}}$	2.380E+12	2.380E+12
Electron eigenvalue 1 (eV)	-7.719E-02	-8.184E-02
Electron eigenvalue 2 (eV)	2.189E-02	2.019E-02
Electron eigenvalue 3 (eV)	6.089E-02	5.997E-02
Electron eigenvalue 4 (eV)	8.388E-02	8.325E-02
Electron eigenvalue 5 (eV)	1.000E-01	9.959E-02
Electron eigenvalue 6 (eV)	1.125E-01	1.121E-01
Electron eigenvalue 7 (eV)	1.227E-01	1.224E-01

6.5 Figures

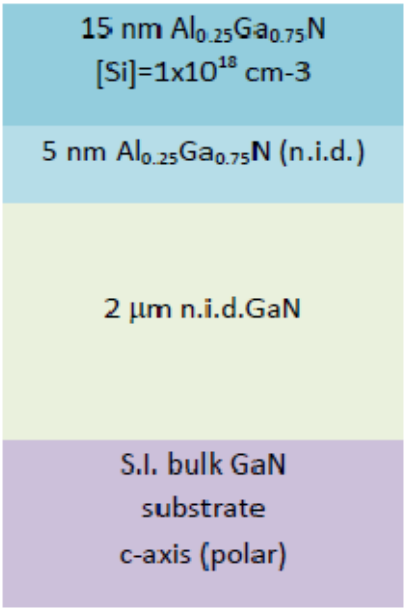


Figure 6.1 Schematic of heterostructure with 15 nm Si-doped $Al_{0.25}Ga_{0.75}N$ barrier, 5 nm n.i.d. $Al_{0.25}Ga_{0.75}N$ spacer and 2 µm n.i.d. GaN buffer.



Figure 6.2 Schematic of heterostructure with 20 nm n.i.d. $Al_{0.25}Ga_{0.75}N$ barrier and 2 µm n.i.d. GaN buffer.

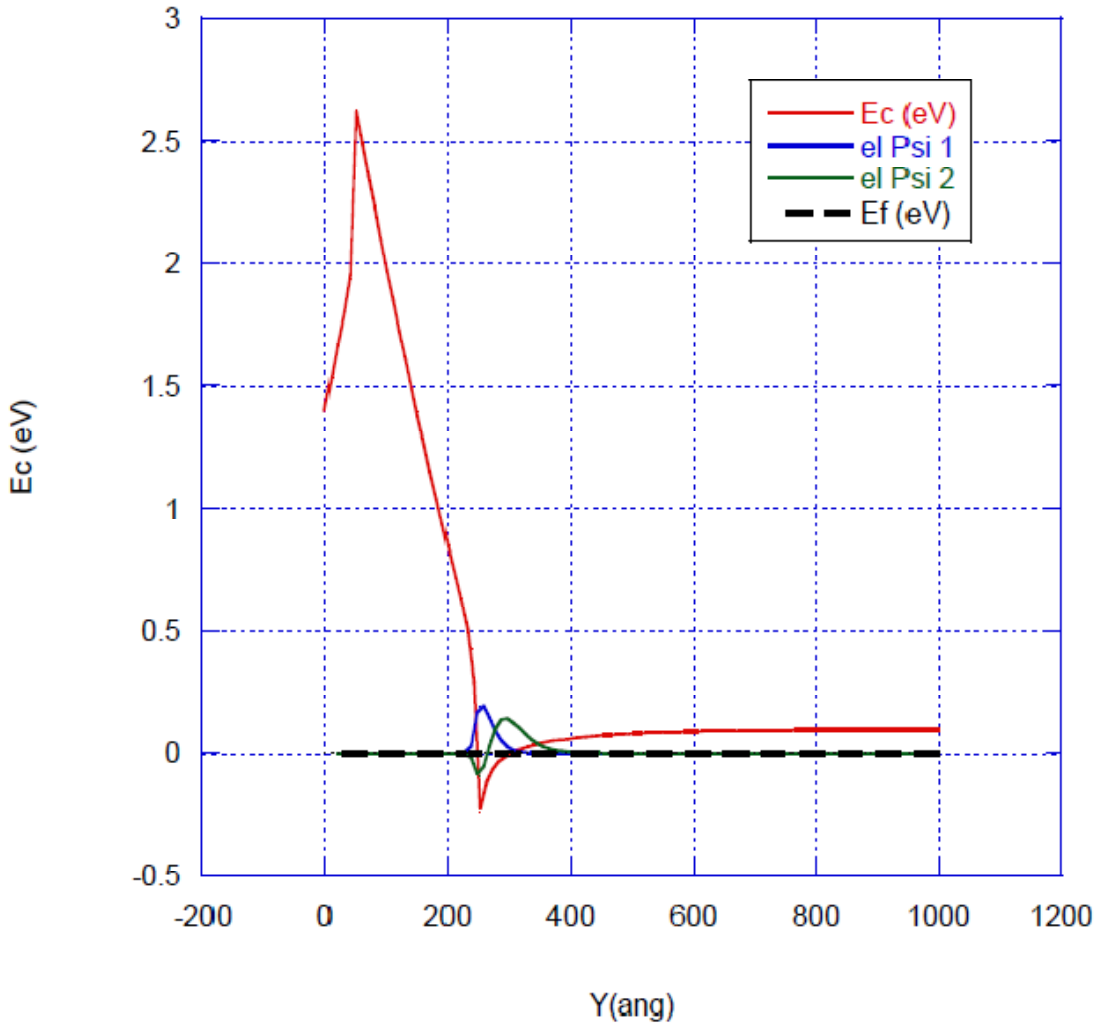


Figure 6.3 Band diagram with eigenwavefunctions for heterostructure of Fig. 6.1.

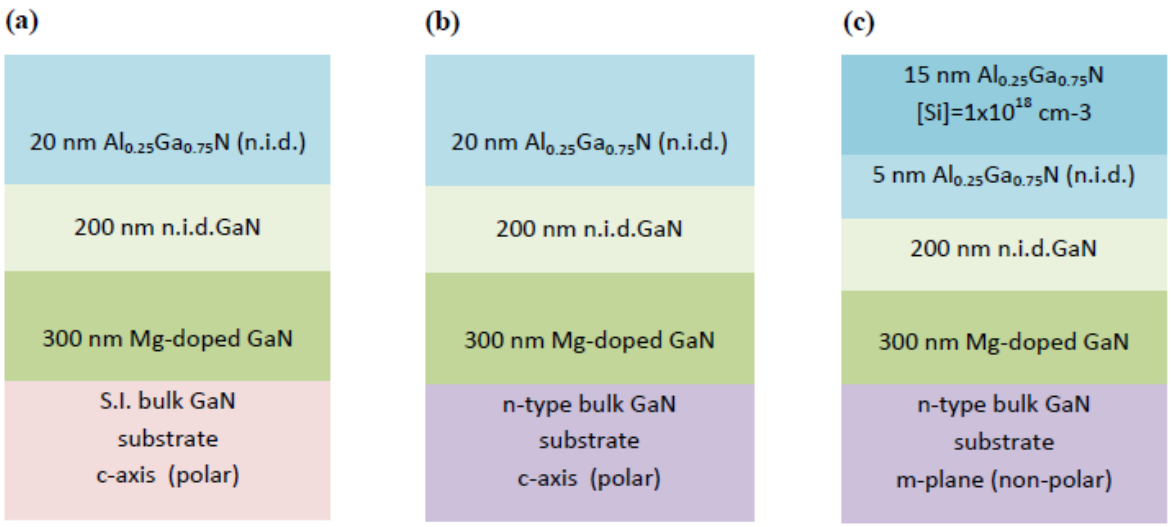


Figure 6.4 Schematic of Mg-doped heterostructure growth (a) on S.I. c-axis bulk GaN (b) on n-type c-axis bulk GaN (c) on n-type m-plane bulk GaN substrate.

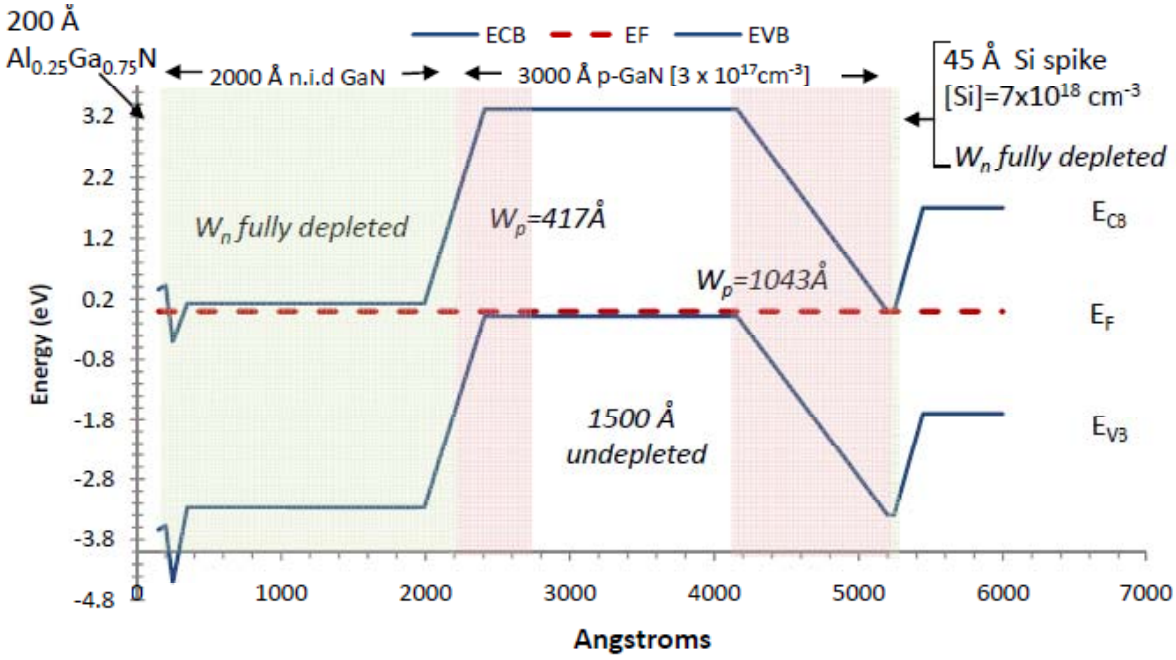


Figure 6.5 Energy band diagram for Mg-doped heterostructure of Fig. 6.4(a). Depletion widths are marked at the n^-/p^- interface between the 2000 Å n.i.d. GaN and the 3000 Å p-GaN layer and the p^-/n^+ interface created by the Mg-doped GaN layer and the Si spike at the bulk GaN interface.

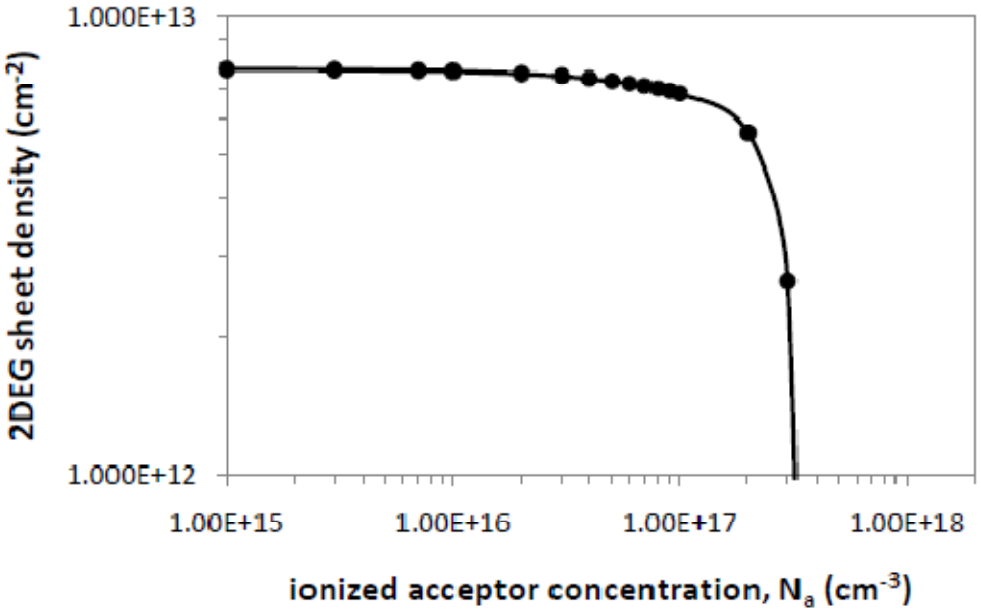


Figure 6.6 2DEG sheet density behavior as a function of ionized acceptor concentration shows that Mg acceptor concentrations exceeding 1×10^{17} cm^{-3} result in a precipitous drop in sheet density. The upper limit of sheet density for Mg-doped structures is ~7.7×10^{12} cm^{-2}.

7. PHYSICAL PROPERTIES OF AlGaN/GaN HETERO-STRUCTURES GROWN ON VICINAL SUBSTRATES

J.A. Grenko, C.L. Reynolds, Jr., D.W. Barlage, and M.A.L. Johnson
Department of Materials Science and Engineering
North Carolina State University, Box 7919, Raleigh, NC 27695

G. J. Duscher
Department of Materials Science and Engineering
University of Tennessee, Knoxville, TN

S. E. Lappi
Department of Chemistry
North Carolina State University, Raleigh, NC 27695

C.W. Ebert
Veeco Turbodisc, 392 Elizabeth Avenue, Sommerset NJ 08873

E.A. Preble, T. Paskova, K.R. Evans
Kyma Technologies, 8829 Midway West Road, Raleigh, NC 27617

7.1 Abstract

We report on the growth of $Al_{0.25}Ga_{0.75}N$/GaN heterostructures grown on low dislocation density vicinal surfaces of semi-insulating c-axis GaN substrates. AFM, PL, CL, HRXRD, SIMS, Hall and Raman spectroscopy have been used to assess structural and electrical properties as a function of offcut. Bulk GaN substrates with vicinal offcut between 0.5^o and 1.8^o may be optimal with respect to surface roughness and dopant incorporation. Raman spectroscopy has been correlated to AFM, PL and CL to show decreasing Mg incorporation with increasing offcut. HRXRD analysis shows decreasing dislocation density with increasing offcut angle. Raman spectroscopy has been used to explain the high sheet carrier densities and low mobilities measured for the heterostructures grown in this experiment were the result of nitrogen vacancy formation after an ex situ anneal leading to self-compensation in p-GaN films and an n-type conductive layer in the undepleted region of the p-GaN layer.

7.2 Introduction

Gallium Nitride and the III-N alloy semiconductors are of great promise due to their applicability in both short wavelength LEDs and laser diodes [1] and high-power, high frequency electronic devices such as heterostructure field effect transistors (HFET) [2]. Growth of these devices on native GaN substrates with low dislocation densities, ρ_D, on the order of 10^6 cm^{-2}, should reduce the threading dislocation density in the epilayers, which can limit HFET mobilities [3, 4]. In addition to improved mobility, devices grown on low dislocation bulk GaN substrates should offer improved power performance by realizing

higher substrate thermal conductivities, *K* [5]. However, wide availability of bulk GaN substrates is currently limited, which has led to use of foreign substrates, mostly sapphire and SiC. It is the substantial in-plane lattice mismatch between the GaN film and the non-native substrate that generates a highly resistive nucleation layer that contributes to lower than expected *K* and high ρ_D [6]. Furthermore, since the substrate/epitaxy interfaces for homoepitaxial GaN structures are nearly strain-free, another source of reliability loss and backgating in HFET structures [7] is potentially eliminated.

To obtain high performance in AlGaN/GaN HFET devices, it is necessary to improve the surface morphology and electrical properties. The use of vicinal substrates has been known to be an effective method to obtain improved surface morphology and decreased dislocation density. Surface morphologies of GaN and AlN layers transform from spiral mounds to evenly spaced steps by using vicinal substrates [8-22] and the full-width at half-maximum (FWHM) of high resolution X-ray diffraction (HRXRD) for GaN and AlN layers decreases with increasing vicinal angle [14,17,21]. In this paper, we report an investigation on the effect of substrate offcut angle on structural, luminescent, and electrical properties of homoepitaxially grown AlGaN/GaN HFET structures grown by organometallic vapor phase epitaxy on vicinal bulk GaN substrates. The offcut angles for substrates used in this study ranged from 0.3^o to 1.7^o off [0001] toward $[10\bar{1}0]$ and 1.8^o off [0001] toward $[11\bar{2}0]$. Atomic force microscopy, AFM, was employed to assess the presence of more steps and ledges for adatom attachment with increasing offcut angle. High resolution XRD around the symmetric (002) and asymmetric (105) reflections provided a means to assess dislocation

density as a function of offcut angle. Van der Pauw Hall measurements of sheet density and room and low temperature mobility were obtained and will be discussed.

It is well-known that dopant incorporation and activation in III-V semiconductors are dependent on the substrate orientation, which is related to the atomic species and bonding in the lattice. It was observed that the net S and Si donor concentrations were greater on the B surface while the net Zn acceptor concentration was less on the B face than on the A one [23]. In InP, the incorporation of Fe and Si on different crystal orientations has revealed species competition for the substitutional In lattice site with the Si atom being the preferred species [24]. More importantly, the understanding that Fermi level pinning controls species activation emphasizes the need to understand the role of vicinal surfaces. Since these heterostructures included a magnesium-doped GaN layer in addition to a not-intentionally doped GaN layer, room temperature photoluminescence (PL) and cathodoluminescence (CL) were used to track the magnesium incorporation as a function of vicinal offcut angle in agreement with that measured by secondary electron microscopy (SIMS). Raman spectroscopy measurements on all heterostructures grown were correlated with the aforementioned characterization techniques to substantiate our conclusions about the growth of AlGaN/GaN heterostructures on vicinal surfaces of bulk GaN (0001) substrates. Raman spectroscopy is shown to correlate well with luminescent and Hall data and to enable us to achieve an understanding of the behavior of these heterostructures grown on vicinal substrates. Biaxial strain analysis by means of Raman spectral lines is explored and identification of local vibration modes provides a mechanism to explain Hall measurements.

7.3 Experimental Procedure

The AlGaN/GaN heterostructures in this study were grown by organometallic vapor phase epitaxy (OMVPE) in a vertical reactor at 1040°C and 60 torr on 330 μm thick, semi-insulating bulk GaN substrates with H_2 as the carrier gas. Fe-doped, c-axis GaN substrates were grown in a conventional vertical hydride vapor phase epitaxy (HVPE) reactor at a growth rate of approximately 100 μm/hr. The cleaved 10 mm x 10 mm substrates were chemical-mechanically polished to incorporate vicinal offcuts of 0.3°, 0.4°, 0.5°, 0.7°, 1.4°, and 1.7° from the c-axis toward $<10\bar{1}0>$ and of 1.8° from the c-axis toward $<11\bar{2}0>$. Atomic force microscopy measurements of these as-received substrates revealed a root mean surface (RMS) roughness ranging from 0.45 to 1.7 nm for multiple scans of a 10 x 10 μm^2 area.

Capacitance-voltage (CV) measurements (Fig. 7.1) indicated that the free carrier concentration in the semi-insulating GaN substrate was $5x10^{13}$ cm^{-3}. The same CV measurements showed a free carrier concentration $>10^{18}$ cm^{-3} in the first 20 nm of the substrate (see also [25, 26]). Secondary ion mass spectroscopy (SIMS) measurements of AlGaN/GaN heterostructures on representative semi-insulating bulk GaN substrates (Fig. 7.2) confirmed the atomic silicon concentration ([Si]) to be $>10^{19}$ cm^{-3} at the bulk GaN/epitaxial interface. Areal silicon concentration ($[Si]_{areal}$) at the bulk GaN/epitaxial interface was determined to be $1.6x10^{14}$ cm^{-2}. The interfacial Si enables substantial buffer leakage, which potentially limits use of heterostructures on these substrates for electronic devices unless the influence of the interfacial charge can be negated.

Figure 7.3(a) shows a schematic of the structure grown in a two-step process. The growth interrupt after the Mg-doped layer was performed to mitigate any Mg memory effect [22, 27]. From the substrate, the heterostructures consisted of a 300 nm Mg-doped GaN layer, [Mg] = 3 x 10^{19} cm^{-3}, followed by 200 nm not-intentionally doped (n.i.d.) GaN buffer layer, and 20 nm n.i.d. $Al_{0.25}Ga_{0.75}N$ barrier. An in situ nitrogen anneal at 800^{o}C was performed after the Mg-doped GaN layer was grown to dissociate the hydrogen from the Mg acceptors. Atomic force microscopy (AFM) measurements were taken to assess surface roughness attributed to the Mg-doped GaN. The MOVPE reactor and substrate holder were baked at 1100^{o}C to remove residual Mg prior to subsequent growth of the remaining layers. The substrate was reloaded and the GaN buffer and $Al_{0.25}Ga_{0.75}N$ barrier were then grown. AFM measurements were repeated to monitor surface roughness changes. The heterostructure grown on the 0.7^{o} offcut substrate, (see Fig. 7.3(b)), was accomplished in a one-step growth process, that is, without an interrupt after the Mg-doped layer. It included a thicker, 1.5 μm n.i.d. GaN layer to reduce the background [Mg] by 2 orders of magnitude prior to growth of the $Al_xGa_{1-x}N$ barrier layer. AFM measurements for this heterostructure were obtained after the completion of the $Al_xGa_{1-x}N$ barrier layer.

Heterostructures were analyzed using a Philips X'Pert PRO MRD HR diffraction system (HRXRD) equipped with a CuKα source for X-ray generation and rocking curve plus triple axis optics on the diffracted beam side and a five movement motorized cradle. High resolution rocking curves of the (002) and the (105) reflections were used to generate alloy composition and thickness data. Reciprocal space maps of the asymmetric (105) reflection were obtained by setting the 2θ angle and then performing a continuous $2\theta-\omega$ scan as the

specimen was rotated in incremental ω steps to generate a square grid in reciprocal space. Unpolarized, local Raman measurements were performed using an Horiba Jobin Yvon LabRam ARAMIS. Room temperature measurements were made by focusing a 632 nm laser beam to a 1 mm spot on a sample and detecting the back-scattered light. An 1800 nm grating was used for measurements taken between 0 – 4000 cm^{-1} and a 1200 nm grating was used for the 4000 – 7000 cm^{-1} range. Cathodoluminescence (CL) measurements were acquired with an Oxford MonoCL unit attached to a JEOL JSM 6400 SEM at an accelerating voltage was 5 kV. Light was collected by an elliptical mirror and fiber-optically transferred through 5μm slits to a monochromator and detected with a photomultiplier tube (PMT). Room temperature (RT) photoluminescence (PL) was also performed using a HeCd laser (325 nm) with an excitation intensity of 2.5 W/cm^2 at the sample surface, analyzed by a double monochromator with a spectral resolution of 1-2 meV, and detected by a lock-in amplifier. After completion of optical measurements, Ni/Au contacts were evaporated on the surfaces that had been patterned with Hall test pads. Each sample was annealed in a nitrogen ambient rapid thermal annealing system for 10 minutes at 800^oC to achieve ohmic contact to the semiconductor. Van der Pauw Hall measurements were made on an HMS-3000 Ecopia Hall Effect Measurement system using a 0.55 Tesla permanent magnet. Raman measurements were repeated to assess shifts in vibration frequency introduced by this ex situ anneal. Concentration depth profiles for Si, Mg, and Fe were obtained by secondary ion mass spectroscopy (SIMS) using an O^{2+} primary ion beam. Transmission electron microscopy measurements were acquired with a VG603 microscope equipped with a Nion aberration

correcting lens at 300 kV to inspect the crystalline lattice for presence of stacking faults and dislocations.

7.4 Results and Discussion

7.4.1 AFM

Measurements of vicinal substrates after the 300 nm p-GaN growth showed that RMS surface roughness increased significantly for the lowest offcut angle (0.3^o, 0.4^o) substrates but decreased significantly for the highest offcut angle (1.7^o, 1.8^o) substrates. AFM roughness for scans of 10 x 10 μm^2 areas increased by 1 to 2 nm from measurements prior to growth for low offcut substrates as shown in Fig. 7.4(a) while they decreased by 0.5 to 1 nm for high offcuts. There was little change in roughness for layers grown on vicinal substrates with offcuts of 0.5^o and 1.4^o. The uninterrupted growth of the heterostructure on the 0.7^o offcut substrate prohibited direct measurement after p-GaN growth, therefore measurements reflect the RMS roughness after $Al_xGa_{1-x}N$ barrier growth. Comparable AFM measurements for all other vicinal substrates, taken after the n.i.d. GaN buffer and AlGaN barrier were grown (Fig. 7.4(b)) revealed that film roughness decreased relative to their post p-GaN measurement. AFM images of 5 x 5 μm^2 areas of the complete heterostructure grown on the 0.3^o and 0.4^o offcut substrates, as shown in Fig. 7.5(a), revealed coalescence of islands while faint terracing was observed on the 0.5^o and 0.7^o offcut substrates. Distinct terracing is shown in Fig. 7.5(b) for the heterostructures grown on the 1.4^o offcut substrate. Pits observed in the AFM image originate from threading dislocations while discontinuities in the terraces are edge dislocation terminations. The 1.7^o and 1.8^o offcut substrates are compared

in Fig. 7.5(c) and (d) to accentuate the similarity of the morphologies and to concur [28, 29] that offcut direction appears to be less important than the degree of offcut. Fig. 7.6 summarizes the AFM roughness trends observed as a function of vicinal offcut. The low AFM RMS roughness values determined for all vicinal substrates study is consistent with the absence of step bunching [28] previously reported for Mg-doped films [29] on vicinal bulk GaN substrates. The higher RMS roughness values for the lowest offcut (0.3^o, 0.4^o) substrates suggests an increased Mg incorporation relative to the substrates with offcut angles $\geq 0.5^o$, which is confirmed by SIMS measurements discussed below.

7.4.2 HRXRD

The lattice constant c of GaN was determined for each vicinal substrate from the 2θ substrate peak of the symmetric (0002) $\omega-2\theta$ diffraction measurements after heterostructure growth. The value, $c = 5.188 \pm 0.002$ Å, is in excellent agreement with the theoretical $c_o = 5.1856 +/- 0.0001$ Å [3]. The lattice constant a of GaN was determined from $\omega-2\theta$ diffraction measurement from the asymmetric $(10\bar{1}5)$ diffraction. The value, $a = 3.203 \pm 0.004$ Å is a 0.44% increase from the theoretical value of $a_0 = 3.1879 \pm 0.0003$ Å [30]. The bulk GaN was doped with Fe atoms, at a concentration, [Fe] = 1.5 x10^{18} cm^{-3} by SIMS, to compensate Si atoms incorporated during HVPE growth. The increase in lattice constant cannot be explained by the substitution of Fe, with an atomic radius of 0.124 nm, on a Ga-site because its atomic radius is nearly the same, 0.122 nm. However, substitution of

Mg, with an atomic radius of 0.16 nm, on a Ga-site could explain the augmented lattice parameter.

The (002) $\omega-2\theta$ scan was used to determine the composition of the strained $Al_xGa_{1-x}N$ by determining the $a_{Al_xGa_{1-x}N}$ and $c_{Al_xGa_{1-x}N}$ of the ternary layer, then calculating the elastic stiffness constants and linearly interpolating using [31],

$$\frac{c_{Al_xG_{1-x}N}-c_0}{c_0}=-2\frac{c_{13}}{c_{33}}\frac{a_{Al_xGa_{1-x}N}-a_0}{a_0} \tag{7.1}$$

These compositions in turn were used to simulate the thickness of the $Al_xGa_{1-x}N$ barrier by using an algorithm that inputs composition and initial thickness and tests to a goodness of fit criteria. Fig. 7.7 shows those simulated compositions and thicknesses of the $Al_xGa_{1-x}N$ barrier as a function of vicinal offcut. $Al_xGa_{1-x}N$ barriers grown on lower offcut substrates have a higher Al incorporation rate relative to those on higher offcut substrates. The higher aluminium incorporation is consistent with an effectively lower gallium flux and reduced film thickness based on our earlier studies.

XRD measurements of threading dislocation density give insight about strain fields produced by dislocations giving rise to partial loss of long-range coherence of the crystal lattice and inhomogeneous rotation and dilation of the crystal planes. These distortions of the real-space lattice lead to corresponding broadening of the reciprocal lattice points [32]. The FWHM of the (002) $\omega-2\theta$ symmetric scan was compared with that of the (105) $\omega-2\theta$ asymmetric reflection for each vicinal offcut. Fig. 7.8(a) shows that the out-of-plane variation of the symmetric (002) FWHM, which is a direct measurement of tilt, is approximately constant for all vicinal substrates in this study. However, the FWHM of the

(105) reflection, which is composed of both tilt and twist components, indicates that lower offcut (0.3^o,0.4^o) substrates generate heterostructures, grown according to Fig. 7.3(a), that have higher FWHM; while the FWHM for heterostructures grown on substrates with offcuts $\geq 0.5^o$ is nearly constant. Threading dislocation density D_{dis} was estimated from these FWHM values of the HRXRD profiles. Following the method outlined in reference [21] for one symmetric and one asymmetric reflection, the tilt spread β_{tilt} and the twist spread β_{twist} are expressed by the following equation [33]:

$$\beta_{hkl}^{n} = (\beta_{tilt} \cos\chi)^n + (\beta_{twist} \sin\chi)^n + (2\pi / L)^n / \left|K_{hkl}\right|^n \qquad (7.2)$$

where β_{hkl} is the measured FWHM of (hkl) diffraction, K_{hkl} is the reciprocal lattice vector, χ is the angle between K_{hkl} and the (0001) surface normal, L is the coherence length and n [34] is,

$$n = 1 + (1 - f) \qquad (7.3)$$

where f is the percent Lorentzian character. The individual terms were determined using a pseudo-Voigt (1<n<2) fit of the $\omega - 2\theta$ angles for the (002) and (105) rocking curves. The Lorentzian character was determined for each heterostructure in this study. For f=1, the function exactly matches a Lorentzian (n=1) and for f=0, the function is best described by a Gaussian (n=2). For our data, β_{tilt} and β_{twist} were derived by assuming $L = \infty$. Dislocation density, D_{dis}, was then estimated by the following equations [32,35]:

$$D_{screw} = \beta_{tilt}^2 / 4.36 b_{screw}^2 \qquad (7.4)$$

$$D_{edge} = \beta_{twist}^2 / 4.36 b_{edge}^2 \tag{7.5}$$

$$D_{dis} = D_{screw} + D_{edge} \tag{7.6}$$

where D_{screw} is the screw dislocation density, D_{edge} is the edge dislocation density, and b is the Burgers vector ($b_{screw} = 0.4982$ nm, $b_{edge} = 0.3112$ nm). The FWHM corresponding to tilt, β_{tilt}, has a direct relationship to β_{002} while the β_{twist} is a function of both β_{105} and β_{002}. Figure 7.8(b) graphically displays D_{screw} and D_{edge}. Total dislocation density ranged from 2.1 x 10^7 to 5.5 x 10^6 cm^{-2}. Edge dislocation density for the vicinal substrates studied had a bimodal distribution of 1.8 x 10^7 cm^{-2} for offcut angles $\leq$ 0.5° and 1.8 x 10^6 cm^{-2} for greater offcuts while D_{screw} was constant at 1.82 ± 0.06 x 10^6 cm^{-2} across the entire range. The error incurred by not including the coherence length is < 20% [33, 34]. Panchromatic cathodoluminescence studies revealed the D_{dis} of ~1.2 x 10^7 cm^{-2} for the vicinal substrate with the 0.3° offcut while the 1.4° offcut had D_{dis} of 1 x 10^6 cm^{-2}.

Triple axis scattering enables one to distinguish between regions which are tilted with respect to each other, i.e., subgrains, and those that are strained or mismatched, i.e., ternary layers [36]. Figure 7.9(a) compares the reciprocal space maps for HFET structures grown on the 0.3° and 0.4° offcut surfaces. The substrate peak is the position of maximum intensity. The strong diffuse scatter surrounding the substrate reciprocal lattice point is indicative of defects within the Mg-doped GaN and/or n.i.d. GaN layers. The elongation of the scattering extending from the normal to the substrate peak but at a +35° angle is the analyzer, or detector, streak that caused the scattering vector to smear out radially from the origin. The

analyzer streak emanates from the angular divergence of the incident beam, which causes a small spread in the diffracted beam angle 2θ. Sub-surface polishing damage may also result in a distribution of tilts giving rise to scattered intensity in reciprocal space. This sub-surface damage has been observed in TEM analysis. The $Al_xGa_{1-x}N$ barrier layer does not lie in the same q_x direction as the substrate peak but is instead at a -20° angle to its normal because the substrate is tilted toward the $< 10\bar{1}0 >$ for all substrates except the 1.8° substrate which is tilted toward the $< 11\bar{2}0 >$. The $Al_xGa_{1-x}N$ barrier is under tensile stress and its displacement in the q_y direction represents that strain. In the reciprocal space maps (RSM) of Fig 7.9, the width of the $Al_xGa_{1-x}N$ barrier in the q_x direction is wider for the 0.3° offcut surface relative to the 0.5° offcut surface indicating less dispersion in the AlGaN barrier. The thickness fringes of the thin $Al_xGa_{1-x}N$ barrier become contours of intensity that elongate in the q_y direction. The GaN layer in RSM of heterostructures grown on substrates with higher offcuts (0.7°, 1.4°, 1.7°) merges with the $Al_xGa_{1-x}N$ barrier. This indicates that the $Al_xGa_{1-x}N$ barrier is coherent with the GaN layer, i.e., there is no strain relaxation in the GaN layer, but that the barrier is modulating the GaN layer. RSMs of heterostructures grown on the lower offcuts (0.3°, 0.4°, 0.5°) show distinct separation between the $Al_xGa_{1-x}N$ barrier and the GaN layer as does the RSM of the 1.8° offcut tilted toward $< 11\bar{2}0 >$.

7.4.3 PL

In OMVPE films, there is site selection for the Mg atom to substitute on either the Ga acceptor site or the N donor site. Interstitial sites and the N substitutional site are higher in total energy for than the Ga substitutional site by about 1.5 eV. The 325 nm

photoluminescence measurements at 300K of heterostructures grown on vicinal substrates revealed three peaks per spectra corresponding to the conduction band to valence band (CB $\rightarrow$ VB), conduction band to Mg acceptor (CB $\rightarrow$ ACC), and the Mg deep donor 1 to valence band (DD1 $\rightarrow$ VB) or Mg deep donor 2 to valence band (DD2 $\rightarrow$ VB) transitions, as illustrated by the schematic in Fig. 7.10. Each of the spectra was fitted to a Gaussian profile and peaks were determined by best fit peak finding analysis. A Pseudo-Voigt peak fitting analysis was used to locate PL transistions, and peak fitting was used to determine the FWHM (see example in Fig. 7.11). The CB $\rightarrow$ VB transition at 3.381 ± 0.001 eV was in excellent agreement with the theoretically predicted bandgap of 3.39 eV at 300K [37]. The presence of the CB $\rightarrow$ ACC transition at 3.236 ± 0.005 eV, which corresponds to an acceptor ionization energy of 0.16 eV, was present in PL measurements of heterostructures on all vicinal offcut substrates in this study. However the DD1 $\rightarrow$ VB transition at 3.130 ± 0.001 eV was seen only for the lower offcut (0.3^o, 0.4^o) substrates, while the DD2 $\rightarrow$ VB transition at 2.830 ± 0.025 eV was only present for measurements on the higher offcut ($\geq 0.5^o$) substrates. The former transition represents a deep donor ionization energy of 0.26 eV and the latter of 0.53 – 0.56 eV. Measurements as function of temperature and excitation dependence would help to clarify the exact nature of the transitions observed. This intent of this study was to correlate RT photoluminescence behavior with other physical properties of these $Al_xGa_{1-x}N$/GaN heterostructures, in particular, how the Mg incorporation in the film influences properties. SIMS analysis of the [Mg] of p-GaN layers grown by varying the Mg flux using an on-orientation substrate confirmed the linear behaviour for films below the saturation value of [Mg] = 2×10^{19} cm^{-3} [38] as,

$$\frac{[Mg]}{N} = (A/\alpha)\cdot(\gamma F/G) \tag{7.7}$$

where atomic volume of N atoms is 4 x 10^{22} cm^{-3}, A is cross-section for the capture of physisorbed atoms into chemically bonded states, α is the desorption coefficient for physisorbed atoms, F is the Mg flux , G is the growth rate and γ is the effective flux coefficent. A value of $(A/\alpha) = 0.17$ was found for our p-GaN films which implies 17% of the incident atoms are incorporated. We define $\gamma=1$ for on-axis substrates and attribute the reduction in effective flux coefficient to the effect of growth on the vicinal substrates with increasing offcut angle as shown in Table 7.1.

Both the CB $\rightarrow$ ACC and the DD $\rightarrow$ VB transitions were normalized to the band edge to compare intensities of those transitions. The data reveals that transitions associated with Mg, whether due to the presence of the Mg acceptor or donor, are higher for heterostructures grown on lower offcut (0.3^o, 0.4^o) substrates. These data support that there is increased incorporation of Mg for heterostructures grown on lower offcut (0.3^o, 0.4^o) substrates. Decreasing Mg incorporation with increasing vicinal offcut is consistent with decreasing surface roughness after p-GaN growth, as noted by the similar behavior exhibited in Fig. 7.12 for normalized PL ratios and surface roughness versus vicinal offcut angle.

7.4.4 CL

The 300K cathodoluminescence measurements of heterostructures grown on vicinal substrates revealed subtle differences from the photoluminescence measurements. While the CB $\rightarrow$ VB and the CB $\rightarrow$ ACC transitions were present, there was no evidence of the DD1 $\rightarrow$ VB or the DD2 $\rightarrow$ VB transitions. In addition, the DD1 $\rightarrow$ ACC pair recombination was

observed at 2.97 eV. This recombination corresponded to donor and acceptor ionization energies of 0.26 and 0.16 eV respectively. The difference in transitions between these two analytical techniques most likely reflects the difference in excitation intensity of the source. Since no direct measurement of beam current was taken, an absolute value in W/cm^2 is not available. CASINO Monte Carlo simulations performed at 5 keV for the heterostructure of Fig. 7.3(a) confirmed an electron penetration depth of 240 nm was sufficient to enable donor-acceptor transitons. A summary of the cathodoluminescence transitions is illustrated in Fig. 7.13. Peak analysis was again performed using a Pseudo-Voigt fitting routine and an example of this for the CL spectra is given in Fig. 7.14.

By normalizing the DD1 $\rightarrow$ ACC and the CB $\rightarrow$ ACC transition intensities to those of the band-to band transition intensities, the probability of Mg being in either an acceptor site or a donor site was not found to be a function of vicinal offcut, which is shown in Fig. 7.14. However, CL data as a function of vicinal offcut did correlate well with Raman data as will be discussed later.

Two additional heterostructure growths were performed on 10 x 10 mm^2 substrates from a semi-insulating GaN template with a 0.8^o offcut. One heterostructure was grown in an identical manner as the structure shown in Fig. 7.3(a). The intent was to compare the heterostructure growth on S.I. GaN templates, 10 μm thick GaN films on sapphire substrates, with the heterostructures grown on vicinal bulk GaN substrates in this study. The CB $\rightarrow$ VB transition at 3.424 eV and CB $\rightarrow$ ACC transition at 3.327 eV are clearly seen in Fig. 7.16. For this growth, the CL suggests that all of the Mg resides at the Mg acceptor level 0.16 eV above the valence band. The second structure was grown similar to that of Fig. 7.3(b), but

the Mg-doped GaN layer was omitted. The intent was to determine if there were transitions present that were masked by the dominant CB $\rightarrow$ ACC transition. The CL spectrum for this growth (Fig. 7.17) showed that indeed the nitrogen vacancy donor (V_N) $\rightarrow$ VB transition at 3.34 eV corresponding to an ionization energy of 0.08 eV exists in this material. The presence of V_N is evidence that sites are available to enable n-type conductivity. Additionally, the CB $\rightarrow$ Fe acceptor transition at 2.95 eV was clearly visible. This corresponded to an acceptor ionization energy of 0.46 eV which is in agreement with that reported in reference [39]. The value in performing these growths was to ascertain what other ionized species exist within the epitaxial material that may influence the electrical properties.

7.4.5 Hall Measurements

As mentioned previously, Ni-Au contacts were made to the HFET structure, and an ex situ anneal was performed at 800^{o}C in order to achieve an ohmic contact as determined by linear IV measurements. Heterostructures grown on 0.3^o, 0.5^o, 1.7^o and 1.8^o offcut substrates were still too resistive. For heterostructures grown on the 0.4^o, 0.7^o, and 1.4^o offcut substrates, the IV characteristics were linear over the current range of 5 to 10 μA. Sheet resistances for these were 65,000 Ω/sq. with corresponding sheet densities of 1.3 x 10^{15}, 2.35 x10^{14} and 3.38 x 10^{13} cm^{-2}, respectively. All samples exhibited n-type conductivity.

A freeware Poisson solver [40,41] was used to determine the subband energies by solving the one-dimensional Schrodinger and Poisson equations. The program used a method of finite differences to construct the band diagram for the heterostructure based on

the layers outlined in Fig. 7.3(a) and allowed incorporation of a 45 Å silicon spike at the substrate/epitaxy interface to represent the accumulation of charge in this region that was observed in the CV measurement (Fig. 7.1). The sheet densities were then calculated for varying ionized Mg impurity concentrations in the p-GaN layer. Figure 7.18 shows that the calculated sheet density in the 2DEG channel maximized at 7.7×10^{12} cm^{-2} and dropped precipitously as the ionized acceptor concentration became $\geq 1 \times 10^{17}$ cm^{-3}. This calculation clearly demonstrates that incorporation of a Mg-doped GaN layer has deleterious impact on the 2DEG transport properties.

Room temperature Hall sheet density measurements showed a 2 order of magnitude decrease with increasing offcut angle from 0.4^{o} to 1.4^{o}. The high sheet densities measured suggest additional carrier transport paths other than the 2DEG channel. The relationship between Hall sheet density and SIMS analysis of Mg in these samples was studied. The SIMS profile was separated into three distinct regions: Mg in the p-GaN, Mg in the n.i.d. GaN layer, and the Mg-spike at the interface of these two layers. A Gaussian fitting program was used to integrate the Mg area corresponding to each region. Figure 7.19(a) shows the correlation between Hall sheet density and SIMS integrated area of Mg (atoms/cm^2) as a function of vicinal offcut. The higher n-type sheet density corresponded to higher Mg areal concentrations in the p-GaN layer. Raman data supporting this trend are discussed in the next section. The trend for the integrated areas of both the Mg spike and the Mg in n.i.d. GaN was opposite that of the sheet density but upon further inspection, they were well correlated to n_s.as shown in Fig. 7.19(b). This data reflects what is seen in the SIMS analysis, specifically, that as the offcut angle increases, Mg migrates out of the p-GaN creating a spike

at the p-GaN/n.i.d. GaN interface. Hence, there is residual Mg in the p-GaN, which was behaving as a donor, therefore contributing n-type conductivity. Since Mg acceptors would compensate n-type carriers, these data suggest Mg donors located 0.26 and 0.6 eV below the CB may play a role in the n-type conductivity measured for these samples. However, calculations based on mean free path for low field carrier velocity would predict a 2DEG channel mobility of ~600 $cm^2V^{-1}sec^{-1}$ if Mg alone acted as a scattering center. Measured Hall mobilities were $\leq$ 50 $cm^2V^{-1}sec^{-1}$ suggesting additional scattering mechanisms or interface roughness.

7.4.6 Raman Spectroscopy

Raman scattering occurs as a result of modulation of the electronic polarizability induced by excitation of phonons and plasmons in the solid. In the case of Raman scattering by phonons, the scattering efficiency is higher in covalent crystals than in ionic crystals, because the valence electrons are less localized and larger fluctuation of the polarizability can be induced by lattice vibration [42]. Raman scattering studies are ideal for nitride semiconductors because they are a mixture of both covalent and ionic bonds and they are tolerant to laser irradiation. In this study, the 633 nm He source was used as the excitation source for heterostructure film vibration measurements. Raman spectra were taken in the backscattering configuration with the laser beam along the c-axis of the wurzite structure (z-direction) as well as perpendicular to it (x-direction). The Porto notation for this configuration is $Z(X,-)\bar{Z}$. The polarization of the scattered light is denoted (-), as it has not been analyzed. A charge-coupled device, CCD, was used for signal collection. Spectral

resolution for the 0 - 4000 cm^{-1} range was dictated by the 1800 nm grating. Raman selection rules allow the A_1 (LO) and E_2 modes. The three principle peaks are the E_2 (low), E_2 (high) and A_1 (LO) acoustic phonon modes, as shown in Fig. 7.20. The A_1 mode is Raman and infrared (IR) active, meaning there is a net difference resulting in a dipole moment, while the two E_2 modes are only Raman active.

Lattice strain caused by lattice mismatch and difference in thermal expansion coefficient between heteroepitaxial layers or between a homoepitaxial layer and its substrate may cause in-plane uniaxial or biaxial strain. Additionally, the lattice structure may be distorted in the neighbourhood of native defects or by incorporated impurities. These point defects will introduce a three-dimensional strain such as hydrostatic stress if the defects are uniformly distorted. Wurtzite layers grown on bulk GaN substrates will have uniform biaxial strain in the c-plane with strain tensor components $\varepsilon_{xy} = \varepsilon_{yz} = \varepsilon_{zx} = 0$, $\varepsilon_{xx} = \varepsilon_{yy} \neq 0$ and $\varepsilon_{zz} = 0$ for biaxial (0001) stress meaning that the layers are uniformly compressed or expanded in the c-plane, and in a reverse manner along the c-axis. Biaxial strain in the c-plane of the hexagonal GaN layer is most easily probed by observing the E_2(high) mode by means of Raman scattering [43-46] because of its atomic displacement along the c-axis (Fig. 7.20.) and since this mode conveniently gives the strongest spectrum. The phonon **strain-free** E_2(high) frequency for bulk c-axis GaN is 567.5 ± 0.2 cm^{-1} [47]. A large biaxial stress will cause the E_2(high) mode to shift and is indicative of a high density of structural defects. The magnitude of the shift rate for hexagonal GaN grown on sapphire substrates can be estimated from 2.9 $cm^{-1}GPa^{-1}$ for E_2(high) [46]. The E_2 (high) peak for each vicinal substrate

was evaluated by a Voigt profile where the character of the Gaussian and Lorentizian lines are combined in a Fourier Transform integral.

Demangeot et al [46] also observed biaxial stress shift for the A_1(LO) mode by measuring GaN films at liquid nitrogen temperature and evaluated that shift rate as 0.8 $cm^{-1}GPa^{-1}$. The A_1(LO) peak position for each vicinal offcut was also determined by a Voigt profile. The phonon strain-free A_1(LO) frequency used for bulk c-GaN [47] was 733.6 ± 0.1 cm^{-1} . Based on the A_1(LO) mode, the lowest stress occurs at a vicinal offcut of 0.7^o. The biaxial shift rates for the E_2(low) mode were reported [43] to be -0.5 $cm^{-1}GPa^{-1}$. Biaxial stress was calculated for the E_2(low) mode using a free-standing GaN film value of 144 cm^{-1} [48]. A summary of biaxial stress for the E_2(high), A_1(LO) and E_2(low) modes is given in Figure 7.21. Biaxial stress evaluated using the E_2(low) mode is consistent with that of E_2(high) in that both modes show a transition in stress from compressive to tensile at an offcut of approximately 1.4^o suggesting that vicinal substrates between 0.5^o and 1.4^o are ideal with respect to minimized in-plane strain.

Kozawa [45] reported that the variation of the line shape of the A_1(LO) mode with n-type carrier concentration indicated that a broad and weak A_1(LO) phonon mode could be coupled with an overdamped plasmon. The presence of free carriers can result in an additional high frequency shift of LO-phonon lines due to the formation of mixed plasmon-LO-phonon modes [45, 49]. More recent work [50] suggested that a broad and weak A_1(LO) phonon mode could be associated with residual n-type doping. We found that the median A_1(LO) mode shift was 733.6 cm-1 before the ex situ anneal and that no trend was observed as a function of offcut angle. However, after the ex situ anneal, heterostructures grown on

the 0.5° and 0.7° offcut exhibit a Raman shift to 734.1 cm^{-1} (Fig. 7.22(a)). Additionally, after anneal, the intensity of the Raman peaks for those structures grown on the 0.5°, 0.7° and 1.4° offcuts were lower than their counterparts. There was a coincident broadening of the FWHM of the A_1(LO) mode for the 0.5° offcut. SIMS analysis showed that the background [Si] was at or below the detection limit of 1 x 10^{17} cm^{-3} thereby eliminating background [Si] as the cause for the Raman shift.

It has been reported [51, 52] that the frequencies of the A_1(LO) and E_1(LO) modes in $Al_xGa_{1-x}N$ shift toward higher energy with increasing Al concentration. The A_1(LO) has also been correlated with Al composition, *x*, for $Al_xGa_{1-x}N$ ($0 < x < 1$) films, 2 – 4 mm thick, grown on c-plane sapphire [53]. The 20 nm $Al_xGa_{1-x}N$ barriers in this structure produced a weak signal that was shifted from the A_1(LO) peak. A peak finding algorithm was used to determine the centroid of highest intensity in terms of integrated area and this value was assigned as the Raman shift representing alloy composition for heterostructure growth on each vicinal substrate. These data are compared with HRXRD determination of alloy composition in Fig. 7.23. Our Raman analysis of Al composition is based on the equation and bowing parameter for the A_1(LO) shift as a function of *x*,

$$A_1(LO) = 734 + 153x - b_{A_1(LO)}x(1-x) \tag{7.8}$$

reported by Davydov, et al [53]. The alloy composition evaluated from Raman scattering using their bowing parameter, $b_{A_1(LO)} = -75$ cm^{-1}, is ~20% higher than the alloy composition found by HRXRD. A bowing parameter of $b_{A_1(LO)} = -120$ cm^{-1} would bring the Raman alloy composition into better agreement with our HRXRD data. This difference may reflect the

difference in host substrate. The error bars are placed on these data to acknowledge the dispersion in the $Al_xG_{1-x}N$ composition.

A characteristically broad band below 400 cm^{-1} was observed in the Raman spectra of our vicinal substrates taken after heterostructure growth and the in situ anneal at 800^oC under nitrogen. After the ex situ anneal at 800^oC was performed, Raman measurements were repeated, and this broad signal was weaker. Harima [54, 55] found that this broad band below 400 cm^{-1} is not a phonon signal, but an electronic signal attributed to what is called the inter-valence-band transition of the hole (IVBTH). That is, the appearance of the broad band is evidence of p-type conductivity. Additionally, the amplitude of the signal was annealing temperature dependent. Since the intensity of this Raman continuum band is nearly proportional to the hole density [54, 55], the integrated area of the IVBTH peak for our heterostructures before ex situ anneal was analyzed by integrating the area under the band extending from 260 – 400 cm^{-1} as shown in Fig. 7.24(a). The integrated area for each heterostructure growth was then compared to the cathodoluminescence data, specifically the DD1 $\rightarrow$ ACC transition to the CB $\rightarrow$ VB transition ratio, which represents the Mg donor-acceptor pair recombination intensity normalized to the band edge. The agreement between these alternative electrical measurements is excellent as shown in Fig. 7.24(b). These data show that the p-type concentration as determined by Raman spectroscopy is consistent with the deep donor to acceptor transitions as measured by CL and that an understanding of these data is key to origin of high Hall sheet densities as will be discussed later.

The Mg activation process in GaN is initiated by thermal annealing in a N_2 atmosphere and follows an Arrhenius behavior. An anneal temperature of 718^oC is sufficient

to break the 1.31 eV Mg-N bond. As depicted in the inset of Fig. 7.25(c), hydogen atoms that intervene between Mg-N bonds in as-grown films are released during the anneal, thereby activating the Mg acceptors [56, 57]. The hydogen atoms then diffuse in the host lattice until they find new bonding partners or are removed from the film. In our study, two Mg activation events took place, an in situ anneal, which enabled the p-conductivity and an ex situ anneal, both at 800°C. A reduction in integrated area under the Raman 260 - 400 cm^{-1} continuum band was assessed after the ex situ-anneal in an identical manner as described above and depicted in Fig. 7.25(a). That difference in integrated area is described by $(I_o - I)/I_o$ where I_0 is the integrated area before the ex situ anneal and I is the integrated area after the ex situ anneal. The parameter $(I_o - I)/I_o$ was compared to the Mg areal density determined by SIMS for the 0.4°, 0.7°, and 1.4° offcut substrates. As shown in Fig. 7.25(b), the reduction in integrated area was proportional to the density of the Mg species. The implication of this behavior is that a self compensating process that reduces p-type conductivity has occurred and that its probability increases with increasing areal density of Mg. This Mg compensation is plotted relative to the Hall sheet density in Fig. 7.25(c). Note that there was no Mg compensation for the heterostructure grown on the 1.4° offcut substrate after the 800°C ex situ anneal. The correspondence in sheet density to Mg compensation supports the argument that compensating donors, specifically Mg atoms diffusing and bonding to a vacant N-site, have been created during the ex situ anneal. A necessary condition for this mechanism to take place is the presence of nitrogen vacancies, V_N, and identification of a corresponding plasmon-phonon coupled mode would be direct evidence.

Resolution for the Raman shift in the 4000-7000 cm^{-1} range was dictated by a 1200 nm grating. The charge transfer peak or the plasmon wavelength, λ_p, for our heterostructures was 656.8 ± 38.7 meV. The intersubband transition peak, also known as the charge transfer band, was observed near 5500 cm^{-1} and is associated with the presence of free electrons in the film. When the 633 nm excitation source hits the film the absorptive process kicks an electron out of its state in a frequency-dependent way. For instance, if we moved further into the IR by using the 780 nm source, we would not excite the charge transfer band as efficiently. However, since high energy photons give low energy emission, using the 325 nm source would give a more intense charge transfer band. Since GaN is attractive as an optically-active substrate, we may want to tune the transfer charge band by adding dopants to optimize the intersubband absobance. Doping the substrate effectively changes the local environment around the atoms in the film and subsequently shifts and intensifies the charge transfer peak energy. The energy and intensity of the charge transfer peak for each heterostructure growth was determined by a Gaussian fit algorithm. The absorbance, A, for each vicinal substrate was calculated as

$$A = -\log_{10}(T_{offcut} / T_{ref}) \tag{7.9}$$

where T_{offcut} / T_{offcut} is the transmission of each offcut substrate relative to a reference semi-insulating bulk GaN substrate with no growth. The results are graphically displayed in Fig. 7.26.

We can use the frequency of this charge transfer band to calculate *n*, the n-type carrier concentration, in the film [58]. We questioned the expectation of seeing a charge transfer

band by comparing SIMS data to the calculated plasmon frequency, ω_p. A Gaussian peak fitting program was used to determine the median [Mg], [Fe], and [Si] in p-GaN and the [Mg] in the n.i.d. GaN layer, and a Lorentzian was used to determine the [Si] at the epitaxy/bulk interface from multiple SIMS measurements of heterostructures grown on 0.4°, 0.7°, and 1.4° offcut substates. The plasmon energy, λ_p, as determined by the peak fitting data of the charge transfer signal was used to determine the plasmon frequency, ω_p, from [59],

$$\omega_p = \frac{2\pi c}{\lambda_p} \tag{7.10}$$

The plasmon frequency was calculated to be (0.9 – 1.02) x 10^{15} sec^{-1} for each heterostructure. The carrier concentration, *n*, is then found from the plasmon frequency using the following equation,

$$n = \frac{\omega_p^2 m^* \varepsilon_\infty \varepsilon_o}{e^2} \tag{7.11}$$

where m^* is the effective mass of GaN $\left(\frac{m^*}{m_o} = 0.23\right)$, and the dielectric constant, $\varepsilon_\infty = 5.8$ [60], ε_o is the permittivity, and e is electronic charge. Carrier concentrations were determined to be 4.4 x 10^{20} cm^{-3}, 4.2 x10^{20} cm^{-3} and 3.5 x 10^{20} cm^{-3} for the 0.4°, 0.7°, and 1.7°, offcuts respectively. These carrier concentrations are higher than any species measured by SIMS for our heterostructures. An alternative source of n-type carrier that could be present at these concentrations but not measured by SIMS is the nitrogen vacancy, V_N,

previously suggested as the necessary vehicle for acceptor compensation in our heterostructures.

The Raman shift at ~420 cm^{-1} that was observed for all heterostructures in this study was more intense after the 800°C ex situ anneal than it was prior to the anneal as shown in Fig. 7.27(a) for heterostructure growth on the 1.4° offcut substrate. A plasmon energy of 52.1 meV corresponds to this shift. Accordingly, we determined ω_p to be 7.9 x10^{13} sec^{-1} with a carrier concentration, n, corresponding to this plasmon frequency of 2.6 x 10^{18} cm^{-3}. Inspection of SIMS profiles for [Si] in the n.i.d.GaN layer ruled out Si as the source of this peak because [Si] was below the detection limit of SIMS. Instead, we suggest that since the formation energy of nitrogen vacancies, V_N, is relatively low in p-GaN [61] and that in our structure E_F is only 0.08 eV above the valence band maximum, VBM, the increased intensity of 420 cm^{-1} Raman peak is evidence that V_N are acting as compensating centers to the Mg acceptors. The diffusion coefficient, D, follows an Arrhenius behavior,

$$D = D_o \exp\left(-\frac{E_a}{k_b T}\right) \tag{7.12}$$

Using the pre-exponential factor, $D_o = 2.8x10^{-7}\,cm^2s^{-1}$, and an activation energy, $E_a = 1.9$ eV [62] for magnesium diffusion by a substitutional mechanism, the diffusion distance for Mg, $x_{Mg} = \sqrt{2Dt}$, effected by a 10 min ex situ N_2 anneal at 800°C is ~ 60 Å. Therefore, a Mg atom could easily diffuse from an acceptor Ga-site to a donor N-site resulting in a self-compensation process.

We believe the shifts in low-energy band of the Raman spectra to be correlated with magnesium. A rough estimate of the magnesium local vibrational mode frequency from the effective masses of GaN and the local vibration mode, LVM, is given by [63]

$$\frac{\omega_{GaN}}{\omega_{LVM}} = \sqrt{\frac{\mu_{LVM}}{\mu_{GaN}}} \tag{7.13}$$

Assuming that magnesium occupies a nitrogen site, we obtain a value of 456 cm^{-1} for Ga-Mg vibrations using $\omega_{GaN} = \omega[E_2^{high}] = 567\ cm^{-1}$. The 419.4 cm^{-1} mode which was present after the in situ anneal and the 484.8 cm^{-1} mode which appeared after the ex situ anneal are identified in Fig. 7.27(a). We note that others [58] have identified the 418 cm^{-1} as a sapphire substrate signal but that cannot be the case in the analysis of these heterostructures grown on bulk GaN substrates. We suggest that the 419.4 cm^{-1} vibrational mode is overlapping an acoustic overtone. The sharpening of the 419.4 cm^{-1} peak after ex situ anneal supports the ascertion of overlapping modes, specifically, that the vibrational one is stimulating the long range behavior of the acoustic one.

Furthermore, electron excitations can be due to free carriers, either single particle or collective excitation (plasmons), as well as coupled modes of electronic excitation and lattice vibration referred to as LO phonon-plasmon coupled modes (LOPC). LOPC modes consist of upper- and lower-frequency branches (denoted as L^+ and L^-, respectively). With increasing carrier density, n, the L^+ mode shifts to higher frequency. However, the L^- mode sharpens, unlike the L^+ mode, at larger n (10^{19}-10^{20} cm^{-3}) [65]. We suggest that the 419.4 cm^{-1} is the L^- branch and 846.5 cm^{-1} and 905.6 cm^{-1} LVM pair make up the L^+ branch of the LOPC generated by the in situ anneal. These frequencies (Fig 7.27(b)) represent an electron

concentration of 1 x 10^{19} cm^{-3}. Applying Eq. (7.13), we determine μ_{LVM} = 5.2 suggesting that a hydrogen-decorated native defect, Mg-H, is the lines origin. Secondly, we suggest that the 484.8 cm^{-1} mode is the L^- branch and the 1650 cm^{-1} to 1760 cm^{-1} band (Fig 7.27(d)) as the L^+ branch of the LOPC generated by the ex situ anneal. The assignment of the L^+ and L^- branches for both the before and after ex situ anneal LOPC modes is consistent with the literature [42, 63-66] as shown in Fig. 7.27(g).

There are no LOPC modes for p-type conductivity as for n-conductivity. But more interestingly, the Mg-N LVM expected at ~650 cm^{-1} was **not** seen. This LVM would correspond to Mg substitution on a Ga-site. Although the LVM was not observed in our Raman spectra, we suggest that the 1381.95 cm^{-1} mode present before the ex situ anneal (Fig. 27(c)) is an optical overtone overlaying an acoustic overtone and more specifically, that that optical overtone represents hydrogen diffused from the host lattice during the in situ anneal. The isochronal appearance of the 1324.35 cm^{-1} and 1444.34 cm^{-1} lines and the sharpening of the 1381.95 cm^{-1} mode with the disappearance of the 990.2 cm^{-1} line (Fig 27(b)) after ex situ anneal is consistent with the assignment of isolated hydrogen in the lattice at 1456 cm^{-1} [67] since the 990.2 cm^{-1} line is molecular nitrogen [68] in the film that is driven out by the ex situ anneal. The increase in intensity of the 1381.95 cm^{-1} line afer ex situ anneal supports our analysis that there were two discrete activation steps, one during the in situ anneal and the other during the ex situ anneal.

Reboredo and Pantelides [69] suggested that hydrogen bound at substitutional/ interstitial complexes give rise to high energy modes in highly Mg-doped GaN. Their independent calculations agreed within an experimental uncertainty of 200 cm^{-1} and

corroborated that the defect complex in the vicinity of 2200 cm^{-1} originates during anneal in a H- or N-rich atmosphere [70]. These modes were attrtibuted [63, 70, 71] to H-decorated N vacancies (V_N) or extended defects. We suggest that the appearance of the lines in the 2200 cm^{-1} to 2500 cm^{-1} band (se Fig. 7.27(e)) confirm the formation of V_N after the ex situ anneal enabling self-compensation in Mg-doped GaN films as supported by our 260 – 400 cm^{-1} integrated area studies before and after ex situ anneal discussed previously.

Based upon ab initio calculations, Neugebauer and van de Walle [72] found that Mg-H complexes are likely to form in GaN. They claimed that hydrogen prefers nitrogen antibonding sites and determined the frequency of the H stretch mode to be close to the value of the H stretch mode in NH_3 (3444 cm^{-1}). In Fig. 7.27(f), two inequivalent sites of the Mg-H complex shown at 3476.5 cm^{-1} and 3459.9 cm^{-1} are in reasonable agreement with the calculated frequencies of 3490 cm^{-1} for the Mg-H bond parallel to the c-axis and 3450 cm^{-1} for the Mg-H bond almost in the c-plane [57]. The lines at 3027 cm^{-1} and 3139 cm^{-1} have been ascribed to the N-H stretch mode of the Ga vacancy defects decorated by hydrogen (V_{Ga}-H) [67, 73]. Since the formation energy for V_{Ga} in n-type GaN is relatively high, the disappearance of the 3036.7 cm^{-1} mode after ex situ anneal may be associated with the increased intensity of isolated hydrogen in the film.

7.4.7 TEM

A high angle dark field (HADF) image taken in the $11\bar{2}0$ zone axis is shown in Fig. 7.28. The observed area is free of dislocations and stacking faults. There is no evidence of any strain fields in the limited field of view. This image supports HRXRD analysis and

panchromatic CL imaging analysis suggesting lower dislocation densities for heterostructures grown on higher ($\geq 0.7^{o}$) vicinal offcut surfaces. However, a second HADF shown in Fig. 7.29 shows that the GaN (light,left)/AlGaN(dark, right) interface interface clearly exhibits a roughness of >10 Å. Interface roughnesses on this order for AlGaN/GaN heterostructures have been shown to exhibit low RT and LT mobility [74]. Electron energy loss spectroscopy (EELS) confirmed the presence of background levels (~100 ppm) of Mg at a distance of 250 nm, 200 nm, 100 nm, and 10 nm from the GaN/AlGaN interface region suggesting ionized impurity scattering may also contribute to the deteriorated RT mobility. EELS confirmed ~ 5% higher Mg concentration in the AlGaN barrier suggesting that the AlGaN is gettering the Mg from the GaN buffer. A more detailed analysis is the subject of a separate paper. AlGaN barrier thickness was determined from lower magnification HADF images to be 157 Å. The error in this measurement is estimated to be as high as 15% because of the difficulty in delineating the interface between the AlGaN surface and the PdAu protective layer applied during focused-ion beam (FIB) preparation.

7.5 Analysis of Heterostructure Results

In order to understand the sheet carrier density results for our heterostructures grown according to Fig. 7.30(a), the energy band diagram for the heterostructure was calculated, as shown in Fig. 7.30(b). The $Al_xGa_{1-x}N$ barrier is not intentionally doped and should not contribute free carriers to the sheet density. Instead, the polarization induced charge at the bottom and top surfaces of the $Al_xGa_{1-x}N$ layer determine the magnitude of the electric field within this layer. The sheet charge density, $\sigma_{(P_{SP}+P_{PE})}$, at the top and bottom faces can be

lowered by the introduction of compensating charges, i.e., a negative charge sheet 2DEG close to the positive polarization charge sheet at the lower $Al_xGa_{1-x}N$/GaN interface and a positive charge sheet at the top surface of the $Al_xGa_{1-x}N$ layer. Such a positive sheet charge can arise from ionized donor states at the surface. Since the Fermi level at the surface is pinned at a level φ_S below the conduction band of the $Al_xGa_{1-x}N$ due to the presence of these donor-like states, the negative sheet charge will occupy the energy levels between the Fermi level and $(\varphi_{S\partial} - \Delta E_C)$ below the Fermi level, denoted as E_{fo}. An electrostatic analysis for an $Al_xGa_{1-x}N$ layer of thickness, d, which is greater than the minimum thickness, d_{CR} to sustain a polarization dipole is given by Vetury [75]

$$q \cdot n_s = \sigma_{(P_{SP}+P_{PE})} \cdot (1 - d / d_{CR}) - \varepsilon \cdot E_{fo} / d \tag{7.14}$$

and

$$d_{CR} = \varepsilon \cdot (q \cdot \varphi_S - \Delta E_C) / \sigma_{(P_{SP}+P_{PE})} \tag{7.15}$$

where q is electronic charge, n_s the sheet density, and ε is the dielectric constant.

For the heterostructures in this study, the n.i.d. doped GaN layer ([Si]=5 x 10^{16} cm^{-3}) next to the $Al_xGa_{1-x}N$ barrier is fully depleted as a result of its interface with the p-GaN ([Mg]=3 x 10^{19} cm^{-3}, ionized at 1%). This interface is a p-n junction, and depletion widths on the p-side of the junction were determined accordingly as 417 Å. The p-GaN interface at the semi-insulating bulk GaN substrate is also depleted as a result of the Si charge layer (see Fig. 7.1). The depletion widths for this p-n junction were found to be 1043 Å in the p-region and fully depleted for the 45 Å charge region. Thus, one concludes that there is a 1500 Å

layer in the middle of the p-GaN layer that is undepleted. If the Mg acceptors were not activated, this undepleted layer would not exhibit p-type conductivity. We intentionally performed an in situ anneal, and our Raman spectroscopy studies showed that a p-conductive layer was formed as indicated by the presence of the inter-valence band transition below 400 cm^{-1} (Fig. 7.24(a)). However, the ex situ anneal necessary to form an ohmic contact to the semiconductor initiated a self-compensating mechanism by generating V_N, which in turn became substitutional sites for Mg atoms diffusing through the heterostructure. The V_N formation energy in the p-GaN layer is ~ 1eV as shown in Fig. 7.31(c). Hence, we propose that the 1500 Å layer became n-type after the ex situ anneal and contributed to the measured sheet density. In addition, because V_N act as electron-hole scattering centers, the mobility is severely degraded.

From our previous work [76], the carrier density contributed by the polarization induced charge was 4.9 x 10^{12} cm^{-3}. Therefore, in order to explain the high sheet densities measured for heterostructures grown on the 0.4°, 0.7° and 1.4° offcut substrates, the contribution of carriers from the 1500 Å undepleted region, $w_{undepleted}$ in the p-GaN was determined by

$$w_{undepleted} * N^{LOPC} = 3.9x10^{13} cm^{-2} \quad (7.16)$$

where N^{LOPC} = 2.6 x 10^{18} cm^{-3} represents the carrier density of the LOPC at 484.8 cm^{-1}. This charge density would completely explain the sheet density of the 1.4° offcut substrate.

In order to understand the even higher sheet densities of the heterostructures grown on the 0.4° and 0.7° offcut substrates, we integrated the areas under the plasmon peak (Figs.

7.24(a), 7.25(a) and 7.31(b)) referred to as the intersubband transition. Hall sheet densities and the integrated area are plotted for each vicinal offcut in Fig. 7.31(a). The carrier density for these plasmon peaks is on the order of 4 x 10^{20} cm^{-3}. The trend of integrated area is strikingly similar to the measured n_s. We suggest that the integrated area of the plasmon is also indicative of the formation of nitrogen vacancies in the film which contribute n-type carriers to the sheet density.

7.6 Conclusions

Our study of AlGaN/GaN heterostructures grown on GaN vicinal substrates by AFM, HRXRD, PL, CL, Hall and Raman spectroscopy has yielded complimentary results that are valuable for determining the most appropriate offcut angle. The AFM studies showed that offcuts $\geq$ 0.5^o yields surfaces with minimal surface roughness after p-GaN growth as well as after growth of n.i.d. GaN layers followed by $Al_xGa_{1-x}N$ barriers. HRXRD data suggest that vicinal substrates result in epitaxial growth with lower dislocation densities than on-axis ones. PL and CL data confirmed presence of both acceptor and donor transitions in our heterostructures. AFM roughness analysis and PL CB $\rightarrow$ ACC and DD $\rightarrow$ VB transitions followed similar trends. Since CL and Raman are both electrical measurements, the striking agreement between intervalence band intensity and the DD1 $\rightarrow$ ACC transitions is not unexpected. Biaxial stresses based on the E_2 (low), E_2 (high) and A_1 (LO) were low for all heterostructures grown on all vicinal offcuts but indicated that offcut angles between 0.5^o and 1.4^o may be optimal. Based on Poisson solver calculations, measured sheet carrier densities were unexpectedly high. However, Raman spectroscopy has provided insight about the material properties that support our hypothesis that nitrogen vacancies formed after the ex

situ anneal were responsible for the self-compensation in p-GaN films and an n-type conductive layer in the undepleted region of the p-GaN layer. TEM analysis confirmed that GaN buffers observed were dislocation- and stacking fault-free. However, AlGaN/GaN interface roughness assessed as >10 Å has contributed to degraded Hall mobility. In addition, we believe that once Mg is introduced in the heterostructure, the Mg memory effect may be insurmountable in attaining high mobility by minimizing ionized impurity scattering.

7.7 Acknowledgements

The authors acknowledge Kyma Technologies for the bulk GaN substrates used in this study. Special thanks to Fred Stevie, NCSU Analytical Instrumentation Facility, for the SIMS analysis.

7.8 References

[1] S. Nakamura and G. Fasol (eds.), *The Blue Laser Diode* (Springer-Verlag, Berlin 1997).

[2] M. Kuzuhara, H. Miyamoto, Y. Ando, T. Inoue, and Y. Okamoto, Phys. *Stat. Sol. (a),* **200** (2000) 161.

[3] D. Jena, A.C. Gossard, and U.K. Mishra, *Appl. Phys. Lett.,* **76** (2000) 1707.

[4] D. Jena, and U.K. Mishra, *Appl. Phys. Lett.,* **80** (2002) 64.

[5] Mion, C. et al, *Superlattices and Microstructures,* **40** (2006) 338.

[6] Mion C. et al, *Appl. Phys. Lett*. **89** (2006) 092123.

[7] Wurfl, J., *Microelectron. Reliab*. **39** (1999) 1737-1757.

[8] K. Hiramatsu, H. Amano, I. Akasake, H. Kato, N. Koide, K. Manabe, *J. Crystal Growth,* **107** (1991) 509.

[9] M.H. Xie, S.H. Cheung, L.X. Zheng, Y.F. Ng, H. Wu, N. Ohtani, S.Y. Tong, *Phys. Rev. B,* **61** (1999) 9983.

[10] J.T. Yuasa, Y. Ueta, Y. Tsuda, A. Ogawa, M. Taneya, K. Takao, *Jpn. J. Appl. Phys.,* **38** (1999) LL703.

[11] M.H. Xie, L.X. Zheng, S.H. Cheung, Y.F. Ng, H. Wu, S.Y. Tong, N. Ohtani, *Appl. Phys. Lett.,* **77** (2000) 105.

[12] Y. Cui, L. Li, *Phys. Stat. Sol. (a),* **188** (2001) 583.

[13] S.H. Cheung, L.X. Zheng, M.X. Xie, S.Y. Tong, N. Ohtani, *Phys. Rev B,* **64** (2001) 033304.

[14] C.D. Lee, R.M. Feenstra, O. Shigiltchoff, R.P. Devaty, W.J. Choyke, *MRS Internet J. Nitride Semicond. Res.,* **7** (2002) 2.

[15] D. Lu, D.I. Florescu, D.S. Lee, V. Merai, A. Parekh, J.C. Ramer, S.P. Gou, E. Armour, *Phys. Stat. Sol. (a),* **200** (2003) 71.

[16] X.Q. Shen, M. Shimizu, H. Okumura, *Jpn. J. Appl. Phys.,* **42** (2003) L1293.

[17] J. Brault, E. Bellet-Amalric, S. Tanakal, F. Enjalbert, D. Le Si Dang, E. Sarigiannidou, J.–L. Rouviere, G. Feuillet, B. Daudin, *Phys. Stat. Sol. (b),* **240** (2003) 314.

[18] A. Nakajima, Y. Furukawa, S. Koga, H. Yonezu, *J. Crystal Growth,* **265** (2004) 351.

[19] X. Q. Shen, M. Shimizu, T. Yamamoto, Y. Honda, H. Okumura, *J. Crystal Growth,* **278** (2005) 56.

[20] N. Onojima, J. Kaido, J. Suda, T. Kimoto, *Phys. Stat. Sol. (c),* **2** (2005) 2643.

[21] A. Nakajima, Y. Furukawa, H. Yokoya, S. Yamaguchi, and H. H. Yonezu, Jpn. J. Appl. Phys **45** (2006) 2422.

[22] L.S. McCarthy, I.P. Smorchkova, H. Xing, P. Kozodoy, P. Fini, J. Limb, D. L. Pulfrey, J.S. Speck, M.J.W. Rodwell, S.P. DenBaars, and U.K. Mishra, *IEEE Trans. Electron Dev.,* **48** (2001) 543.

[23] C.L. Reynolds, Jr. and J.A. Grenko, *Phys. Stat. Sol. (a),* **206** (2009) 691.

[24] R. Bhat, C. Caneau, C.E. Zah, M.A. Koza, W.A. Bonner, D.M. Hwang, S.A. Schwarz, S.G. Menocal, and F.G. Favine, *J. Cryst. Growth,* **107** (1991) 772.

[25] W. Lee, J.–H. Ryou, D. Yoo, J. Limb, R.D. Dupuis, D. Hanser, E. Preble, N.M. Williams, and K. Evans, *Appl. Phys. Lett.,* **90** (2007) 093509.

[26] J.P. Liu, J.-H. Ryou, D. Yoo, Y. Zhang, J. Limb, C.A. Horne, S.-C. Shen, R.D. Dupuis, A.D. Hanser, E.A. Preble, and K.R. Evans, *Appl. Phys. Lett.,* **92** (2008) 133513

[27] H. Xing, D. Green, H. Yu, T. Mates, P. Kozokoy, S. Keller, S.P. DenBaars, and U.K. Mishra, *Jpn. J. Appl. Phys.,* **42** (2003) 50.

[28] M.V. R. Murty, P. Fini, G.B. Stephenson, C. Thompson, J.A. Eastman, A. Munkholm, O. Auciello, R. Jothilingam, S.P. DenBaars, and J.S. Speck, *Phys. Rev. B,* **62** (2000) R10661.

[29] X. Xu, P.P. Vaudo, J.F. Flynn, J. Dion, G.R. Brandes, *Phys. Stat. Sol.,* **202** (2005) 200461521.

[30] H. Morkoc, *Nitride Semiconductors and Devices,* (Springer-Verlag, Berlin 1999).

[31] T. Takeuchi, H. Takeuchi,S. Sota, H. Sakai, H. Amano, and I. Akasaki, *Jpn. J. Appl. Phys.,* **36** (1997) L177.

[32] R. Chierchia, T. Bottcher, H. Heinke, S. Einfeldt, S. Figge and D. Hommel, *J. Appl. Phys.,* **93** (2003) 8918.

[33] S.R. Lee, A.M. West, A.A. Allerman, K.E. Waldrip, D.M. Follstaedt, P.P. Provencio, D.D. Koleske and C.R. Abernathy, *Appl. Phys. Lett.,* **86** (2005) 241904.

[34] V. Srikant, J.S. Speck, and D.R. Clark, *J. Appl. Phys.,* **82** (1997) 4286.

[35] Metzger, R. Holper, E. Born, O. Ambacher, M. Stutzmann, R. Stommer, M. Schuster, H. Gobel, S. Christiansen, M. Albrecht and H.P. Strunk, *Philos. Mag A,* **77** (1998) 1013.

[36] D.K. Bowen and B.K. Tanner, *High Resolution X-ray Diffractometry and Topography* (T.J. International Ltd, Padstow, UK 1998).

[37] T.P. Chow and Ghezzo, *SiC power devices in III-Nitride, SiC, and Diamond Materials for Electronic Devices.* Eds. Gaskill D.K, Brandt C.D. and Nemanich R.J., *Material Research Society Symposium Proceedings,* Pittsburgh, PA., **423** (1996), 69.

[38] D.J. Dewsnip, J.W. Orton, D.E. Lacklison, L. Flannery, A.V. Andrianov, I. Harrison, S.E. Hooper, T.S. Cheng, C.T. Foxon, S.N. Novikov, B. Ya Ber, and Yu A. Kudriavtsev, *Semicond. Sci. Tech.,* **13** (1998) 927.

[39] H. Witte, K. Fluege, A. Dadgar, A. Krtschil, A. Krost and J. Christen, *Mat. Res. Soc. Symp.,* **798** (2004) Y5.37.1.

[40] L. Snider, I.-H. Tan, and E.L. Hu, *J. App. Phys.,* **68** (1990) 2849.

[41] I.-H. Tan, G.L. Snider, and E.L. Hu, *J. App. Phys.,* **68** (1990) 4071.

[42] H. Harima, *J. Phys.: Condens. Matter.,* **14** (2002) R967.

[43] V.Y. Davydov, N.S. Averkiev, I.N. Goncharuk, D.K. Nelson, I.P. Nikitina, A.S. Polkovnikov, A.N. Smirnov, M.A. Jacobson, and O.K. Semchinova, *J. Appl. Phys.,* **82** 5097.

[44] C. Kisielowski, J. Kruger, S. Ruvimov, T. Suski, J.W. Ager III, E. Jones, Z.L. Weber, M. Rubin, E.R. Weber, M.D. Bremser, and R.F. Davis, *Phys. Rev. B,* **54** (1996) 17745.

[45] T. Kozawa, T. Kachi, H. Kano, H. Nagase, N. Koide and K. Manabe, *J. Appl. Phys.,* **77** (1995) 4389.

[46] F. Demangeot, J. Frandon, M. A. Renucci, O. Briot, B. Gil, and R.L. Aulombar, *Solid State Commun.,* **100** (1996) 207.

[47] T. Paskova (ed.), *Nitrides with Nonpolar Surfaces* (Wiley-VCH, Weinham, Germany 2008), 239.

[48] J. Nakahara, T. Kuroda, H. Amano, I. Akasaki, S. Minomura, and I. Grzegory, *Ninth Symposium Record of Alloy Semiconductor Physics and Electronics,* (1990) 391.

[49] H. Harima, H. Sakashita, T. Inoue, and S. Nakashima, *J. Cryst. Growth,* **189/190** (1997) 672.

[50] A.P. Vajpeyi, A. Georgakilas, G. Tsiakatouras, K. Tsagaraki, M. Androulidaki, S.J. Chua, S. Tripathy, *Physica E,* **41** (2009) 427.

[51] A. Cros, H. Angerer, R. Handschuh, O. Ambacher, and M. Stutzmann, *Solid State Comm.,* **104** (1997) 35.

[52] F. Demangeot, J. Groenen, J. Frandon, M.A. Renucci, O. Briot, S. Clur, and R.L. Aulombard, *Appl. Phys. Lett.,* **72** (1998) 1760.

[53] V. Y. Davydov, I. N. Goncharuk, A. N. Smirnov, A.R. Smirnov, A.E. Nikolaev, W.V. Lundin, A.S. Uskkov, A.A Klochikhin, J. Aderhold, J. Graul, and O. Semchinova, *Phys. Rev. B,* **65** (2002) 125203.

[54] H. Harima, T. Inoue, S. Nakashima, M. Ishida, and M. Taneya, *Appl. Phys. Lett.,* **75** (1999) 1383.

[55] H. Harima, T. Inoue, Y. Sone, S. Nakashima, M. Ishida, and M. Taneya, *Phys. Status Solidi (b),* **216** (1999) 789.

[56] S. Nakamura, T. Mukai, M. Senoh, and N. Iwasa, *Jpn. J. Appl. Phys.,* **31** (1992) L1332.

[57] Y. Okamoto, M. Saito, and A. Oshiyama, *Jpn. J. Appl. Phys.,* **35** (1996) L807.

[58] F. Demangeot, J. Frandon, M.A. Renucci, C. Meny, O. Briot and R. L. Aulombard, *J. Appl. Phys.,* **82** (1997) 1305.

[59] C. Kittel, *Introduction to Solid State Physics* (Wiley, Hoboken, NJ 2005) 359.

[60] O. Madelung, U. Rossler, and M. Shulz, *Group IV Elements, IV-IV and III-V Compunds, Part b-Electronic, Transport, Optical and Other Properties* (Springer-Verlag, 1982) 1.

[61] C.G. Van de Walle and J. Neugebauer, *J. Appl. Phys.,* **95** (2004) 3851.

[62] Z. Benzarti, I. Halidou, Z. Bougrioua, T. Boufaden, and B. El Jani, *J. Cryst. Growth,* **310** (2008) 3274.

[63] A. Kashner, H. Siegle, G. Kaczmarczyk, M. StraBburg, A. Hoffmann, and C. Thomsen, *Appl. Phys. Lett.,* **74** (1999) 3281.

[64] H. Harima, H. Sakashita, and S. Nakashima, *Mater. Sci. Forum,* **264-8** (1998) 1363.

[65] P. Perlin, J. Camassel, W. Knap, T. Taliercio, J.C. Chervin, T. Suski, I. Grzegory and S. Porowski, *Appl. Phys. Lett.,* **67** (1995) 2524.

[66] T. Kozawa, T. Kachi, H. Kano, Y. Taga, M. Hashimoto, N. Koide, and K. Manabe, *J. Appl. Phys.,* **75** (1994) 1098.

[67] R.N. Pereira, B. Bech Nielsen, M. Stavola, M. Sanati, S.K. Esteicher, M. Mizuta, *Physica B,* **376-377** (2006) 464-467.

[68] G.V. Chertihin, L. Andrews, M. Neurock, *J. Phys. Chem.,* **100** (1996) 14609.

[69] F.A. Reboredo and S.T. Pantelides, Phys. Rev. Lett. **82** (1999) 1887.

[70] A. Kaschner, G. Kaczmarczyk, A. Hoffmann, C. Thomsen, U. Birkle, S. Einfeldt, D. Hommel, *Phys. Stat. Sol. (b),* **216** (1999) 551.

[71] M.S. Brandt, J.W. Ager III, W. Gotz, N.M. Johnson, J.S. Harris, Jr., R.J. Molnar and T.D. Moustakas, *Phys. Rev. B,* **49** (1994) 14758.

[72] J. Neugebauer and C. G. Van de Walle, *Phys. Rev. Lett.,* **75** (1995) 4452.

[73] W. Gotz, N.M. Johnson, D.P. Bour, M.D. McCluskey, and E.E. Haller, *Appl. Phys. Lett.,* **69** (1996) 3725.

[74] Z. Bougrioua, M. Azize, P. Lorenziini, M. Laugt, and H. Haas, *Phys. Stat. Sol. (a),* **202** (2005) 536.

[75] R. Vetury, I.P. Smorchkova, C.R. Elsass, B. Heying, S. Keller, and U.K. Mishra, U.K., *Mat. Res. Soc. Symp.,* **622** (2000) T2.5.1.

[76] J.A. Grenko, C.W. Ebert, C.L. Reynolds, M.A.L. Johnson, A.D. Hanser, E.A. Preble, T. Paskova, K.R. Evans, *Phys. Stat. Solidi (c),* **6** (2009) S1037.

7.9 Tables

Table 7.1 γ values for selected vicinal substrates.

offcut angle	median [Mg] cm^{-3}	([Mg]/N)/(A/α) ($\times 10^{-4}$)	γ
0.4°	1.89×10^{19}	28.3	0.81
0.7°	6.33×10^{18}	9.48	0.27
1.4°	4.79×10^{18}	7.17	0.21

7.10 Figures

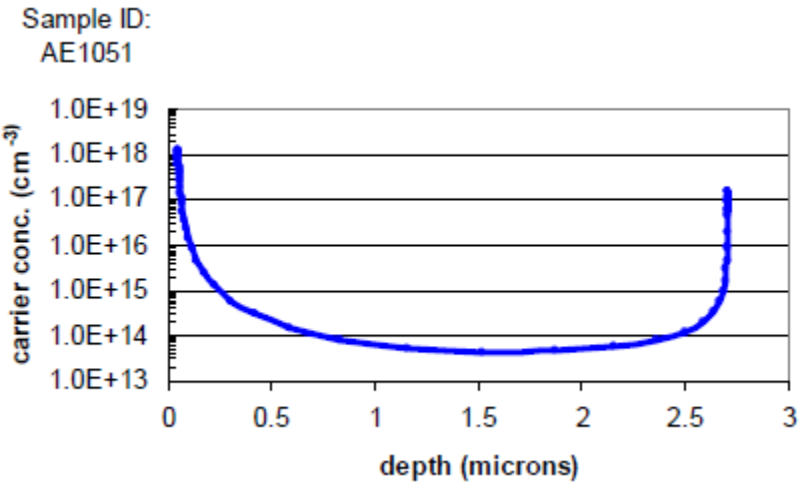


Figure 7.1 CV profile of free carrier concentration versus depth for the semi-insulating GaN substrate.

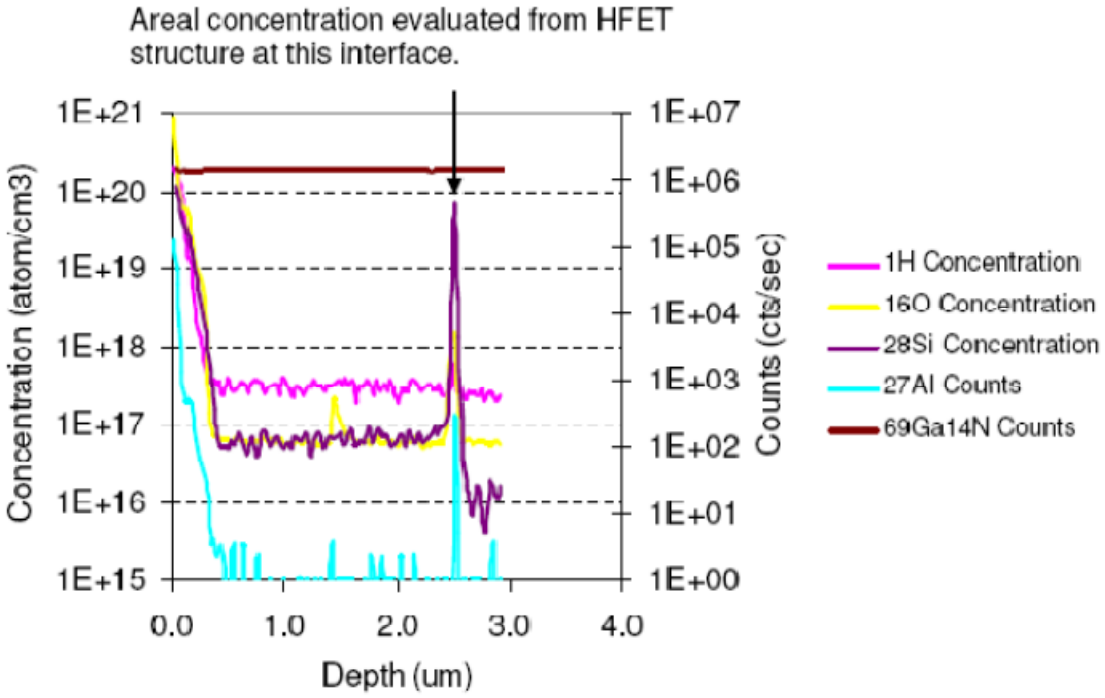


Figure 7.2 SIMS analysis confirming atomic silicon concentration at the epitaxy/bulk GaN interface.

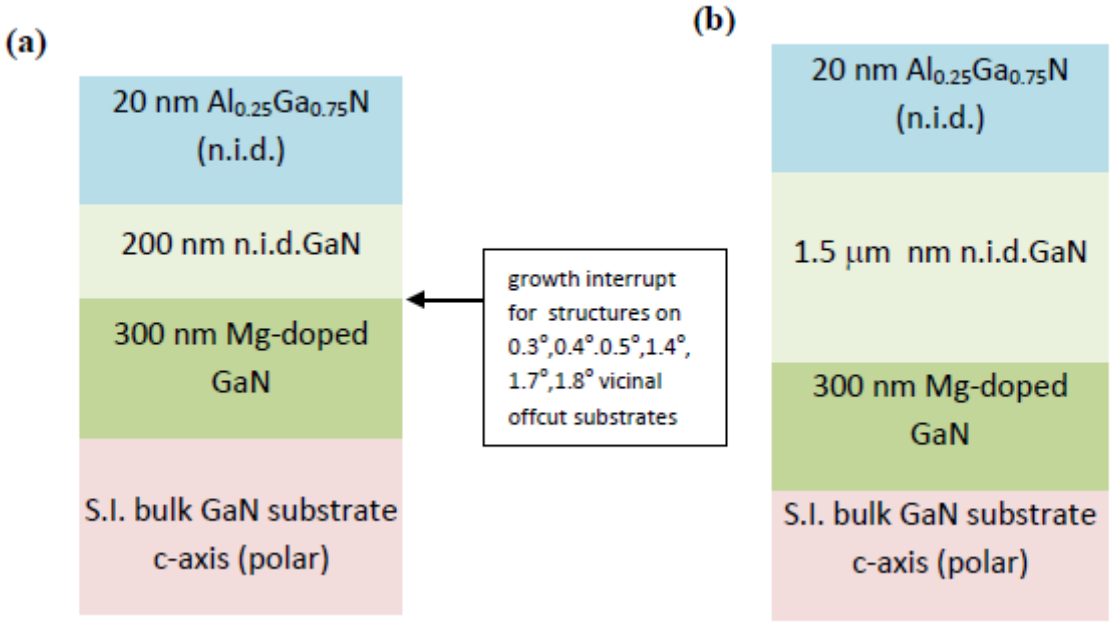


Figure 7.3 (a) Schematic of heterostructure grown on S.I. bulk GaN vicinal substrates. (b) The heterostructure growth on the 0.7° offcut substrate was not interrupted after the p-GaN layer.

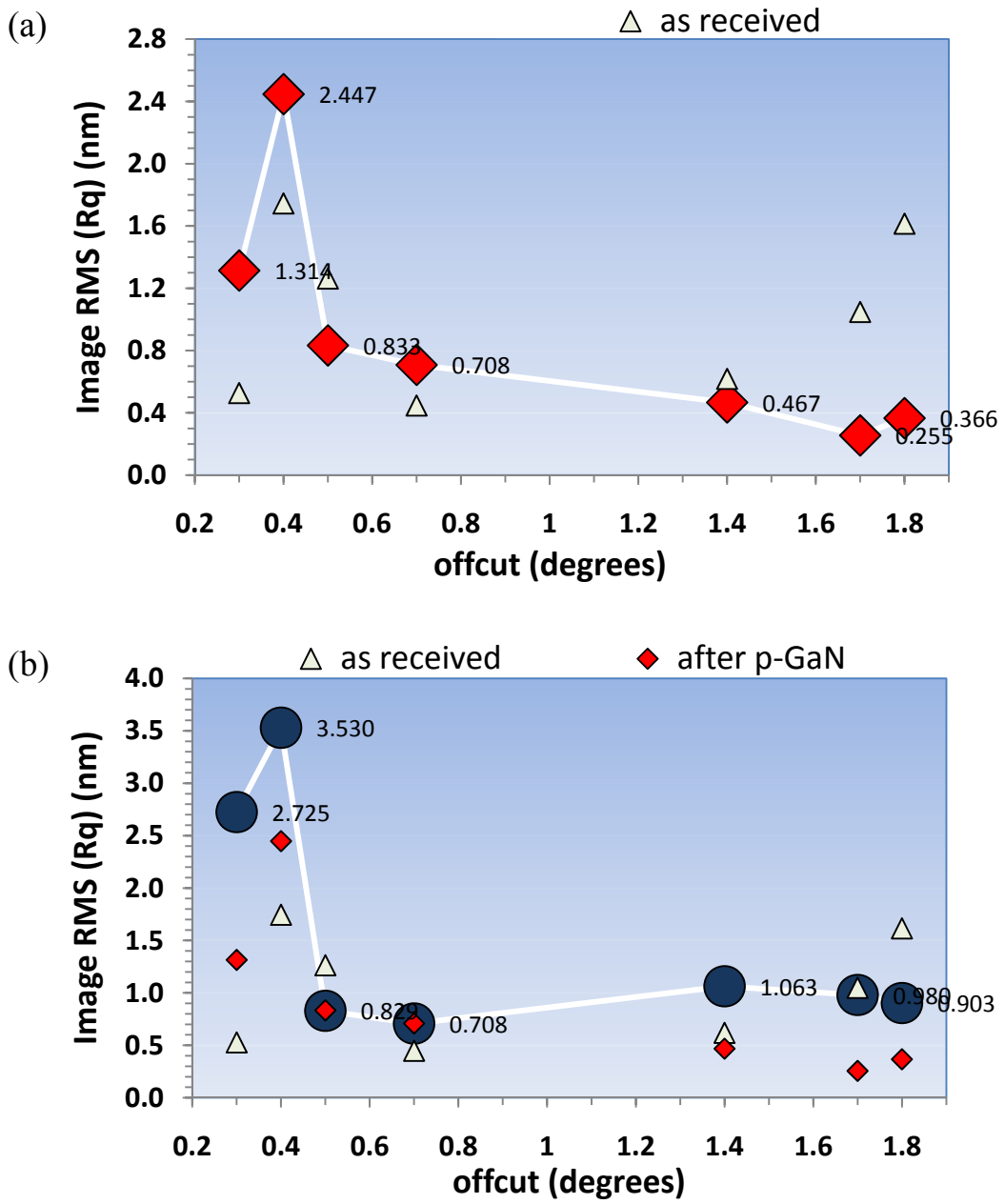


Figure 7.4 (a) AFM RMS roughness data for 10 x 10 μm scans of vicinal substrates as received and after p-GaN growth show increased roughness after p-GaN growth for offcuts of 0.3° and 0.4°. (b) AFM RMS roughness data for 10 x 10 μm^2 scans of vicinal substrates after n.i.d. GaN and $Al_xGa_{1-x}N$ growth show roughnesses ≤ 1.2 nm for offcuts ≥ 0.5°.

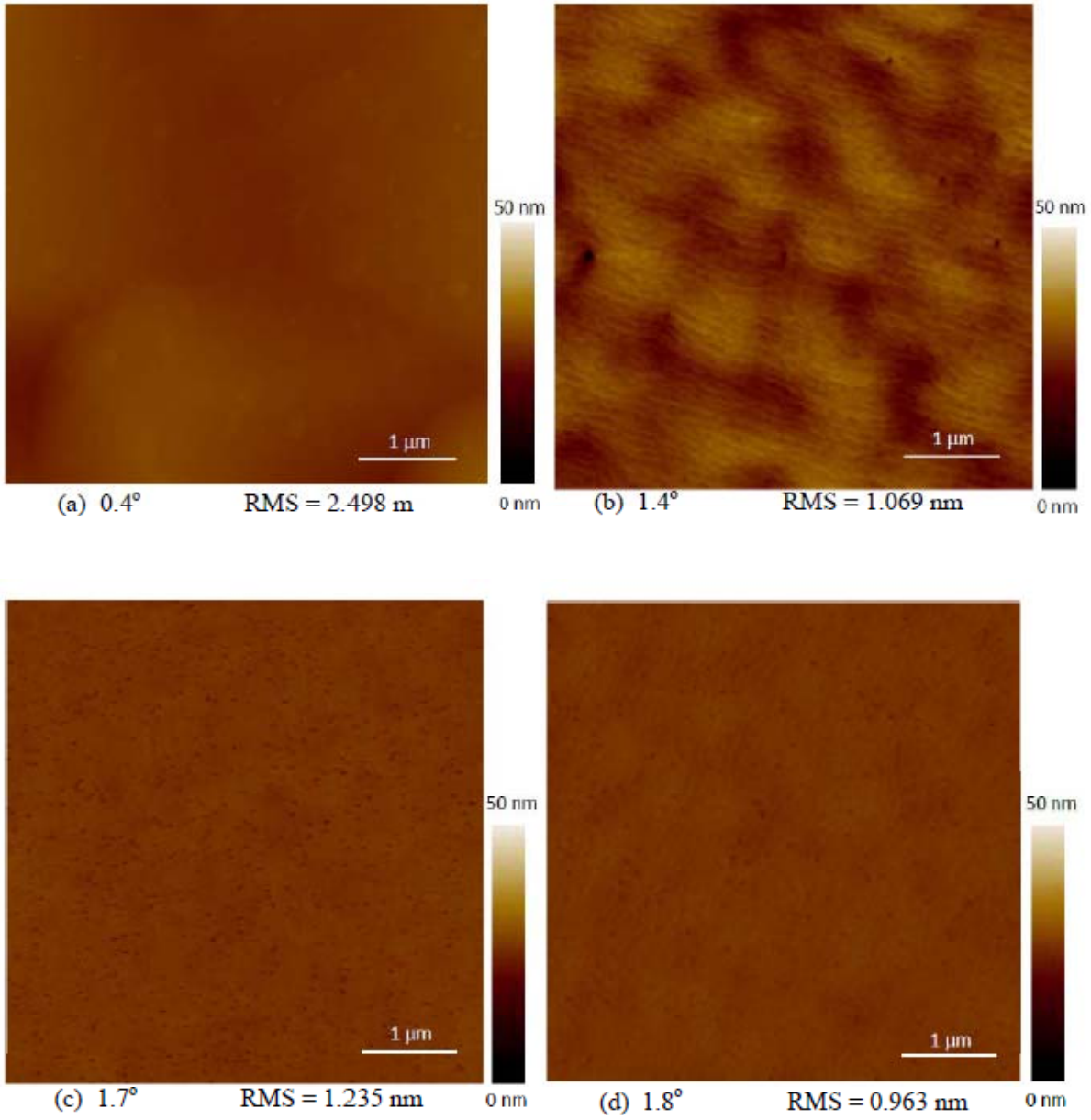


Figure 7.5 (a), (b), (c) AFM scans of AlGaN/GaN heterostructures grown on vicinal substrates with offcut angle as indicated from <0001> toward $<10\bar{1}0>$ and (d) from <0001> toward $<11\bar{2}0>$.

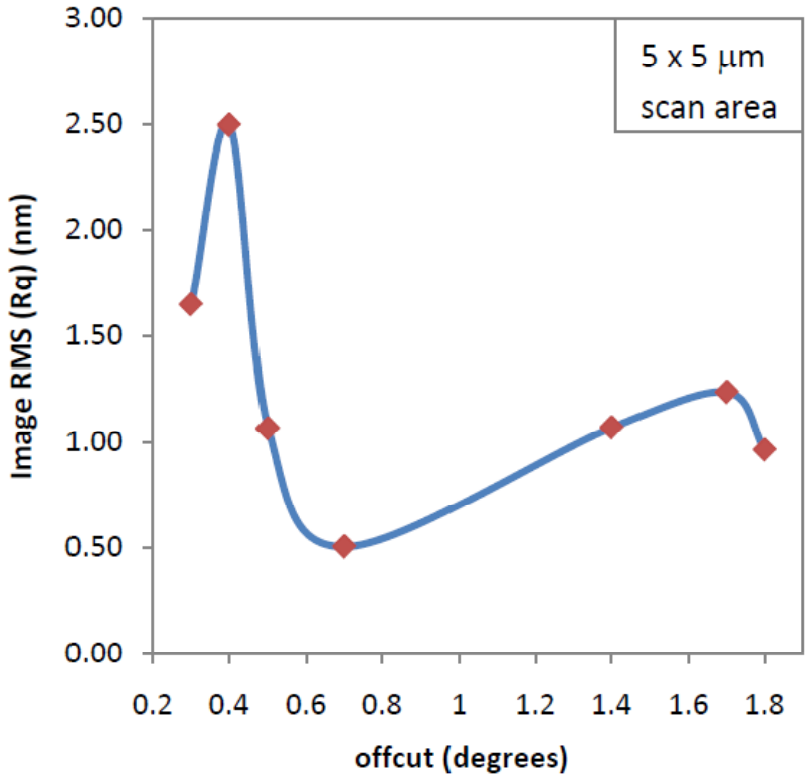


Figure 7.6 AFM roughness analysis after complete heterostructure growth indicates that vicinal substrates with offcut angles between 0.5^{o} and 1.8^{o} had an RMS roughness $\leq$ 1.2 nm.

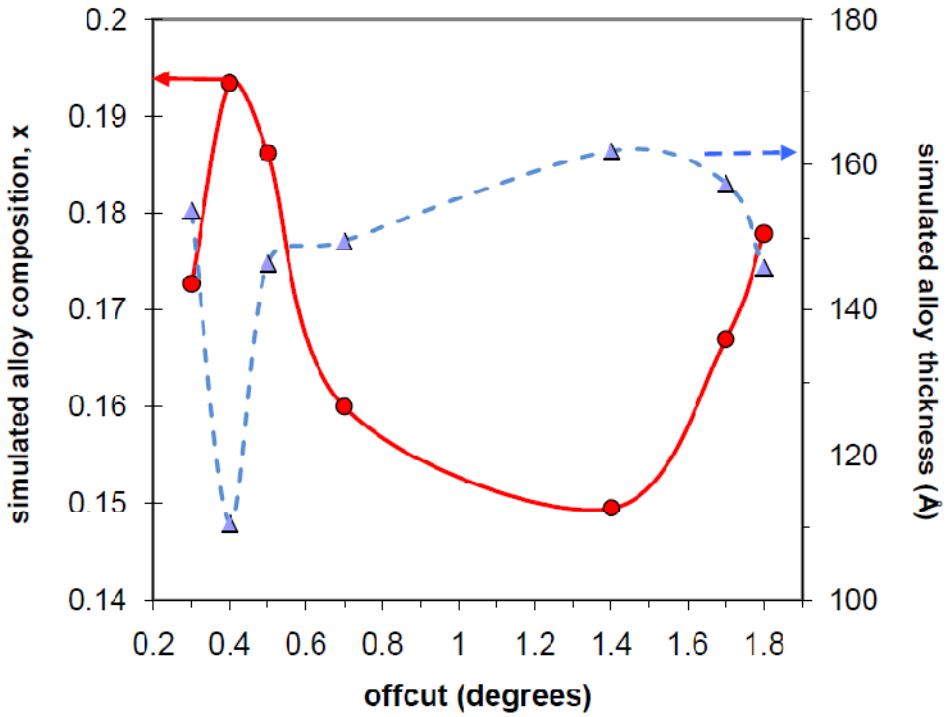


Figure 7.7 Simulated alloy composition and thickness for $Al_xGa_{1-x}N$ barrier.

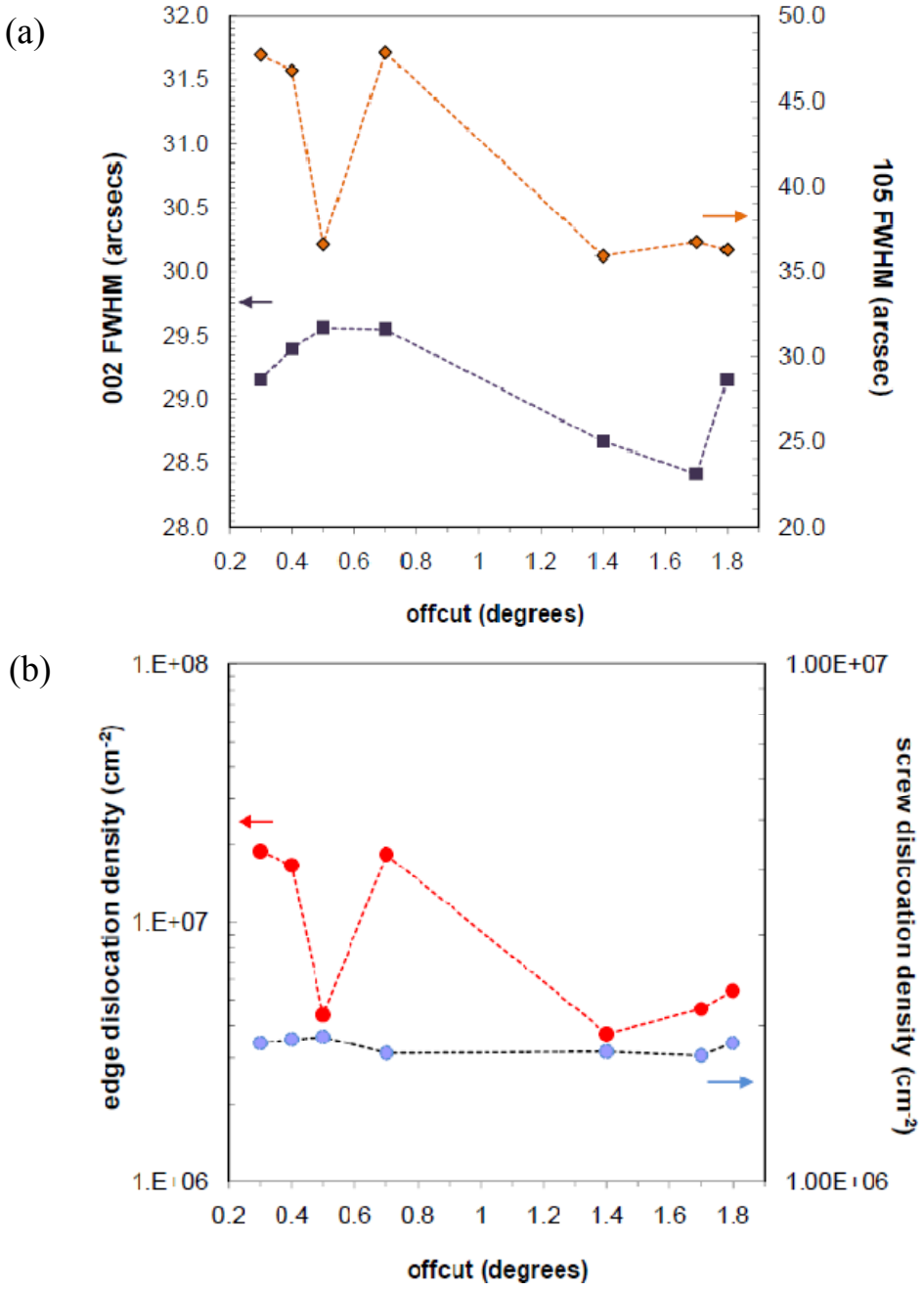


Figure 7.8 (a) FWHM of the symmetric (002) scan is essentially constant for all vicinal substrates studied. The in-plane FWHM decreased for vicinal offcuts $\geq 0.5^{o}$. (b) Screw dislocation density is given directly by β_{002}. Edge dislocation density is a function of both β_{105} and β_{002}.

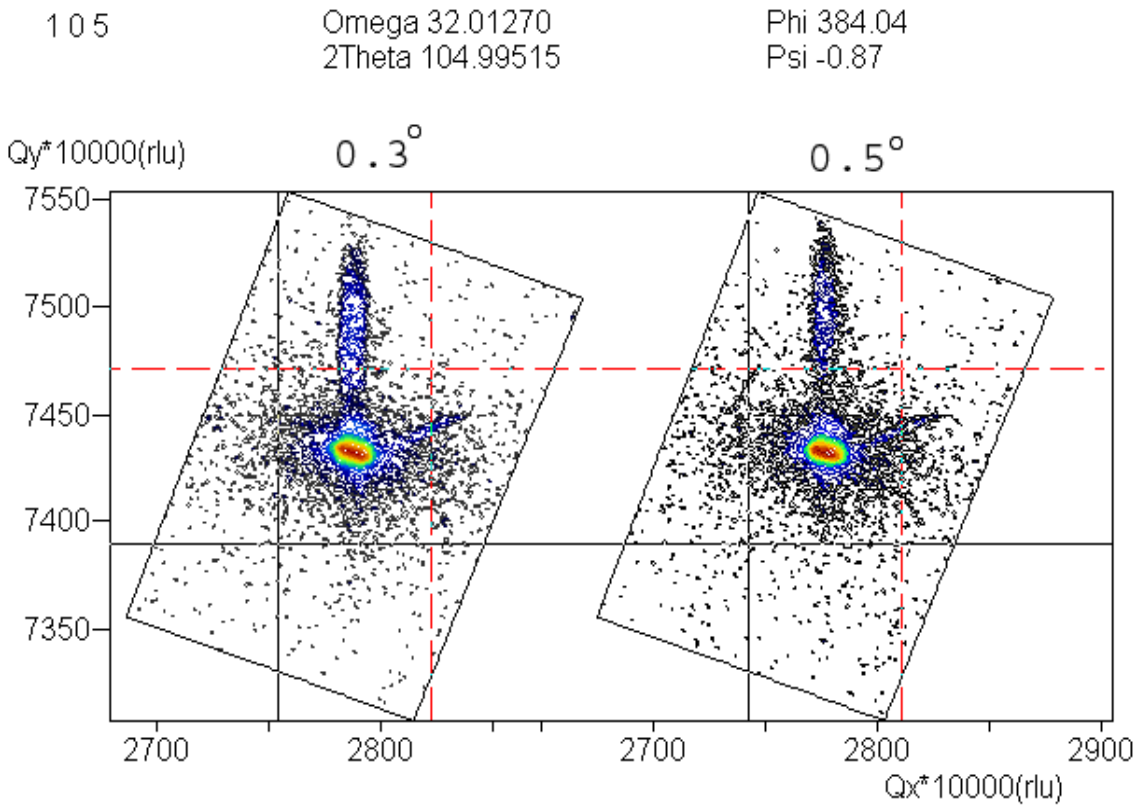


Figure 7.9 Reciprocal space maps for heterostructures show less dispersion in the $Al_xGa_{1-x}N$ film for the higher vicinal offcut.

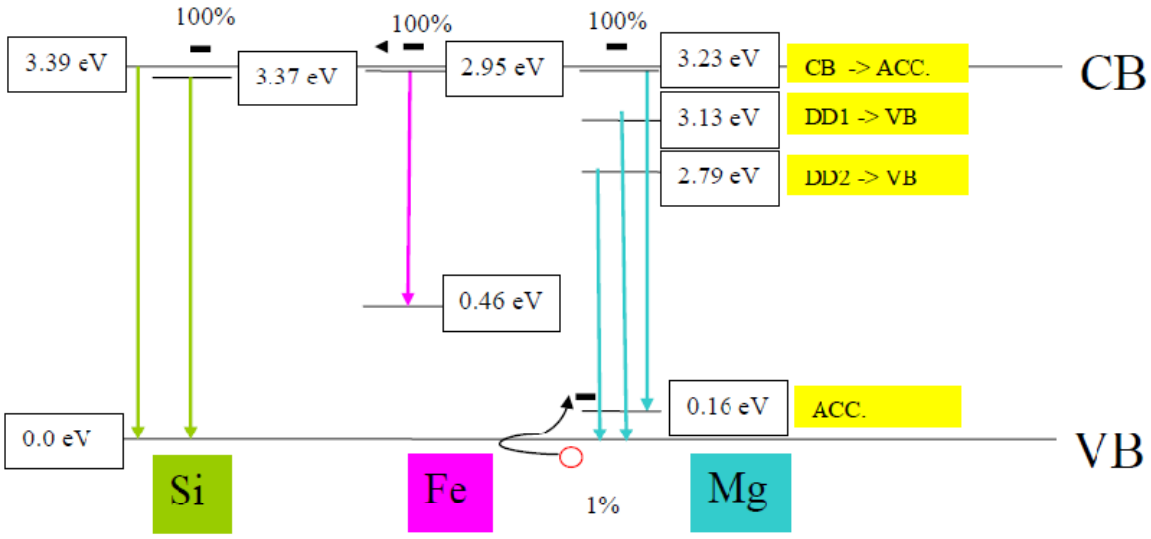


Figure 7.10 Photoluminescence transitions of GaN involve band-to-band, conduction band to acceptor and deep donor 1 to valence band or deep donor 2 to valence band.

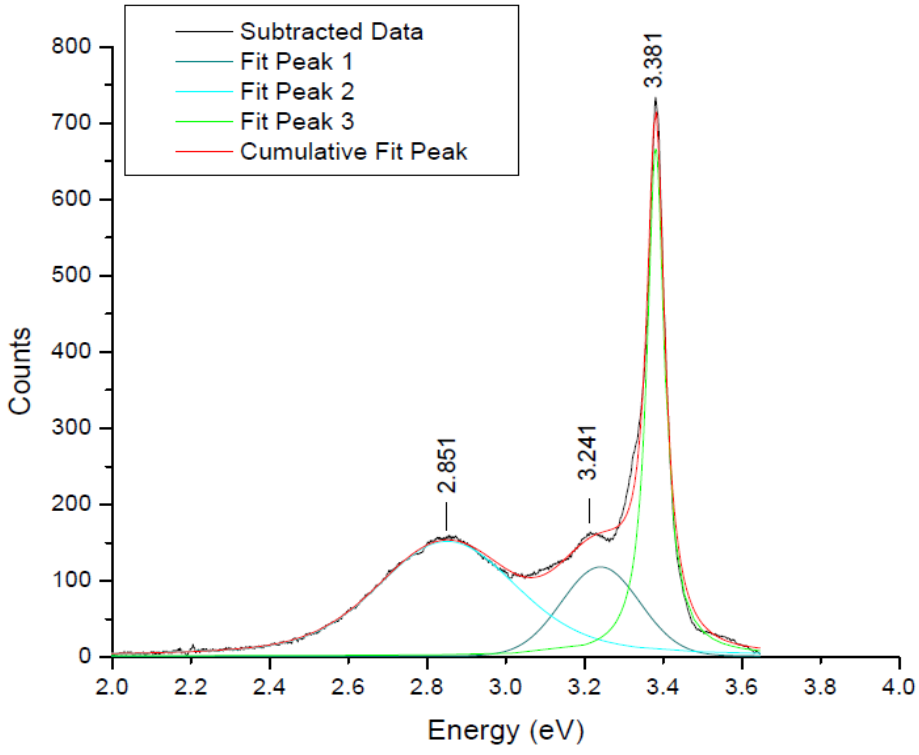


Figure 7.11 Pseudo-Voigt peak fitting analysis was used to locate PL transistions and peak fitting was used to determine the FWHM of each peak.

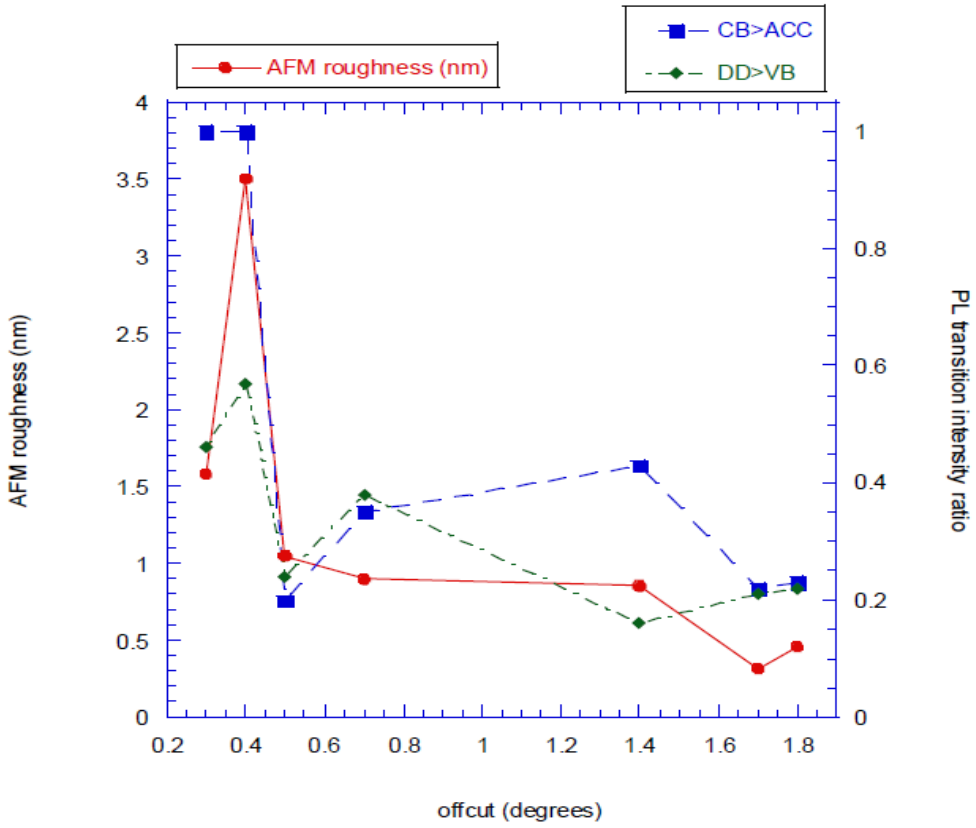


Figure 7.12 Increased magnesium incorporation at lower vicinal offcuts is suggested by increased AFM roughness and increased CB → ACC and DD → VB PL transitions normalized to the BE.

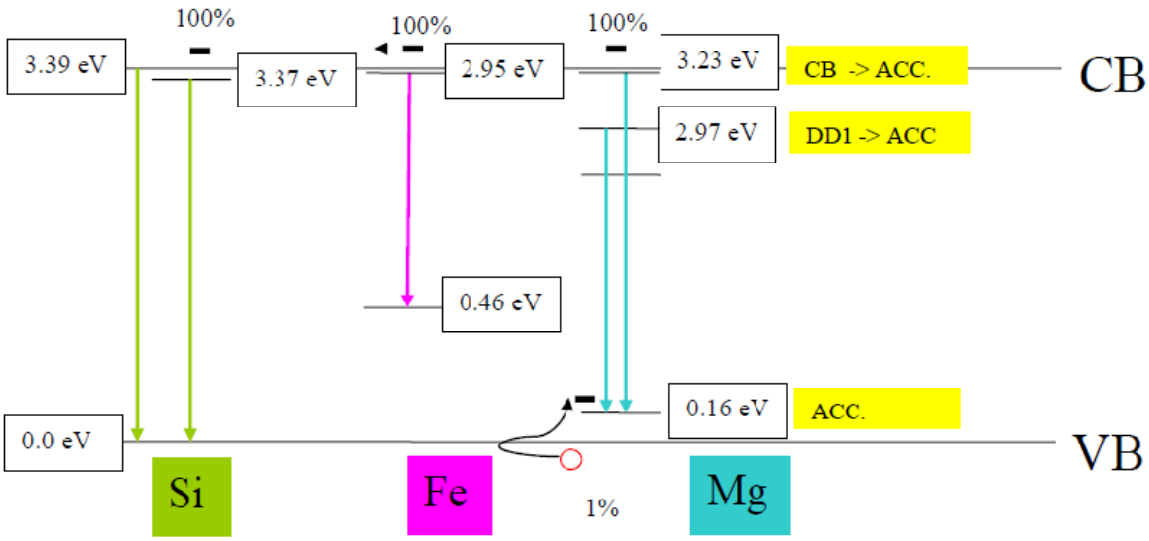


Figure 7.13 Cathodoluminescence transitions in GaN involve band-to-band, conduction band to acceptor and deep donor 1 to acceptor pair recombination.

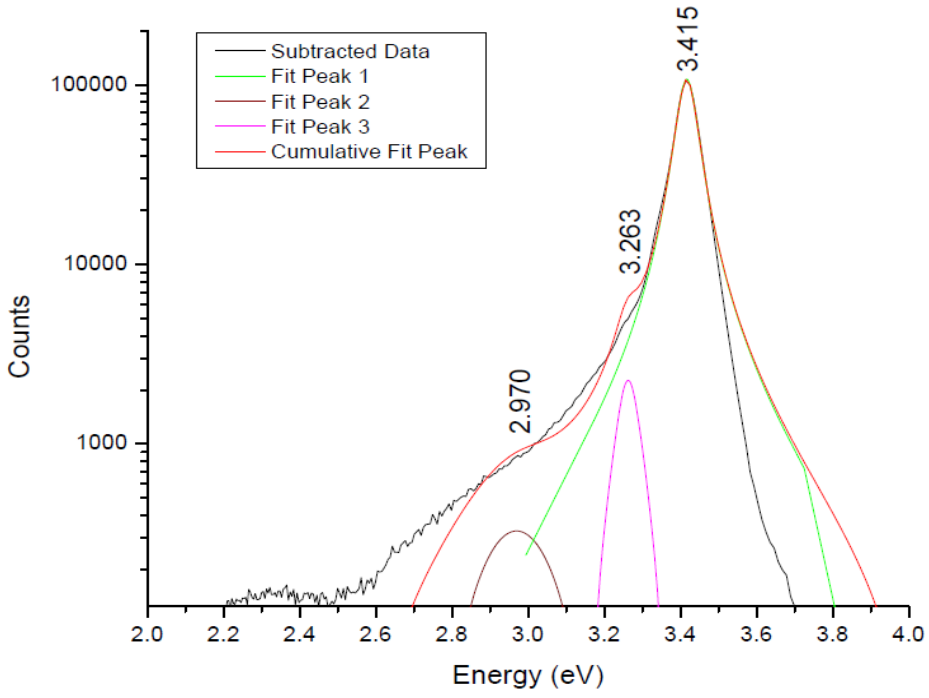


Figure 7.14 Pseudo-Voigt fit of cathodoluminescence transitions in AlGaN/ GaN heterostructure.

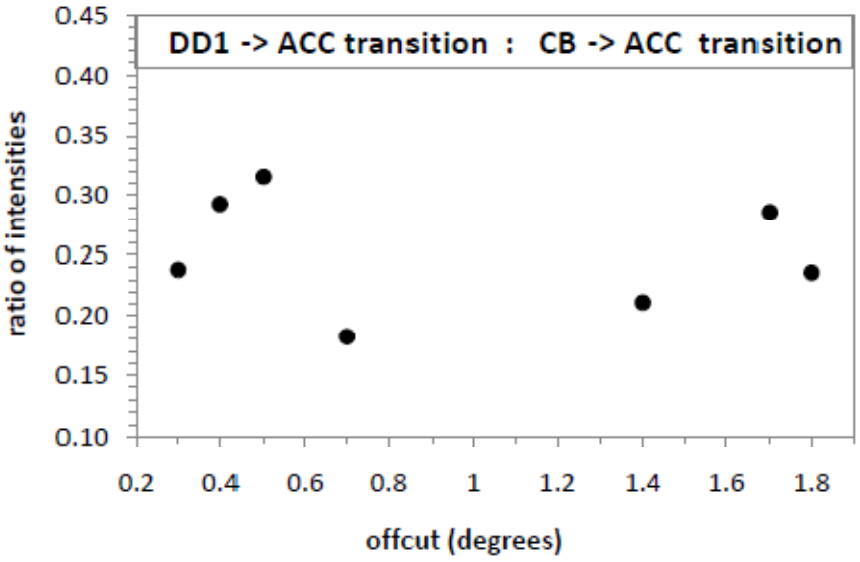


Figure 7.15 The DD → ACC to CB → ACC transition intensity ratio as measured by CL shows no trend with respect to offcut of the vicinal substrate.

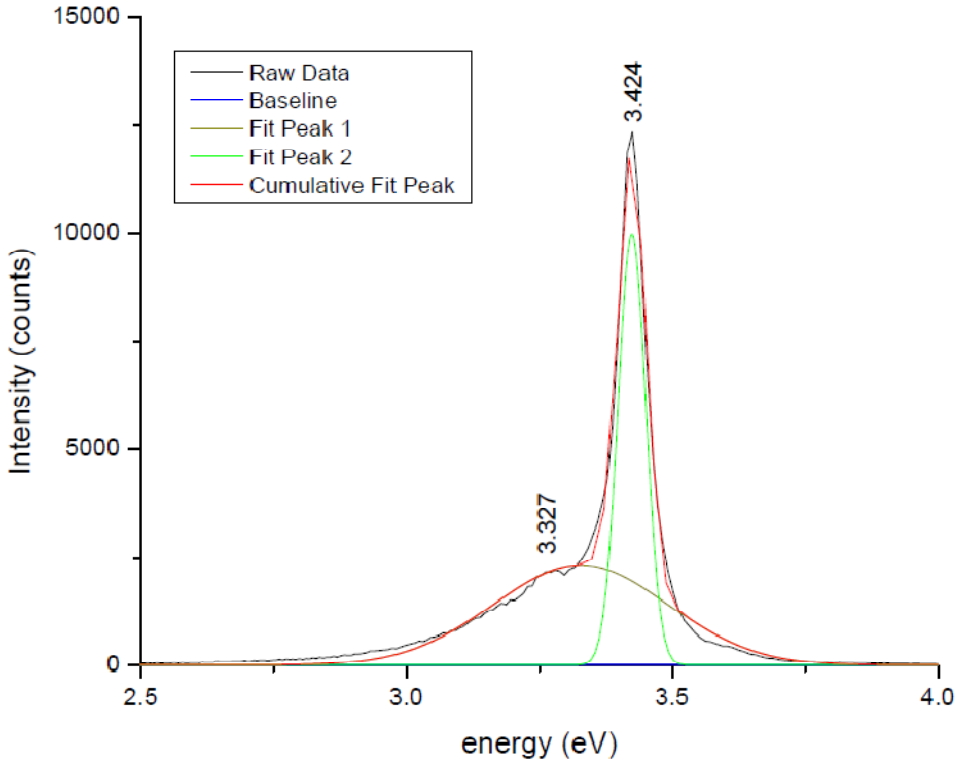


Figure 7.16 Only the CB → Mg acceptor transition was visible for the p-GaN/n.i.d.GaN/$Al_xGa_{1-x}N$ heterostructure growth on S.I. GaN template.

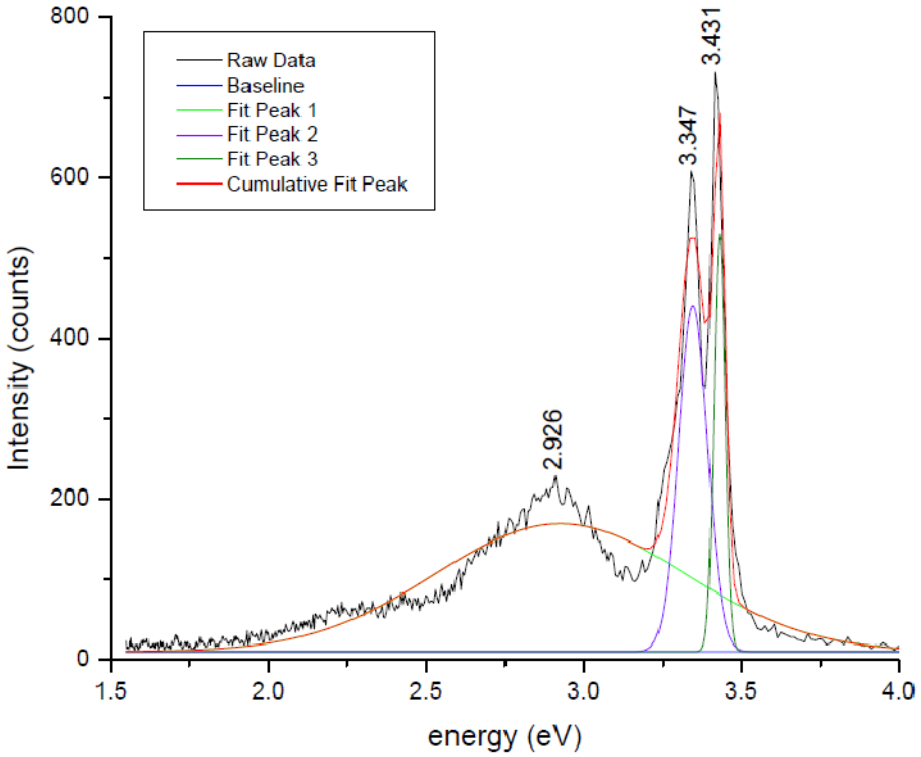


Figure 7.17 $V_N \rightarrow$ VB transition at 3.347 eV and the CB $\rightarrow$ Fe acceptor transition at 2.926 eV were observed for growth of a heterostructure with1.5 µm of n.i.d. GaN followed by 20 nm $Al_xGa_{1-x}N$ barrier on a S.I. GaN template.

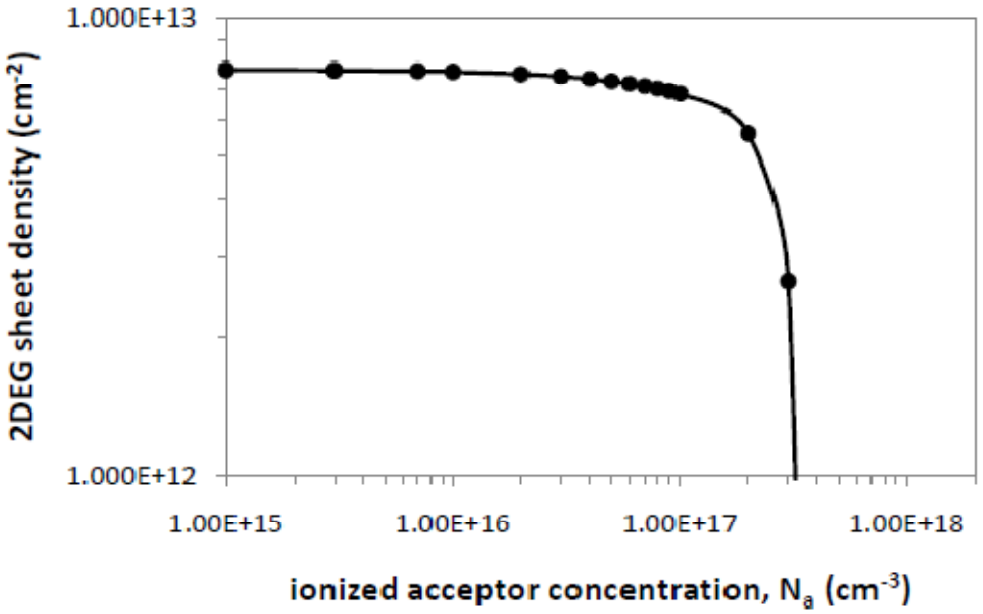
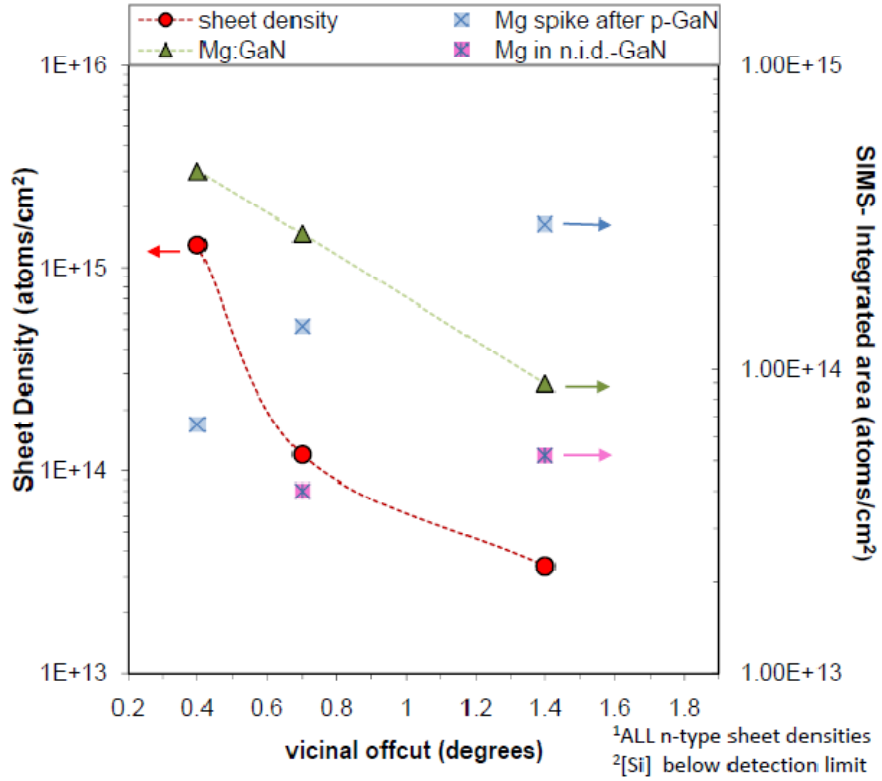


Figure 7.18 2DEG sheet density for heterostructures of Fig. 7.3(a), calculated by Poisson solver, is maximum for an ionized acceptor concentration of 1 x 10^{15} cm^{-3} and drops precipitously for ionized acceptor concentrations exceeding 1 x10^{17} cm^{-3}.

(a)



(b)

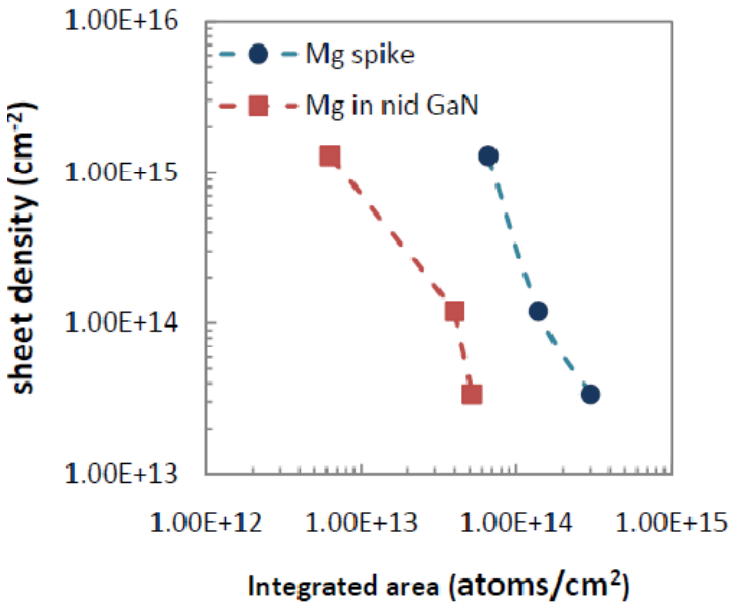


Figure 7.19 (a) Hall sheet density correlated to SIMS integrated area for Mg in layers described in Fig. 7.3(a) and (b) as a function of vicinal offcut. (b) Hall sheet density correlated to SIMS integrated area for Mg spike and Mg in n.i.d. GaN layers.

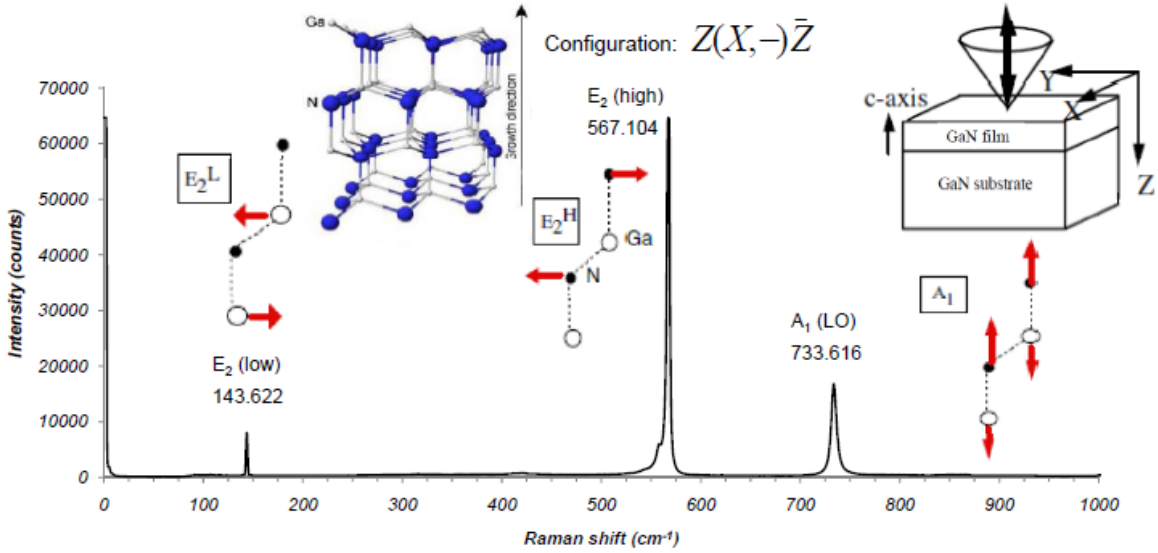


Figure 7.20 Raman selection rules allow three vibrations for the $Z(X,-)\bar{Z}$ configuration, two transverse optical modes: E_2(low) and E_2(high) with atomic displacements perpendicular to the c-axis, and a longitudinal optical A_1 mode with atomic displacement parallel to the c-axis [42].

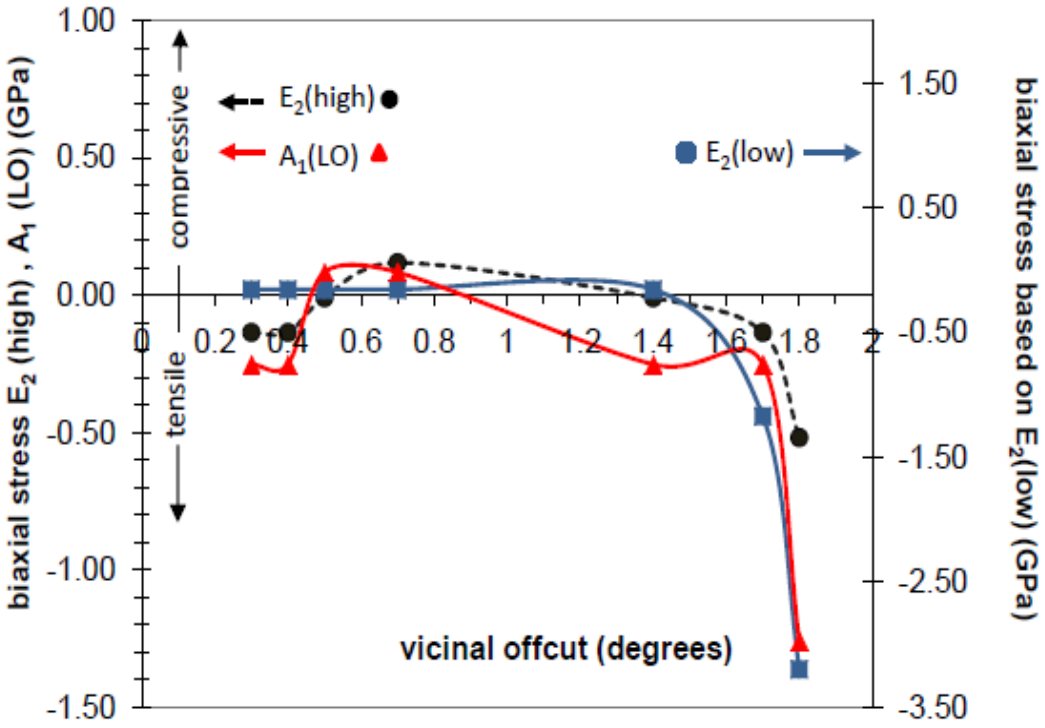


Figure 7.21 Compilation of biaxial stress based on internal stress rates for the E_2(low), E_2(high) and A_1(LO) modes for heterostructures grown on vicinal substrates.

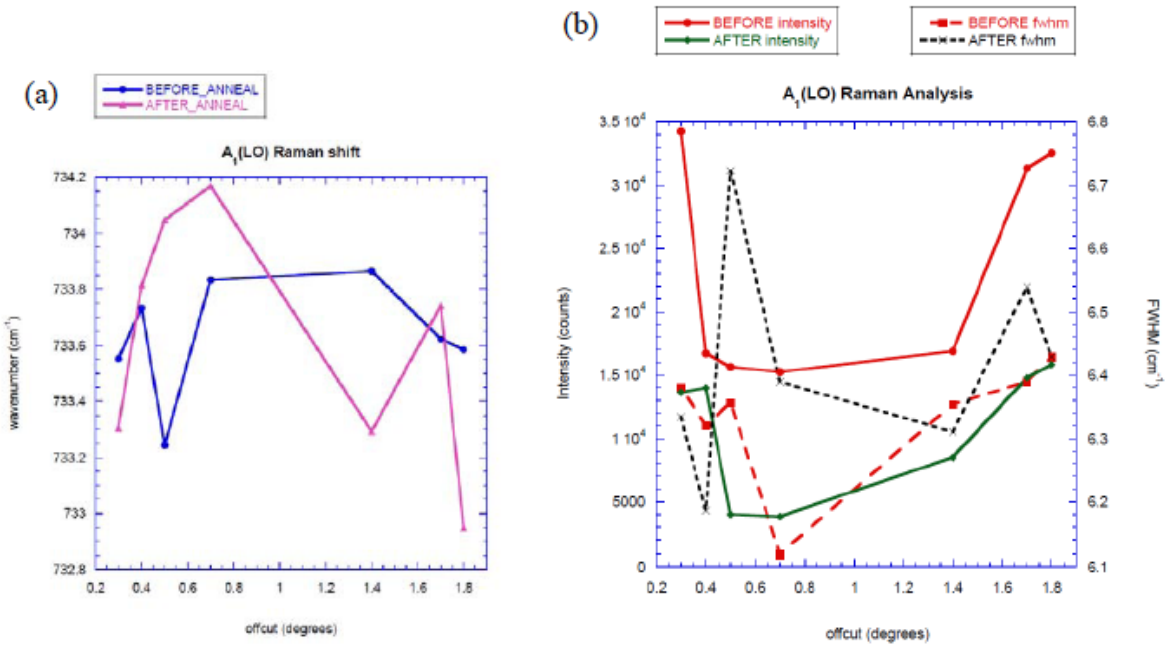


Figure 7.22 (a) A_1(LO) Raman shift and analysis before and after ex situ anneal shows no discernable trend associated with vicinal offcut. (b) Intensity and FWHM of the A_1(LO) mode.

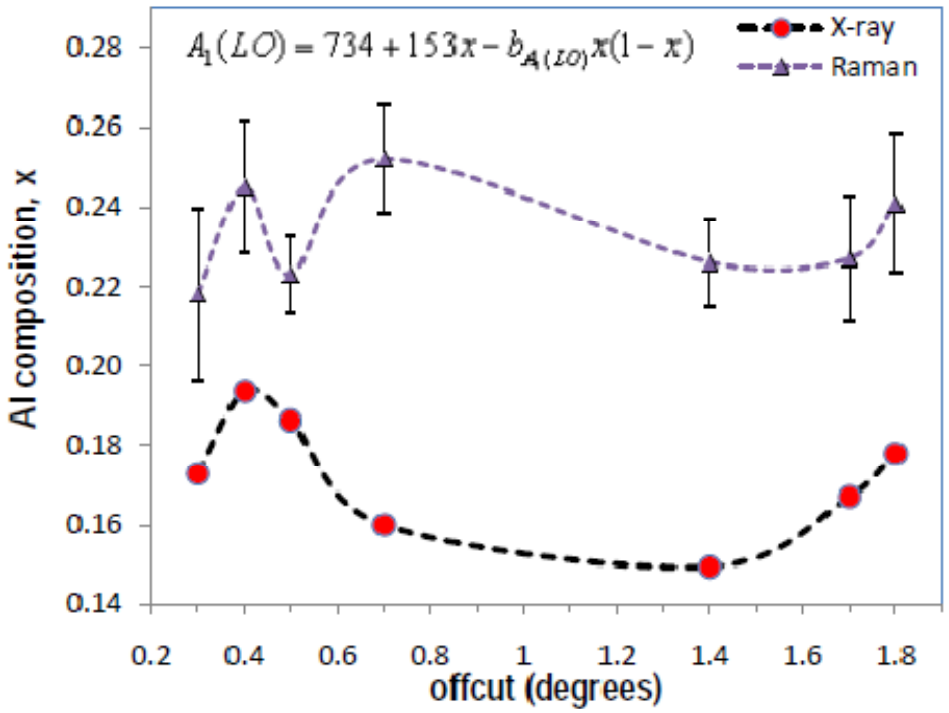


Figure 7.23 The alloy composition predicted by the A_1(LO) Raman shift where b_{A1}(LO)= -75 cm^{-1} [53] was higher than that determined as a function of alloy composition by HRXRD, but the trend was consistent.

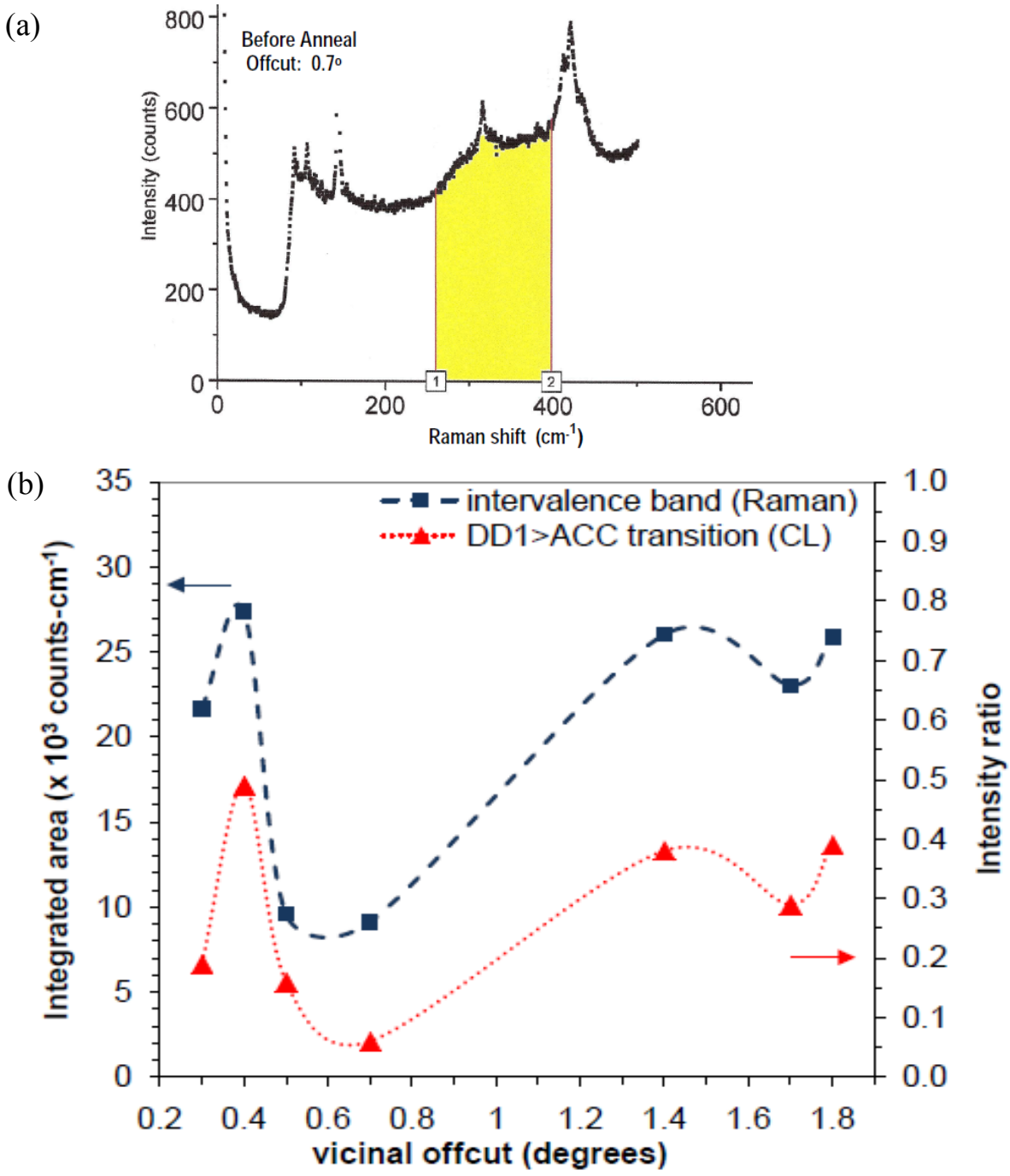


Figure 7.24 (a) Integrated area between 260 – 400 cm^{-1} represents hole density. (b) Raman intervalence band correlates with the DD1 → ACC transition measured by CL.

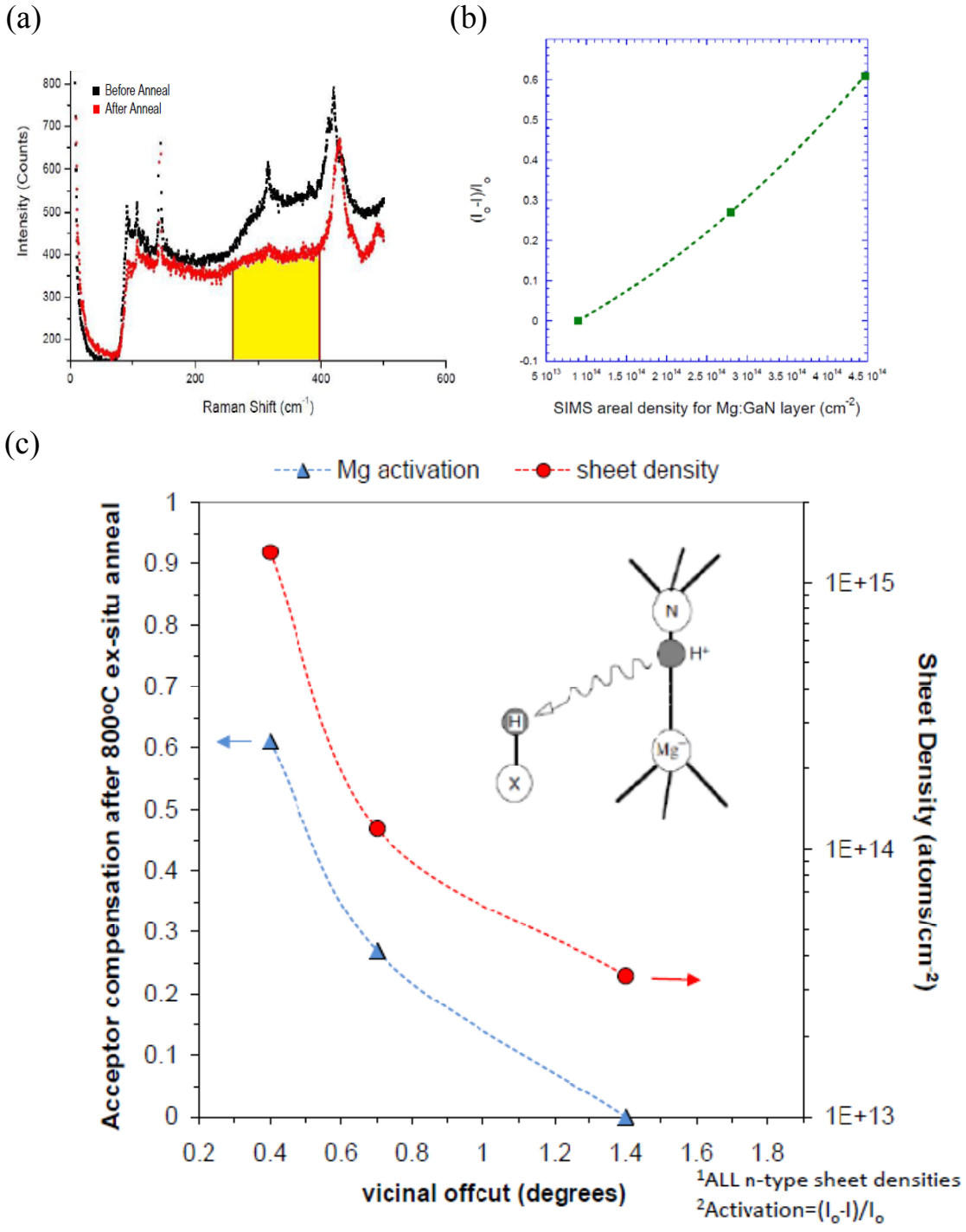


Figure 7.25 (a) Integrated area between 260 – 400 cm^{-1} representing hole density is less after the ex situ anneal. (b) Difference in integrated area relative to SIMS areal density for vicinal offcut substrate. (c) Acceptor compensation assessed by Raman compared to Hall sheet density.

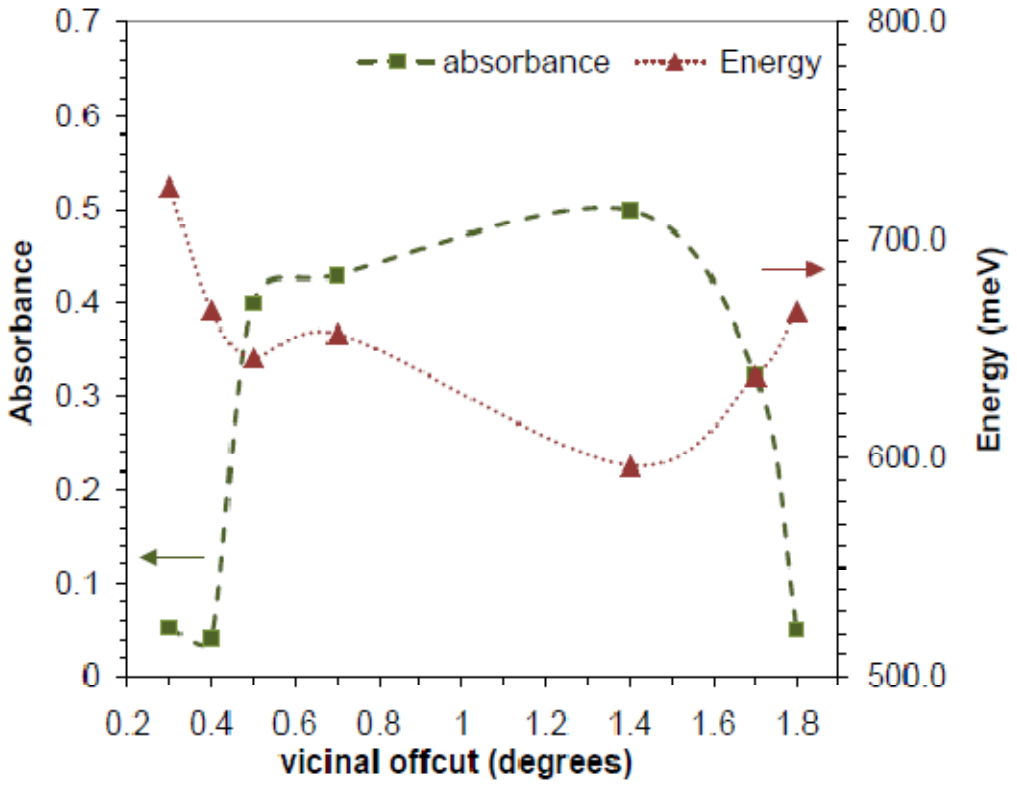


Figure 7.26 Absorbance and energy of the intersubband transition peak.

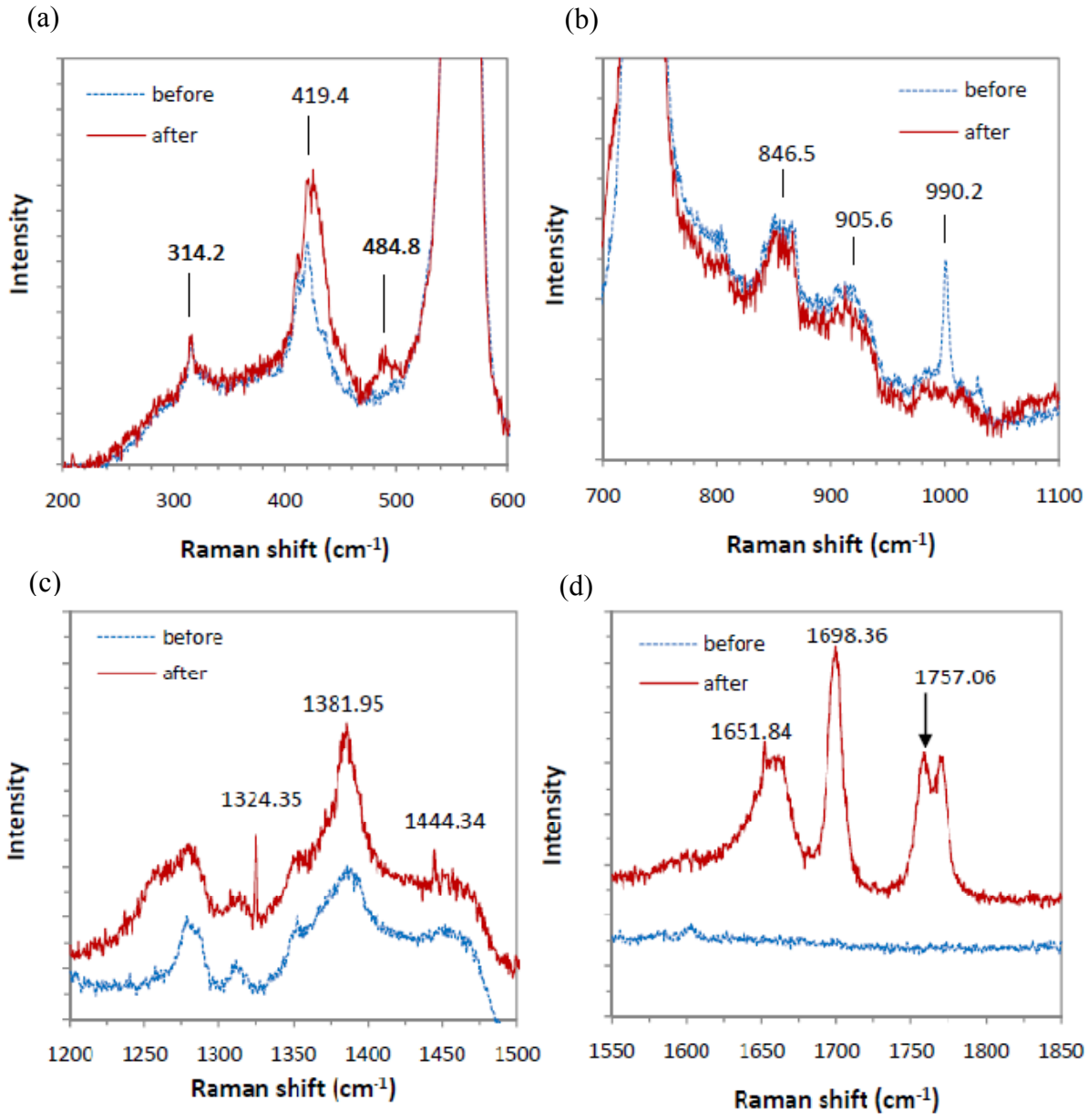


Figure 7.27 (a) L^+ branch of LOPC at 419.4 cm^{-1} before and L^+ branch of LOPC at 484.8 cm^{-1} after ex situ anneal. (b) L^- branch pair of LOPC at 846.5 cm^{-1}, 905.6 cm^{-1} before ex situ anneal. (c) Isolated hydrogen before and after ex situ anneal. (d) L^- branch of LOPC after ex situ anneal.

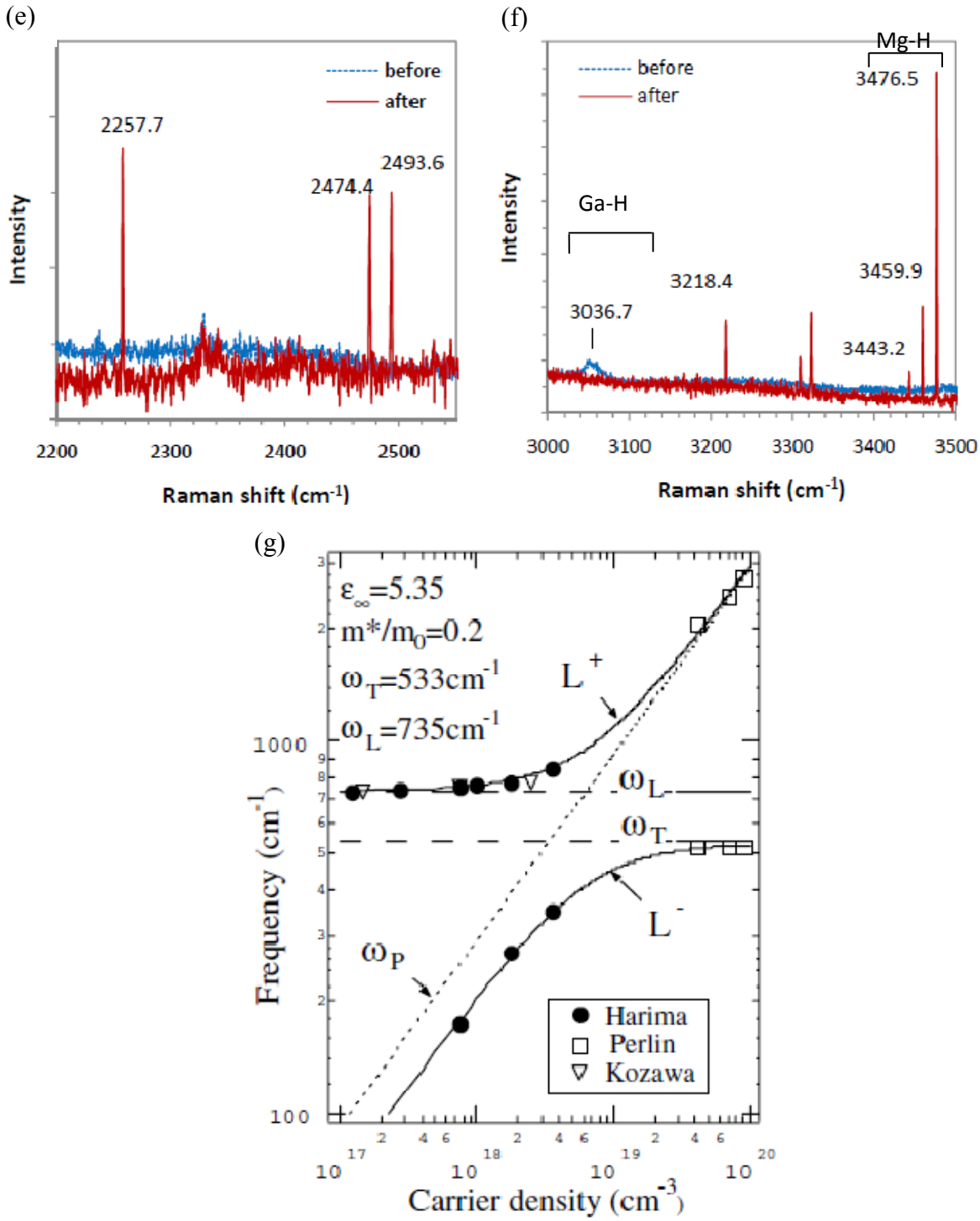


Figure 7.27 (e) Defect LVM asssociated with nitrogen vacancies. (f) Ga-H and Mg-H complexes associated with the NH_3 bending stretch. (g) The carrier density dependence of the axial LOPC-mode frequency in n-type wurtzite GaN [42].

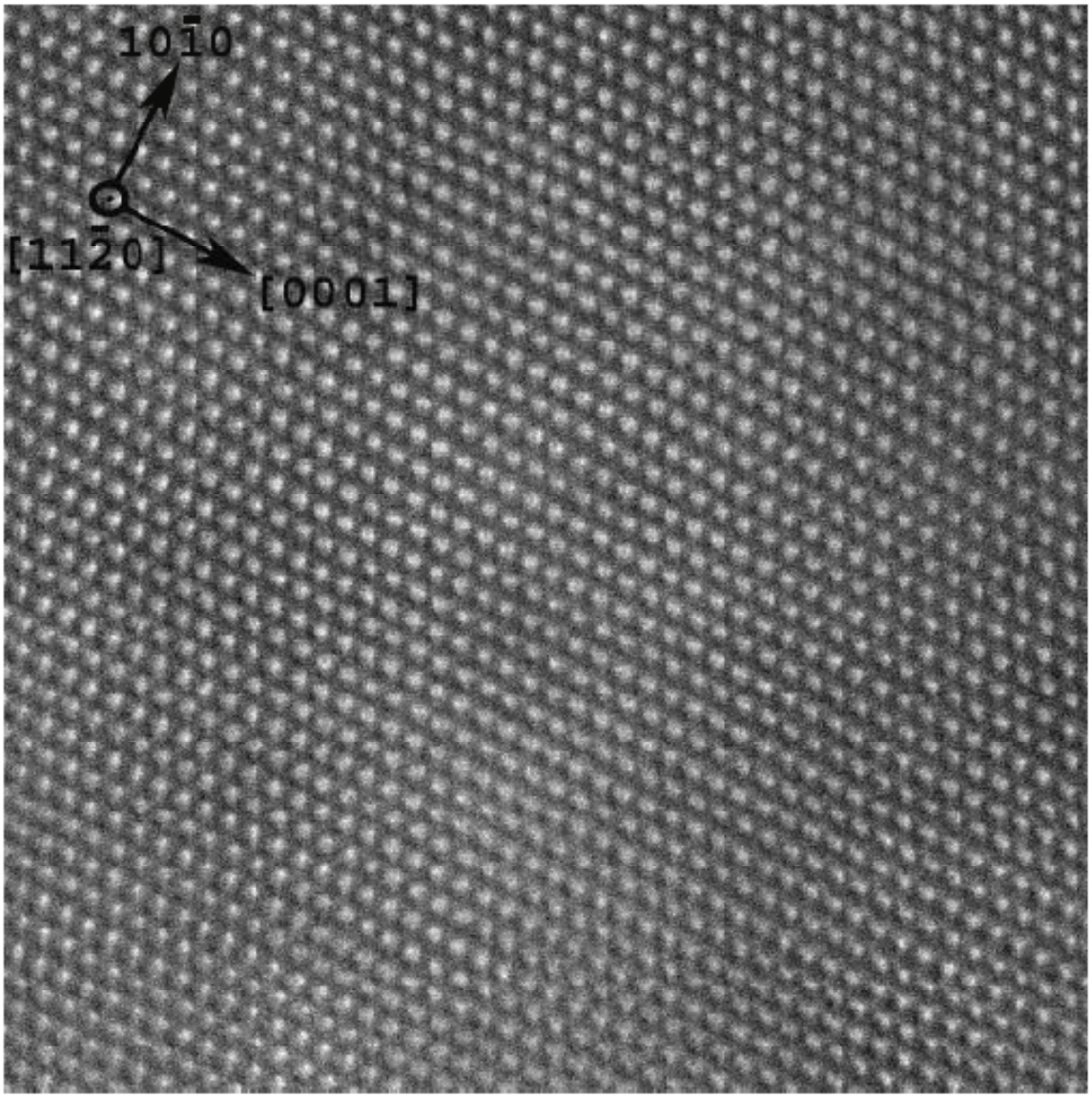


Figure 7.28 High angle diffraction TEM image of GaN buffer for heterostructure grown on a 1.4^{o} offcut substrate. There is no evidence of dislocations or stacking faults.

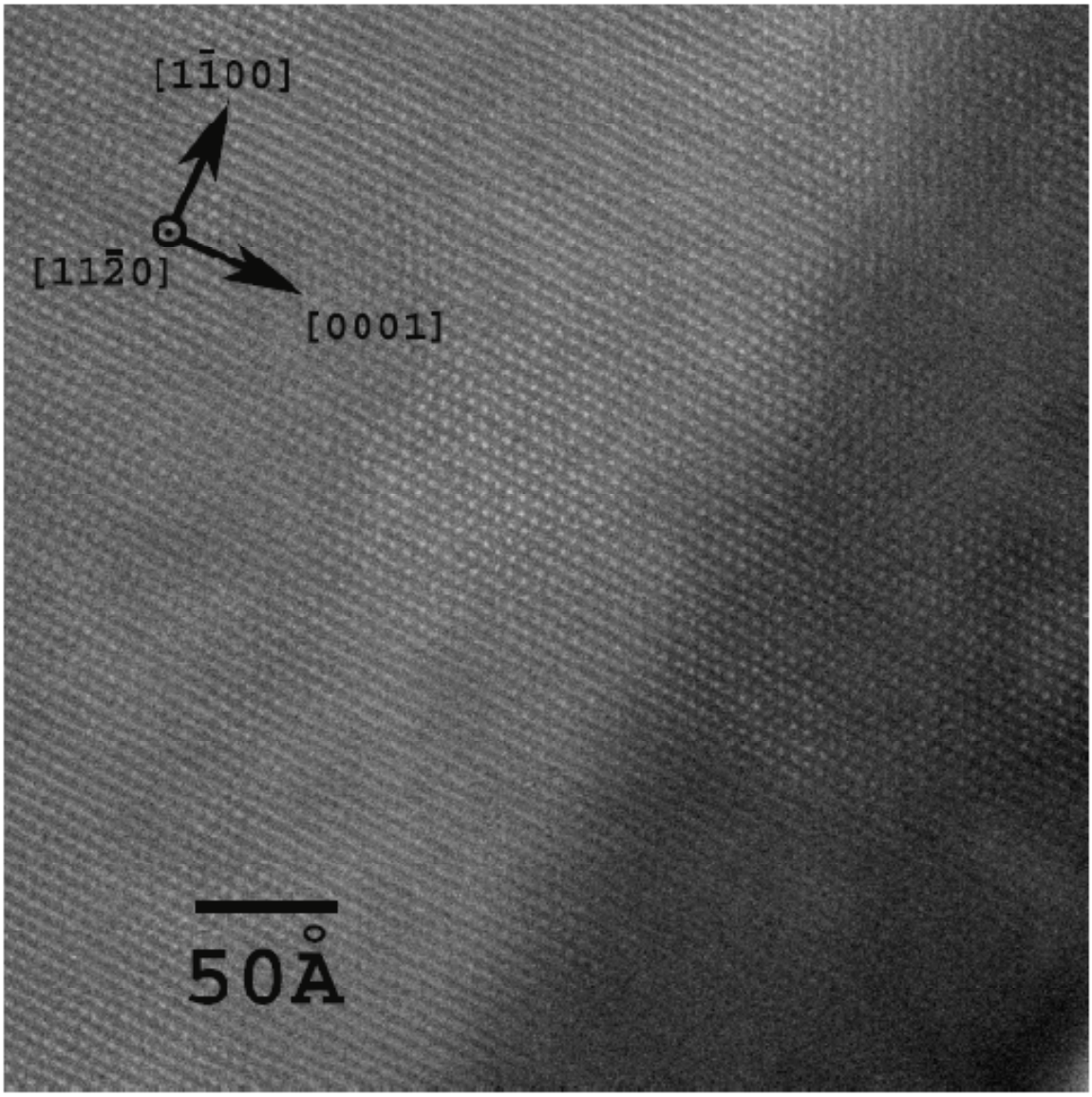


Figure 7.29 High angle diffraction TEM image of GaN/AlGaN interface shows GaN/AlGaN interface roughness >10 Å.

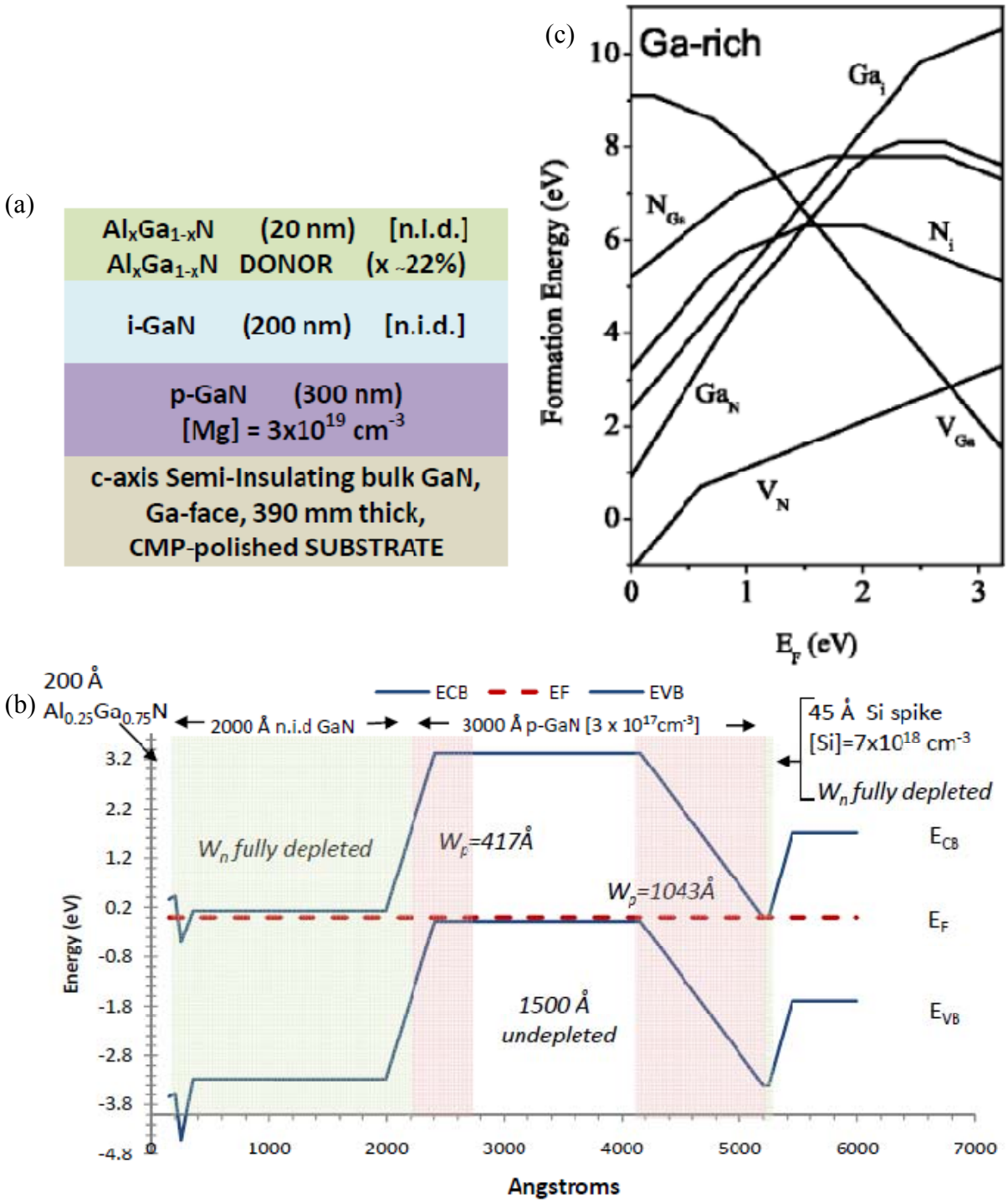


Figure 7.30 (a) Heterostructure schematic, and (b) corresponding energy diagram showing 1500 Å undepleted region where V_N might form as supported by (c) the formation energy diagram [61].

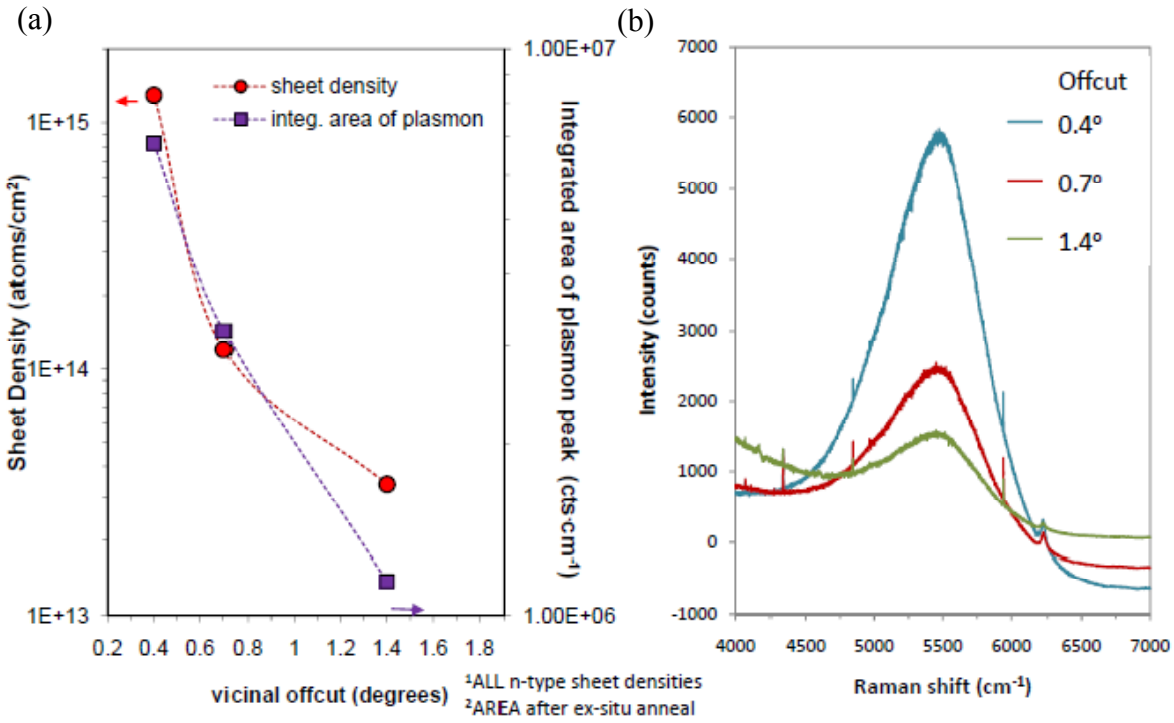


Figure 7.31 (a) Hall sheet density compared to integrated intensity of the intersub-band transition plasmon peak. (b) Intensity of each plasmon peak as a function of Raman shift.

8. PHYSICAL PROPERTIES OF AlGaN/GaN HETERO-STRUCTURES GROWN ON NONPOLAR M-PLANE BULK GaN AND POLAR C-AXIS N-TYPE BULK GaN SUBSTRATES

J.A. Grenko, C.L. Reynolds, Jr., D.W. Barlage and M.A.L. Johnson
Department of Materials Science and Engineering
North Carolina State University, Box 7919, Raleigh, NC 27695

G. J. Duscher
Department of Materials Science and Engineering
University of Tennessee, Knoxville, TN

S. E. Lappi
Department of Chemistry
North Carolina State University, Raleigh, NC 27695

E.A. Preble, T. Paskova, K.R. Evans
Kyma Technologies, 8829 Midway West Road, Raleigh, NC 27617

8.1 Abstract

We report on the growth of $Al_{0.25}Ga_{0.75}N$/GaN heterostructures grown on low dislocation density $(1\bar{1}00)$ and (0001) surfaces of n-type GaN substrates. AFM, PL, CL, HRXRD, SIMS, Hall and Raman spectroscopy have been used to assess structural and electrical properties of modulation-doped nonpolar and polar heterostructures. AFM analysis shows triangular-shaped defects oriented along $[000\bar{1}]$ similar to V-defects seen for GaN growth on (0001) surfaces. HRXRD reveals lower growth rates for heterostructure layers on the $(1\bar{1}00)$ with respect to the (0001) surface but comparable Al incorporation efficiency. Raman spectroscopy reveals minimal biaxial stress for heterostructure growth on m-plane GaN substrates. It has confirmed the existence of vibrational frequencies in nonpolar heterostructures consistent with those measured in polar heterostructures that resulted in nitrogen vacancy formation after an ex situ anneal leading to self-compensation in p-GaN films and an n-type conductive layer in the undepleted region of the p-GaN layer. Room temperature mobility measurements averaging 550 $cm^2V^{-1}s^{-1}$ are consistent for a heterostructure design that incorporated Mg-doped GaN layers at the epitaxial/n-type substrate interface. Hall measurements at 77K have provided insight about the potential deleterious effect of insufficient $Al_{0.25}Ga_{0.75}N$ spacer thickness in the modulation-doped $(1\bar{1}00)$ heterostructure.

8.2 Introduction

Gallium Nitride and the III-N alloy semiconductors are of great promise due to their applicability in both short wavelength LEDs and laser diodes [1] and high-power, high frequency electronic devices such as heterostructure field effect transistors (HFET) [2]. Growth of these devices on native GaN substrates with low dislocation densities, on the order of 10^6 cm^{-2}, should reduce the threading dislocation density in the epitaxial layers which can limit HFET mobilities [3, 4]. AlGaN/GaN HFET structures grown on c-axis bulk GaN benefit from a polarization charge density derived solely from the electric field. This polarization charge density results in high sheet densities (~10^{13} cm^{-2}) and improved two-dimensional electron gas (2DEG) mobilities (>2000 $cm^2V^{-1}s^{-1}$) without the introduction of dopants that can act a potential scattering centers. However, the presence of this polarization charge leads to an inherent 2DEG sheet density that makes the successful fabrication of $Al_xGa_{1-x}N$/GaN enhancement-mode devices on the [0001] bulk GaN substrates difficult to achieve. Therefore, it would be desirable to have a nonpolar AlGaN/GaN HFET which would rely only on the actual doping in the $Al_xGa_{1-x}N$ barrier to generate the two dimensional electron gas.

Anisotropy of the 2DEG mobility, μ_{2DEG}, of AlGaN/GaN HEMTs grown on (0001) 4H-SiC has been observed [5]. Directionally-dependent electrical transport in p-type $(10\bar{1}0)$ oriented GaN films grown by molecular beam epitaxy have given insight as to a possible source of anisotropic scattering in nonpolar and semi-polar films [6]. Hence, there is interest

in studying an $Al_xGa_{1-x}N$/GaN HFET structures grown on an m-plane $(1\bar{1}00)$ bulk GaN substrates in order to separate any benefit of electrical transport anisotropy from the detrimental effects of electron-electron interactions and polar optical phonons at room temperature (RT) and ionized impurity scattering at low temperature by introduction of a dopant impurity. However, the present availabity of m-plane substrates is limited to those with n-type ([Si]=1 x 10^{18} cm^{-3}) which make them unattractive for the fabrication of electronic devices. Therefore, in order to estimate the impact of the Si-doping in the substrate, one must employ n-type (0001) polar bulk GaN substrates, as a control to separate the contribution of the free charge from the substrate as shown in the capacitance-voltage (CV) profile of Fig 8.1 from that associated with the 2DEG.

To obtain high power performance in enhancement-mode AlGaN/GaN HFET devices, it is necessary to improve the AlGaN/GaN interface and the AlGaN surface morphology and to shift $V_{threshold}$ to ensure a zero drain current at zero bias. The use of $(11\bar{2}0)$ GaN substrates for heterostructure growth and its effect on interface roughness is in the early stages of development. It is the intent of this study to assess whether there are improved structural and electrical properties for AlGaN/GaN heterostructures grown on $(1\bar{1}00)$ substrates relative to those grown on (0001) and vicinal offcut surfaces of (0001) substrates.

It is well-known that dopant incorporation and activation in III-V semiconductors are dependent on the substrate orientation, which is related to the atomic species and bonding in the lattice. Since these nonpolar heterostructures must include Si-doping in the barrier, the

incorporation rate of silicon as well as the incorporation rate of Al is important. Atomic force microscopy and high resolution X-ray diffraction will provide surface roughness and strain data, respectively, to assess incorportation rates of Al. Room temperature photoluminescence (PL) and cathodoluminescence (CL) will be used to track the magnesium incorporation in agreement with that measured by secondary electron microscopy (SIMS) as it depends on vicinal offcut. Raman spectroscopy measurements on all heterostructures grown on the nonpolar surface will be correlated with the aforementioned characterization techniques to substantiate conclusions about the growth of AlGaN/GaN heterostructures on nonpolar surfaces relative to those on polar surfaces.

8.3 Experimental Procedure

The AlGaN/GaN heterostructures in this study were grown by organometallic vapor phase epitaxy (OMVPE) in a vertical reactor at 1040^{o}C and 60 torr on 330 μm thick, Si-doped bulk GaN substrates. The n-type m-plane $(1\bar{1}00)$ GaN substrates were grown along the c-axis [0001] in a conventional vertical hydride vapor phase epitaxy (HVPE) reactor at a growth rate of approximately 100 μm/hr to a thickness exceeding 10 mm [7]. The original 3 inch substrates were then sawed in 5 mm increments along the $[1\bar{1}00]$ to acquire a nonpolar surface for growth. The cleaved 5 mm x10 mm m-plane surface was then chemical mechanically polished to generate an on-axis substrate. The offcut angle for the m-plane GaN substrate was 0.1^{o} toward the $[11\bar{2}0]$ and 0.1^{o} toward the [0001]. Atomic force

microscopy measurements of this surface before growth revealed a root mean surface (RMS) roughness $\leq$ 1 nm for 5 x 5 μm^2 scans.

Since free carriers from the n-type substrate can deleteriously affect the 2DEG sheet density and mobility, an HFET structure which included a Mg-doped GaN buffer at the epitaxy/bulk interface was proposed to compensate n-type carriers. That structure is schematically shown in Fig. 8.2(c) along with the complimentary structures grown on semi-insulating (SI) polar GaN and n-type polar (0001) GaN substrates. All heterostructtructures in this experiment were grown in a two step process. The growth interrupt performed after p-GaN growth was intended to mitigate the Mg memory effect [8, 9]. From the substrate, the nonpolar heterostructures consisted of a 300 nm Mg-doped GaN layer, ([Mg]~3 x 10^{19} cm^{-3}), followed by a 200 nm not-intentionally doped (n.i.d.) GaN buffer layer, a 5 nm undoped $Al_{0.25}Ga_{0.75}N$ barrier and a 15 nm n-$Al_{0.25}Ga_{0.75}N$ barrier ([Si]~1 x 10^{18} cm^{-3}).

An in situ nitrogen anneal at 800^{o}C was performed after the Mg-doped GaN layer was grown to dissociate the hydrogen from the acceptors. Atomic force microscopy (AFM) measurements were obtained to assess surface roughness attributed to the Mg-doped GaN. The OMVPE reactor and substrate holder were baked out at 1100^{o}C to remove residual Mg prior to the second growth step. The substrate was reloaded and then the n.i.d. GaN buffer and $Al_{0.25}Ga_{0.75}N$ barriers were grown. As stated previously, n-type (0001) bulk GaN substrates were used as a control to understand the contribution of free carriers from the substrate to Hall measurements compared to those heterostructures previously grown on semi-insultating (SI) vicinal bulk GaN substrates (Fig. 8.2(a)). Therefore, the heterostructure growth sequence for this group of heterostructures was according to the details already

outlined for the nonpolar heterostructures with the exception that the entire $Al_{0.25}Ga_{0.75}N$ barrier was undoped.

AFM measurements were repeated to compare surface roughness differences associated with growth of the n.i.d. GaN buffer and $Al_{0.25}Ga_{0.75}N$ barrier. Heterostructures were analyzed using a Philips X'Pert PRO MRD HR diffraction system (HRXRD) equipped with a hybrid monochromator delivering CuKα X-rays on the incident beam side and rocking curve plus triple axis optics on the diffracted beam side and a five movement motorized cradle. High resolution rocking curves of the $(1\bar{1}0)$ and the (210) reflections of the nonpolar surface were used to generate alloy composition and thickness data. Reciprocal space maps of the symmetric $(1\bar{1}0)$ reflection and the asymmetric (210) were obtained by setting the 2θ angle and then performing a continuouos $2\theta-\omega$ scan as the specimen was rotated in steps of ω to generate a square grid in reciprocal space. Unpolarized, local Raman measurements were then performed using an Horiba Jobin Yvon LabRam ARAMIS. Room temperature measurements were made by focusing a 632 nm laser beam to a 1 mm spot on a sample and detecting the back-scattered light. An 1800 nm grating was used for measurements taken between 0 – 4000 cm^{-1} and a 1200 nm grating was used for the 4000 – 7000 cm^{-1} range. Cathodoluminescence (CL) measurements were acquired with an Oxford MonoCL unit attached to a JEOL JSM 6400 SEM at an accelerating voltage of 5 keV. The light was collected by an elliptical mirror and fiber-optically transferred through 5μm slits to a monochromator and detected with a photomultiplier tube (PMT). Room temperature (RT) photoluminescence (PL) was excited at 325 nm by a HeCd laser with an output power of 20

mW and a 1 mm spot size at the sample surface, analyzed by a double monochromator with a spectral resolution of 1-2 meV, and detected by a lock-in amplifier. After completion of optical measurements, Ni/Au contacts were evaporated on the surfaces patterned with Hall test pads. Each sample was annealed in a nitrogen ambient rapid thermal annealing system for 10 minutes at 800^{o}C to achieve ohmic contact to the semiconductor. Van der Pauw Hall measurements were made on an HMS-3000 Ecopia Hall Effect Measurement system using a 0.55 Tesla permanent magnet. Raman measurements were repeated to assess shifts in vibration introduced by the ex situ anneal. Secondary ion mass spectroscopy, using an O^{2+} primary ion for Si, Mg, Fe analysis was performed. Transmission electron microscopy measurements were acquired with aVG603 microscope equipped with a Nion aberration correcting lens.

8.4 Results and Discussion

8.4.1 AFM

Measurements of nonpolar surface after the 300 nm p-GaN growth showed RMS roughness of 1.993 nm for a 10 x 10 μm^2 scans. The increase in surface roughness relative to measurements taken before growth is consistent with the 1 to 2 nm increase in roughness recorded for growth of heterostructures on vicinal offcut substrates. Measurements of the surface of the nonpolar heterostructure after the GaN buffer and $Al_{0.25}Ga_{0.75}N$ barrier were grown revealed a 1 nm lower RMS roughness for multiple 5 x 5 μm^2 scans. This observation is consistent with the lower film roughnesses reported for heterostructure growth on vicinal surfaces of (0001) GaN relative to their post p-GaN measurement. AFM images of 5 x 5

μm^2 areas of the complete heterostructure grown on the nonpolar substrate as shown in Fig. 8.3 exhibit an RMS roughness of 0.758 nm. Both the AFM images taken after p-GaN growth and after the GaN/$Al_xGa_{1-x}N$ barrier growth, revealed triangular-shaped defects with tips oriented in the $[000\bar{1}]$ with a density of ~ 4 x 10^8 cm^{-2}. Others [10] have observed similar crystallographic defects for growth on a-plane $(11\bar{2}0)$ surfaces. These defects appear to be less well defined than V defects which are characteristically observed under conditions of kinetically-limited growth of c-plane GaN [11]. The slight rounding of the features suggests that at the V defects were initiated during the island growth and coalescence at the early stage of the p-GaN growth, suggesting that the temperature was not ideal. However, as growth proceeded, the unstable facets of the V defects begin to round out. The V-defect then begins to stretch along the a-axis resulting in the rounded shape of the V and a wider base. One aspect that is unclear is whether the Mg incorporation acted in anyway to promote the initiation of the V defects or to assist in smoothing the facets as growth proceeded. We suggest two alternatives. First, the presence of these defects may serve as scattering centers in the 2DEG channel or conversely, they may provide screening for the 2DEG channel from free carriers at the epitaxy/bulk interface. Since the observed V-defect density is 2 orders of magnitude higher than the defect density observed by panchromatic CL imaging, we suggest that the V-defects are not the origin of edge and screw dislocations found in heterostructures grown on nonpolar $(1\bar{1}00)$ surfaces of GaN.

8.4.2 HRXRD

The d_{hkl} values from the high diffraction angle $(1\bar{1}00)$ and $(20\bar{2}1)$ planes were used to determine the two unknowns, a_{AlGaN} and c_{AlGaN}. The high–angle $1\bar{1}0$ symmetric reflection was used to determine a_{AlGaN} by applying the following equation that relates the d_{hkl} value to the lattice parameters a and c of the hexagonal systems:

$$\frac{1}{d^2} = \frac{4}{3}\frac{h^2 + hk + k^2}{a^2} + \frac{l^2}{c^2} \tag{8.1}$$

The a lattice parameter for $Al_xGa_{1-x}N$ was found as $a_{Al_xGa_{1-x}N} = 3.114$ Å. The high angle 201 asymmetric reflection was used to determine c_{AlGaN} by using Eq. (8.1) and applying the a_{AlGaN} value determined from the symmetric reflection. The c lattice parameter was calculated to be $c_{AlGaN} = 5.148$ Å. The $Al_xGa_{1-x}N$ composition was subsequently found by calculation of the elastic stiffness constants and linearly interpolation using [12],

$$\frac{c_{Al_xG_{1-x}N} - c_0}{c_0} = -2\frac{c_{13}}{c_{33}}\frac{a_{Al_xGa_{1-x}N} - a_0}{a_0} \tag{8.2}$$

where c_0 and a_0 are the relaxed parameters for GaN. The $Al_xGa_{1-x}N$ barrier compositions was determined to be $x = 0.20$. This composition is consistent with results for vicnal surfaces of (0001) bulk GaN with low ($\leq 0.3^o$) offcuts.

The reciprocal space map (RSM) of the symmetric $1\bar{1}0$ reflection is shown in Fig. 8.4. In general, the broadening in reciprocal space for any epitaxial film is due to lattice tilt

and twist. Dislocations, stacking faults and point defects can also contribute to weak diffuse scattering surrounding each spot. Since planes for symmetric reflections have no lateral component, horizontal broadening about the substrate peak arising from changes in composition and strain gradients are not applicable. However, broadening in the vertical direction can be due to small layer thickness, as is the case for our thin AlGaN barriers, or small vertical width of coherently diffracting domains or vertical strain or composition fluctuations. The wavelength, or sample, streak causes the scattering vector to smear out radially from the origin in the +z-direction. The analyzer, or detector, streak smears radially from the origin which is at a 20^{o} angle in our case. The analyzer streak comes from the angular divergence of the incident beam, which causes a small spread in the diffracted beam angle 2θ. Since our heterostructure is in tensile strain with respect to the GaN substrate, the composition of the AlGaN barrier can be determined from its positive $2\theta/\omega$ deviation from that of the substrate.

Since the asymmetric RSM of the 201 reflection (Fig. 8.5) does have a lateral component, the offcut angle of the substrate is immediately evident from the -10^{o} tilt of the wavelength streak. The relatively tight scatter about the substrate peak, in the horizontal direction is consistent with the high degree of broadening observed for epitaxial film growth on nonpolar surfaces. In the same manner as the symmetric RSM, the AlGaN barrier composition can be determined from the positive displacement in $2\theta/\omega$ from the substrate peak.

8.4.3 PL

In OMVPE films, there is site selection for the Mg atom to substitute on either the Ga acceptor site or the N donor site. The interstitial sites and the N substitutional site are higher in total energy than the Ga substitutional site by ~ 1.5 eV. The 325 nm photoluminescence measurements at 300K of heterostructures grown on the nonpolar substrate revealed three peaks per spectra corresponding to the conduction band to valence band (CB $\rightarrow$ VB), conduction band to Mg acceptor (CB $\rightarrow$ ACC), and the conduction band to Ga antisite (CB $\rightarrow$ Ga_N) as illustrated in Fig. 8.6. Each of the spectra was fit and peaks were found by a Gaussian fitting analysis. The CB $\rightarrow$ VB transition 3.354 $\pm$ 0.002 eV is slightly lower than that for c-axis S.I. bulk GaN by 27 meV. The CB $\rightarrow$ ACC transition at 3.199 $\pm$ 0.003 eV corresponds to an acceptor ionization energy of 0.15 eV which is similar to that in the polar surface. The CB $\rightarrow$ Ga_N transition at 2.417 eV corresponds to an acceptor ionization energy of 0.937 eV. The gallium antisite has singlet and doublet states in the bandgap [13]. The substitutional Ga atom forms four covalent-like bonds to the surrounding nearest neighbor Ga atoms, with a Ga-Ga bond length of ~2.1 Å in the neutral charge state [14], which is much shorter than the bond length in bulk Ga (2.44 Å) [15]. In spite of this significant compression, the Ga-Ga bond length is still ~12% larger than the bulk Ga-N bond length (1.85 Å) which is indicative of a large strain [13]. The formation energy of these defects in p-GaN is ~1 eV; therefore, the presence of gallium antisites in our structure is highly reasonable. Photoluminescence measurements as function of temperature and excitation dependence would help to clarify the exact nature of the transitions observed. The intent of this study was to correlate RT photoluminescence behavior with other physical properties of

these $Al_xGa_{1-x}N$/GaN heterostructures grown on nonpolar surfaces, in particular, Mg incorporation in the film. Low temperature PL measurements may be useful in clarifying the absence of the deep donor to valence band (DD $\rightarrow$ VB) and deep donor to acceptor (DD $\rightarrow$ ACC) transitions seen in HFET growth on c-axis S.I. bulk GaN substrates. When the CB $\rightarrow$ ACC and the CB $\rightarrow$ Ga_N transitions were normalized to the band edge to compare intensities of those transitions, the data revealed the transition associated with Mg is 2.3 times that of the one to Ga_N.

8.4.4 CL

The 300K cathodoluminescence measurements of heterostructures grown on the nonpolar substrate only revealed the CB $\rightarrow$ VB at 3.423 ± 0.003 eV and the CB $\rightarrow$ ACC transition at 3.291 ± 0.006 eV. This latter recombination corresponds to an acceptor ionization energy 0.13 eV which is 30 meV less than that observed on the polar surface. The CB $\rightarrow$ ACC transition measured by CL was much weaker than that measured by PL. There was no evidence of the CB $\rightarrow$ Ga_N peak. Peak analysis was performed using a Gauss fitting routine and the CL spectra for the heterostructure growth on the nonpolar substrate is given in Fig. 8.7.

8.4.5 Raman Spectroscopy

Raman scattering occurs in nonpolar films in the crossed-polarization mode relative to that of films grown on c-axis substrates. In this study, the 633 nm He source was used as the excitation source for heterostructure film vibration measurement. Raman spectra were taken in the backscattering configuration with the laser beam along the $[1\bar{1}00]$ of the

nonpolar wurzite structure (x-direction) as well as perpendicular to it (y-direction). The Porto notation for this configuration is $X(Y,-)\bar{X}$. The polarization of the scattered light is denoted (-) as it has not been analyzed. A charge-coupled device, CCD, was used for signal collection. Spectral resolution for the 0 - 4000 cm^{-1} range was dictated by the 1800 nm grating. Raman selection rules allow the A_1 (TO), E_1(TO) and E_2 modes as shown in Fig. 8.8. The A_1 and E_1 modes are both Raman and infrared (IR) active, meaning there is a net difference resulting in a dipole moment, while the two E_2 modes are only Raman active.

The most intense peak measured for the heterostructure grown on the m-plane surface was the E_2(high) shift. We used that Raman shift of that peak for comparative analysis of biaxial stress with polar substrates. The E_2(high) peak position was determined by a Voigt profile. Using a phonon strain-free E_2(high) 567.5+/-0.3 [16] and a biaxial shift rate of 2.9 $cm^{-1}GPa^{-1}$ [17], the biaxial stress evaluated for this 0.1^o offcut substrate was 0.0093 GPa. This negligible biaxial stress is lower than previous values reported for heterostructure growth on low offcut angles (0.3^o, 0.4^o) of vicinal (0001) GaN surfaces. The difference in strain may reflect the absence of Fe (atomic radius = 0.118 nm) compensating centers in the semi-insulating substrates and the localized effect on their vibrational environment.

While the E_2(high) line broadening in polar material was instructive in corroborating HRXRD alloy composition results, the linewidth changes for AlGaN films grown on nonpolar surfaces is poorly approximated by a linear fit [18]. The A_1(TO) phonon line is insensitive to the fluctuation in the Al content, x, except for a small range of compositions of $x \cong 0.5\text{-}0.7$ where the dispersion in the Brillouin zone and the density of the phonon states at

the spectrum edge becomes large enough [18]. Therefore independent confirmation of Al composition was not made for our nonpolar heterostructure.

The Raman shift in vibration frequencies recorded before the high temperature ex situ anneal for the nonpolar heterostructure was similar to that found in the vicinal substrate study [19] in that the 324.93 cm^{-1} mode (Fig. 8.9(a)) representing p-type conductivity as a result of Mg acceptor activation is also observed [20, 21]. The Mg-N local vibration mode (LVM) expected at ~650 cm^{-1} was also **not** seen. The LO-phonon–plasmon coupled modes with a sharp L^- mode at 419.79 cm^{-1} and a corresponding L^+ branch at 849.92 cm^{-1} and 908.99 cm^{-1} [22-26] were visibile in Figs. 8.9(a) and 8.9(b). Molecular nitrogen is present at 999.46 cm^{-1} [27]. It was only after the 800^{o}C ex situ anneal that the molecular nitrogen disappeared and the ~1380 cm^{-1} (Fig. 8.9(c)) mode sharpened and discrete peaks appeared for the LVMs in the 1200 cm^{-1} to 1450 cm^{-1} band. The Ga-H LVM at 3048.6 cm^{-1}, representing a gallium vacancy defect mode [28, 29], was more intense for the nonpolar heterostructure than it had been for the vicinal substrate study but the Mg-H LVM at 3477.6 cm^{-1} [30] (Fig. 8.9(d)) was not intense. Lastly, the absence of lines in the 2200 cm^{-1} – 2500 cm^{-1} [23, 31, 32] band before ex situ anneal spectra indicates that the formation of nitrogen vacancies is primarily driven by the 800^{o}C ex situ anneal.

8.4.6 Hall Measurements

Ni-Au contacts were made to the HFET structure and an ex situ anneal was performed at 800^{o}C in order for the contact to be ohmic as determined by linear I-V measurements. Over the current range of 5 to 10 μA, the measured sheet resistance of 17 Ω/square is indicative of parallel conduction paths for the current. Possible conduction paths

are (a) across the heterostructure film, (b) across the Si charge layer at the epitaxy/bulk GaN interface and (c) through the n-type substrate itself.

A freeware Poisson solver [33, 34] was used to determine the subband energies by solving the Schrodinger equation and the sheet charge density. The program used the method of finite differences to find the one-dimensional band diagram for the heterostructure based on the layers outlined in Fig. 8.2 and including a 45 Å silicon spike at the n.i.d. GaN epitaxy/bulk GaN interface. The sheet densities were determined by varying the ionized Mg impurity in the p-GaN layer. Calculated sheet density in the 2DEG channel maximized at 7.7×10^{12} cm^{-2} and dropped precipitously as the ionized acceptor concentration became $\geq 1 \times 10^{17}$ cm^{-3}.

Room temperature Hall sheet density measurements for heterostructure growth on m-plane substrates showed an n-type sheet density, n_s, of 8.75×10^{14} cm^{-2} and 9.98×10^{14} cm^{-2} with corresponding mobilities of 458 $cm^2V^{-1}sec^{-1}$ and 566 $cm^2V^{-1}sec^{-1}$ respectively (Table 8.1). The high sheet densities measured suggest alternative carrier transport paths to the 2DEG channel. The n_s at 77K was measured as 2.61×10^{14} cm^{-2} with a corresponding 77K mobility of 1399 $cm^2V^{-1}sec^{-1}$. These data suggest that 6.75×10^{14} cm^{-2} carriers freeze-out as temperature is lowered to 77K. Room temperature n_s for the heterostructure grown on the c-axis n-GaN substrate was 6.95×10^{14} cm^{-2} with a corresponding mobility of 537 $cm^2V^{-1}sec^{-1}$ which is comparable to that of the nonpolar heterostructure. However, the 77K sheet density and 2DEG mobility data for this heterostructure was 1.71×10^{14} cm^{-2} with a corresponding mobility of 2540 $cm^2V^{-1}s^{-1}$. These data suggest that 5.24×10^{14} cm^{-2} carriers freeze-out as

temperature is lowered to 77K. It is interesting that the ratio of n_s (77K) to n_s (300K) in both instances is 0.25. The activation energy, E_A, can be determined as follows:

$$\frac{e^{-E_A/k\cdot(77K)}}{e^{-E_A/k\cdot(300K)}} = 0.25 \tag{8.3}$$

An activation energy of 0.02 eV corresponds to the donor ionization energy of silicon suggesting that silicon ionized impurities freeze-out when the temperature is lowered to 77K. We suggest that heterostructures grown on polar and nonpolar surfaces exhibit similar n_s behavior and that the differences in Hall measurements due to Si doping in the $Al_xGa_{1-x}N$ barrier cannot be made based on sheet density measurements. However, the significantly higher μ_{77K} for the heterostructure grown on the c-axis n-type bulk GaN substrate than that μ_{77K} for the nonpolar heterostructure suggests that degraded mobility may be the result of ineffective separation of the 2DEG from the ionized impurities in the n-$Al_xGa_{1-x}N$ barrier because of an insufficient thickness of the undoped $Al_xGa_{1-x}N$ barrier spacer which was the direct result of the lower growth rate on the m-plane surface. SIMS data show there was no significant difference in Mg incorporation in the films grown on the nonpolar [3 x 10^{19} cm^{-3}] relative to that on the polar surface [5 x 10^{19} cm^{-3}]. However, SIMS did reveal significantly lower atomic silicon concentration for the nonpolar substrate, [Si] = 1 x 10^{18} cm^{-3}, while [Si] = 4 x 10^{19} cm^{-3} for the polar n-type substrate. The HRXRD analysis showed comparable Al incorporation rates for the nonpolar versus the polar substrates. Interface roughness at GaN/AlGaN interface of the heterostructure grown on the m-plane substrate was on the order of the atomic radius of a Ga atom. Previous studies have shown RT mobilities of 2065

$cm^2V^{-1}s^{-1}$ [35] for heterostructures grown with thick (≥ 2 μm) n.i.d.GaN buffers without modulation doping in the $Al_xGa_{1-x}N$ barrier. A primary difference in this heterostructure design is incorporation of the Mg-doped GaN layer near the eptixy/bulk interface. Since the mean free path, l_{MFP}, can be equated to the separation distance between Mg atoms, l_{Mg} ,where for a Mg atomic concentration of 1 x 10^{20} cm^{-3},

$$l_{Mg} = \sqrt[3]{\frac{1}{N_{Mg}}} = 2.2x10^{-7} cm. \tag{8.4}$$

Assuming the low field velocity to be v ~3 x 10^6 $cm{\cdot}s^{-1}$, the relaxation time can be estimated as

$$\tau = \frac{l_{Mg}}{v} = 7.3x10^{-14} \text{ sec}, \tag{8.5}$$

from which one can estimate the RT mobility to be

$$\mu = \frac{e\tau}{m_e^*} = 557 cm^2V^{-1}s^{-1} \tag{8.6}$$

with reduced mass for GaN, $m_e^* = 0.23m_e$ where m_e is the rest mass of an electron and e is electron charge. This estimated RT mobility is consistent with measured values for our heterostructures. As in previous analyses [19], we calculate the band diagram for this heterostructure design and find that starting at the AlGaN/GaN heterointerface, the 200 nm GaN buffer is fully depleted of carriers as a result of the p-n junction imposed by the 300 nm p-GaN region. The top 417 Å of the p-GaN layer is likewise depleted. Now, because of the p-n junction at the p-GaN/n-type GaN substrate interface, 1050 Å on the p-side of that interface is depleted of carriers and 210 Å on the n^+-side is also depleted. This

heterostructure design results in an ~1500 Å region of undepleted p-GaN in the middle of the p-GaN layer. In our previous study of heterostructures grown on vicinal surfaces of bulk GaN, we proposed a mechanism whereby nitrogen vacancy formation, initiated by an 800^{o}C ex situ anneal, was responsible for self-compensation of Mg acceptors. However, as seen in Fig. 8.10, the measured RT Hall mobilities for that group, labeled c-axis S.I. bulk GaN, were ≤ 50 cmV^{-1}sec^{-1} suggesting additional scattering mechanisms or increased interface roughness. High interface roughness (~10 Å) was observed in TEM analysis for that study [19]. The lack of improvement in the 77K mobility measurements supports that interface roughness contributed to poor mobility. However, improved LT mobility was found for both nonpolar and polar heterstructures grown on Si-doped substrates. The greater improvement in 77K mobility for polar heterostructures relative to nonpolar heterostructures suggest that ionized impurity scattering from the silicon-doped AlGaN barrier may be a contributing factor. Therefore, at a temperature of 77K, the p-n junctions in our heterostructure are effectively eliminated and impact of the 1500 Å undepleted region is diminished. However, the higher μ_{77K} for the polar heterostructure is the direct result of absence of Si free carrier contribution from the $Al_xGa_{1-x}N$ barrier because the heterostructure design depended solely on polarization doping. However, the low growth rate in the $[1\bar{1}00]$ may have resulted in an inadequate spacer thickness that precipitated a 50% reduction in 77K mobility relative to its polar counterpart (Fig. 8.11(a)). The order of magnitude increase in sheet densities from RT to 77K suggests that free carrier contribution from the bulk substrate is responsible for the higher than expected 2DEG sheet densities (Fig. 8.11(b)).

8.4.7 TEM Analysis

The high angle dark field image in Fig. 8.12 shows a dislocation-free, stacking fault–free area of the GaN buffer in the [0001] zone axis. The absence of stacking faults in this image accentuates the advantage of nonpolar material fabricated by bulk GaN growth in the [0001] direction and subsequent slicing to produce the $(1\bar{1}00)$ growth surface. The microstructure of heteroepitaxial lateral overgrowth (ELOG) of a-plane GaN grown on r-plane Al_2O_3 substrates has been reported [36] to have stacking faults in the (0001) plane whose density can only be reduced with increasing distance from the window region after ~1mm of [0001] lateral overgrowth. A similar planar defect defect reduction is not seen for $[000\bar{1}]$ overgrowth [36]. This observation confirms a slower growth rate in the $[000\bar{1}]$ and is associated with presence of stable triangular pits oriented in the $[000\bar{1}]$ for heteroepitaxial ELOG growth. Similarly, the low temperature nucleation layer necessary for growth on non-native substrates promotes the formation of stacking faults. Under the island nucleation growth mode at low substrate temperatures, i.e., 500^{o}C, the two-dimensional bilayer (BL) (c=5.16 Å) height islands form on terraces that show triangular shape due to the growth anisotropy of GaN [37]. The fast growing type-A steps ultimately makes the terrace step disappear and they become bounded by slower-growing low energy type B steps. The 180^o orientation of triangular islands on the same terrace are the result of wurtzite ABAB… stacking taking on cubic ABCA… stacking instead. Elimination of the low temperature nucleation layer should eliminate stacking faults and twin boundaries in the GaN film.

Figure 8.13 is a high angle diffraction image of the the GaN buffer, $Al_xGa_{1-x}N$ barrier and protective PdAu and Pt layers that were added to the AlGaN surface during FIB processing. The $Al_xGa_{1-x}N$ barrier was grown under identical growth conditions as the polar heterostructures. The 62 Å AlGaN barrier reflects a significantly reduced growth rate on the nonpolar surface and is indicative that the edge atoms on this slower growth plane have only a single dangling bond [37]. Hence their advance depends on the creation of kink sites and one-dimensional islands. The interface between the GaN buffer and $Al_xGa_{1-x}N$ barrier shown in the high angle diffraction image of Fig. 8.14 is atomically flat within 1-2 Å suggesting that interface roughening of the 2DEG channel **is not** the primary contributor to low RT mobility.

8.5 Conclusions

Our study of $Al_xGa_{1-x}N$/GaN heterostructure growth on $(1\bar{1}00)$ and (0001) GaN substrates by AFM, HRXRD, PL, CL, Hall, TEM and Raman spectroscopy have yielded significant results with regard to measured differences in 2DEG sheet carrier densities and RT and 77K mobilities for modulation-doped versus polarization-charged $Al_xGa_{1-x}N$ barriers. The AFM studies revealed triangular-shaped defects with tips oriented in the $[000\bar{1}]$ which may serve as scattering centers in the 2DEG channel or conversely may provide screening for the 2DEG channel from free carriers at the epitaxy/bulk GaN interface. HRXRD analysis of the $1\bar{1}0$ symmetric and 201 asymmetric reflections indicate that the growth rate on the $(1\bar{1}00)$ surface is a factor of three lower than that for (0001) surfaces. The thinner undoped

$Al_xGa_{1-x}N$ spacer that is a consequence of this suppressed growth rate may have resulted in insufficient separation of ionized impurities in the $Al_xGa_{1-x}N$ barrier from the 2DEG channel.

PL data confirmed the presence of CB to Mg acceptor and CB to Ga antisite transitions in our heterostructures. Since formation energy for the $CB \rightarrow Ga_N$ is ~1eV, the presence of these defects is not unexpected. Their role in parallel n-type conduction paths for our heterostructure design requires futher understanding. Since CL and Raman are both electrical measurements, the confirmation of p-conductivity from luminescence and vibrational analysis is expected. Biaxial stresses of the heterostructure film on $(1\bar{1}00)$ surfaces based on the E_2 (high) mode confirm negligible biaxial stress (0.0093 GPa). This value is lower than that measured for heterstructures grown low angle vicinal offcut surfaces of S.I. c-axis substrates [19].

Based on Poisson solver calculations, unexpectedly high sheet carrier densities were measured. However room temperature and 77K mobilities were consistent with expectations for a heterostructure designed with Mg scattering centers due to a Mg memory effect in OMVPE-grown films. TEM analysis confirmed that layers grown on the $(1\bar{1}00)$ surface have excellent atomic layer smoothness (1-2 Å) and that the deleterious effect of interface roughness scattering could be minimal for optimized growth on nonpolar surfaces. Additional growths are required to optimize the $Al_xGa_{1-x}N$ spacer based on the slower growth rate for m-plane GaN. Careful attention to the details of μ_{77K} as a function of the $Al_xGa_{1-x}N$ spacer thickness would enable that optimization and allow valuable studies in directional electron transport in nonpolar 2DEG channels.

8.6 Acknowledgements

The authors acknowledge Kyma Technologies for the bulk GaN substrates used in this study. Special thanks to Fred Stevie, NCSU Analytical Instrumentation Facility, for the SIMS analysis.

8.7 References

[1] S. Nakamura and G. Fasol (eds.), The Blue Laser Diode (Springer-Verlag, Berlin 1997).

[2] M. Kuzuhara, H. Miyamoto, Y. Ando, T. Inoue, and Y. Okamoto, *Phys. Stat. Sol. (a),* **200** (2000) 161.

[3] D. Jena, A.C. Gossard, and U.K. Mishra, *Appl. Phys. Lett*., **76** (2000) 1707.

[4] D. Jena, and U.K. Mishra, *Appl. Phys. Lett.,* **80** (2002) 64.

[5] N. Nakamura, K. Furuta, X.Q. Shen, T. Kitamura, K. Nakamura, H. Okumura, *J. Cryst. Growth,* **301-302** (2007) 452.

[6] M. McLaurin and J. Speck, *Phys. Stat. Sol.(RRL),* **1** (2007) 110.

[7] K.Y. Lai, V.D. Wheeler, J.A. Grenko, M.A.L. Johnson, A.D. Hanser, E.A. Preble, L. Lui, T. Paskova, and K.R. Evans, *Phys. Stat. Sol. (c),* **5** (2008) 1886.

[8] L.S. McCarthy, I.P. Smorchkova, H. Xing, P. Kozodoy, P. Fini, J. Limb, D. L. Pulfrey, J.S. Speck, M.J.W. Rodwell, S.P. DenBaars, and U.K. Mishra, *IEEE Trans. Electron Dev.,* **48** (2001) 543.

[9] H. Xing, D. Green, H. Yu, T. Mates, P. Kozokoy, S. Keller, S.P. DenBaars, and U.K. Mishra, *Jpn. J. Appl. Phys.,* **42** (2003) 50.

[10] F. Wu, M. Craven, S.-H. Lim, J.S. Speck, *J. App. Phys.,* **94** (2003) 942.

[11] X. Wu, C. Elsass, A. Abare, M. Mack, S. Keller, P. Petroff, S. DenBaars, J. Speck, and R. Rosner, *Appl. Phys. Lett.,* **72** (1998) 692.

[12] T. Takeuchi, H. Takeuchi,S. Sota, H. Sakai, H. Amano, and I. Akasaki, *Jpn. J. Appl. Phys.,* **36** (1997) L177.

[13] C.G. Van de Walle and J. Neugebauer, *J. Appl. Phys.,* **95** (2004) 3851.

[14] J. Neugebauer and C.G. Van de Walle, Festkorperprobleme/Advances in Solid State Physics **35**, edited by R Heilbig (Vieweg, Braunschweig/Wiesbaden, 1996) 25.

[15] R.W.G. Wyckoff, *Crystal Structures* (Interscience Publishers, New York, 1963) **1**.

[16] T. Paskova (ed.), *Nitrides with Nonpolar Surfaces*, (Wiley-VCH, Weinham, Germany 2008), 239.

[17] F. Demangeot, J. Frandon, M. A. Renucci, O. Briot, B. Gil, and R.L. Aulombar, *Solid State Commun.,* **100** (1996) 207.

[18] V.Y.Davydov, I.N. Goncharuk, M.V. Baidakova A.N. Smirnov, A. Subashiev, J. Aderhold, J. Stemmer, T. Rotter, D. Uffmann, O. Semchinova, *Mat. Sci. Eng.,* **B59** (1999) 222.

[19] J.A. Grenko, C.L. Reynolds, Jr., G. J. Duscher, .S. E. Lappi, C.W. Ebert, D.W. Barlage, M.A.L. Johnson, T. Paskova, E. Preble, and K. Evans, to be published.

[20] H. Harima, T. Inoue, S. Nakashima, M. Ishida, and M. Taneya, *Appl. Phys. Lett.,* **75** (1999) 1383.

[21] H. Harima, T. Inoue, Y. Sone, S. Nakashima, M. Ishida, and M. Taneya, *Phys. Status Solidi (b),* **216** (1999) 789.

[22] H. Harima, *J. Phys.: Condens. Matter.,* **14** (2002) R967.

[23] A. Kashner, H. Siegle, G. Kaczmarczyk, M. StraBburg, A. Hoffmann, and C. Thomsen, Appl. Phys. Lett. **74** (1999) 3281.

[24] H. Harima, H. Sakahita, and S. Nakashia, *Mater. Sci. Forum,* **264-8** (1998) 1383.

[25] P. Perlin, J. Camassel, W. Knap, T. Taliercio, J.C. Chervin, T. Suski, I. Grzegory and S. Porowski, *Appl. Phys. Lett.,* **67** (1995) 2524.

[26] T. Kozawa, T. Kachi, H. Kano, Y. Taga, M. Hashimoto, N. Koide, and K. Manabe, *J. Appl. Phys.,* **75** (1994) 1098.

[27] G.V. Chertihin, L. Andrews, M. Neurock, *J. Phys. Chem.,* **100** (1996) 14609.

[28] R.N. Pereira, B. Bech Nielsen, M. Stavola, M. Sanati, S.K. Esteicher, M. Mizuta, *Physica B,* **376-377** (2006) 464-467.

[29] W. Gotz, N.M. Johnson, D.P. Bour, M.D. McCluskey, and E.E. Haller, *Appl. Phys. Lett.,* **69** (1996) 3275.

[30] Y. Okamoto, M. Saito, and A. Oshiyama, *Jpn. J. Appl. Phys.,* **35** (1996) L807.

[31] A. Kaschner, G. Kaczmarczyk, A. Hoffmann, C. Thomsen, U. Birkle, S. Einfeldt, D. Hommel, *Phys. Stat. Sol. (b),* **216** (1999) 551.

[32] M.S. Brandt, J.W. Ager III, W. Gotz, N.M. Johnson, J.S. Harris, Jr., R.J. Molnar and T.D. Moustakas, *Phys. Rev. B,* **49** (1994) 14758.

[33] L. Snider, I.-H. Tan, and E.L. Hu, J. App. Phys., **68** (1990) 2849.

[34] I.-H. Tan, G.L. Snider, and E.L. Hu, *J. App. Phys.,* **68** (1990) 4071.

[35] J.A. Grenko, C.L. Reynolds, Jr., G. J. Duscher, C.W. Ebert, D.W. Barlage, M.A.L. Johnson, T. Paskova, E. Preble, and K. Evans, to be published.

[36] B.A. Haskell, F. Wu, M.D. Craven, S. Matsuda, P.T. Fini, T. Fujii, K. Fujito, S.P. DenBaars, J.S. Speck, and S. Nakamura, *Appl. Phys. Lett.,* **83** (2003) 64.

[37] M.H. Xie, S.M. Seuter, W.K. Zhu, L.X. Zheng, H. Wu, S.Y. and Tong, *Phys. Rev. Lett.,* **82** (1999) 2749.

8.7 Tables

Table 8.1 Comparison of sheet densities and Hall mobilities for heterostructure growth on different substrates.

substrate for heterostructure growth	Room Temperature		77K	
	sheet density, n_s (cm^{-2})	Hall mobility, μ ($cm^2V^{-1}sec^{-1}$)	sheet density, n_s (cm^{-2})	Hall mobility, μ ($cm^2V^{-1}sec^{-1}$)
m-plane n-GaN	9.98E+14	566	2.61E+14	1399
c-axis n-GaN	6.95E+14	537	1.71E+14	2540
c-axis SI-GaN	9.56E+14	45	1.04E+15	35

8.8 Figures

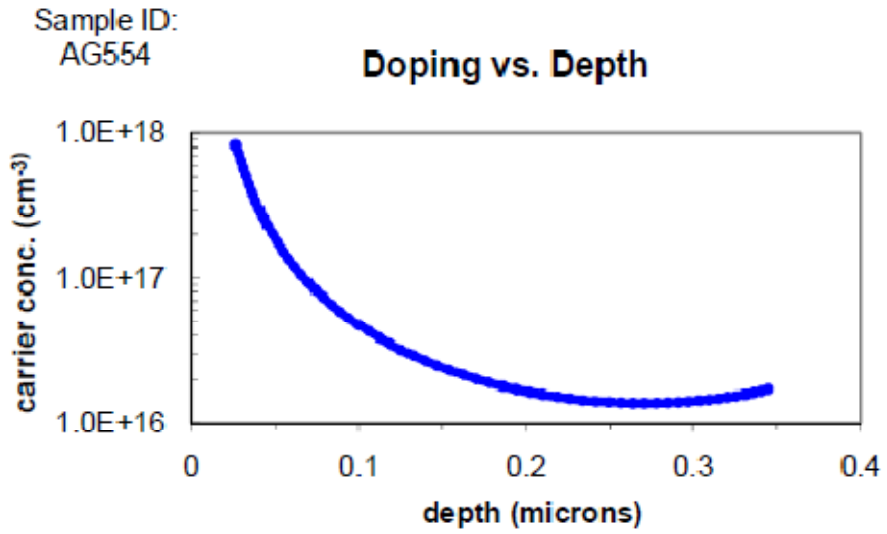


Figure 8.1 CV profile of free carrier concentration versus depth for the n-type GaN substrate.

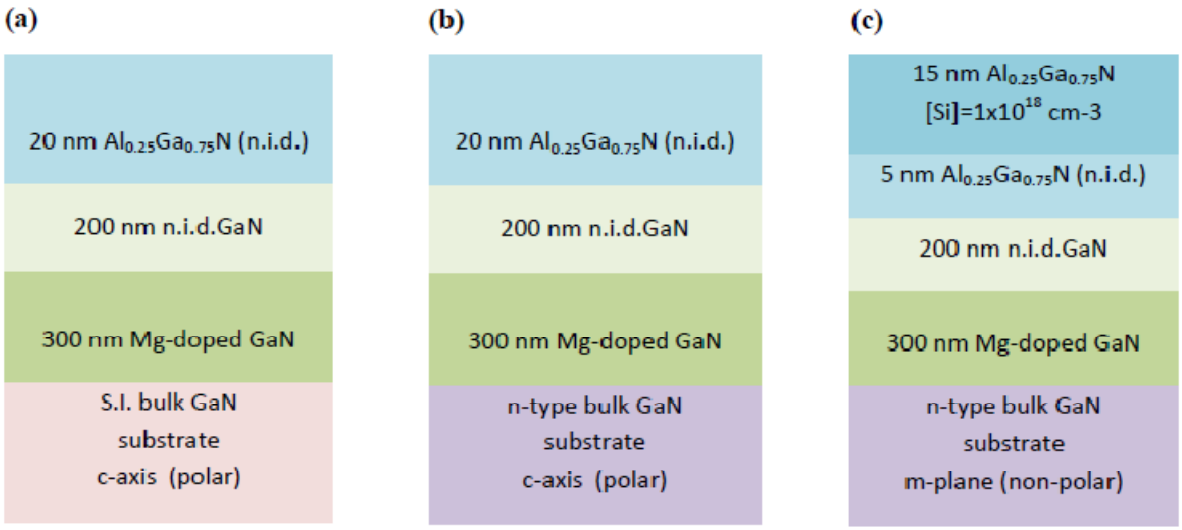


Figure 8.2 Schematic of heterostructure grown on (a) semi-insulating c-axis vicinal substrates. (b) n-type c-axis substrates. (c) n-type m-plane nonpolar substrates.

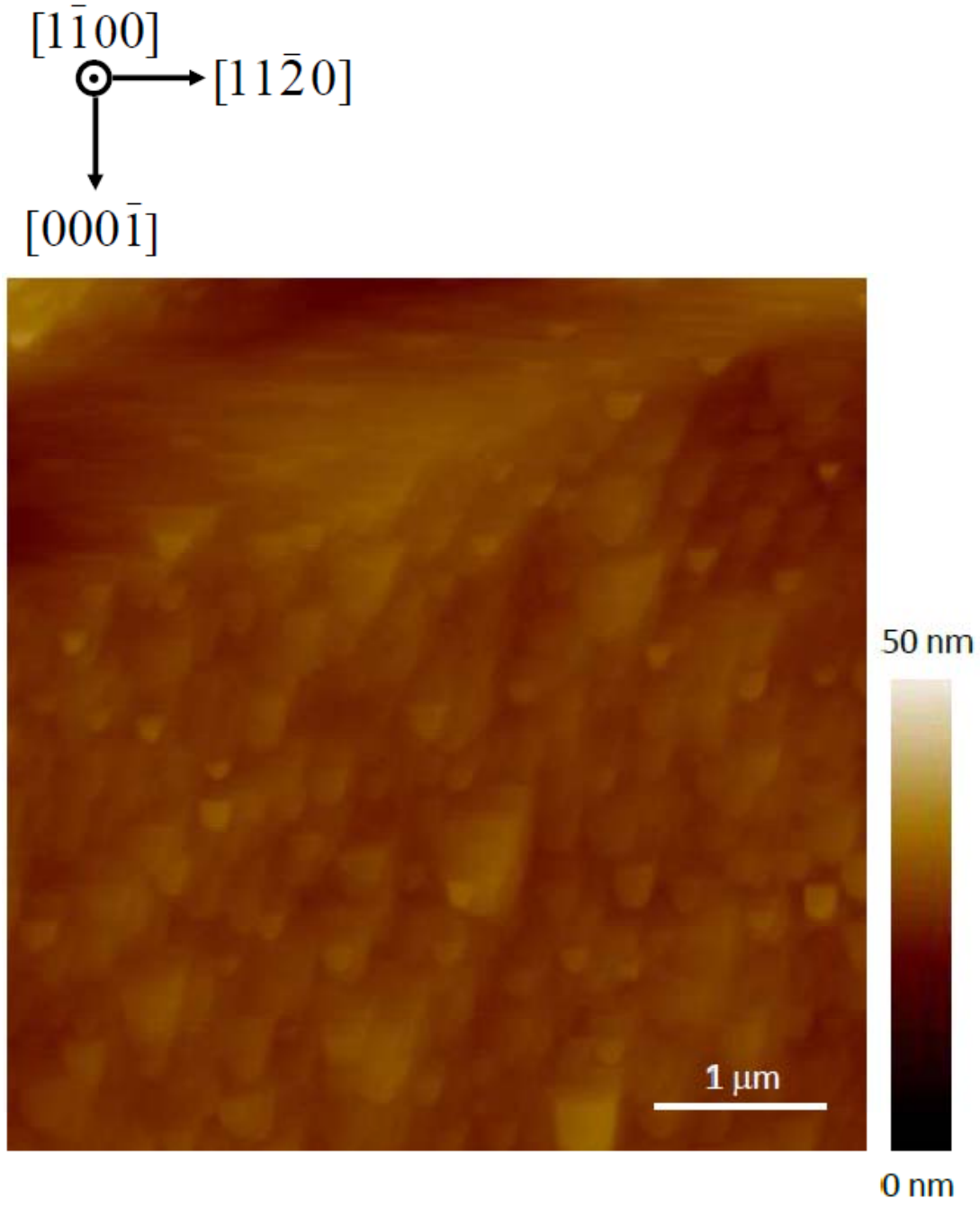


Figure 8.3 AFM image of nonpolar surface after full heterostructure growth. The RMS roughness for this 5 x 5 μm^2 area was 0.756 nm. Triangular-shaped defects are oriented in the $[000\bar{1}]$.

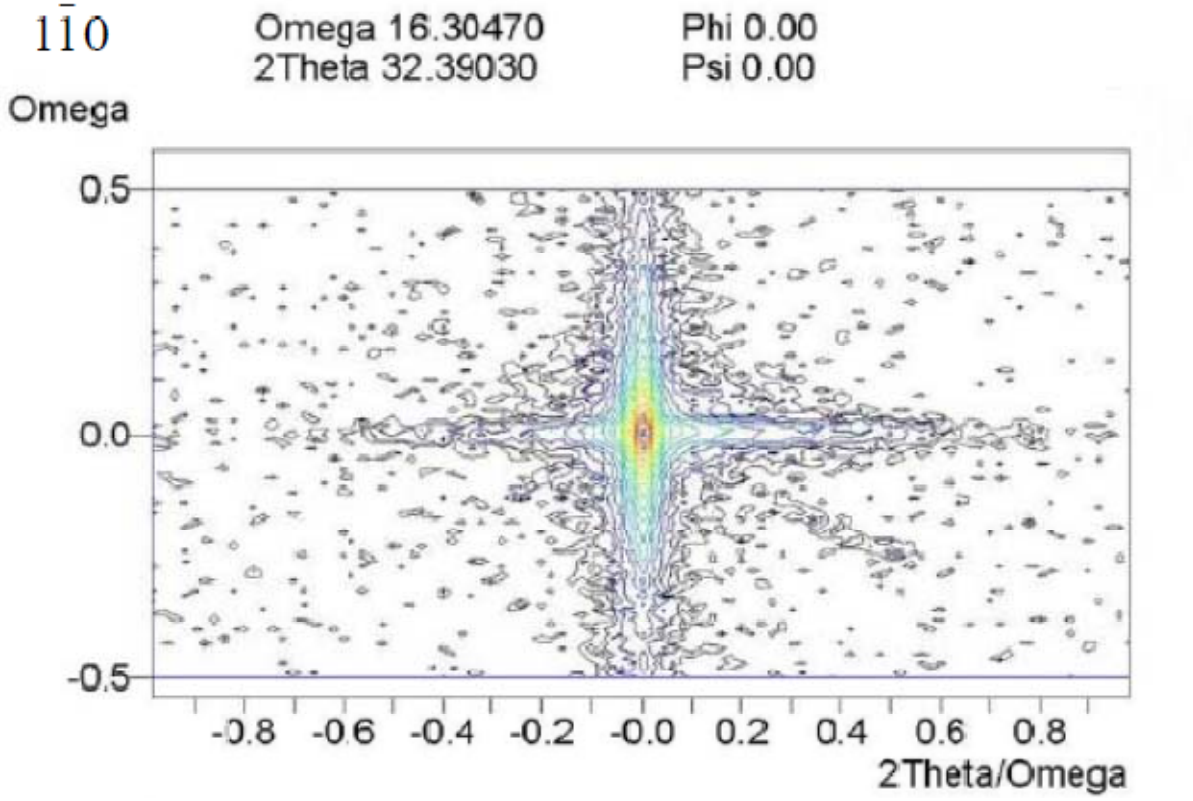


Figure 8.4 Reciprocal space map of the 1$\bar{1}$0 symmetric reflection. The horizontal axis (in this orientation) defines the compositional fluctuation of the $Al_xGa_{1-x}N$ barrier. Lateral components of broadening do not apply to the symmetric reflection.

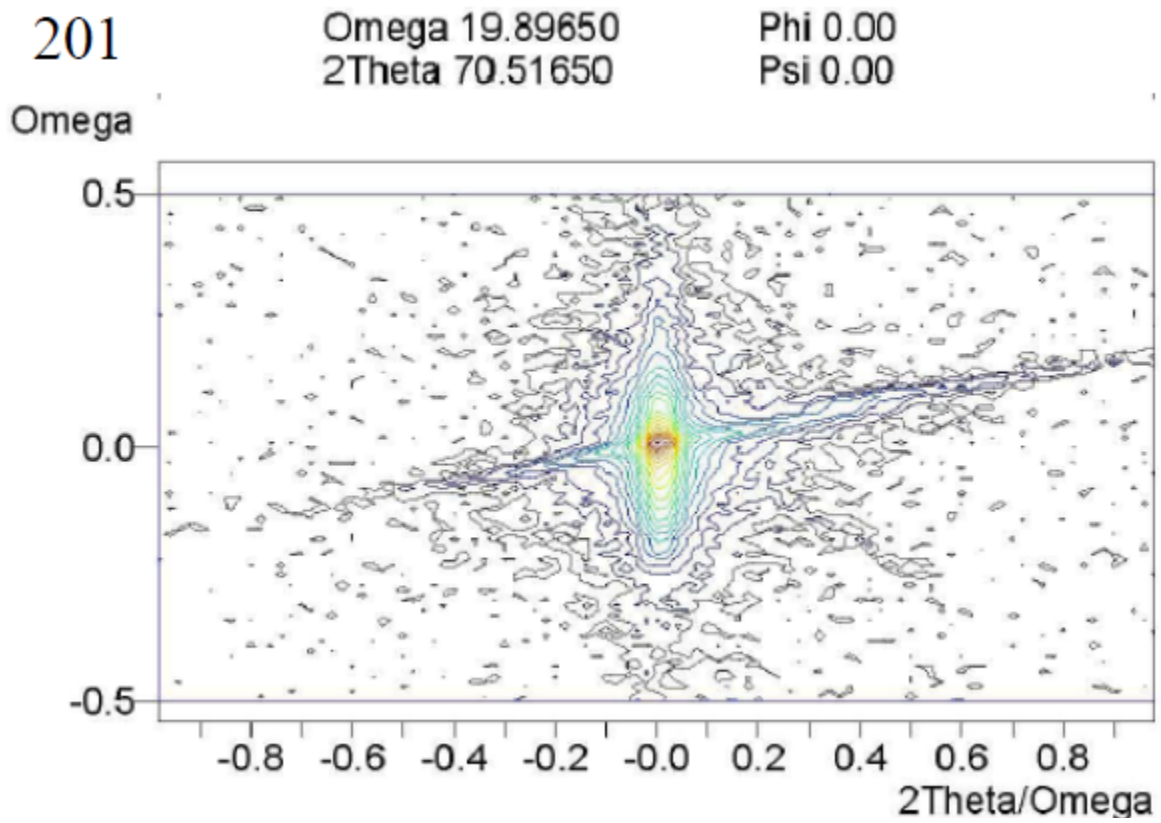


Figure 8.5 Reciprocal space map of the 201 asymmetric reflection. The horizontal axis (in this orientation) defines compositional fluctuation. Lateral components of broadening expand along the Omega (horizontal) axis.

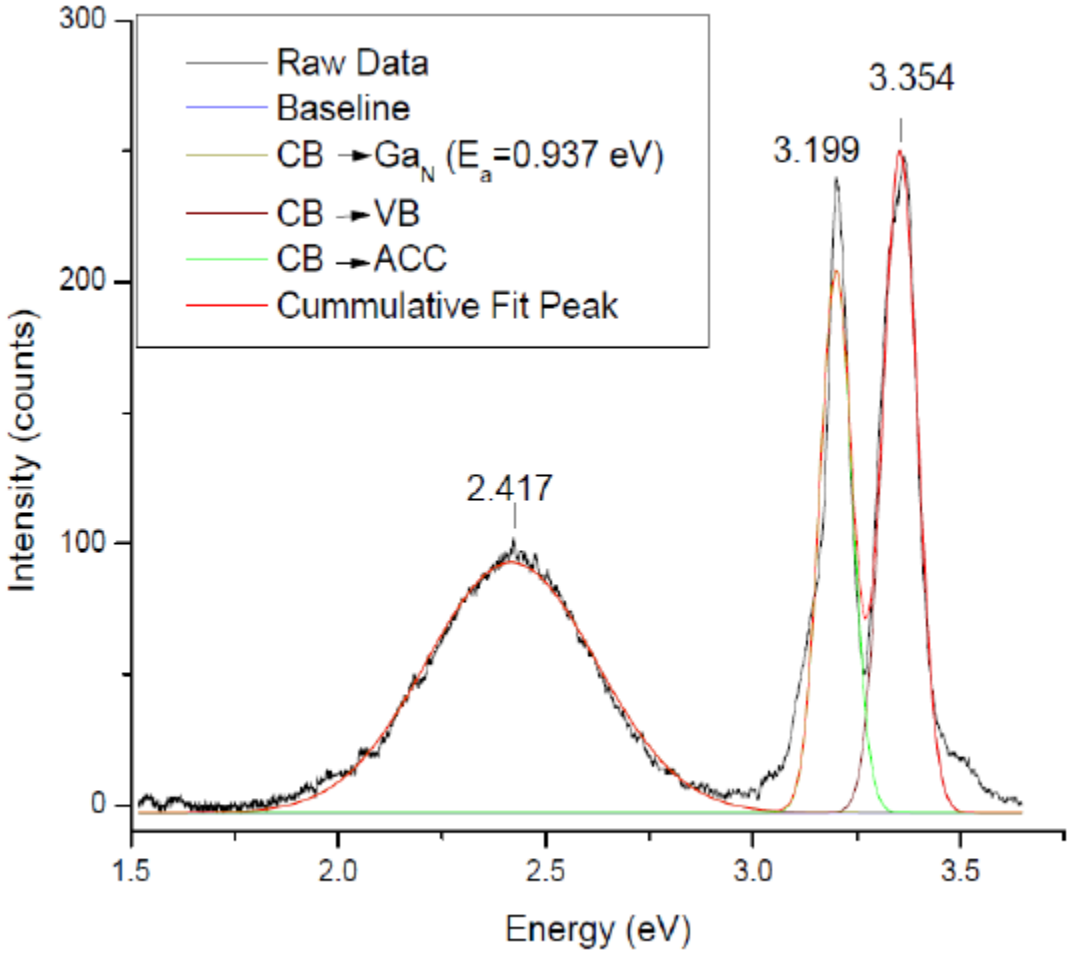


Figure 8.6 PL analysis reveals the CB → VB transition at 3.354 eV and the CB → ACC transition corresponding to an ionization energy of 0.16 eV and the CB → Ga_N corresponding to an ionization energy of 0.937 eV.

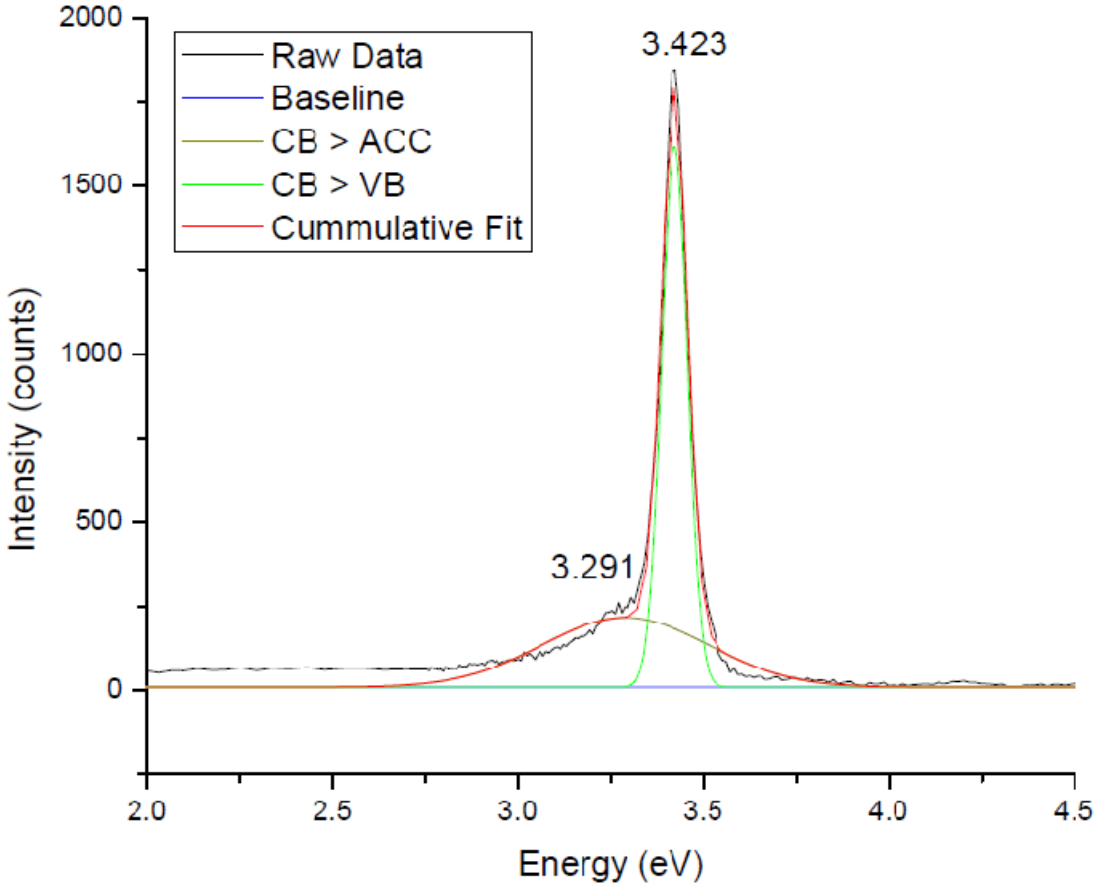


Figure 8.7 CL analysis revealed only the CB → VB transition at 3.423 eV and a weak CB → ACC transition corresponding to an ionization energy of 0.16 eV.

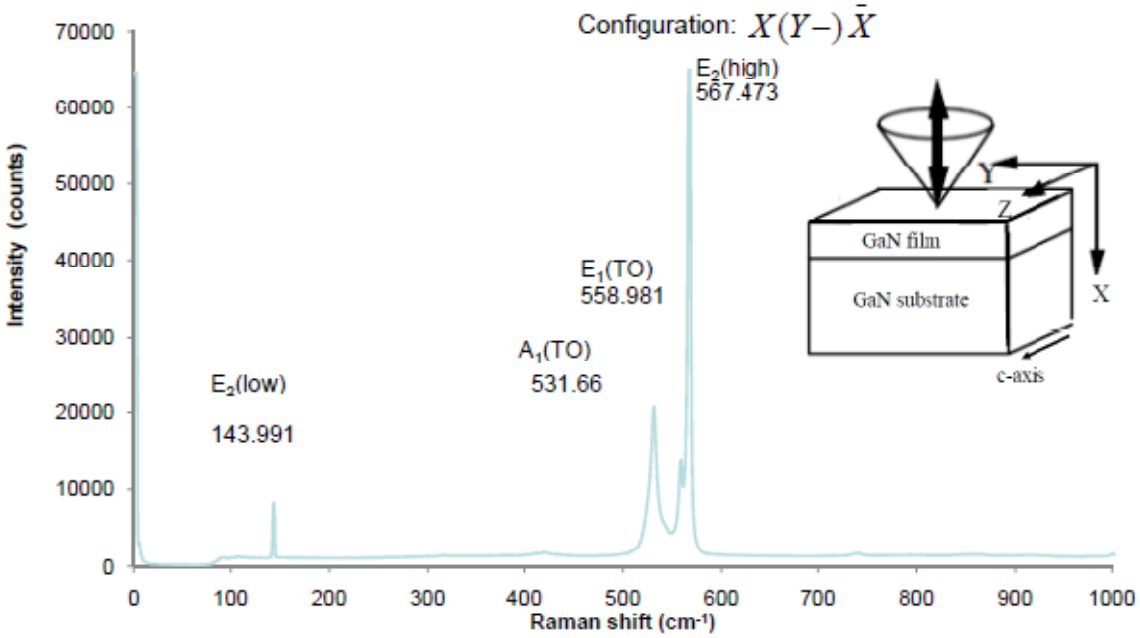


Figure 8.8 Porto notation for nonpolar m-plane GaN and the allowed modes by Raman selection rule [37].

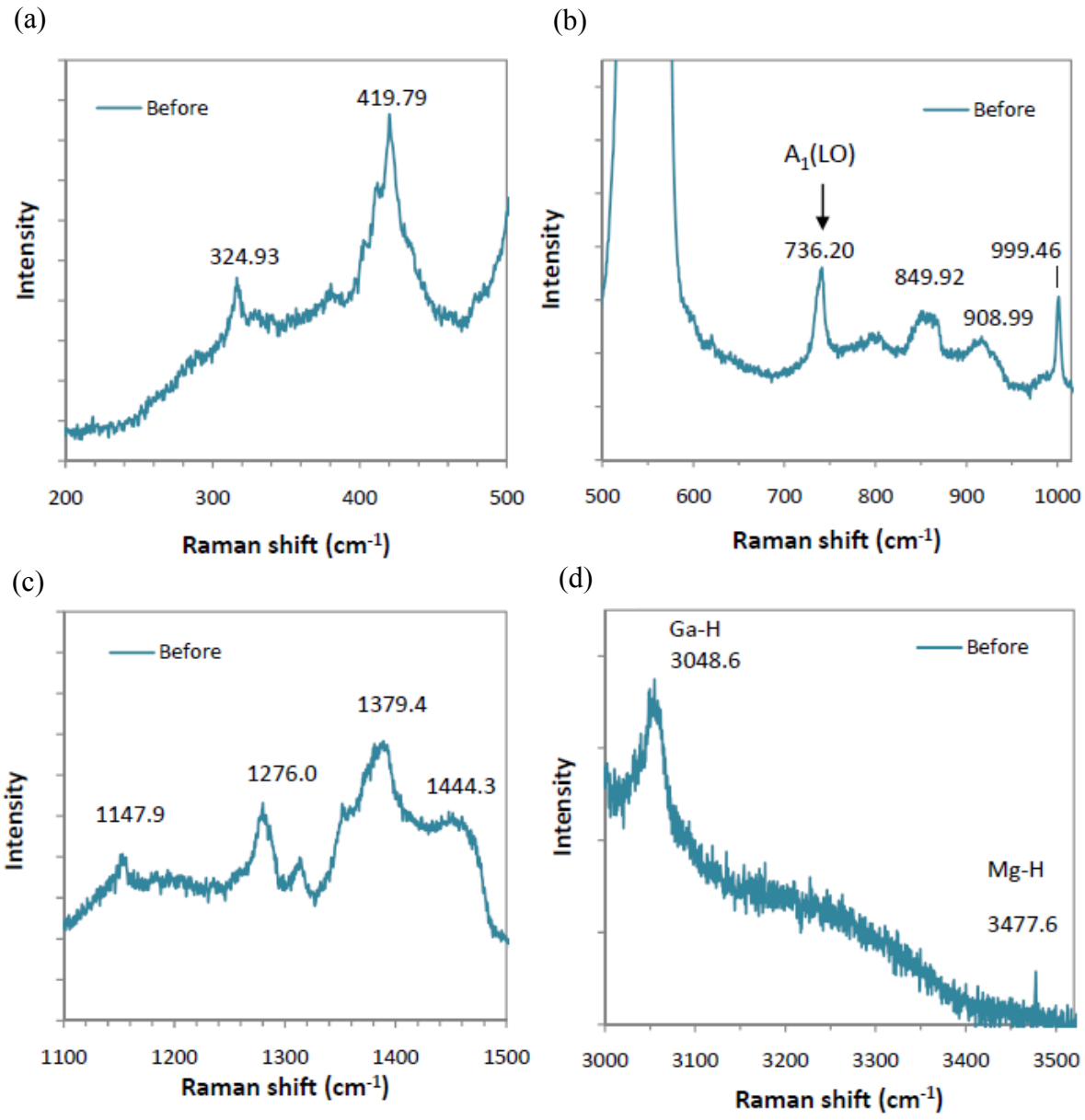


Figure 8.9 Raman shifts from HFET structure on m-plane bulk-GaN.

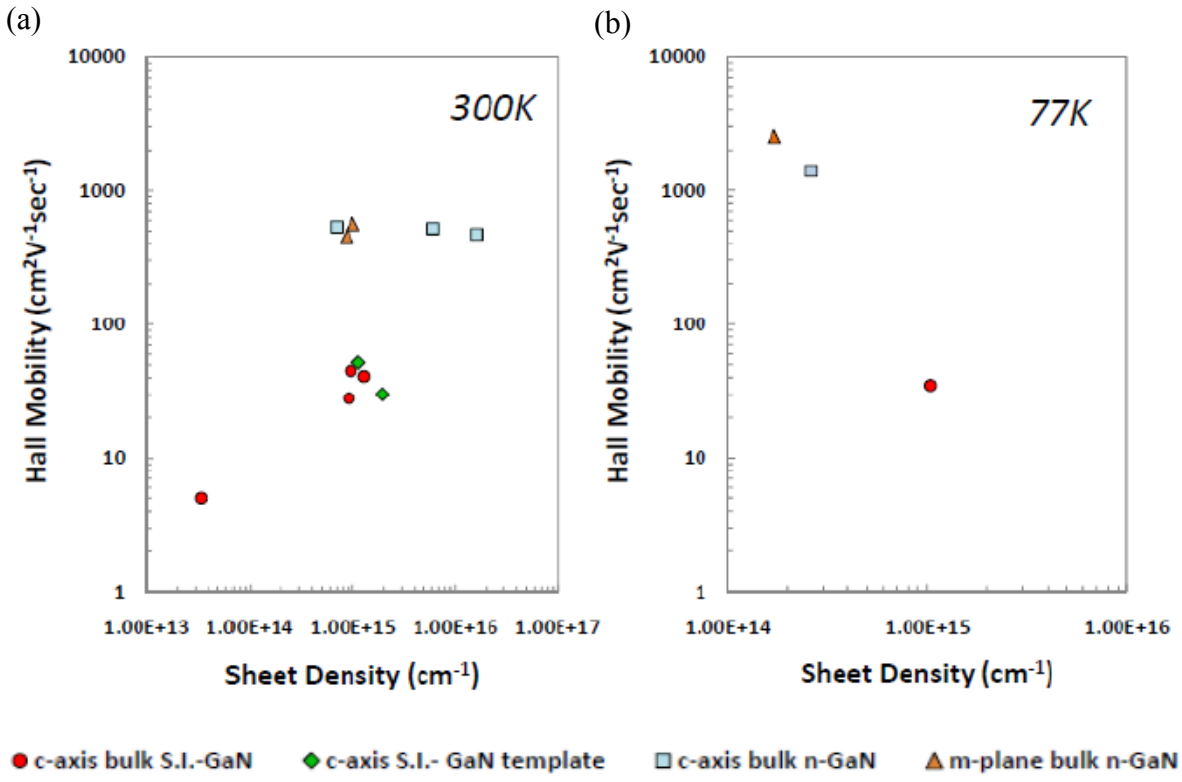
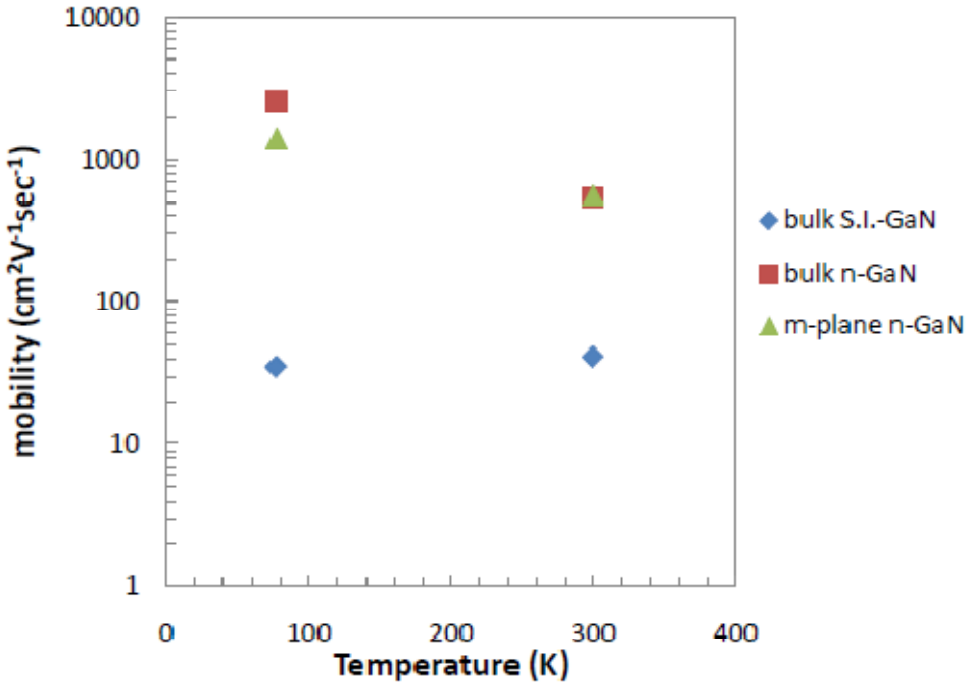


Figure 8.10 (a) Hall mobility vs. sheet density for all substrates studied reveal higher mobilities for bulk n-GaN (c-axis) as well as m-plane bulk GaN at RT and (b) at 77K.

(a)



(b)

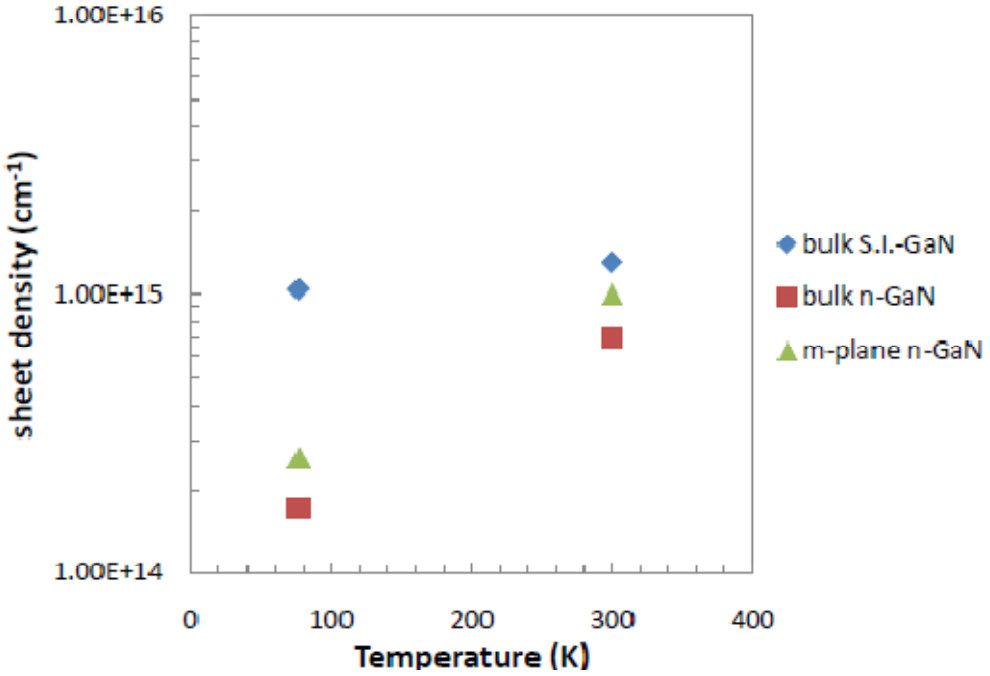


Figure 8.11 (a) Hall mobility vs. temperature and (b) sheet density vs. temperature for c-axis bulk n-GaN and m-plane bulk GaN.

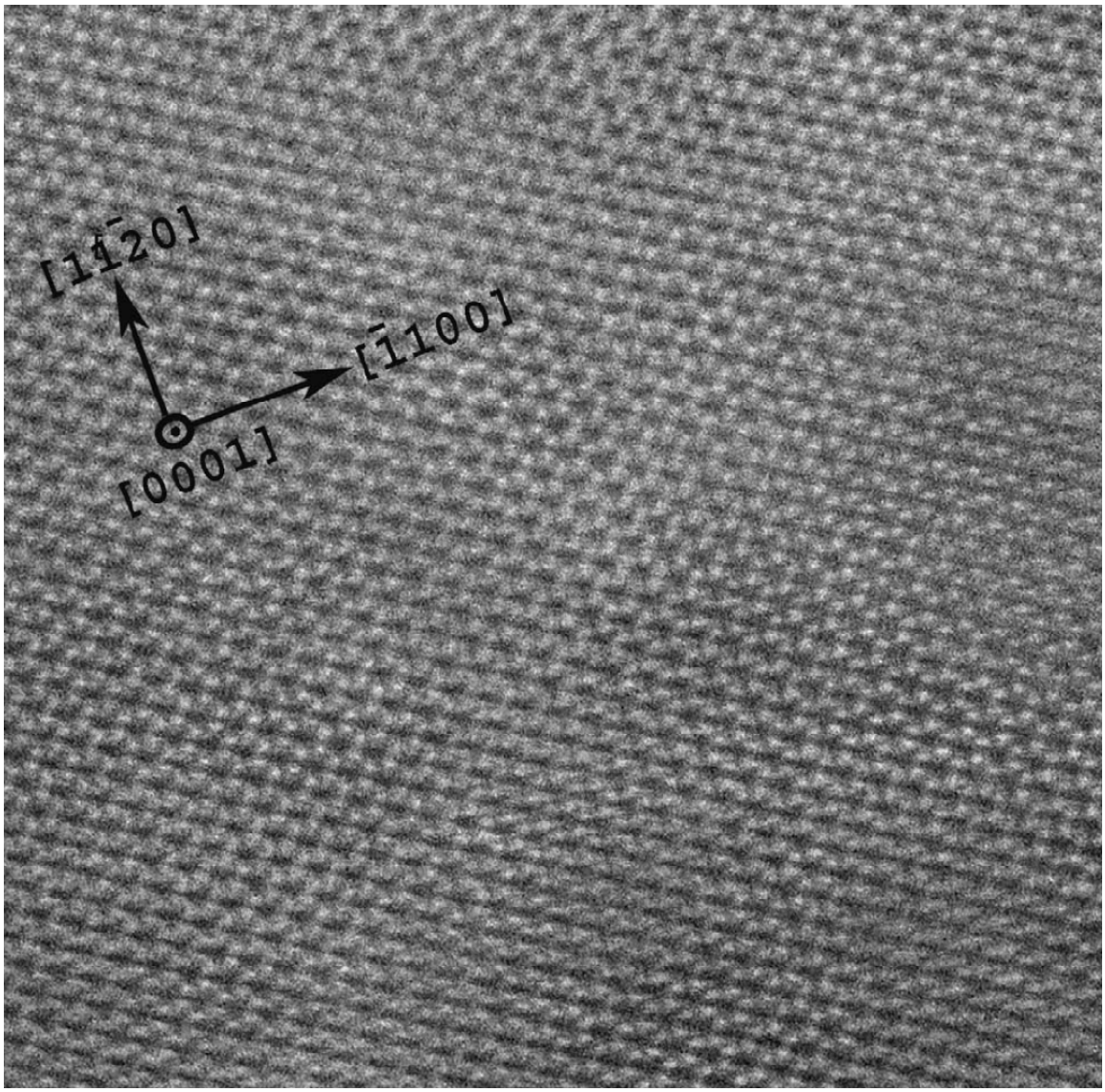


Figure 8.12 High angle dark field image of dislocation-free, stacking fault-free GaN buffer in heterostructure growth on m-plane nonpolar bulk GaN substrate.

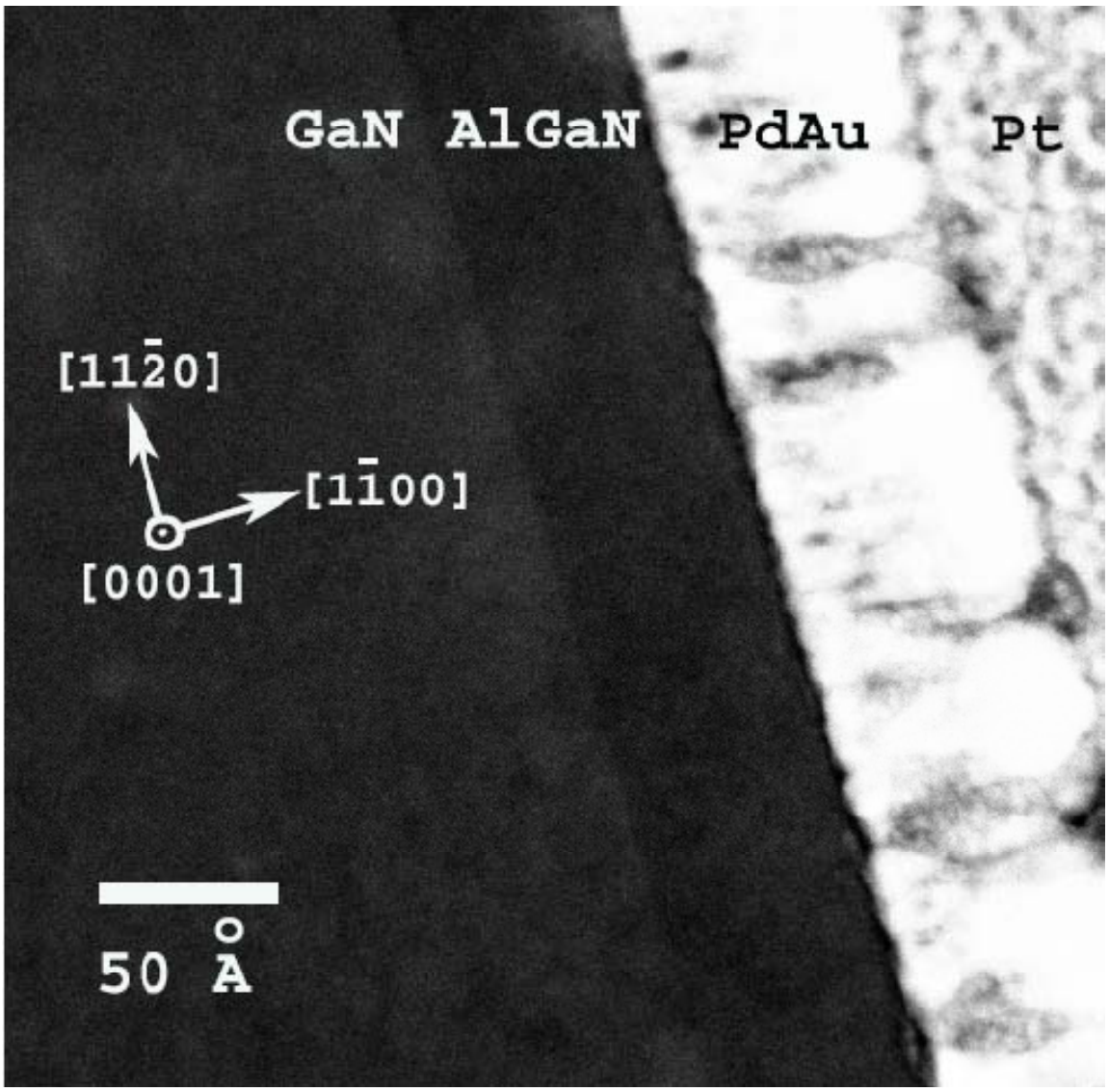


Figure 8.13 High angle dark field image showing GaN/interface with PdAu and Pt protective layers added during FIB processing.

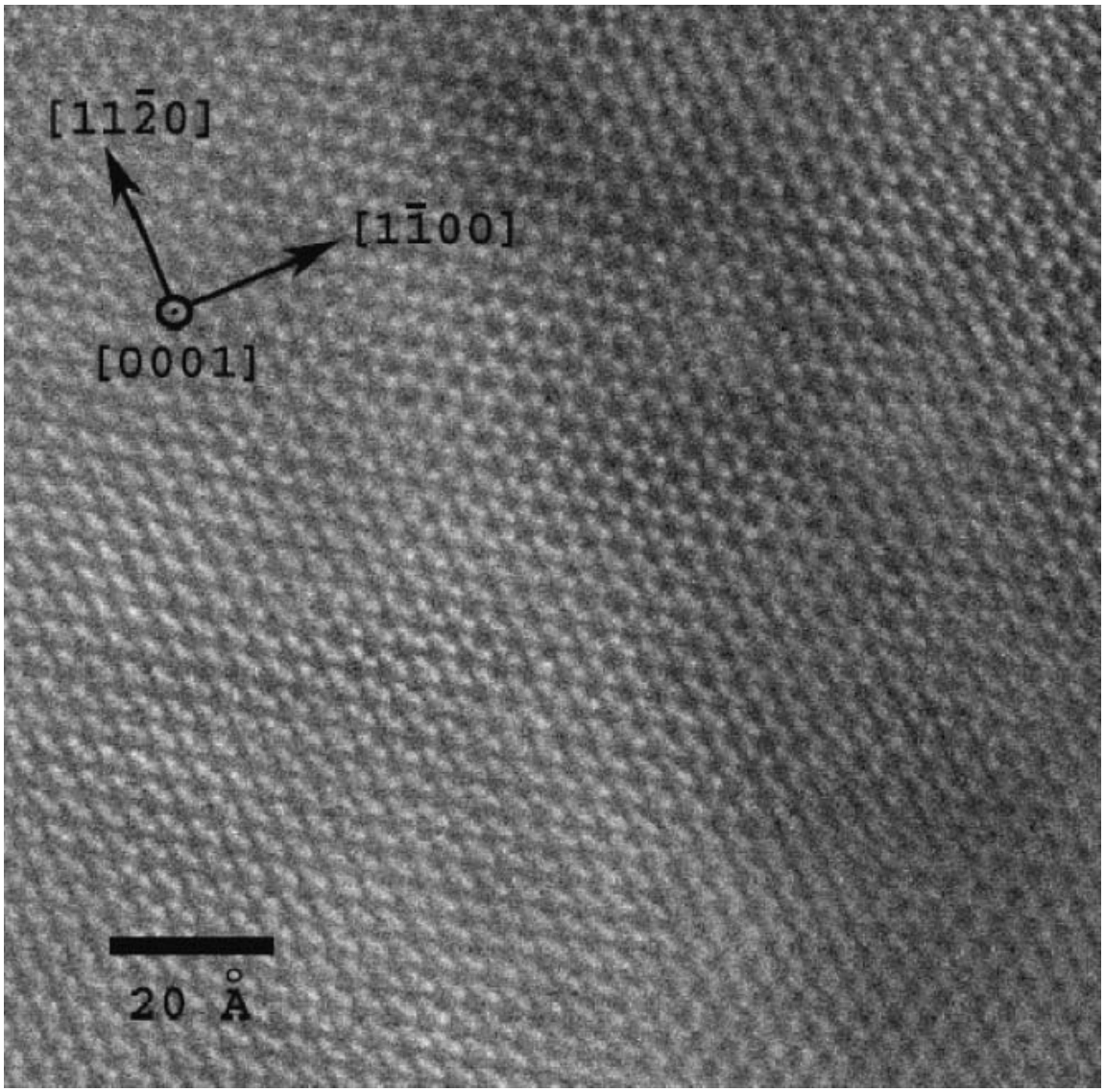


Figure 8.14 High angle diffraction image of GaN/AlGaN interface revealing GaN/AlGaN interface roughness ≤ 2 Å.

9. SUMMARY AND CONCLUSIONS

9.1 Summary of Experimental Work

$Al_{0.25}Ga_{0.75}N$/GaN heterostructures have been grown by OMVPE on polar (0001) and vicinal surfaces of semi-insulating and n-type bulk GaN, as well as nonpolar $(1\bar{1}00)$ surfaces. The electrical transport properties of these heterostructures, specifically the sheet carrier densities and the mobilities of the 2DEG have been compared for different heterostructure designs and substrate types. The presence of a charge layer at the epitaxy/bulk GaN interface necessitated exploring whether a Mg-doped GaN layer would provide an effective compensation mechanism for interfacial donors. Since a potential device outcome of this research would be the design of an enhancement-mode HFET, we wanted to compare 2DEG transport properties of heterostructures associated with polarization doping ((0001) growth surface), with those primarily dependent on modulation doping ($(1\bar{1}00)$ growth surface).

9.1.1 Heterostructures without Mg

We were able to perform RT Hall measurements on all $Al_{0.25}Ga_{0.75}N$/GaN heterostructures grown without Mg (Type I and II shown in Fig. 9.1). The 2DEG sheet densities were measured to be ~ 10^{13} cm^{-2}. However, the 2DEG mobilities were modulated by the interface charge at the epitaxy/bulk GaN. This modulation was clearly demonstrated by a dependence of the mobility and sheet density on GaN buffer thickness for both the modulation- and polarization-doped heterostructure designs.

The separate contributions from the ionized donors and the polarization charge to the room temperature 2DEG sheet density was assessed by evaluating results for Type I heterostructures grown with GaN buffer thicknesses $\geq$ 0.75 μm. The sheet charge density attributed to ionized donors, n_s^{id}, was determined to be 4.5 x 10^{12} cm^{-2} while that due to polarization charge, n_s^{polar}, was found to be 4.9 x 10^{12} cm^{-2} [1]. The highest room temperature 2DEG mobility for Type I heterostructures was 1805 $cm^2V^{-1}cm^{-1}$ [1]. The polarization charge density, $\sigma_{(P_{SP}+P_{PE})}$, predicted by an electrostatic analysis [2] was 3.0 x 10^{-7} coul·cm^{-2} compared to the experimentally determined polarization charge for Type I heterostructures of 1.5 x 10^{-7} coul·cm^{-2}. The electric charge, εE_d, contributed by the ionized donors in Type I heterostructures was 2.2 x 10^{-6} coul·cm^{-2}.

A second group of $Al_{0.25}Ga_{0.75}N$/GaN Type I and II heterostructures grown on SI (0001) bulk GaN substrates was grown to separate the effect of ionized carriers from the effect of Al scattering centers on the RT 2DEG sheet density. Elimination of unintentional Al scattering centers increased n_s^{polar} from 4.9 x 10^{12} cm^{-2} to 8.3 x 10^{12} cm^{-2} [3]. A coincident increase in RT 2DEG mobility, μ_{2DEG}^{RT}, from 1805 to 2065 $cm^2V^{-1}cm^{-1}$ was comparable to the best that have been reported using high mobility designs and was only 30% below the value predicted for AlGaN/GaN heterostructures with dislocation densities < 7 x 10^7 cm^{-2} [4]. Another factor contributing to the improved μ_{2DEG}^{RT} was the atomically smooth interface for the Type II heterostructure confirmed by high-angle dark field transmission electron micrographs. The experimental polarization charge density was determined to be 2.63 x 10^{-7} coul·cm^{-2}. We suggest that the 56% increase in $\sigma_{(P_{SP}+P_{PE})}$ is associated with reduced

scattering at the AlGaN/GaN interface and with the elimination of the ~ 1000 ppm unintentional Al background in the n.i.d. GaN buffer.

9.1.2 Heterostructures with Mg pre-ex situ anneal

We were unable to perform Hall measurements on AlGaN/GaN heterostructures with Mg-doped GaN layers grown on S.I. and n-type bulk GaN surfaces (see Fig. 9.2) prior to an 800^{o}C ex situ anneal because of the high sheet resistances associated with the fully-depleted n.i.d. GaN region and the presence of p-n junctions at the epitaxy/bulk GaN interface and the p-GaN/n.i.d. GaN interface. The presence of the p-n junctions within the heterostructure is analogous to pnin blocking layers used in photonic devices to restrict current flow to the active area. Shifts in the Raman spectra of the heterostructures revealed the presence of Mg donors, Mg atoms on nitrogen (N) sites, at a concentration of 2 x 10^{18}cm^{-3}. Magnesium acceptors, Mg atoms on gallium (Ga) sites, were also present, as evidenced by the inter-valence-band transition of the hole (IVBTH) in the Raman spectra. Photoluminescence and cathodoluminescence of the heterostructures confirmed the presence of both Mg donor and acceptor species.

9.1.3 Heterostructures with Mg post-ex situ anneal

After an 800^{o}C ex situ anneal, we were able to obtain linear I-V curves and therefore to perform Hall measurements on AlGaN/GaN heterostructures with Mg-doped GaN layers grown on S.I. and n-type bulk GaN surfaces (see Fig. 9.2). Room temperature sheet carrier densities on the order of 10^{15} cm^{-2} with significantly reduced mobilities were measured [5]. Shifts in the Raman spectra showed increased Mg donors (~2 x 10^{18} cm^{-3}) relative to the pre-

ex situ anneal concentrations as well as the presence of nitrogen vacancies, N_V, which were absent prior to the ex situ anneal. The presence of N_V in these heterostructures is consistent with the lower formation energy for N_V of ~ 1 eV in p-type GaN [6]. We concluded that the presence of Mg in the heterostructure significantly altered the HFET properties by reducing carrier confinement in the potential well and altering the ionization energies of the deep donors leading to compensation of acceptors. As a result, the absence of Mg acceptors at the epitaxy/bulk GaN interface allowed significant parallel conduction with measured sheet densities on the order of 10^{15} cm^{-2}.

The room temperature sheet density, n_s^{RT}, from n.i.d. AlGaN/GaN heterostructures grown on vicinal S.I. bulk GaN surfaces was 9.6 x 10^{14} cm^{-2}. At 77K, the sheet density, n_s^{77K}, was unchanged at 1.0 x 10^{15} cm^{-2}. The RT and 77K mobilities were 45 $cm^2V^{-1}cm^{-1}$ and 35 $cm^2V^{-1}cm^{-1}$ respectively. The presence of Mg in the heterostructure resulted in a predicted sheet charge density of $\sigma_{(P_{SP}+P_{PE})}$ = 2.2 x 10^{-7} coul·cm^{-2}.

The room temperature sheet density for heterostructures with 20 nm n.i.d. AlGaN barriers with 200 nm n.i.d. GaN buffers and 300 nm p-GaN compensation layers grown on n-type (0001) bulk GaN was 6.9 x 10^{14} cm^{-2}. There was a four-fold reduction in sheet density measured at 77K to 1.7 x 10^{14} cm^{-2} which was attributed to the freeze out of Si donors. Assuming that only Mg atoms act as scattering centers, calculations based on mean free path associated with the separation between these Mg atoms and using the low field carrier velocity, estimate a room temperature 2DEG channel mobility of ~600 $cm^2V^{-1}sec^{-1}$ [5]. The measured μ_{2DEG}^{RT} was 537 $cm^2V^{-1}sec^{-1}$. There was nearly a five-fold increase in mobility at low temperature. The improvement of μ_{2DEG}^{77K} to 2540 $cm^2V^{-1}sec^{-1}$ [7] suggested improved

mobility due to freeze out of Si donors at the epitaxy/bulk GaN interface. Again, the presence of Mg in the heterostructure reduced the predicted sheet charge density to 2.2 x 10^{-7} coul·cm^{-2}.

The n_s^{RT} for heterostructures with 15 nm n-AlGaN barriers and 5 nm n.i.d. AlGaN spacers with 200 nm n.i.d. GaN buffers and 300 nm p-GaN compensation layers grown on nonpolar n-type $(1\bar{1}00)$ bulk GaN was 1.0 x 10^{15} cm^{-2}. There was nearly a six-fold reduction in sheet density measured at 77K to 1.7 x 10^{14} cm^{-2}. The n_s^{77K}/n_s^{RT} ratio of 0.25 for the nonpolar heterostructure was equivalent to that of the polar heterostructures previously discussed. By taking the ratio of the Arrhenius behaviors at 77K relative to 300K, an activation energy of 0.02 eV was found, which corresponds to the donor ionization energy of silicon, suggesting that silicon ionized impurities freeze-out when the temperature is lowered to 77K. The room temperature mobility was 566 $cm^2V^{-1}sec^{-1}$, which reflects the effect of the Mg scattering centers on RT mobility. There was only a 2.5-fold improvement in 77K mobility to 1399 $cm^2V^{-1}sec^{-1}$. The unexpectedly high n_s at both RT and 77K for the polar and nonpolar n-type substrates prevented a clear determination of the effect of polarization-doping versus modulation-doping on that transport property. However, the significantly higher μ_{2DEG}^{77K} for the heterostructure grown on the c-axis n-type bulk GaN substrate relative to the μ_{2DEG}^{77K} for the nonpolar heterostructure suggests that degraded mobility may be the result of ineffective separation of the ionized impurities in the $Al_xGa_{1-x}N$ barrier from electrons in the 2DEG due to insufficient thickness of the undoped $Al_xGa_{1-x}N$ spacer. The thin AlGaN spacer was the direct result of the lower growth rate on the m-plane surface. In

order to determine whether the 2DEG transport properties for heterostructures grown on $(1\bar{1}00)$ bulk GaN surfaces are comparable or improved relative to their (0001) counterparts, the experiment must be repeated with a sufficient $Al_xGa_{1-x}N$ spacer thickness to insure spatial separation of the electrons in the 2DEG channel from the ionized donors in the AlGaN barrier.

9.2 Conclusions

The bulk GaN substrates used in this study are not acceptable for electronic device fabrication due to the presence of a charge layer at the epitaxy/bulk GaN interface. Direct evidence for this statement is the modulation of room temperature mobility observed for the $Al_{0.25}Ga_{0.75}N$/GaN heterostructures grown on S.I. (0001) bulk GaN. This charge layer may lead to parallel conduction in HFET devices as evidenced by the higher RT sheet densities measured for heterostructures with 2DEG channels in close proximity to the epitaxy/bulk GaN interface. In enhancement-mode AlGaN/GaN HFET devices, parallel conduction can lead to insufficient $V_{threshold}$ to ensure a zero drain current at zero bias. Shubnikov de Haas measurements have the potential to directly measure whether over-population of subbands by contribution of free electrons from the epitaxy/bulk GaN interface has caused a modulation of the 2DEG mobility. Deleterious impact of the interfacial charge layer was confirmed by large leakage currents between two ohmic contact pads [8].

We have shown that an ionized acceptor concentration $\geq 2 \times 10^{17}$ cm^{-3} is sufficient to compensate donors at the epitaxy/bulk GaN interface. However, at those concentrations, the

200 nm n.i.d.-GaN layer becomes depleted of n-type carriers resulting in insufficient electron confinement in the potential well. While electron confinement in the potential well can be achieved with ionized acceptor concentrations $\leq 1 \times 10^{17}$ cm^{-3}, compensation of the donors at the epitaxy/bulk GaN interface is insufficient. More importantly, our studies have shown that Mg barrier layers are an ineffective means of blocking charge at the epitaxy/bulk GaN interface from the 2DEG channel because the required annealing step necessary to form ohmic contacts to the device causes formation of nitrogen vacancies leading to self-compensation in p-GaN films and an n-type conductive layer in the undepleted region of the p-GaN layer.

9.3 Future Directions

Homoepitaxial growth of $Al_{0.25}Ga_{0.75}N$/GaN heterostructures shows great promise with regard to reduction of the threading dislocation density by elimination of the thermally resistive nucleation layer required to initiate epitaxial growth on non-native substrates. The improved thermal conductivities realized by the reduction of dislocation density in the bulk GaN substrate [9, 10] offer the potential for high breakdown voltage devices. However, an essential aspect of homoepitaxial growth is the development of non-conducting substrates and substrate preparation techniques that do not leave a charge layer at the epitaxy/bulk GaN interface.

Others have shown improved 2DEG mobilities and sheet densities [11] by incorporating an AlN barrier at the AlGaN/GaN interface. Inclusion of an AlGaN barrier can only be accomplished by optimizing the growth kinetics for AlGaN/GaN heterostructures which can be most efficiently performed using in situ diagnostic tools such as reflectance

anisotropic spectroscopy for growth rate analysis and dual zone pyrometer control of the substrate block temperature. The substantial cost of bulk GaN polar and nonpolar substrates warrants more effective means to find optimal conditions for growth kinetics. The reduced growth rate on m-plane surfaces relative to c-plane surfaces and the subtle differences in growth kinetics introduced by vicinal offcuts of those surfaces warrants in situ diagnostic capability a minimum requirement to advance the development of wide bandgap heterostructures.

9.4 References

[1] J.A. Grenko, C.W. Ebert, C.L. Reynolds, Jr., M.A.L. Johnson, A.D. Hanser, E.A. Preble, T. Paskova, and K.R. Evans, *Phys. Stat. Solidi (c),* **6** (2009) S1037.

[2] R. Vetury, I.P. Smorchkova, C.R. Elsass, B. Heying, S. Keller, and U.K. Mishra, U.K., *Mat. Res. Soc. Symp.,* **622** (2000) T2.5.1.

[3] J.A. Grenko, C.L. Reynolds, Jr., G. J. Duscher, C.W. Ebert, D.W. Barlage, M.A.L. Johnson, T. Paskova, E. Preble, and K. Evans, to be published.

[4] Z. Bougrioua, M. Azize, P. Lorenzini, M. Laugt, and H. Haas, *Phys. Stat. Sol. (a),* **202** (2005) 536.

[5] J.A. Grenko, C.L. Reynolds, Jr., G. J. Duscher, S. E. Lappi, C.W. Ebert, D.W. Barlage, M.A.L. Johnson, T. Paskova, E. Preble, and K. Evans, to be published.

[6] C.G. Van de Walle and J. Neugebauer, *J. Appl. Phys.,* **95** (2004) 3851.

[7] J.A. Grenko, C.L. Reynolds, Jr., G. J. Duscher, S. E. Lappi, C.W. Ebert, D.W. Barlage, M.A.L. Johnson, T. Paskova, E. Preble, and K. Evans, to be published.

[8] A. Crespo, unpublished.

[9] C. Mion et al, *Superlattices and Microstructures,* **40** (2006) 338.

[10] C. Mion et al, *Appl. Phys. Lett*., **89** (2006) 092123.

[11] M. Germain et al, *Mat. Res. Symp. Proc.,* **798** (2004) Y10.22.1.

9.5 Figures

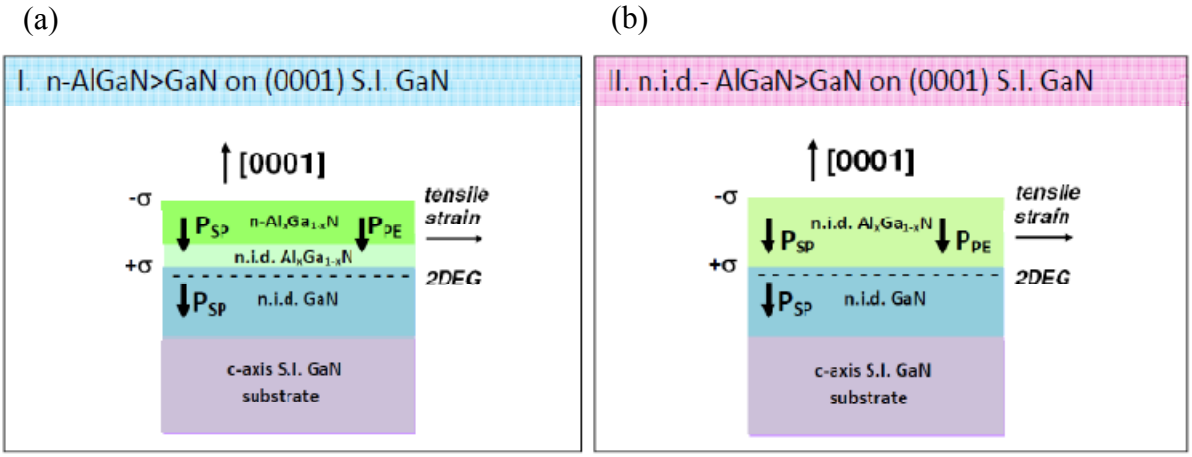


Figure 9.1 $Al_{0.25}Ga_{0.75}N$/GaN heterostructures grown (a) with 15 nm n-AlGaN barriers and 5 nm n.i.d. AlGaN spacers (Type I) (b) with 20 nm n.i.d. AlGaN barriers (Type II) on n.i.d. GaN buffers on S.I. (0001) bulk GaN measured RT Hall sheet densities of 10^{13} cm^{-2} for the 2DEG. However, μ_{RT}^{2DEG} was modulated by charge at the epitaxy/bulk GaN interface.

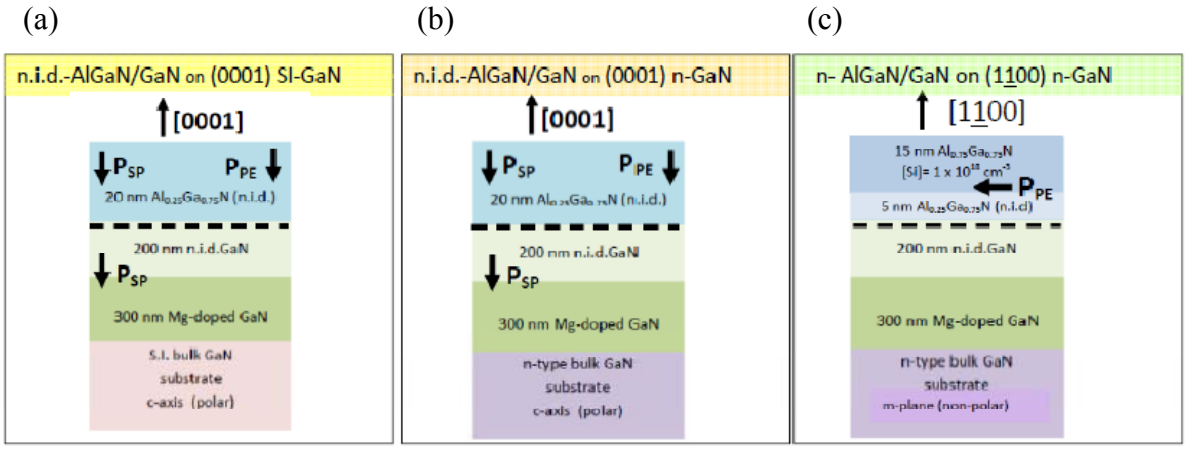


Figure 9.2 $Al_{0.25}Ga_{0.75}N$/GaN heterostructures grown with 20 nm n.i.d. AlGaN barrier/ 200 nm n.i.d. GaN buffer/ 300 nm Mg-doped GaN layer on (a) S.I. and (b) n-type (0001) bulk GaN substrates. (c) 15 nm n-AlGaN barrier/ 5 nm n.i.d. AlGaN spacer/200 nm n.i.d. GaN buffer/ 300 nm Mg-doped GaN on n-type $(1\bar{1}00)$ bulk GaN substrate. The Mg-doped GaN layer was intended to compensate charge at the epitaxy/bulk GaN interface.